UNIVERSITY OF SOUTHAMPTON

FACULTY OF ENGINEERING AND THE ENVIRONMENT

Power Flow Analysis of Nonlinear Dynamical Systems

by

Jian Yang

Thesis for the degree of Doctor of Philosophy

April 2013

UNIVERSITY OF SOUTHAMPTON

ABSTRACT

FACULTY OF ENGINEERING AND THE ENVIRONMENT

Doctor of Philosophy

Power Flow Analysis of Nonlinear Dynamical Systems

by Jian Yang

The power flow analysis approach, which arose from high-frequency vibration problems, has been developed into a powerful technique to characterise the dynamic behaviour of complex structures and coupled systems. It has been extensively used to study various linear systems. However, because of the complexity in modelling and simulation, the power flow behaviour of nonlinear dynamical systems remains largely unexplored. This thesis aims to develop power flow analysis approaches for nonlinear dynamical systems, to investigate the effects of damping and/or stiffness nonlinearities on their power flow behaviour, and to apply the findings to enhance the performance of energy harvesting devices as well as vibration control systems.

Power flow characteristics of the Duffing and the Van der Pol (VDP) oscillators are investigated to address the distinct power input and dissipation behaviour due to stiffness and damping nonlinearities, respectively. It is shown that in a nonlinear velocity response with multiple frequency signatures, only the in-phase component of the same frequency as the harmonic excitation contributes to the time-averaged input power. It is demonstrated that bifurcations can cause significant jumps of time-averaged power flows, whereas the associated time-averaged input power of a chaotic response is insensitive to the initial conditions but tends to an asymptotic value as the averaging time increases. It is also found that the time-averaged input power of the unforced VDP oscillator can become negative in some ranges of excitation frequencies.

Power flow behaviour of two degrees-of-freedom systems with nonlinear stiffness/-damping is also studied using the developed methods to enhance vibration isolation/absorption performance. It is demonstrated that the stiffness and damping nonlinearities in the system affects time-averaged power flows mainly in a narrow frequency range around resonance frequencies.

The work described in this thesis provides new insights into power flow generation, transmission and dissipation mechanisms in nonlinear dynamical systems and facilitates more reliable and effective designs with improved dynamic performance. The ability of the VDP oscillator to extract external energy sheds light on energy harvesting using flow-induced vibrations of a nonlinear flapping foil system. A nonlinear isolator with a negative stiffness mechanism is proposed providing less input power in an enlarged frequency range. These studies thus yield an improved understanding of power flow behaviour in nonlinear dynamical systems.

Contents

List of Figures

List of Tables

Declarations of Authorship

I, Jian Yang, declare that the thesis entitled "*Power flow analysis of nonlinear dynamical systems*" and the work presented in the thesis are both my own, and have been generated by me as the result of my own original research. I confirm that:

- this work was done wholly or mainly while in candidature for a research degree at this University;
- where any part of this thesis has previously been submitted for a degree or any other qualification at this University or any other institution, this has been clearly stated;
- where I have consulted the published work of others, this is always clearly attributed;
- where I have quoted from the work of others, the source is always given. With the exception of such quotations, this thesis is entirely my own work
- I have acknowledged all main sources of help;
- where the thesis is based on work done by myself jointly with others, I have made clear exactly what was done by others and what I have contributed myself;
- parts of this work have been published as given in the list of publications.

Signed: ..... *Jian Yang* .....

Date: ..... *26 April 2013* .....

Acknowledgements

I wish to express my sincere gratitude to my supervisors Dr. Ye Ping Xiong and Professor Jing Tang Xing for academic supervision, guidance, and encouragement in every aspect of this project over the past three years. I would also like to thank Professor Tianyun Li from Huazhong University of Science and Technology for his personal help and support since my undergraduate study.

I am also grateful to many friends in I met in Southamtpon, especially to Deng Pan and Chaotan Sima, for sharing the ups and downs of PhD study with me right from the start, to Fanfan, Shufeng, Tauseef, Pareecha, Aichun, Wei, Yuan, Judy, Adam, Nick and many others in the Fluid Structure Interactions Research Group for making it such a nice place to work in, to excellent hosts and friends Ian and Lucy Castro for making me feel at home in the UK, especially during each Christmas, and of course, to my girlfriend Joyce Chi who deserves a special mention for standing by me and being supportive of my study all the time.

However, all my personal developments would not have been possible without the constant presence, care and support of my family. I hope my mum and dad, and my brother can accept this completion of PhD as a reward for their enduring love. This thesis is dedicated to my parents.

Acronyms

DOF	degree-of-freedom
FEA	finite element analysis
FRF	frequency response function
HB	harmonic balance
LCO	limit cycle oscillation
NSM	negative stiffness mechanism
PFA	power flow analysis
RK	Runge-Kutta
SDOF	single degree-of-freedom
SEA	statistical energy analysis
TAIP	time-averaged input power
TADP	time-averaged dissipated power
VDP	Van der Pol

Nomenclature

b	half chord of the foil
B	magnetic flux density
c	damping coefficient
c_h	damping coefficient in the heave DOF
c_α	damping coefficient in the pitch DOF
$[C]$	damping matrix in Chapter 3
$[C_l]$	the linear part of damping matrix in Chapter 3
$C_l(\tau)$	aerodynamic lift coefficient
$C_m(\tau)$	aerodynamic moment coefficient
E_c	the change in the energy stored in an inductor
E_d	dissipated energy
E_g	generated energy (energy consumed by resistor R)
E_{in}	input energy
$E(r)$	complete elliptical integral of the second kind
f	non-dimensional excitation amplitude in Chapters 4 and 5
f_0	non-dimensional excitation amplitude in Chapters 6,7 and 9
$\{f_e(t)\}$	external force vector
F	lift force in Chapter 8
F_M	electro-magnetic force
h	displacement in the heave DOF
i	$=\sqrt{-1}$
i	dynamic current
I_α	mass moment of inertia
k	stiffness coefficient
K	kinetic energy

$\dot{K}$	the rate of change of kinetic energy
$[K]$	stiffness matrix in Chapter 3
$[K_l]$	the linear part of stiffness matrix in Chapter 3
K_{max}	maximum kinetic energy
K_h	stiffness in the heave DOF
K_{h1}	linear stiffness coefficient
K_{h2}	nonlinear stiffness coefficient
$K(r)$	complete elliptic integral of the first kind
K_α	stiffness in the pitch DOF
K_{α_1}	linear stiffness coefficient
K_{α_2}	nonlinear stiffness coefficient
l	effective length of the moving coil
L	electric inductance
m	mass
m_1	mass of the base structure in Chapter 6;
	mass of the primary structure in Chapter 7
m_2	mass of the excited mass in Chapter 6;
	mass of the absorber in Chapter 7
M	pitching moment in Chapter 8
$[M]$	mass matrix in Chapter 3
$[M_l]$	the linear part of mass matrix in Chapter 3
p_a	instantaneous absorbed power
$\bar{p}_a$	time-averaged absorbed power
p_c	rate of change of energy stored in an electric inductor
p_d	dissipated power
$\bar{p}_d$	time-averaged dissipated power
p_g	generated power, i.e., power consumed by resistor R
p_{in}	instantaneous input power
$\bar{p}_{in}$	time-averaged input power
p_t	instantaneous transmitted power
$\bar{p}_t$	time-averaged transmitted power
P	compression force
$\bar{P}_{in}$	upper bound of time-averaged input power

r_α	non-dimensional radius of gyration
R	electrical resistance
S	mass static moment
t	non-dimensional time in Chapters 4 and 5;
	physical time in Chapters 6, 7, 8, 9
U	potential energy
$\dot{U}$	the rate of change of potential energy
V	velocity of air current
V^*	non-dimensional velocity of air current
x_α	non-dimensional distance from elastic axis to centre of mass
α	linear stiffness coefficient of the Duffing oscillator;
	damping parameter of the Van der Pol oscillator;
	nonlinear damping parameter of the isolator in Chapter 6;
	nonlinear stiffness parameter of the primary structure in Chapter 7;
	pitching angle of the foil in Chapter 8
	non-dimensional stiffness parameter in Chapter 9
β	nonlinear stiffness coefficient of the Duffing oscillator;
	linear stiffness coefficient of the Van der Pol oscillator;
	nonlinear stiffness parameter of the isolator in Chapter 6;
	nonlinear stiffness parameter of the absorber in Chapter 7;
β_α	non-dimensional nonlinear stiffness coefficient in pitch DOF
β_ξ	non-dimensional nonlinear stiffness coefficient in heave DOF
γ	frequency ratio
δ	dynamic deflection of the nonlinear isolator in Chapter 6;
	dynamic deflection of the nonlinear absorber in Chapter 7
ϵ	non-dimensional nonlinear stiffness coefficient in Chapter 6;
	non-dimensional nonlinear stiffness coefficient in Chapter 7
ζ_ξ	non-dimensional damping coefficient in the heave motion
ζ_α	non-dimensional damping coefficient in the pitch motion
η	non-dimensional nonlinear damping coefficient in Chapter 6;
	non-dimensional nonlinear stiffness coefficient in Chapter 7
μ	mass ratio
ξ	non-dimensional damping coefficient in Chapters 4 and 9;

	non-dimensional displacement in heave DOF in Chapter 8
ξ_1, ξ_2	non-dimensional damping coefficient
ρ	density of air
$\Psi_1, \Psi_2, \epsilon_1, \epsilon_2$	constants in Wagner function
τ	non-dimensional time
$\phi(\tau)$	Wagner function
ω	excitation frequency (non-dimensional in Chapters 4 and 5)
ω_r	frequency components in response/power
ω_α	uncoupled natural frequency in pitch motion
ω_ξ	uncoupled natural frequency in heave motion
Ω	non-dimensional excitation frequency

Chapter 1

Introduction

1.1 Engineering background

The dynamic behaviour of a system accounts for an important aspect of its overall performance, but to obtain the detailed dynamic characteristics might be a difficult task. For simple structures such as uniform rods, beams or plates with ideal boundary conditions, governing equations of motion can be obtained using classical mechanics theory and their solutions allow analytical representation of the responses. However, in many practical situations, where either the geometrical or material properties of a structure may vary, or the boundary conditions cannot be described by simple functions, or the structure consists of different types of components, it is impossible to obtain an analytical solution to the equations of motion satisfying the boundary conditions. Under these circumstances, the analytical approach is unable to address complicated dynamical problems. The situation remained largely unchanged until the 1960s when the development of computing technology allowed finite element analysis (FEA) of large and complex structures (see, for example, Petyt (2010)). Ever since, FEA has become a powerful numerical method for analysing the dynamics of complex structures.

In finite element analysis, a continuous structure is discretised into a number of elements. The motion within each element is approximated by assuming particular shape functions. Governing equations are obtained by applying the force balance condition of each element. Together with compatibility conditions at the element joints and boundary conditions, the dynamic response of the structure is obtained numerically. Although in principle, FEA can be used to analyse any arbitrary structure, as it may be considered as an assembly of smaller and simpler structures, difficulties arise when analysing high-frequency vibration problems. One reason is that to ensure the accuracy of FEA results, the size of each element has to be much smaller than the corresponding wavelength of the considered frequency. As frequency increases, the response of the system is affected by an increasing number of modes. Consequently, at high frequencies, the

rapid increase in the size of the finite element model and the number of modes that need to be considered brings about a high computation and analysis cost. Furthermore, with the increase of mode order, modal resonance frequencies and relative modal phase responses become more and more sensitive to small changes in structural details, especially boundary conditions and damping distributions (see, Fahy (1994)). However, because of manufacturing tolerances as well as fabrication imperfections, uncertainties concerning structural details and variability of product properties are unavoidable. Consequently, the distributions of higher order modes begin to overlap (see, for example, Manohar and Keane (1994)), and the results derived by a frequency response analysis become more and more unreliable. This is especially true for the high-frequency dynamic behaviour of structure components joints (see, for example Ibrahim and Pettit (2005)). As a result, high-frequency vibration responses of nominally identical structures obtained using FEA are observed to differ, sometimes greatly (see Kompella and Bernhard (1993)).

The development of energy based modelling approaches arose from a need to avoid the deficiencies of FEA in addressing structural dynamical response of systems excited at high frequencies. An important example of these methods is statistical energy analysis (SEA), developed in the 1960s to predict the vibrational response of flights (see, Fahy (1994)). A SEA model comprises a statistical set of subsystems described by their gross geometric forms, dimensions and material properties (see, for example, Lyon (1975)). The ensemble-average behaviour of each subsystem that shares those properties is considered in terms of power and energy, instead of the exact detailed response of an individual structure. Energy balance is guaranteed by ensuring that the total input power into a subsystem equals the sum of dissipated power within the subsystem and coupling powers with other subsystems. Coupling powers are assumed to be proportional to the difference in modal energies between substructures.

One of the earliest applications of SEA to study simple vibration systems was conducted by Lyon and Maidanik (1962). In their study, a modal theory was employed to study the power flow between two randomly excited linear oscillators with weak coupling. It was found that for conservative coupling, the power flow between these two oscillators was proportional to the difference in their average modal energy. It was thus proposed that the high-frequency vibration problem is analogous to a thermal one in which vibration energy density plays the role of temperature. Lyon (1975) further developed SEA theory with applications to more complex vibration systems. Langley (1992) presented a wave approach for SEA. Manning (1994) proposed a mobility approach and formulated SEA parameters with mobility functions. Fahy (1994) comprehensively reviewed the origin, development and potential research areas of SEA. Keane and Price (1997) and Fahy and Price (1998) later presented more recent developments and advances in SEA theory and its applications to complex vibration systems. Mace (2003, 2005) examined the validity of the underlying assumptions of SEA by a modal formulation and found that indirect

coupling loss factors were negligible only when the system modes were local or in the limit of high modal overlap.

While SEA is suitable in the high-frequency range, as an overall dynamic system resolution, loss of detailed knowledge of local spatial distributions of response variables is encountered. Many assumptions are made in SEA, which also confine its applications. In contrast, the application of power flow analysis is not restricted to the high-frequency range (see, for example, Goyder and White (1980a,b,c)). Vibrational power flow, or the rate of energy exchange, combines the effects of force and velocity responses as well as their relative phase angle, and thus provides a good descriptor of vibration transmission between the substructures. The magnitude and direction of the power flow transmitted through the joints of subsystems with reference to the input power provide a measure of the amount of energy dissipated in each structural component. In the low-frequency range with a low modal density, the power flow variables may be expressed as a modal function aggregation to retain the resonant behaviour of the individual and global structures. At high frequencies with large modal densities, the mobility describing finite substructures may be expressed in an equivalent manner to infinite substructures. Therefore, in this situation the PFA results are similar to those obtained by SEA.

Since the introduction of the concepts of vibrational power flows, extensive research has been conducted to investigate the power flow behaviour of various dynamical systems. The findings have been widely used to improve the dynamic performance of linear systems by enhancing/mitigating the power transmission through a particular path. Previous applications of the PFA approach were mainly focused on vibration control, determination of vibration transmission paths for noise reduction, damage detections as well as evaluations of coupling loss factors in SEA.

1.1.1 Applications to vibration control

A common objective for vibration control is to reduce the net power transmission into a structure and to minimise the power flow within the structure. The concept of vibrational power flow is valuable as it combines both force and velocity characteristics together. Any attempt to reduce vibration by considering individual force or velocity amplitude without accounting for their relative phase difference might not necessarily be successful. However, improvement can be guaranteed by decreasing the amount of power flow to a structure (see, for example, Goyder and White (1980a,b,c)).

In terms of vibration isolation, a system of interest usually consists of a machine, with passive isolators and/or active control units, mounted on base structures composed of beam and plate elements. By conducting power flow analysis, power transmission from the machine into the base structure can be identified, which is a more appropriate indicator of isolation performance than the traditional force or displacement transmissibility.

For this reason, many researchers have focused their attention on analysis and control of vibrational power flows of dynamical systems (see, for example, Pinnington and White (1981); Pan et al. (1992); Gardonio et al. (1997a,b); Mahajan and Redfield (1998); Li and Lavrich (1999); Xiong et al. (2000) and Xiong et al. (2003)).

Recently, it was shown that the concept of power flow can also be used in nonlinear vibration absorption of dynamical systems. Vakakis et al. (2008) discovered the phenomenon of nonlinear energy pumping or targeted energy transfer, which corresponds to one way channelling of the vibrational energy from a linear system to a passive nonlinear energy sink where it localises and diminishes with time due to damping dissipation. Based on this phenomenon, nonlinear vibration absorbers were designed to suppress the undesirable vibrations from seismic excitations (Nucera et al. (2007)) and to improve the stabilities of aeroelastic or drill-string systems (see, Lee et al. (2007b); Viguié et al. (2009)).

1.1.2 Applications to noise reduction

In many applications, noise created by structure vibrations contributes to a major factor of discomfort. For example, in airplanes vibration energy generated by the engines travels from the wings to fuselage and finally radiates as structure-borne sound into the cabin (see, for example, Unruh (1987), Gardonio and Elliott (1999)). Similarly, in buildings vibration energy flows through walls and floors and then radiates into rooms in the form of noise (see Luzzato and Ortola (1988)). By carrying out a power flow analysis, variables such as power flow density vectors within a structure can be quantified. Subsequently, this yields the identifications of the dominant power flow paths such that measures can be taken to reduce the vibration transmission. For example, damping materials or active control units can be inserted to certain positions of a vibrating structure for better absorption and dissipation of vibration energy. In this way, the structure-borne noise can be greatly mitigated.

1.1.3 Applications to damage detection

Damage may be introduced to structures under fatigue or extreme impact loads and measures for their early detections and locations have received extensive investigations. Applying approaches such as acoustic or ultrasonic methods and magnetic or thermal field methods, is time consuming and costly (see, for example, Li et al. (2001)). Knowledge about the vicinity of the damage is required in advance, which is not practical in many situations. To avoid the shortcomings, model-based approaches have been developed, which examine the changes in global vibration characteristics of a structure. An important one of these approaches is the modal method which employs the fact that damage can lead to a decrease in dynamic stiffness, which in turn reduces the natural

frequency of an undamped system. However, this method fails to work when the damage locates on a nodal point of a certain mode as the corresponding natural frequency will remain unchanged.

The basic idea of damage detection using the power flow approach is that damage of any form introduces changes in structures which will result in differences in power flow behaviour of the perfect and the damaged structures. Based on this, Li et al. (2001, 2004a,b) applied power flow analysis on a damaged Euler beam and a circular plate structure. It was shown that vibrational power flow is highly dependent on the degree and location of damage. Khun et al. (2003) studied the power flow pattern of a plate with single or multiple cutouts, using a finite element method. Lee et al. (2006) extended their work and showed that this feature can be used to locate the crack. Zhu et al. (2006, 2007) examined a cracked Timoshenko beam as well as a thin cylindrical shell with a circumferential surface crack and found that the power flow passing through the crack was highly sensitive to its location and depth. Wang et al. (2009) investigated power flow features associated with vibration modes of both intact and damaged beams and suggested that the modal power flow behaviour can be used for damage detection.

1.1.4 Applications to evaluations of coupling loss factors

As stated earlier, one basic assumption made in SEA is that the coupling powers between substructures are proportional to the differences in average modal energy. The use of this assumption allows simple formulations of dynamical quantities such as coupling loss factors to describe the energy flow in the dynamical system using linear differential equations. However, a strict experimental determination of coupling loss factors can be difficult as by their definition, samples of infinite size are needed. An alternative approach is to use the results from power flow analysis in the low or middle frequency range to solve energy flow problems and estimate coupling loss factors. This can also improve the prediction by SEA in the low or middle frequency range. Such studies were conducted by Simmons (1991); Steel and Craik (1994); Fredö (1997) and Shankar and Keane (1997), in which FEA models were used to calculate the energy flow between subsystems and estimate the coupling loss factors between different substructures. Mace and Shorter (2000) proposed computationally efficient energy flow models based on finite element analysis, in which the results of FEA were post-processed to obtain the time or frequency average energies as well as input or dissipated powers.

1.2 Development and current state of research in PFA

The concepts of vibrational power flow were firstly discussed by Goyder and White (1980a,b,c). Since then, different approaches, such as the dynamic stiffness method

(see, Langley (1989)), the mobility method (see, Cuschieri (1990a)), the travelling wave approach (see, Langley (1992)), the finite element based energy flow approach (Mace and Shorter (2000)) and the progressive approach (Xiong et al. (2001)) have been proposed and developed to address the power flow characteristics. Instead of investigating individual structures such as periodic structures or beam/plate-like structures, Xing and Price (1999a,b) proposed a more general PFA approach using the fundamental principles of continuum dynamics, in which energy flow equations, vectors and potentials were defined. However, solutions to the power flow equations of complex structures need further study.

Recent advances in power flow analysis methods include the development of power flow mode theories. A mobility-based power flow mode approach was proposed by Ji et al. (2003), in which the eigenproperties of the real part of the mobility matrix and power mode force vector were used to describe the time-averaged power input of the excitation forces applied to a system. However, to predict input power and power transmission by this method, full knowledge of the system's mobility is required. To avoid the complexity, a damping-based power flow mode theory was developed by Xiong et al. (2005b) to describe the natural power flow behaviour of a dynamic system using its inherent damping information. A system's characteristic damping matrix was constructed. The eigenvalues and eigenvectors of this matrix can identify natural power flow characteristics. These eigenvectors were chosen as a set of base vectors spanning the power flow space and completely describe the power flow in the system. The power flow response vector can be found by decomposition of the generalised coordinate of velocity vector in this space. Based on this theory, power flow design approaches were proposed to identify energy flow patterns satisfying vibration control requirements. Kwon et al. (2011) proposed a power flow boundary element approach to address multi-domain problems excited in the middle to high frequency range. Power flow density and intensity of simply-supported coupled beams and coupled plates were obtained and the results agreed well with those of the conventional power flow analysis approaches.

Recently, many studies were performed on linear dynamical systems using the PFA approach. Cho et al. (2006) proposed a level set approach for topological optimisation of power flow problems at high frequencies. Compared with the other optimisation methods, it was shown that the developed approach can avoid numerical instability such as checkerboard problems. Zong et al. (2006) investigated the power flow in human head subject to impact loading using a three-dimensional FEA model. The results showed that the structural intensity field can be used to assess injury patterns, which are difficult to identify using stress-based method. Dong et al. (2008) studied the power absorption by hand and arm substructures when operating vibrating tools. The trends observed in vibration power absorptions distributed in the substructures were consistent with some major findings of various physiological and epidemiological studies. Researchers also used vibration power flow quantities to assess the performance of different passive

or active vibration control systems. For example, Niu et al. (2008) provided an active vibration control model for coupled flexible systems using power flow transmission as the control function. Choi et al. (2009) evaluated the performance of a floating raft sandwich isolation system using power flow quantities. Liu et al. (2010) investigated the active control scheme of power flow at the junctions of connected plates. Advance in damage detection through PFA was reported by Wong et al. (2009) in which the power flow characteristics of a damaged plate were investigated using modal power flow analysis. The results showed that modal power flow was more sensitive to the change in plate stiffness than the strain mode shape. Guyomar et al. (2011) proposed the detections of impact or shock loads by examining the associated vibrational power flow patterns. It was shown experimentally that this approach was able to provide a rough estimation of the impact location.

There is also growing interest in PFA of nonlinear dynamical systems. Royston and Singh (1996) employed vibratory power transmission as a performance index in optimisation of multiple degrees-of-freedom nonlinear mounting systems. The same authors also examined an automotive hydraulic engine mount and investigated the vibratory power flow from an excited rigid body through a nonlinear path into a resonant receiver (see, Royston and Singh (1997)). It was found that although modelling the isolation path with a "softened" nonlinear expression may only moderately alter the fundamental harmonic response, it could significantly alter high harmonic responses. Xiong et al. (2005a) studied an interactive system consisting of a machine, a nonlinear isolator as well as a flexible ship excited by sea waves. The nonlinear isolator was characterised by a pth power damping model as well as a qth power stiffness model. The input power spectrum was found to be not globally sensitive to the nonlinearities in damping and stiffness of the isolator, but affected significantly around resonance frequencies of the coupled system. More recently, Xiong and Cao (2011) investigated the nonlinear power flow characteristics of a two degrees-of-freedom system with nonlinear stiffness created by a pair of oblique springs. Xing et al. (2011) presented a mathematical model with solution approaches for an integrated electric converter, a nonlinear oscillator and water interaction system to harness wave energies. Yang et al. (2011) evaluated the energy harvesting capability of a nonlinear flapping foil system using PFA. They also investigated the time-averaged power flows of nonlinear vibration isolation systems to assess the isolation performance (see, Yang et al. (2012a, 2013)) and the instantaneous power flow characteristics of the Duffing oscillator (see, Yang et al. (2012b)).

1.3 Motivations of the research

Previous research on power flow analysis has been mainly focused on the investigation of linear dynamical systems and the developments of different approaches for this purpose. The power flow behaviour of nonlinear dynamical systems remains largely unexplored,

mainly because of the complexity and difficulty associated with nonlinearity. However, many dynamical systems encountered in engineering practice are inherently nonlinear. For example, the mounts for hydraulic engine used in automobiles possess nonlinearity in both damping and stiffness (see Kim and Singh (1995)). Orifice dampers exhibit nonlinear damping with varying damping coefficients dependent on the internal geometry, frequency of flow oscillation and the Reynolds number (see, Popov and Sankar (1995)). Significant nonlinearities are also encountered in rotor/stator contact problems in turbomachineries (see, for example, von Groll and Ewins (2001)). Ships in regular waves can experience extreme motions due to parametrically excited roll resonances (see, for example, Ahmed et al. (2010)). In these systems, the transmission path between the vibration source and the receiver may contain significant localised nonlinear elements and thus the adoption of linear models to predict vibration levels can not provide satisfactory results.

On the other hand, nonlinear elements are increasingly used to enhance the dynamic performance of systems for better applications. For example, to improve the isolation performance of linear isolators, different configurations of nonlinear vibration isolators have been proposed and analysed (see, for example, Ibrahim (2008); Yang et al. (2013)). These nonlinear isolations systems can display inherently nonlinear behaviour such as multiple stable solutions, sub-/super- harmonic resonances, bifurcations and chaos, which are absent from linear systems. Similarly, it was shown that nonlinear vibration absorbers can enlarge the working frequency range of their linear counterparts (see, for example Oueini et al. (1998)).

Either unavoidable or intentionally introduced, nonlinear dynamics problems are frequently confronted with by engineers and researchers. One usual approach to deal with them is to transform a nonlinear system into its corresponding linear form such that linear vibration theories can be adopted. However, such transformation results in loss of dynamic response information arising from the nonlinearity. Alternatively, theories and analysis methods in nonlinear dynamics research can be used to qualitatively or quantitatively investigate the response characteristics of nonlinear systems (see, for example, Nayfeh and Mook (1979); Guckenheimer and Holmes (1983)). The latter approach has been successful in revealing some nonlinear phenomena, such as different types of bifurcation and chaotic motions. However, individual displacement or velocity responses were emphasized in nonlinear dynamics research. The power flow information of nonlinear dynamical systems has usually been ignored, although it can offer better indications of the actual vibration level of a system.

The motivation for the present research lies in the scientific and engineering values of a deeper understanding of the fundamental mechanisms governing power generation, transmission and dissipation mechanisms in nonlinear dynamical systems. There is also a strong need to clarify the influences of various types of nonlinearities, such as nonlinear damping and nonlinear stiffness, on the flows of vibration energy through different parts of a system, or between subsystems of an integrated structure. Moreover, due

to the difficulty in modelling and simulation of nonlinear dynamical systems, there is a lack of power flow theory and effective methods to deal with systems involving complex nonlinear phenomena, such as multiple solutions, sub-/super harmonic resonances, bifurcation and chaos. As a result, the power flow behaviour of nonlinear systems remains unclear and needs exploration. By developing power flow analysis techniques to reveal dynamic characteristics of nonlinear systems, the research can lead to potential findings and knowledge, which will provide inspirations as well as guidelines for designing nonlinear systems with high dynamic performance for engineering applications.

1.4 Aims and objectives

The primary aim of this study is to develop the power flow analysis approach to investigate power flow behaviour of nonlinear dynamical systems, especially when they exhibit complex nonlinear phenomena. This thesis also seeks to understand the effects of different types of damping and stiffness nonlinearities on power generation, transmission and dissipation mechanisms. In addition, the current research intends to demonstrate the applications of the developed methods as well as the findings to passive vibration control and energy harvesting.

To achieve these goals, the following objectives have been set:

- to develop power flow analysis methods for nonlinear dynamical systems;
- to investigate typical nonlinear dynamical systems, such as the Duffing oscillator and the Van der Pol oscillator, from the power flow perspective for a better understanding the influences of nonlinear stiffness/damping on power flows;
- to study two degrees-of-freedom nonlinear systems with different configurations of stiffness and damping nonlinearities to clarify vibration power input, dissipation, transmission and absorption to improve the effectiveness of nonlinear vibration isolators/absorbers;
- to examine the associated power flows of nonlinear systems when they exhibit intrinsic nonlinear phenomena such as multiple solutions, super-/sub- harmonic resonances, bifurcation and chaos;
- to demonstrate the applications of power flow analysis in designs or investigations of nonlinear systems for energy harvesting or vibration control.

1.5 Thesis outline

In Chapter 2, basic concepts in power flow analysis as well as in nonlinear dynamics are presented. Power flow analysis approaches developed for linear systems are briefly reviewed. Fundamental knowledge in nonlinear dynamics such as the types of dynamic responses, analysis methods as well as different nonlinear phenomena is provided.

In Chapter 3, a general power flow formulation for nonlinear dynamical systems is proposed. The method of harmonic balance and the method of averaging are developed for derivation of power flow variables. The use of numerical methods to obtain power flow quantities is also discussed.

In Chapter 4, the power flow behaviour of a typical nonlinear stiffness system, i.e., the Duffing oscillator, is investigated. The effects of different nonlinear phenomena, such as sub-/super- harmonic resonances, bifurcation and chaos on power flows are studied. The influences of system parameters, initial conditions and averaging time on the time-averaged input power are examined. Both the instantaneous and time-averaged power flow characteristics of the system are analysed. The harmonic balance method is adopted to obtain approximate analytical solutions of power flow variables while the numerical simulations based on the Runge-Kutta method are used to provide more accurate results associated with periodic as well as chaotic responses.

In Chapter 5, the power flow characteristics of a typical nonlinear damping system, i.e., the Van der Pol oscillator, are studied. Both the instantaneous and time-averaged power flows of the unforced and forced system exhibiting periodic or quasi-periodic responses are investigated using numerical as well as analytical approaches. The variations of time-averaged input power due to bifurcation are examined. The conditions for negative time-averaged input power are discussed.

In Chapter 6, power flow analysis of a two degrees-of-freedom nonlinear system with a nonlinear isolator is performed. The system includes a harmonically-excited mass, mounted on a one-DOF base through an isolator with nonlinearities both in damping and stiffness. Averaging approximations as well as numerical simulations are conducted to obtain the time-averaged input, dissipated and transmitted powers as well as maximum kinetic energies, and their variations with system parameters.

In Chapter 7, power flow analysis of a two degrees-of-freedom nonlinear system with a nonlinear absorber attached to a nonlinear primary structure is carried out. The averaging method is employed to obtain analytical formulations of time-averaged input, dissipated, as well as absorbed powers. Together with numerical simulations, the performance of the absorber is assessed considering different configurations of stiffness nonlinearities in the primary structure and/or the absorber.

Chapter 8 proposes a nonlinear vibration energy harvesting system design, which is inspired by the findings in Chapter 5. The system consists of a flapping foil supported by nonlinear springs in both pitch and heave degrees-of-freedom, and an electro-magnetic generator. The energy input, transmission as well as generation behaviour of the coupled system is revealed using power flow analysis so as to examine the energy harvesting capability of the device.

In Chapter 9, the dynamic and power flow behaviour of a nonlinear vibration isolation system is studied. The system includes a linear spring, configured in parallel with a negative stiffness mechanism (NSM), which is created by a pair of bars under constant compression. Using a power flow analysis, it is successfully demonstrated that the NSM can assist in vibration isolation by reducing time-averaged input power over a large band of excitation frequencies.

In Chapter 10, some conclusions are drawn and future research areas are given.

Chapter 2

Basic aspects of power flow analysis and nonlinear dynamics

Since the introduction of the concepts of vibrational power flows, theories as well as analysis approaches have been put forward to analyse the flow of vibration energy in engineering dynamical systems. Although they were primarily proposed for linear systems, insights may still be obtained to develop effective power flow methods for nonlinear dynamical systems. Also, knowledge in nonlinear dynamics, such as the analysis tools, the type of dynamic responses, and typical nonlinear phenomena, is needed to understand nonlinear dynamic behaviour and to interpret it from the power flow perspective. For these purposes, this chapter reviews the basic concepts, formulations and established methods in power flow analysis. Some fundamental information used in nonlinear dynamics research is provided for later references.

2.1 Basic concepts in power flow analysis

The fundamental concepts of power flows were discussed and described by Goyder and White (1980a,b,c). In their study, the rate of change of vibration energy was employed to characterise the dynamic response of a system. The use of power flow is valuable as it combines force and velocity characteristics together, and can better reflect vibration transmission between sub-structures within an integrated system. Any attempt to reduce vibration level by only considering force or displacement amplitude but not their phase angle may not necessarily be successful. However, improvement can be made by decreasing the net power flow into the structure.

In dynamical analysis, it is usual to represent harmonic quantities mathematically with real harmonic functions. For example, a harmonic force $f(t)$ with amplitude F and frequency ω, and a velocity $v(t)$ with amplitude V and frequency ω with a relative

phase angle of θ are given as

$$f(t) = F\cos\omega t, \tag{2.1}$$

$$v(t) = V\cos(\omega t + \theta), \tag{2.2}$$

respectively. Alternatively, these quantities can be expressed in a complex form

$$\tilde{f}(t) = Fe^{\mathrm{i}\omega t} = \tilde{F}e^{\mathrm{i}\omega t}, \tag{2.3}$$

$$\tilde{v}(t) = Ve^{\mathrm{i}(\omega t+\theta)} = \tilde{V}e^{\mathrm{i}\omega t}, \tag{2.4}$$

where in these exponential notations, $\mathrm{i} = \sqrt{-1}$; the tilde denotes a complex quantity; $\tilde{F} = F$ and $\tilde{V} = Ve^{\mathrm{i}\theta}$ are complex variables. For equivalence of representations, only the real part of a complex quantity is used here to represent the corresponding physically measurable quantity, so that

$$f(t) = \mathrm{Re}\left\{\tilde{f}(t)\right\} = \frac{1}{2}(\tilde{f} + \tilde{f}^{\star}), \tag{2.5}$$

$$v(t) = \mathrm{Re}\left\{\tilde{v}(t)\right\} = \frac{1}{2}(\tilde{v} + \tilde{v}^{\star}). \tag{2.6}$$

where a star denotes the complex conjugate of a variable.

It should be noted that although complex representations of quantities facilitate mathematical flexibility, only the instantaneous real part carries physical meaning (see, Xing and Price (1999b)). Thus, a safe course of action is to take the real part of a complex quantity before any operation is performed.

In power flow analysis, power flow is defined as the rate of work done and thus it is a measurable quantity. At time t, the real power flow is written as

$$p(t) = f(t)v(t). \tag{2.7}$$

It can also be given in a complex form of notation, i.e.,

$$p(t) = \mathrm{Re}\{\tilde{f}(t)\}\mathrm{Re}\{\tilde{v}(t)\} = \frac{1}{4}(\tilde{f} + \tilde{f}^{\star})(\tilde{v} + \tilde{v}^{\star}) = \frac{1}{2}\mathrm{Re}\left\{\tilde{f}\tilde{v} + \tilde{f}\tilde{v}^{\star}\right\} = \frac{1}{2}\mathrm{Re}\left\{\tilde{f}\tilde{v} + \tilde{f}^{\star}\tilde{v}\right\}. \tag{2.8}$$

The real power averaged over averaging time t_p is

$$\bar{p} = \frac{1}{t_p}\int_0^{t_p} \mathrm{Re}\{\tilde{f}(t)\}\mathrm{Re}\{\tilde{v}(t)\}\,\mathrm{d}t. \tag{2.9}$$

For a periodic response with an oscillation frequency of ω, the averaging time may be taken as a cycle of oscillation, i.e., $t_p = 2\pi/\omega$. Then Eq. (2.9) can be expressed in a complex form as

$$\bar{p} = \frac{1}{2}\mathrm{Re}\left\{\tilde{F}\tilde{V}^{\star}\right\} = \frac{1}{2}\mathrm{Re}\left\{\tilde{F}^{\star}\tilde{V}\right\} = \frac{1}{2}\left(\mathrm{Re}\left\{\tilde{F}\right\}\mathrm{Re}\left\{\tilde{V}\right\} + \mathrm{Im}\left\{\tilde{F}\right\}\mathrm{Im}\left\{\tilde{V}\right\}\right). \tag{2.10}$$

The instantaneous complex power may be defined mathematically as

$$\tilde{p}(t) = \tilde{f}(t)\tilde{v}(t) = \tilde{F}\tilde{V}e^{2\mathrm{i}\omega t}, \tag{2.11}$$

with this average value being

$$\overline{\tilde{p}(t)} = \frac{\omega}{2\pi}\int_0^{\frac{2\pi}{\omega}} \tilde{f}\tilde{v}\,\mathrm{d}t = 0. \tag{2.12}$$

Eqs. (2.10) and (2.12) clearly show the difference between a physical power and a complex power. In power flow analysis, real power is usually considered.

Frequency response functions (FRFs) are widely used in vibration analysis to characterise dynamic responses of a structure subject to harmonic excitations. There are two types of FRFs, input FRFs and transfer FRFs. For the former, force and response are considered to be at the same point of the structure and in the same direction while for latter, force and response are taken at different points and/or in different directions. In a PFA, mobility and impedance functions are often used as they provide relations between force and velocity amplitudes, which are defined as $\tilde{Y} = \tilde{V}/\tilde{F}, \tilde{Z} = \tilde{F}/\tilde{V}$, respectively. Using these two FRFs, the mean real power flow in Eq. (2.9) can be expressed as

$$\bar{p} = \frac{1}{2}|\tilde{F}|^2\mathrm{Re}\left\{\tilde{Y}\right\} = \frac{1}{2}|\tilde{V}|^2\mathrm{Re}\left\{\tilde{Z}\right\}. \tag{2.13}$$

2.2 Review of power flow analysis approaches

In the past few years, different analytical approaches, such as the dynamic stiffness method (see, Langley (1989)), the receptance method (see, Clarkson (1991)), the mobility approach (see, Cuschieri (1990a,b)), the traveling wave and scattering method (see, Langley (1992)), a PFA approach based on continuum dynamics (Xing and Price (1999b)) as well as the progressive approach (see, Xiong et al. (2001)), have been developed to reveal power flow characteristics of linear dynamical systems under different loading and boundary conditions. Finite element based power flow analysis models were also proposed to deal with complex structures (see, Mace and Shorter (2000)). For certain coupled structures, it may be possible to adopt a hybrid substructure approach using analytical, numerical or experimental solutions for each subsystem to reduce computational cost (see, Wang et al. (2002a)). These approaches are briefly reviewed in this section.

2.2.1 Analytical PFA approaches

Langley (1989) proposed the dynamic stiffness method to investigate the transverse response of a row of coupled plates subject to distributed acoustic load. The panel

was stiffened transversely and simply-supported along the longitudinal edges so that the dynamic equation of each uncoupled plate can be derived independently. The dynamic stiffness matrix of each individual component was obtained. The dynamic stiffness matrix of the whole structure was then assembled by using standard finite element techniques. By applying the force balance conditions and geometrical compatibility requirements at the coupling edges, the dynamic behaviour of the whole panel can be obtained. Expressions can thus be derived for the mean energy stored in the individual components and for the power flow between different components. The same approach was adopted by Bercin and Langley (1996) to examine the in-plane vibrations of similar plate frames.

Similar to the dynamic stiffness method, in the receptance method, solutions in terms of characteristics of uncoupled substructures are found. A major difference between this approach and the dynamic stiffness method lies in the degrees of freedom adopted at the interface. For the former method, the degrees of freedom are the coupling forces while for the latter they are the displacements. By applying the compatibility conditions at the interface, the unknown coupling forces can be calculated. This approach was employed to investigate the amount of power flows at joints of beams and plates (Clarkson (1991)) and at the interface of two coupled rectangular plates (see, Dimitriadis and Pierce (1988); Farag and Pan (1996) and Beshara and Keane (1998)).

In the mobility power flow approach, a global structure is divided into a set of coupled substructures with forces and moments introduced at the junctions of substructures. The vibrational power flow into a substructure and between substructures is expressed in terms of input and transfer structural mobility functions, which are defined as the ratio of the rate of change of displacement with time per unit load. For input mobilities, the response and the load are at the same location whereas for transfer mobilities, they are at different locations. The mobility approach was adopted by to obtain the power flow behaviour of periodic beams and L-shaped plates (see Cuschieri (1990a,b)), multiple beams, coupled beam structures under in-plane loading (see Farag and Pan (1996)) as well as elastic cylindrical shells (Ming et al. (1999)).

In the travelling wave and scattering approach (see, for example, Langley (1992)), the solution of each substructure is expressed in terms of exact wave mode. Then forced equilibrium and continuity conditions at the junction are employed to calculate the junction scattering and generation matrices. Power flow results can be extracted from a wave scattering analysis using the wave mode amplitudes as the basic unknowns. This approach was applied to study the power flow in a network of structural members (Miller and Von Flotow (1989)), in beams and joints of beam-like structures (see Horner and White (1991)), in a number of panel arrays (see, Langley (1992)) and in two-/three-dimensional frames (see Beale and Accorsi (1995)).

Xing and Price (1999a,b) proposed a general power flow analysis approach based on the fundamental principles of continuum dynamics. When developing the mathematical model, the concept of energy flow density vector was introduced. Based on this concept, the energy transmission between different parts of a system was uniquely defined. This allows the definitions of energy flow lines, energy flow potentials, and equipotential surfaces. Local equation of energy-flow balance, the equation of energy exchange between subsystems, and time-averaged equations were derived to describe the characteristics of the energy flow within the continuum. The applications of this approach were demonstrated through analysis of some simple dynamical systems. However, the solutions to power flow equations for complex structures are usually difficult to obtain.

Xiong et al. (2001) presented a generalised mobility/impedance power flow model to analyse the dynamical behaviour of complex systems. The model can consider systems containing any number of substructures with various configurations and multiple interaction interfaces. To describe the dynamical behaviour of a substructure, equivalent mobility and equivalent impedance matrices can be constructed upon generalized mobility/impedance matrices. Two progressive approaches were developed which can avoid the generalized inverse operation associated with rectangular matrices when dealing with multi-input/multi-output systems. This method is flexible and can be conveniently extended when additional substructures are further connected to the original structures.

Ji et al. (2003) proposed a mobility-based power flow mode theory to estimate the power transmitted to a flexible receiver by multiple point force excitations. Using eigendecomposition of the real part of the mobility matrix, the vibration power input by the forces was considered as the power input by independent power modes. Approximate expressions for the upper and the lower bounds of power flow as well as the mean value were formulated in terms of the power modes. However, applications of this method require full information of a system's mobility. To avoid this, Xiong et al. (2005b) later presented a damping-based power flow mode theory to describe the natural power flow behaviour of a system by its inherent damping distribution. Based on this theory, design approaches were put forward to achieve specific power flow patterns by modifying damping distributions of a system using passive/active control means.

2.2.2 PFA by FEA models

Although applications of the above theoretical PFA approaches can provide physical insight of the energy and power flow patterns inside structures, they are limited to simple uniform structures. For complex structures, FEA models can be used to obtain their power flow behaviour. Lyon (1975) suggested the use of FEA in predicting coupling loss factors during the early development stage of statistical energy analysis (SEA). A power flow finite element method was proposed by Nefske and Sung (1989) and further

studied by Wohlever and Bernhard (1992). This method were used to predict structure-borne sound transmission (see, for example, Simmons (1991), Steel and Craik (1994)), to study vibrational energies of two coupled beams (Shankar and Keane (1995b)), and to derive energy flow coefficients (Fredö (1997)). In all these studies, the response of a finite element model was expressed in terms of an energy flow model and a global FEA was performed on the global system.

To avoid the complexity associated with a global FEA, Shankar and Keane (1995a, 1997) developed a local FEA method using a receptance approach. The response of each subsystem was described by Green functions to study the energy flow in both simple and complex structures. These functions can be found by the sums of subsystem modes which may be obtained analytically (see Shankar and Keane (1995a)) or by using FEA (see Shankar and Keane (1997)). While this approach can substantially reduce the computational effort, it is restricted to excitation at discrete frequencies and a number of discrete locations. Mace and Shorter (2000) established energy flow analysis models from both global and local FEA models, with the latter based on component-mode synthesis. Computationally efficient methods of determining an energy flow model from a deterministic FEA were described.

2.2.3 Substructure approach

The main advantage of theoretical PFA approaches is that they allow efficient calculation of the power flow transmission between substructures and power flow density vectors within a structure. There are also no convergence issues as the force and displacement are already analytically formulated. However, theoretical models are confined to simple structures with particular boundary conditions as analytical expressions for the responses of complex structures are usually not available. Compared with theoretical approaches, FEA-based PFA models are effective for large and complicated structures, but they bring about a much higher computational cost.

One way to overcome this problem is to use both approaches in a hybrid way. A substructure or a component synthesis approach can be employed to reduce the number of degrees of freedom of a large, complex structure. In this approach, the whole structure is divided into several substructures with free-free interface condition. The solution of each substructure is presented by a modal substitution of a finite element model, a theoretical model or an experimental test model. The response of the whole structure is found by assembling all the substructures using interface conditions. Power flow at the interfaces of the substructures can be determined after the deduction of the displacement contribution of the external and boundary coupling forces. This method was applied to investigate the power flow behaviour of indeterminate rod/beam systems (Wang et al. (2002b)), of L-shaped plates (Wang et al. (2002a)) and of a coupled plate-cylindrical shell system (Wang et al. (2004)).

2.3 Fundamentals of nonlinear dynamics

To investigate power flow behaviour of nonlinear dynamical systems, it is necessary to understand the fundamental concepts and analysis tools used in nonlinear dynamics (see, for example, Guckenheimer and Holmes (1983); Nayfeh and Balachandran (1995)). This section provides some basic information for later use. For a m degrees-of-freedom system governed by a total number of m second-order differential equations, by introducing the velocities in each DOF as new state variables, the dynamic governing equations can be transformed into a set of $2m$ first-order differential equations, i.e.,

$$\dot{\mathbf{x}} = \mathbf{f}(\mathbf{x}, t), \tag{2.14}$$

where $\mathbf{x} = (x_1, x_2, \cdots, x_{2m})^{\mathrm{T}}$ is a state vector evolving in a $2m$-dimensional state space; $\mathbf{f}$ is usually referred to as a vector field, which may or may not depend explicitly on the independent variable t. For the former case, the system is non-autonomous, while for the latter, it's termed an autonomous system. For a linear dynamical system, $\mathbf{f}$ is a linear function of $\mathbf{x}$, but when nonlinearity exists, $\mathbf{f}$ will be a nonlinear function of $\mathbf{x}$.

Nonlinear systems can exhibit unique dynamic behaviour that are absent from their linear counterparts. For example, with prescribed parameter settings, multiple solutions may emerge, which results in the dependence of steady-state response on the initial conditions. Also, dynamic responses of a nonlinear system may contain frequency components that are different from the excitation frequencies. In particular, super- or sub-harmonic resonances can appear even when the excitation frequency is well below or above the linearised natural frequency. Moreover, the principle of superposition is not valid nonlinear systems, and the response amplitude does not grow proportionally to that of a harmonic excitation. Bifurcation occurs when there is sudden topological change of phase portraits due to small smooth variations of parameters. These nonlinear phenomena were discovered with the dynamic behaviour analysed using displacement or velocity responses. However, the associated power flow information has usually been ignored.

2.3.1 Analysis methods

Nonlinear dynamical systems are governed by nonlinear differential equations or nonlinear discrete mappings for which few exact solutions exist. Apart from experimental investigations, qualitative, analytical and numerical approaches are usually used in nonlinear dynamics.

Qualitative approach

The qualitative approach mainly deals with different categories of equilibria, limit cycles and their stabilities. In qualitative analysis of nonlinear dynamical systems, phase

portraits, Poincaré maps and bifurcation diagrams are frequently used to reveal the geometrical characteristics of the dynamic responses (see, for example, Nayfeh and Mook (1979)). Phase portraits can be constructed by plotting trajectories of dynamical systems with prescribed parameter settings. Each trajectory represents a particular system response starting at specific sets of initial conditions. Thus by examining the patterns of the trajectories, the dynamic characteristics of a system can be shown qualitatively.

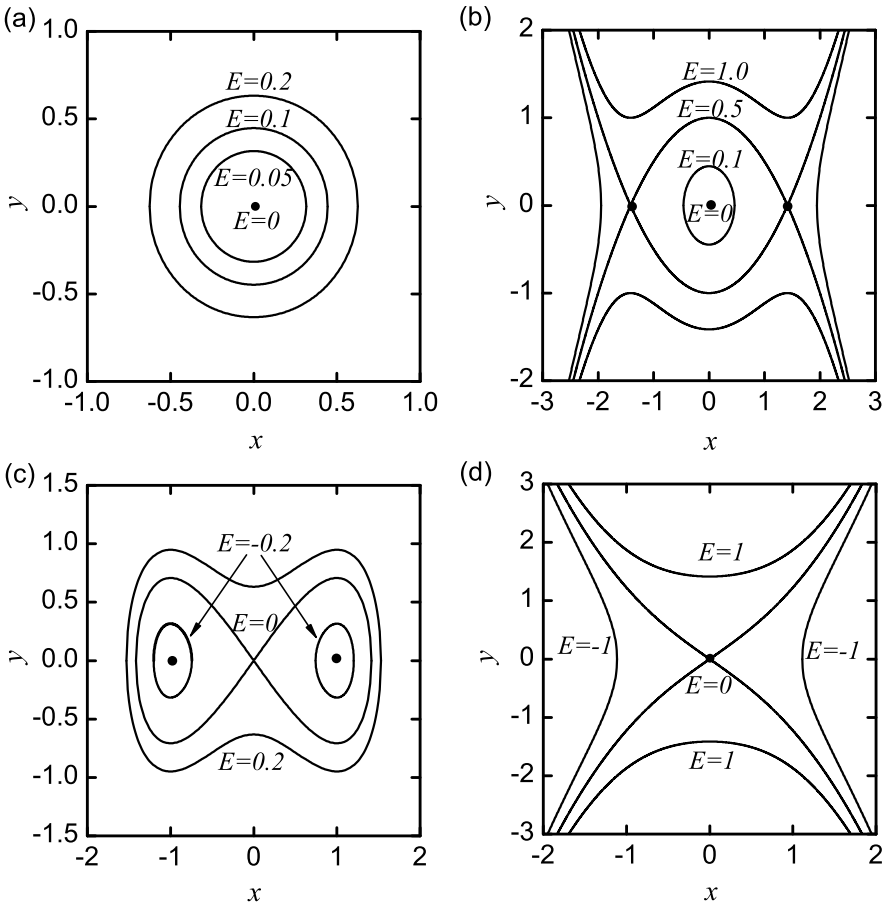

FIGURE 2.1: Phase portraits of the unforce, undamped Duffing oscillator ($\xi = f = \omega = 0$). Parameters for (a) $\alpha = 1, \beta = 0.1$, (b) $\alpha = 1, \beta = -0.5$, (c) $\alpha = -1, \beta = 1$ and (d) $\alpha = -1, \beta = -1$.

To illustrate, Figure 2.1 shows phase portraits of different types of the Duffing oscillator, governed by:

$$\ddot{x} + 2\xi\dot{x} + \alpha x + \beta x^3 = f\cos\omega t. \tag{2.15}$$

The Hamiltonian function of the system is $E = 0.5y^2 + 0.5\alpha x^2 + 0.25\beta x^4$, where $y = \dot{x}$. Figure 2.1(a) represents a hardening stiffness oscillator, while Figure 2.1(b) denotes a softening stiffness system. Figure 2.1(c) and (d) are the phase portraits of the double-well potential system and a system with a single hump in its potential energy, respectively. In these four phase portraits, either the number of fixed points or their stabilities is different. The figure shows that variations of parameter values can cause topological

changes of the phase structure. At a critical parameter value when such change occurs, the system is subject to bifurcation.

While phase portraits can provide useful information of the dynamics of a low-dimensional or autonomous system, they become less advantageous to use when the system is of high dimensions or non-autonomous. In these scenarios, a Poincaré map may be used to reduce the dimension of a continuous system by sampling the original orbits at a certain time interval, i.e., a cycle of excitation. To examine the effects of system parameters on its response, bifurcation diagrams can be employed to reveal the variations of the steady-state response with respect to a varying bifurcation parameter.

Analytical approach

The analytical approach has been extensively used to study transient as well as steady-state response behaviour of nonlinear systems. Compared with the qualitative approach, it focuses on analytical solutions of nonlinear differential equations so that the relationship between the response and system parameters can be established. As few exact solutions exist, analytical approximations are usually pursued using techniques such as different perturbation methods (see, Nayfeh (1973)), the method of harmonic balance, and the method of averaging.

The applications of perturbation methods are usually confined to systems with weak nonlinearities. In these methods, the solutions are approximated using the first few terms of a perturbation expansion and found following an iterative process. In contrast, the method of harmonic balance can be applied to study systems with strong nonlinearities, by considering multiple frequency signatures in the response. Another major difference between these two techniques is that the former uses convergent perturbed series to represent the response, whereas the latter employs harmonic series, which is not convergent. The method of averaging provides a convenient way to derive frequency-response relations if a first-order approximation is sought.

It should be noted that the solutions obtained by using the analytical approach are usually approximations of the actual responses. Therefore, validations by numerical simulations or experimental results are necessary. The stabilities of the analytical solutions may also be assessed as only the stable ones are physical realisable.

Numerical approach

Numerical methods, such as the Runge-Kutta methods, have been widely adopted to study the dynamic response characteristics of nonlinear systems with prescribed parameters and initial conditions. Mathematically, such methods were proposed for numerical solutions of ordinary differential equations (see, for example, Press et al. (1992)). One major advantage of the numerical approach over the above-mentioned analytical approach is that it can be applied to study different types of steady-state responses, e.g.,

periodic, quasi-periodic or chaotic motions. However, it usually costs more computational power and provides less physical insights, compared with the analytical methods. For this reason, this approach is usually used to verify analytical approximations of periodic responses and to investigate quasi-periodic or chaotic motions. It should be noted that potentially significant errors can arise in numerical simulations and factors such as the time step size as well as the orders of accuracy should be carefully chosen.

2.3.2 Categories of dynamic responses

For a linear damped system subject to a harmonic excitation, the steady-state motion will be periodic with the same frequency as that of the excitation. In contrast, the response of a nonlinear dynamical system contains frequencies other than the excitation frequency, and the system can exhibit periodic, quasi-periodic, or chaotic motions.

Equilibrium solutions

For autonomous systems, an equilibrium solutions or a fixed point solution corresponds to $\dot{\mathbf{x}} = 0$ in Eq. (2.14). Thus by solving the first-order equations of $\mathbf{f}(\mathbf{x}) = 0$, the fixed points $\mathbf{x}_s$ of the system can be found. Physically, a fixed point corresponds to an equilibrium position of the system. To assess its local stability, the corresponding linearised system may be examined (Nayfeh and Balachandran (1995)). Assuming a small disturbance $\mathbf{u}$ from the equilibrium solution $\mathbf{x}_s$, i.e.,

$$\mathbf{x} = \mathbf{x}_s + \mathbf{u}(t). \tag{2.16}$$

Substituting Eq. (2.16) back into Eq. (2.14), we have

$$\dot{\mathbf{x}} = \mathbf{f}(\mathbf{x}_s + \mathbf{u}). \tag{2.17}$$

This equation shows that the condition $\mathbf{u} = 0$ corresponds to the original fixed point $\mathbf{x} = \mathbf{x}_s$. A Taylor expansion of or Eq. (2.17) about the equilibrium position retaining only the linear terms, we obtain

$$\dot{\mathbf{u}} = \mathbf{f}(\mathbf{x}_s) + \mathbf{D}_{\mathbf{x}}\mathbf{f}(\mathbf{u})\mathbf{u} + O(||\mathbf{u}||^2) \approx A\mathbf{u}, \tag{2.18}$$

where $O(||\mathbf{u}||^2)$ represents the higher-order terms, $\mathbf{f}(\mathbf{x}_s) = 0$ and $A = \mathbf{D}_{\mathbf{x}}\mathbf{f}(\mathbf{x}_s)$ is the Jacobian matrix expressed by

$$A = \begin{pmatrix} \frac{\partial f_1}{\partial x_1} & \frac{\partial f_1}{\partial x_2} & \cdots & \frac{\partial f_1}{\partial x_{2m}} \\ \frac{\partial f_2}{\partial x_1} & \frac{\partial f_2}{\partial x_2} & \cdots & \frac{\partial f_2}{\partial x_{2m}} \\ \vdots & \vdots & \ddots & \vdots \\ \frac{\partial f_{2m}}{\partial x_1} & \frac{\partial f_{2m}}{\partial x_2} & \cdots & \frac{\partial f_{2m}}{\partial x_{2m}} \end{pmatrix}. \tag{2.19}$$

The eigenvalues of this matrix can be studied to determine the local stability of the fixed point. If the real parts of the eigenvalues are all negative, the solution will be stable. Otherwise, if one of the eigenvalues has a positive real part, the corresponding solution is unstable.

Periodic solutions

A dynamic response of a nonlinear system will be periodic with the least period of T if $\mathbf{x}(t+T) = \mathbf{x}(t)$, and $\mathbf{x}(t+\tau) \neq \mathbf{x}(t)$ when $0 < \tau < T$. Such solution may be transformed into a fixed point in the Poincaré map. A periodic solution may be referred to as a limit cycle, if there are no other periodic solutions sufficiently close to it (see, Nayfeh and Balachandran (1995)).

Quasi-periodic solutions

A quasi-periodic solution of a nonlinear system is characterised by a finite number (two or more) of incommensurate frequency components (see, Nayfeh and Balachandran (1995)). Two frequencies ω_1 and ω_2 are incommensurate if ω_1/ω_2 is an irrational number. More generally, m frequencies $\omega_1, \omega_2, \cdots, \omega_m$ are incommensurate if the equation:

$$n_1\omega_1 + n_2\omega_2 + \cdots + n_m\omega_m = 0$$

holds only when the value of $n_i (i = 1, 2, \cdots, m)$ is zero, where n_i are integers. A quasi-periodic response may be termed a k-period quasi-periodic solution if it contains k incommensurate frequencies (see, Nayfeh and Balachandran (1995)). To examine whether a nonlinear response is quasi-periodic, the corresponding Poincaré map can be depicted. A typical Poincaré section of such motion is a closed orbit.

Chaotic responses

Nonlinear dynamical systems may display chaotic motion, which contains broad band frequency signatures. It is a steady-state response that is bounded in the state space but not an equilibrium solution, a periodic solution or a quasi-periodic solution (see, Nayfeh and Balachandran (1995)). The chaotic attractor cannot be represented by a finite number of fixed points, closed orbits or a torus in the state space, but has complicated geometrical shape with fractal dimensions. Chaotic motions are also characterised by their sensitivity to the initial conditions, i.e., a small variation of the input can result in large differences in the output. To distinguish chaotic motions from periodic or quasi-periodic motions, the Lyapunov exponents, which measure the average rates of expansion and contraction of trajectories surrounding a particular trajectory, may be used (see, for example, Wolf et al. (1985)). For a chaotic response, the associated largest Lyapunov exponent should be positive.

Chapter 3

Power flow analysis methods for nonlinear dynamical systems

In this chapter, methods for analysing the vibrational power flow behaviour of nonlinear dynamical systems are discussed and developed. Firstly, a general power flow formulation for nonlinear dynamical system is presented. The equations of power and energy balance are developed in which each term corresponds to a power or energy quantity. Then, for periodic motions, analytical approximate solutions of power flow quantities are derived using the method of harmonic balance and the method of averaging. For systems with non-periodic responses such as quasi-periodic and chaotic motions, the use of numerical techniques to obtain power flow variables is also discussed.

3.1 General power flow formulations

A general dynamic governing equation of a m degrees-of-freedom nonlinear system may be written as

$$[M]\{\ddot{x}\} + [C]\{\dot{x}\} + [K]\{x\} = \{f_e(t)\}, \tag{3.1}$$

where $\{x\} = \{x_1, x_2, \cdots, x_j, \cdots, x_m\}^{\mathrm{T}}$ is a vector denoting the coordinates; $\{f_e(t)\}$ represents the external force vector; $[M]$, $[C]$ and $[K]$ are mass, damping and stiffness matrices, respectively. Because of nonlinearity, these matrices may not be constant but dependent on displacement and/or velocity as functions of $\{x\}$ and/or $\{\dot{x}\}$.

By pre-multiplying the governing equation (3.1) by the velocity vector $\{\dot{x}\}$, the equation of power balance of the system is obtained:

$$\{\dot{x}\}[M]\{\ddot{x}\} + \{\dot{x}\}[C]\{\dot{x}\} + \{\dot{x}\}[K]\{x\} = \{\dot{x}\}\{f_e(t)\}. \tag{3.2}$$

Alternatively, it may be written in the following form

$$\dot{K} + p_d + \dot{U} = p_{in}, \tag{3.3}$$

where $\dot{K} = \{\dot{x}\}[M]\{\ddot{x}\}$ and $\dot{U} = \{\dot{x}\}[K]\{x\}$ are the rates of change of system kinetic and potential energies, respectively; $p_d = \{\dot{x}\}[C]\{\dot{x}\}$ and $p_{in} = \{\dot{x}\}\{f_e(t)\}$ are instantaneous dissipated and input powers, respectively.

An integration of the power balance equation (3.3) with respect to t lead to

$$\Delta K + E_d + \Delta U = E_{in}, \tag{3.4}$$

where ΔK and ΔU are net changes of kinetic and potential energies; E_d and E_{in} are total dissipated and input energies in the time span, respectively. The change in mechanical energy of the system is obtained by summing ΔK and ΔU. Each term in Eq. (3.3) represents an instantaneous power flow variable. In many applications, time-averaged behaviour of power flows are of concern. Using an averaging time of t_p, the time-averaged dissipated and input powers are

$$\bar{p}_d = \frac{E_d}{t_p} = \frac{1}{t_p}\int_{t_i}^{t_i+t_p} \{\dot{x}\}[C]\{\dot{x}\}\,\mathrm{d}t, \tag{3.5a}$$

$$\bar{p}_{in} = \frac{E_{in}}{t_p}\int_{t_i}^{t_i+t_p} \{\dot{x}\}\{f_e(t)\}\,\mathrm{d}t, \tag{3.5b}$$

respectively, where t_i is the starting time for averaging. It should be noted that for a linear system exhibiting periodic motions, the change in its mechanical energy will vanish over a cycle of oscillation. Correspondingly, the input energy will all be dissipated and time-averaged input and dissipated powers will be equal. However, this may not hold for a nonlinear system as the system motion may become non-periodic.

To obtain the power flow behaviour of a nonlinear dynamical system, it is essential to solve Eq. (3.1). For periodic motions, analytical approximate approaches, such as the method of harmonic balance and the method of averaging, can be used. For quasi-periodic or chaotic motions, numerical solutions of the governing equations are usually needed. The applications of these methods for power flow analysis of nonlinear dynamical systems are discussed in the following sections.

3.2 Analytical approximations

3.2.1 The method of harmonic balance

The method of harmonic balance is a useful tool applied in the frequency domain to study nonlinear dynamical systems (see, von Groll and Ewins (2001)). The basic idea of

this method is to represent the response and nonlinear terms in the governing equation with harmonic series and balance the corresponding terms with the same frequency component to obtain a set of algebraic equations. The solutions to these equations are then found through an iterative procedure. This method was used by Xiong et al. (2005a) to derive the response of a coupled machine, nonlinear isolator and flexible ship interaction system.

For a general representation of obtaining power flow variables using the method of harmonic balance, Eq. (3.1) is firstly split into a linear part and a nonlinear part, i.e.,

$$[M_l]\{\ddot{x}\} + [C_l]\{\dot{x}\} + [K_l]\{x\} = \{f_e(t)\} + \{f_{non}(\{x\},\{\dot{x}\})\}, \tag{3.6}$$

where $[M_l]$, $[C_l]$ and $[K_l]$ are the linear parts of mass, damping and stiffness matrices; $\{f_{non}(\{x\},\{\dot{x}\})\}$ is the nonlinear part combining all the nonlinear effects arising from damping, stiffness, contacting forces, etc. When the system response is periodic with a fundamental oscillation frequency of ω_1, the time histories of the jth ($1 \le j \le m$) coordinate may be represented approximately by a truncated Fourier series with N harmonics:

$$x_j(t) = \hat{x}_{(j,0)} + \sum_{n=1}^{N}(\hat{x}_{(j,2n-1)}\cos n\omega_1 t + \hat{x}_{(j,2n)}\sin n\omega_1 t) = \sum_{n=0}^{N}\tilde{R}_{(j,n)}\mathrm{e}^{\mathrm{i}(n\omega_1 t)}, \tag{3.7}$$

where $\hat{x}_{(j,2n-1)}$ and $\hat{x}_{(j,2n)}$ are the coefficients of the nth harmonic term; $\tilde{R}_{(j,n)}$ is a complex variable for the nth harmonic of the $j$the coordinate. When $n = 0$, $R_{(j,0)} = \hat{x}_{(j,0)}$ and is a real number, whereas when $n > 0$, we have

$$\begin{aligned}\tilde{R}_{(j,n)} \quad = \quad & \Big(\hat{x}_{(j,2n-1)}\cos n\omega_1 t + \hat{x}_{(j,2n)}\sin n\omega_1 t\Big)\cos(n\omega_1 t) - \\ & \mathrm{i}\Big((\hat{x}_{(j,2n-1)}\cos n\omega_1 t + \hat{x}_{(j,2n)}\sin n\omega_1 t)\sin(n\omega_1 t)\Big).\end{aligned} \tag{3.8}$$

Similarly, the jth element in the external force vector $\{f_e(t)\}$ and the corresponding element in the nonlinear force vector $\{f_{non}(\{x\},\{\dot{x}\})\}$ are expanded as

$$f_{e,j}(t) = \hat{s}_{(j,0)} + \sum_{n=1}^{N}(\hat{s}_{(j,2n-1)}\cos n\omega_1 t + \hat{s}_{(j,2n)}\sin n\omega_1 t) = \sum_{n=0}^{N}\tilde{S}_{(j,n)}\mathrm{e}^{\mathrm{i}(n\omega_1 t)}, \tag{3.9}$$

$$f_{non,j}(t) = \hat{q}_{(j,0)} + \sum_{n=1}^{N}(\hat{q}_{(j,2n-1)}\cos n\omega_1 t + \hat{q}_{(j,2n)}\sin n\omega_1 t) = \sum_{n=0}^{N}\tilde{Q}_{(j,n)}\mathrm{e}^{\mathrm{i}(n\omega_1 t)}, \tag{3.10}$$

respectively. Inserting Eqs. (3.7), (3.9) and (3.10) into Eq. (3.6) and balancing the coefficients of the nth harmonic, we have

$$\Big(-(n\omega_1)^2[M_l] + \mathrm{i}(n\omega_1)[C_l] + [K_l]\Big)\{\tilde{R}_n\} = \{\tilde{S}_n\} + \{\tilde{Q}_n\}, \tag{3.11}$$

where $\{\tilde{R}_n\} = \{\tilde{R}_{(0,n)}, \cdots, \tilde{R}_{(j,n)}, \cdots, \tilde{R}_{(m,n)}\}^{\mathrm{T}}$, $\{\tilde{S}_n\} = \{\tilde{S}_{(0,n)}, \cdots, \tilde{S}_{(j,n)}, \cdots, \tilde{S}_{(m,n)}\}^{\mathrm{T}}$ and $\{\tilde{Q}_n\} = \{\tilde{Q}_{(0,n)}, \cdots, \tilde{Q}_{(j,n)}, \cdots, \tilde{Q}_{(m,n)}\}^{\mathrm{T}}$. Note that by balancing the real and imaginary parts, there will be m equations for $\tilde{R}_0$, but $2m$ equations for $\tilde{R}_n$ when $0 < n \leq N$,

Introducing a dynamic stiffness matrix

$$[D_n] = -(n\omega_1)^2[M_l] + \mathrm{i}(n\omega_1)[C_l] + [K_l]$$

for the nth harmonic and combining the balance equations for all the harmonics ($n = 0, 1, \cdots, N$), we have

$$\begin{pmatrix} D_0 & 0 & \cdots & 0 \\ 0 & D_1 & \cdots & 0 \\ \vdots & \vdots & \ddots & \vdots \\ 0 & 0 & \cdots & D_N \end{pmatrix} \begin{pmatrix} \tilde{R}_0 \\ \tilde{R}_1 \\ \vdots \\ \tilde{R}_N \end{pmatrix} = \begin{pmatrix} \tilde{S}_0 + \tilde{Q}_0 \\ \tilde{S}_1 + \tilde{Q}_1 \\ \vdots \\ \tilde{S}_N + \tilde{Q}_N \end{pmatrix}. \tag{3.12}$$

This equation can be transformed into a total number of $(2N+1)m$ nonlinear algebraic equations, with the same number of unknowns. When the number is large, methods such as the Newton-Raphson technique can be used to solve them in an iterative way (see, for example, Press et al. (1992)).

It should be noted that in many practical situations, nonlinearity is only significant in a few coordinates. For example, linear continuous systems may couple with each other through local nonlinear elements (see, Xing and Price (2004)). Using this property, the problem may be simplified by using a sub-structure method to avoid harmonic expansion of the linear DOFs so that the computational cost can be reduced.

The approximate instantaneous input power into the system is obtained by

$$p_{in} = \sum_{j=1}^{m} \dot{x}_j(t) f_{e,j}(t), \tag{3.13}$$

where the approximate expression for the velocity is found by differentiating Eq. (3.7) with respect to t:

$$\dot{x}_j(t) = \sum_{n=1}^{N} n\omega_1(-\hat{x}_{(j,2n-1)} \sin n\omega_1 t + \hat{x}_{(j,2n)} \cos n\omega_1 t). \tag{3.14}$$

The harmonic balance approximation of the time-averaged input power over a cycle of vibration is

$$\bar{p}_{in} = \frac{\omega_1}{2\pi} \int_0^{2\pi/\omega_1} \sum_{j=1}^{m} \dot{x}_j(t) f_{e,j}(t)\, \mathrm{d}t. \tag{3.15}$$

Substituting $f_{e,j}(t)$ and $\dot{x}_j(t)$ using Eqs. (3.9) and (3.14) and completing the integration in Eq. (3.15), it follows that

$$\bar{p}_{in} = \frac{1}{2}\omega_1 \sum_{j=1}^{m} \Big(\sum_{n=1}^{N} n\big(\hat{s}_{(j,2n-1)}\hat{x}_{(j,2n)} - \hat{s}_{(j,2n)}\hat{x}_{(j,2n-1)}\big)\Big), \tag{3.16}$$

where the orthogonal property of trigonometric functions was used. Instantaneous as well as time-averaged dissipated/transmitted power can be obtained in a similar way by taking the product of the Fourier expanded damping/transmitted forces and the corresponding velocities.

3.2.2 The method of averaging

The method of averaging has been widely used to obtain periodic motions of nonlinear systems when only a first-order of approximation of the response is sought (see, Nayfeh and Mook (1979)). To illustrate, the oscillation in jth ($1 \le j \le m$) coordinate in Eq. (3.6) is assumed to be harmonic with the same frequency as the excitation, i.e.,

$$x_j(t) = \hat{x}_{(j,1)} \cos\omega_1 t + \hat{x}_{(j,2)} \sin\omega_1 t = r_j \cos(\omega_1 t + \phi_j), \tag{3.17}$$

where r_j and ϕ_j are the amplitude and phase angle in the steady-state motion, respectively. Assuming that they are slow-varying variables of time, the velocity is found by differentiating Eq. (3.17) with respect to time

$$\dot{x}_j(t) = \dot{r}_j \cos(\omega_1 t + \phi_j) - r_j(\omega_1 + \dot{\phi}_j) \sin(\omega_1 t + \phi_j). \tag{3.18}$$

When a first-order approximation is pursued, the steady-state response will be harmonic so that we have

$$\dot{x}_j(t) = -\omega_1 r_j \sin(\omega_1 t + \phi_j). \tag{3.19}$$

Comparing Eqs. (3.18) and (3.19), it follows that

$$\dot{r}_j \cos(\omega_1 t + \phi_j) - r_j\dot{\phi}_j \sin(\omega_1 t + \phi_j) = 0. \tag{3.20}$$

Differentiating Eq. (3.19) with respect to time, we obtain

$$\ddot{x}_j(t) = -\omega_1\dot{r}_j \sin(\omega_1 t + \phi_j) - \omega_1 r_j(\omega_1 + \dot{\phi}_j) \cos(\omega_1 t + \phi_j). \tag{3.21}$$

Note that from the governing equation (3.6), $\ddot{x}_j(t)$ may be expressed as a function of $\{x\}$ and $\{\dot{x}\}$, i.e., $\ddot{x}_j(t) = g_j(\{x\}, \{\dot{x}\})$. Using this function and Eq. (3.21), we have

$$\dot{r}_j \sin(\omega_1 t + \phi_j) + r_j\dot{\phi}_j \cos(\omega_1 t + \phi_j) = -\frac{1}{\omega_1}\big(g_j + r_j\omega_1^2 \cos(\omega_1 t + \phi_j)\big). \tag{3.22}$$

From Eqs. (3.20) and (3.22), $\dot{r}_j$ and $\dot{\phi}_j$ are expressed as

$$\dot{r}_j = -\frac{1}{\omega_1}\Big(g_j + r_j\omega_1^2\cos(\omega_1 t + \phi_j)\Big)\sin(\omega_1 t + \phi_j), \tag{3.23a}$$

$$\dot{\phi}_j = -\frac{1}{r_j\omega_1}\Big(g_j + r_j\omega_1^2\cos(\omega_1 t + \phi_j)\Big)\cos(\omega_1 t + \phi_j). \tag{3.23b}$$

According to the averaging method, the time change rates of response amplitude $\dot{r}_j$ and phase angle $\dot{\phi}_j$ can be approximated by their average values over a period of oscillation. Such operation leads to

$$\dot{r}_j \approx -\frac{1}{2\pi}\int_0^{2\pi/\omega_1}\Big(g_j + r_j\omega_1^2\cos(\omega_1 t + \phi_j)\Big)\sin(\omega_1 t + \phi_j)\,\mathrm{d}t, \tag{3.24a}$$

$$\dot{\phi}_j \approx -\frac{1}{2\pi r_j}\int_0^{2\pi/\omega_1}\Big(g_j + r_j\omega_1^2\cos(\omega_1 t + \phi_j)\Big)\cos(\omega_1 t + \phi_j)\,\mathrm{d}t. \tag{3.24b}$$

In the steady-state motion, we have $\dot{r}_j = \dot{\phi}_j = 0$ $(1 \le j \le m)$ so that by evaluating the integrations in Eqs. (3.24), a total number of $2m$ algebraic equations are established. Solutions of these equations yield the response amplitudes and phase angles. Subsequently, the power flow variables can be obtained. The expression for time-averaged input power in Eq. (3.16) is simplified by setting $n = 1$ into

$$\bar{p}_{in} = \frac{1}{2}\sum_{j=1}^{m}\Big(\hat{s}_{(j,1)}\hat{x}_{(j,2)} - \hat{s}_{(j,2)}\hat{x}_{(j,1)}\Big), \tag{3.25}$$

where $\hat{x}_{(j,1)} = r_j\cos\phi_j$, $\hat{x}_{(j,2)} = r_j\sin\phi_j$, derived from Eq. (3.17).

3.3 Numerical approaches

To demonstrate this approach, we recall the first-order form of the general governing equation of a nonlinear system:

$$\dot{\mathbf{x}} = \mathbf{f}(\mathbf{x}, t). \tag{3.26}$$

In mathematics, it is usually referred to as an ordinary differential equation, which relates an unknown function $\mathbf{x}(t)$ with its derivative $\dot{\mathbf{x}}(t)$. If the original governing equations are of second order, new state variables can be introduced to reduce them to the first order. When the initial conditions of the system are given as $\mathbf{x}(t_0) = \mathbf{x}_0$, the solution of the dynamic response may be treated as an initial value problem of solving ordinary differential equations. To deal with it, many numerical approaches, such as the Euler's method or the Runge-Kutta methods are readily available.

The general idea of these numerical methods is to discretise the independent variable t into time steps $t_{n+1} = t_n + h, (n = 0, 1, 2, \cdots)$, with a step size of h, by which the

problem is transformed into determinations of function values $\mathbf{x}(t_{n+1})$, i.e., $\mathbf{x}_{n+1}$, at each time step. When the function value at $t = t_n$ is known as $\mathbf{x}_n$, to obtain $\mathbf{x}_{n+1}$ at $t = t_{n+1}$, the slope of the line connecting points $(t_n, \mathbf{x}_n)$ and $(t_{n+1}, \mathbf{x}_{n+1})$ is needed. To approximate the slope value, many methods have been proposed using the derivative information at different locations. Here, only the basic ideas of the Euler's method as well as the Runge-Kutta methods are provided.

3.3.1 Euler's method

In Euler's method, the derivative at the starting point $t = t_n$ of each interval $[t_n, t_{n+1}]$ is extrapolated to estimate the value of $\mathbf{x}_{n+1}$, i.e.,

$$\mathbf{x}_{n+1} = \mathbf{x}_n + h\dot{\mathbf{x}}(t_n). \tag{3.27}$$

To assess the accuracy, a Taylor expansion of $\mathbf{x}_{n+1} = \mathbf{x}(t_n + h)$ at $(t_n, \mathbf{x}_n)$ leads to

$$\mathbf{x}_{n+1} = \mathbf{x}_n + h\dot{\mathbf{x}}(t_n) + \frac{h^2}{2!}\ddot{\mathbf{x}}(t_n, \mathbf{x}_n) + O(h^3), \tag{3.28}$$

where $O(h^3)$ represents the higher-order terms. This method is simple, but very inaccurate and potentially unstable (see, Gerald and Green (2003)). It is reliable only when an extremely small step h is used. Improvement can be made by using an average of the derivatives at $t = t_n$ and $t = t_{n+1}$ for estimation, which leads to a modified Euler method with a local error of $O(h^3)$ at each step.

3.3.2 Runge-Kutta methods

For better accuracy of the results, Runge-Kutta methods can be used, which employ the Taylor's theorem from the start to ensure the desired accuracy (see, Gerald and Green (2003)). For example, in the second-order Runge-Kutta method, the slope of the line connecting points $(t_n, \mathbf{x}_n)$ and $(t_{n+1}, \mathbf{x}_{n+1})$ is approximated by a weighted average of two estimates $\mathbf{k}_1$ and $\mathbf{k}_2$,

$$\mathbf{x}_{n+1} = \mathbf{x}_n + a\mathbf{k}_1 + b\mathbf{k}_2, \tag{3.29}$$

where

$$\mathbf{k}_1 = h\mathbf{f}(t_n, \mathbf{x}_n), \tag{3.30}$$

$$\mathbf{k}_2 = h\mathbf{f}(t_n + \alpha h, \mathbf{x}_n + \beta\mathbf{k}_1). \tag{3.31}$$

The values of four unknowns, namely a, b, α and β, can be properly chosen such that Eq. (3.29) agrees as well as possible with the Taylor series expansion of the differential equation (3.26), i.e.,

$$\mathbf{x}_{n+1} = \mathbf{x}_n + h\dot{\mathbf{x}}_n + \frac{h^2}{2}\ddot{\mathbf{x}}_n + O(h^3) = \mathbf{x}_n + h\mathbf{f}_n + \frac{h^2}{2}\left(\frac{\partial \mathbf{f}}{\partial t}|_{t=t_n} + (\frac{\partial \mathbf{f}}{\partial \mathbf{x}}|_{\mathbf{x}=\mathbf{x}_n})\mathbf{f}_n\right) + O(h^3). \tag{3.32}$$

where $\mathbf{f}_n$ is the abbreviation for $\mathbf{f}(t_n, \mathbf{x}_n)$ and the chain rule was used for differentiation. Similarly, an expansion of Eq. (3.31) in terms of t_n and $\mathbf{x}_n$ gives

$$k_2 = h\mathbf{f}_n + h^2\Big((\frac{\partial \mathbf{f}}{\partial t}|_{t=t_n})\alpha + (\frac{\partial \mathbf{f}}{\partial \mathbf{x}}|_{\mathbf{x}=\mathbf{x}_n})\mathbf{f}_n\beta\Big) + O(h^3). \tag{3.33}$$

Substituting Eqs. (3.30) and (3.33) into the original estimation (3.29), we have

$$\mathbf{x}_{n+1} = \mathbf{x}_n + h(a+b)\mathbf{f}_n + h^2\Big(\frac{\partial \mathbf{f}}{\partial t}|_{t=t_n})\alpha b + (\frac{\partial \mathbf{f}}{\partial \mathbf{x}}|_{\mathbf{x}=\mathbf{x}_n})\mathbf{f}_n\beta b\Big) + O(h^3). \tag{3.34}$$

Note that Eqs. (3.32) and (3.34) are identical if

$$a + b = 1, \quad \alpha b = 1/2, \quad \beta b = 1/2.$$

As there are three equations for four unknown, an arbitrary value can be assigned to one of the unknowns. The traditional choice is $a = b = 1/2$, $\alpha = \beta = 1$, which corresponds to the Euler predictor-corrector method.

Results obtained from the second-order Runge-Kutta method have a local error of $O(h^3)$. Improvement can be made by increasing the number of estimates as well as the orders in Taylor expansions. In the widely used fourth-order Runge-Kutta method, four estimates are made for the value of $\mathbf{x}_{n+1}$, i.e.,

$$\mathbf{x}_{n+1} = \mathbf{x}_n + \frac{1}{6}\big(\mathbf{k}_1 + 2(\mathbf{k}_2 + \mathbf{k}_3) + \mathbf{k}_4\big), \tag{3.35}$$

where

$$\mathbf{k}_1 = h\mathbf{f}(t_n, \mathbf{x}_n),$$

$$\mathbf{k}_2 = h\mathbf{f}(t_n + h/2, \mathbf{x}_n + \mathbf{k}_1/2),$$

$$\mathbf{k}_3 = h\mathbf{f}(t_n + h/2, \mathbf{x}_n + \mathbf{k}_2/2),$$

$$\mathbf{k}_4 = h\mathbf{f}(t_n + h, \mathbf{x}_n + \mathbf{k}_3).$$

The local error for this method will be $O(h^5)$, while the global error is $O(h^4)$.

Once the time histories of displacement and velocity of each degree of freedom are obtained, power flow variables can be calculated. These time-histories may be Fourier transformed so that the dominant response components can be determined, which in turn assists in analytical modelling. The numerical approaches provide results with good accuracy as the effects of many frequency components are considered. They can be used to predict periodic responses, as well as quasi-periodic or chaotic motions. However, they generally cost more computational power, compared with the analytical approaches.

Chapter 4

Power flow analysis of the Duffing oscillator

In this chapter, the power flow characteristics of different forms of the Duffing oscillator, subject to harmonic excitations, are studied to reveal the distinct power input and dissipation behaviour arising from nonlinear stiffness. This oscillator is a frequently used model for a variety of problems such as nonlinear elasticity, midplane stretching (see, Thomsen (2003)) and magnetically buckled beams (see Moon and Holmes (1979)). It has been extensively studied in nonlinear dynamics emphasizing displacement/velocity response (see, for example, Nayfeh and Mook (1979), Guckenheimer and Holmes (1983)). These investigations successfully showed the capability of the system to exhibit a variety of nonlinear phenomena such as sub-/super- harmonic resonances, non-uniqueness of solutions, bifurcations and chaos (see, for example, Ueda (1980)). However, the associated power flow behaviour of the system has not been investigated. To address this issue, both analytical harmonic balance approximations and numerical simulations are used in this chapter to investigate the instantaneous and time-averaged power flows of the system with periodic or chaotic responses.

4.1 Power flow formulations and solutions

4.1.1 Power flow formulations

The Duffing oscillator is governed by the equation

$$\ddot{x} + 2\xi\dot{x} + \alpha x + \beta x^3 = f\cos\omega t, \tag{4.1}$$

in which the restoring force is characterised by a linear term and a cubic nonlinear term. By the signs of parameters α and β, the system may be categorised into four types:

Case I: softening stiffness system when $\alpha > 0, \beta < 0$;
Case II: hardening stiffness system when $\alpha > 0, \beta > 0$;
Case III: double-well potential system when $\alpha < 0, \beta > 0$;
Case IV: unstable system when $\alpha < 0, \beta < 0$.
Case IV refers to a system with a non-positive stiffness, thus it is unstable and will not be investigated in this chapter.

Multiplying by the velocity $\dot{x}$ on both sides of Eq. (4.1), the power flow balance equation of the system is obtained

$$\dot{x}\ddot{x} + 2\xi\dot{x}^2 + \alpha\dot{x}x + \beta\dot{x}x^3 = \dot{x}f\cos\omega t, \tag{4.2}$$

which is rewritten as

$$\dot{K} + \dot{U} + p_d = p_{in}, \tag{4.3}$$

Here

$$\dot{K} = \dot{x}\ddot{x}, \tag{4.4a}$$
$$\dot{U} = \alpha\dot{x}x + \beta\dot{x}x^3, \tag{4.4b}$$
$$p_d = 2\xi\dot{x}^2, \tag{4.4c}$$
$$p_{in} = \dot{x}f\cos\omega t \tag{4.4d}$$

are time change rates of kinetic and potential energies, and dissipated and input powers, respectively. Assuming that the displacement and velocity of the system are x_i and $\dot{x}_i$ at $t = t_i$, and x and $\dot{x}$ at $t = t_i + t_p$, respectively, an integration of Eq. (4.3) over the time period leads to

$$\Delta K + \Delta U + E_d = E_{in}, \tag{4.5}$$

where

$$\Delta K = \frac{\dot{x}^2 - \dot{x}_i^2}{2}, \tag{4.6a}$$
$$\Delta U = \int_{t_i}^{t_i+t_p} (\alpha\dot{x}x + \beta\dot{x}x^3)\,\mathrm{d}t = \frac{\alpha(x^2 - x_i^2)}{2} + \frac{\beta(x^4 - x_i^4)}{4}, \tag{4.6b}$$
$$E_d = \int_{t_i}^{t_i+t_p} 2\xi\dot{x}^2\,\mathrm{d}t, \tag{4.6c}$$
$$E_{in} = \int_{t_i}^{t_i+t_p} \dot{x}f\cos\omega t\,\mathrm{d}t \tag{4.6d}$$

represent the changes in kinetic and potential energies, and total dissipated and input energies of the system, respectively; t_p is the considered time span. The nonlinearity of the system is demonstrated by Eq. (4.6b), with the potential energy being affected by the nonlinear parameter β. For Cases I and II systems, only one minimum point in potential energy exists at $x = 0$. However, for a Case III system, the potential energy at $x = 0$ refers to a local maximum, with two local minima at $x = \pm\sqrt{-\alpha/\beta}$, as shown

in Figure 4.1. Supposing the reference potential energy at $x = 0$ is zero, the difference in the potential energies of the local maximum and minimum points is

$$\Delta U = 0 - (\frac{\alpha}{2}(\sqrt{\frac{-\alpha}{\beta}})^2 + \frac{\beta}{4}(\sqrt{\frac{-\alpha}{\beta}})^4) = \frac{\alpha^2}{4\beta}, \tag{4.7}$$

which becomes more significant as α^2 increases or β decreases. This quantity is important in affecting the dynamics of the Case III systems. As shown in Figure 4.1, the curve of potential energy forms two wells around the local minimum points. If the system firstly oscillates in one of the wells, in order to reach the other it will need enough energy to overcome the potential barrier at $x = 0$.

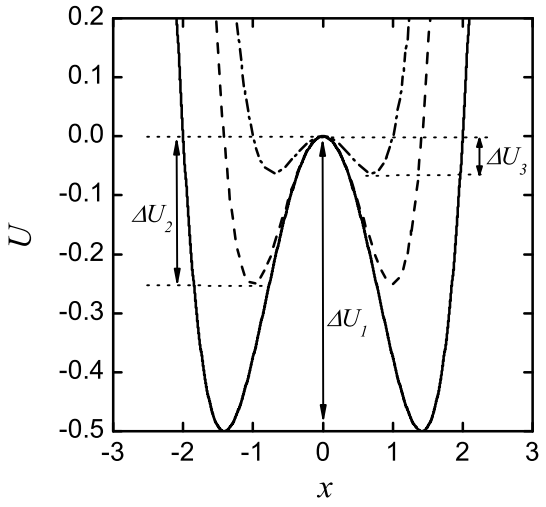

FIGURE 4.1: The potential energy of the double-well potential system. Solid line: $\alpha = -1.0, \beta = 0.5$; dashed line: $\alpha = -1, \beta = 1$ and dash-dot line: $\alpha = -0.5, \beta = 1$.

The time-averaged dissipated and input powers are formulated as

$$\bar{p}_d = \frac{E_d}{t_p} = \frac{1}{t_p}\int_{t_i}^{t_i+t_p} 2\xi\dot{x}^2 \,\mathrm{d}t, \tag{4.8a}$$

$$\bar{p}_{in} = \frac{E_{in}}{t_p} = \frac{1}{t_p}\int_{t_i}^{t_i+t_p} \dot{x} f \cos\omega t \,\mathrm{d}t. \tag{4.8b}$$

For a linear system subject to a harmonic excitation, the steady-state response will also be harmonic. Over a cycle of oscillation, there will be no net change in kinetic and potential energies ($\Delta K = 0, \Delta U = 0$) and the time-averaged dissipated and input powers will be equal. However, this is not generally true for nonlinear systems, as the steady-state response may become non-periodic. For example, they may exhibit quasi-periodic motion when the response frequency components are incommensurate with each other (see, for example, Nayfeh and Balachandran (1995)). Chaotic motions may also be encountered containing infinite frequency components.

4.1.2 Solution approaches

The harmonic balance (HB) method can be used to obtain the power flow characteristics of the system exhibiting periodic solutions. This method represents the steady-state response in a form of truncated Fourier series:

$$x(t) = \hat{x}_0 + \sum_{n=1}^{N} (\hat{x}_{2n-1} \cos n\omega_1 t + \hat{x}_{2n} \sin n\omega_1 t), \tag{4.9}$$

where ω_1 is the fundamental frequency of oscillation; $x_j (j = 0, 1, \cdots, 2N)$ is the coefficient of a harmonic function, N is the highest order of harmonics considered. Using Eq. (4.9), the cubic term in Eq. (4.1) is expressed as

$$x(t)^3 \approx \hat{q}_0 + \sum_{n=1}^{N} (\hat{q}_{2n-1} \cos n\omega_1 t + \hat{q}_{2n} \sin n\omega_1 t), \tag{4.10}$$

where the coefficients are defined by

$$\hat{q}_0 = \frac{\omega_1}{2\pi} \int_0^{\frac{2\pi}{\omega_1}} x^3 \, \mathrm{d}t, \tag{4.11a}$$

$$\hat{q}_{2n-1} = \frac{\omega_1}{\pi} \int_0^{\frac{2\pi}{\omega_1}} x^3 \cos n\omega_1 t \, \mathrm{d}t, \tag{4.11b}$$

$$\hat{q}_{2n} = \frac{\omega_1}{\pi} \int_0^{\frac{2\pi}{\omega_1}} x^3 \sin n\omega_1 t \, \mathrm{d}t. \tag{4.11c}$$

Differentiating Eq. (4.9) with respect to time, we obtain the velocity

$$\dot{x} = \omega_1 \sum_{n=1}^{N} (-n\hat{x}_{2n-1} \sin n\omega_1 t + n\hat{x}_{2n} \cos n\omega_1 t), \tag{4.12}$$

from which, when Eq. (4.4d) is used, it follows that the instantaneous input power

$$\bar{p}_{in} = \frac{f\omega_1}{2} \sum_{n=1}^{N} n \Big(\hat{x}_{2n} \big(\cos(n\omega_1 + \omega)t + \cos(n\omega_1 - \omega)t \big) - \hat{x}_{2n-1} \big(\sin(n\omega_1 + \omega)t + \sin(n\omega_1 - \omega)t \big) \Big), \tag{4.13}$$

containing frequency components of $n\omega_1 \pm \omega (n = 0, 1, \cdots, N)$. It can be seen that p_{in} is periodic with its period being the least common multiple of that of each individual component. Averaging Eq. (4.13) over its period, only the stationary component with $n\omega_1 - \omega = 0$ gives a non-zero value, i.e.,

$$\bar{p}_{in} = \frac{1}{2} f\omega_1 n \hat{x}_{2n}, \tag{4.14}$$

where $n = \omega/\omega_1$. In other words, only the in-phase component of the velocity with the same frequency as that of the excitation will contribute to the time-averaged input power.

Alternatively, numerical simulations can be used to obtain power flow variables, for which the governing equation Eq. (4.1) is firstly transformed into two first-order differential equations, i.e.,

$$\dot{x} = y, \tag{4.15a}$$

$$\dot{y} = -2\xi y - \alpha x - \beta x^3 + f\cos\omega t, \tag{4.15b}$$

Note that when the initial condition (x_0, y_0) is known, it becomes an initial value problem. The fourth-order Runge-Kutta (RK) method, can be used to determine the time histories of the responses. The power flow variables are obtained using Eqs. (4.4) and (4.8). A Fourier transformation of these time histories provides the corresponding frequency spectra, so that the dominant components can be identified and included in analytical approximations.

Comparing these two methods, the numerical one provides more accurate results incorporating the effects of different frequency components on power flows. It is a generalised approach suitable to solve various systems exhibiting either periodic / quasi-periodic or even chaotic motions. However, it is computationally more expensive. The harmonic balance method, in contrast, provides approximate solutions with less computational cost and more physical insight. Therefore, both the HB method and numerical simulations will be used in this chapter. The former will be used to derive analytical approximations of power flow variables when the system exhibits periodic motions, while the latter is employed to verify the HB results and obtain the power flow behaviour of the system exhibiting chaotic motions.

4.2 Power flow behaviour associated with periodic responses

4.2.1 A first-order approximation

Frequency-response relations

For a first-order HB approximation ($N = 1, \omega_1 = \omega$) of power flows, we assume a harmonic response with the same frequency as that of the excitation, i.e.,

$$x = \hat{x}_0 + \hat{x}_1\cos\omega t + \hat{x}_2\sin\omega t. \tag{4.16}$$

The velocity and the nonlinear restoring force term in Eq. (4.1) are expressed as

$$\dot{x} = -\omega\hat{x}_1\sin\omega t + \omega\hat{x}_2\cos\omega t, \tag{4.17a}$$

$$x^3 = \hat{x}_0^3 + \frac{3}{2}\hat{x}_0(\hat{x}_1^2 + \hat{x}_2^2) + \frac{3}{4}(\hat{x}_1^2 + \hat{x}_2^2 + 4\hat{x}_0^2)\hat{x}_1\cos\omega t + \frac{3}{4}(\hat{x}_1^2 + \hat{x}_2^2 + 4\hat{x}_0^2)\hat{x}_2\sin\omega t, \tag{4.17b}$$

respectively. Substituting Eqs. (4.16) and (4.17) into Eq. (4.1) and equating the corresponding harmonic terms, we obtain

$$(\alpha-\omega^2)\hat{x}_1+2\xi\omega\hat{x}_2+\frac{3}{4}\beta(\hat{x}_1^2+\hat{x}_2^2+4\hat{x}_0^2)\hat{x}_1=f, \tag{4.18a}$$

$$(\alpha-\omega^2)\hat{x}_2-2\xi\omega\hat{x}_1+\frac{3}{4}\beta(\hat{x}_1^2+\hat{x}_2^2+4\hat{x}_0^2)\hat{x}_2=0, \tag{4.18b}$$

$$\alpha\hat{x}_0+\beta\hat{x}_0(\hat{x}_0^2+\frac{3}{2}(\hat{x}_1^2+\hat{x}_2^2))=0. \tag{4.18c}$$

A manipulation of Eqs. (4.18a) and (4.18b) leads to

$$(\alpha-\omega^2)r^2+\frac{3}{4}\beta r^2(r^2+4\hat{x}_0^2)=f\hat{x}_1, \tag{4.19a}$$

$$2\xi\omega r^2=f\hat{x}_2, \tag{4.19b}$$

where $r=\sqrt{\hat{x}_1^2+\hat{x}_2^2}$, i.e., the amplitude of the oscillation.

For clarity, we define Type-1 oscillations to represent harmonic vibrations with $\hat{x}_0=0$, i.e., oscillations around the static equilibrium point of $x=0$, so that Eqs. (4.19) are further simplified into

$$\left((\alpha-\omega^2)r+\frac{3}{4}\beta r^3\right)^2+(2\xi\omega r)^2=f^2. \tag{4.20}$$

Similarly, Type-2 oscillations are used to denote harmonic motions with $\hat{x}_0\neq 0$, i.e., a double-well potential system oscillating in one of its potential wells. In this situation, Eq. (4.18c) can be transformed to

$$\beta\hat{x}_0^2=-\alpha-1.5\beta r^2. \tag{4.21}$$

Substituting Eq. (4.21) back into Eqs. (4.19) and further simplifying, we obtain

$$\left((\omega^2+2\alpha)r+3.75\beta r^3\right)^2+(2\xi\omega r)^2=f^2. \tag{4.22}$$

Here, it should be noted that the solution to Eq. (4.22) should satisfy

$$x_0^2=\sqrt{(-\alpha-1.5\beta r^2)/\beta}>0$$

for a physically realizable motion. Also, such oscillations in a single potential well require that $|x_0|>r$ such that the system won't move beyond the point $x=0$.

Basic characteristics of the time-averaged input power (TAIP)

Characteristic 1: TAIP $\bar{p}_{in}$ is proportional to the maximum kinetic energy K_{max} if the damping coefficient ξ is fixed.

To show this, TAIP over a cycle of oscillation $T = 2\pi/\omega$ is formulated by using Eqs. (4.14) and (4.19b), i.e.,

$$\bar{p}_{in} = \xi r^2 \omega^2. \tag{4.23}$$

In steady-state motion, the maximum velocity $x_{max} = r\omega$ of the system corresponds to the maximum kinetic energy:

$$K_{max} = \frac{1}{2} r^2 \omega^2. \tag{4.24}$$

Therefore,

$$\bar{p}_{in} = 2\xi K_{max}. \tag{4.25}$$

and the characteristic 1 is valid.

Characteristic 2: There exists an upper bound $\bar{P}_{in} = \dfrac{f^2}{4\xi}$ of TAIP, independent of parameters α, β and the excitation frequency.

To demonstrate this, we rewrite Eqs. (4.20) and (4.22) as

$$r^2 = \frac{f^2}{(\omega^2 - \alpha - 0.75\beta r^2)^2 + (2\xi\omega)^2}, \tag{4.26a}$$

$$r^2 = \frac{f^2}{(\omega^2 + 2\alpha + 3.75\beta r^2)^2 + (2\xi\omega)^2}, \tag{4.26b}$$

respectively. Using Eqs. (4.23), (4.24) and (4.26), we have

$$\bar{p}_{in} = \frac{\xi f^2}{\left(\dfrac{\omega^2 - \alpha - 0.75\beta r^2}{\omega}\right)^2 + (2\xi)^2}, \tag{4.27a}$$

$$K_{max} = \frac{0.5 f^2}{\left(\dfrac{\omega^2 - \alpha - 0.75\beta r^2}{\omega}\right)^2 + (2\xi)^2}, \tag{4.27b}$$

for Type-1 oscillations and

$$\bar{p}_{in} = \frac{\xi f^2}{\left(\dfrac{\omega^2 + 2\alpha + 3.75\beta r^2}{\omega}\right)^2 + (2\xi)^2}, \tag{4.28a}$$

$$K_{max} = \frac{0.5 f^2}{\left(\dfrac{\omega^2 + 2\alpha + 3.75\beta r^2}{\omega}\right)^2 + (2\xi)^2}, \tag{4.28b}$$

for Type-2 oscillations. Therefore, we have

$$\bar{p}_{in} \leq \frac{f^2}{4\xi} = \bar{P}_{in}, \tag{4.29a}$$

$$K_{max} \leq \frac{f^2}{8\xi^2}, \tag{4.29b}$$

which confirms Characteristic 2. This implies that the upper bound of the time-averaged power depends only on the excitation amplitude f and the damping coefficient ξ.

TABLE 4.1: Conditions for reaching the upper bound of power flows

	System category	Number of peaks	The value of (r^2, ω^2)
Type-1 oscillations with conditions: $\Delta_1 > 0$ $r^2 > 0, \omega^2 > 0$	Case I systems $(\alpha > 0, \beta < 0)$	0, when $\Delta_1 < 0$	NA
		1, when $\Delta_1 = 0$	$(\frac{-2\alpha}{3\beta}, \frac{\alpha}{2})$
		2, when $\Delta_1 > 0$	$(\frac{-2\alpha \pm \sqrt{\Delta_1}}{3\beta}, \frac{2\alpha \pm \sqrt{\Delta_1}}{4})$
	Case II Systems $(\alpha > 0, \beta > 0)$	1, as $\Delta_1 > 0$	$(\frac{-2\alpha + \sqrt{\Delta_1}}{3\beta}, \frac{2\alpha + \sqrt{\Delta_1}}{4})$
	Case III Systems $(\alpha < 0, \beta > 0)$	1, as $\Delta_1 > 0$	$(\frac{-2\alpha + \sqrt{\Delta_1}}{3\beta}, \frac{2\alpha + \sqrt{\Delta_1}}{4})$
Type-2 oscillations with conditions: $\Delta_2 > 0$ $r^2 > 0, \omega^2 > 0$	Case III systems $(\alpha < 0, \beta > 0)$	0, when $\Delta_2 < 0$	NA
		1, when $\Delta_2 = 0$	$(\frac{-4\alpha}{15\beta}, -\alpha)$
		2, when $\Delta_2 > 0$	$(\frac{-4\alpha \pm \sqrt{\Delta_2}}{15\beta}, \frac{-4\alpha \mp \sqrt{\Delta_2}}{4})$

For a Type-1 oscillation to reach the upper bound values of $\bar{P}_{in}$ and K_{max}, the values of ω^2 and r^2 should satisfy

$$\omega^2 - \alpha - 0.75\beta r^2 = 0, \tag{4.30}$$

as well as Eq. (4.20), from which we obtain

$$r^2 = \frac{-2\alpha \pm \sqrt{\Delta_1}}{3\beta}, \quad \omega^2 = \frac{2\alpha \pm \sqrt{\Delta_1}}{4},$$

where $\Delta_1 = 4\alpha^2 + 3\beta^2/\xi^2$. Similarly, for a Type-2 oscillation to achieve the upper bound, it requires

$$\omega^2 + 2\alpha + 3.75\beta r^2 = 0. \tag{4.31}$$

Together with Eq. (4.22), we obtain

$$r^2 = \frac{-4\alpha \pm \sqrt{\Delta_2}}{15\beta}, \quad \omega^2 = \frac{-4\alpha \mp \sqrt{\Delta_2}}{4},$$

where $\Delta_2 = 16\alpha^2 - 15\beta f^2/\xi^2$. Table 4.1 lists the conditions and positive solutions of r^2 and ω^2 to reach the upper bound (maximum/peak value). It is found that for a Case II system, only one set of (r^2, ω^2) leads to the maximum TAIP, whereas for Cases I and III systems, the peak value may be encountered at different locations.

Characteristic 3: In the high-frequency range, $\bar{p}_{in} \approx \dfrac{\xi f^2}{\omega^2 + 4\xi^2}$, independent of parameters α and β.

When the excitation frequency ω is large, $\bar{p}_{in}$ and K_{max} can be approximated by

$$\bar{p}_{in} \approx \frac{\xi f^2}{\omega^2 + 4\xi^2}, \tag{4.32a}$$

$$K_{max} \approx \frac{0.5 f^2}{\omega^2 + 4\xi^2}. \tag{4.32b}$$

Jumps, non-uniqueness of TAIP and its sensitivity to the initial conditions

Solving Eq. (4.20) with a bisection method, the response amplitude and subsequently TAIP of a Case II system with $\alpha = 1.0, \beta = 0.1, \xi = 0.01, f = 0.1$ were obtained and are shown in Figure 4.2. The default dB reference for $\bar{p}_{in}$ and K_{max} is set as 10^{-12} throughout this thesis. This reference is often used in decibel representations of quantities such as sound power and sound pressure. It is seen that $\bar{p}_{in}$ increases with ω on curves $A'C'$ and $D'C'$, and decreases with it on curve $B'D'$. The peak value (upper bound) of $\bar{p}_{in}$ is encountered at point C'. Bifurcations of periodic motions occur at points C' and D', and consequently, the value of $\bar{p}_{in}$ jumps downwards to point E' and upwards to point F', respectively. Between these critical jumping frequencies, there are three possible values of $\bar{p}_{in}$ at a single excitation frequency.

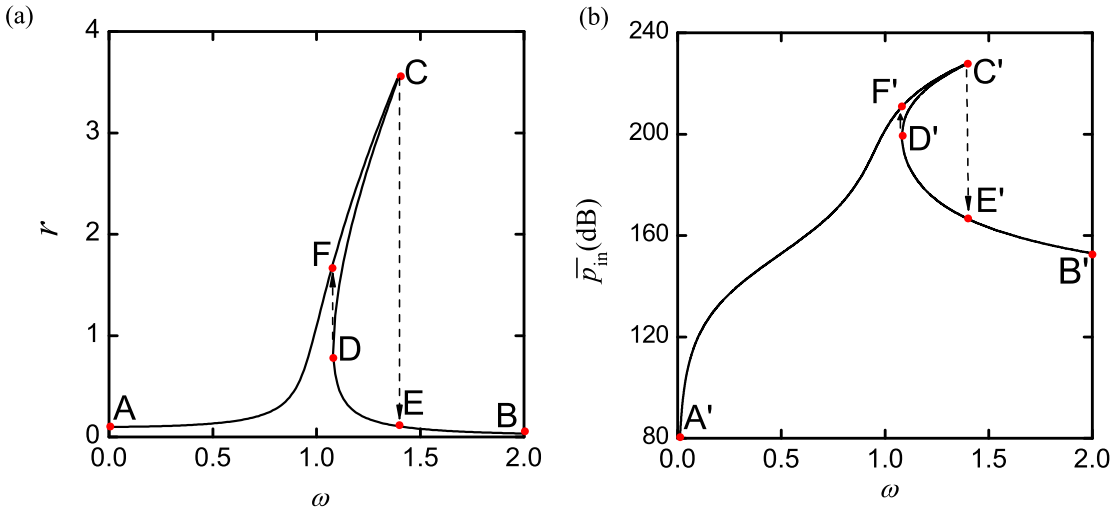

FIGURE 4.2: A Case II system with $\alpha = 1.0, \beta = 0.1, \xi = 0.01, f = 0.1, \omega = 1.1$. (a) Response and (b) the time-averaged input power (TAIP).

In the frequency range of non-unique TAIP, the basins of attraction of the system can be examined to identify different regions of the initial conditions causing variations in time-averaged power flows. Each basin represents a domain of all the initial conditions that lead to the same steady-state response (see, Nayfeh and Balachandran (1995)). To plot the basins of attraction of a system with fixed parameters, numerical simulations need to be conducted for each set of initial conditions to obtain the corresponding motions. Those with the same response are grouped together and marked with the same colour.

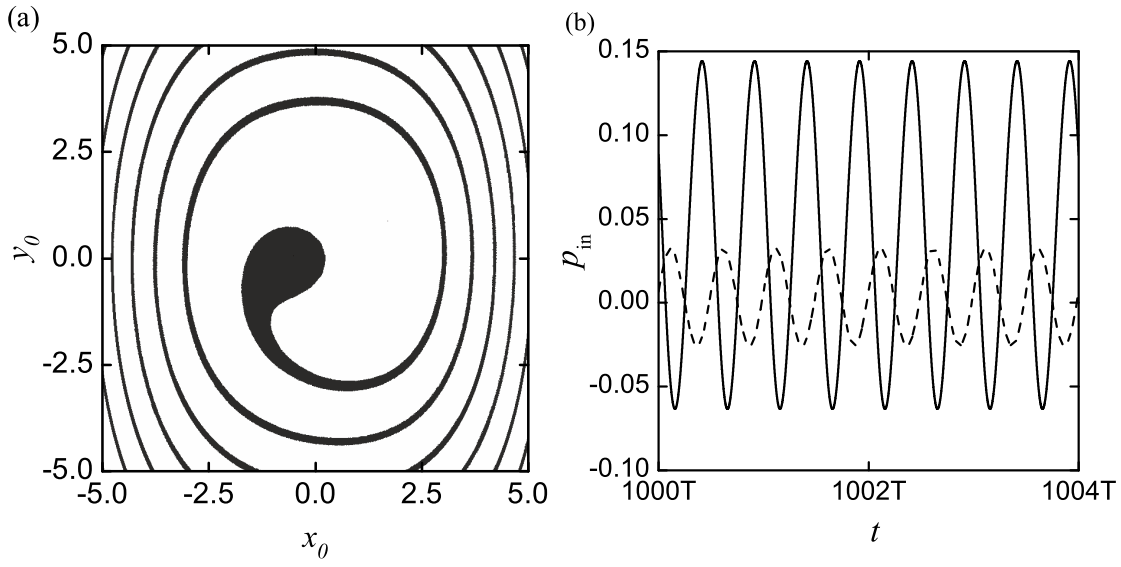

FIGURE 4.3: Effects of initial conditions on power flows of a Case II system ($\alpha = 1.0, \beta = 0.1, \xi = 0.01, f = 0.1, \omega = 1.1$). (a) Basins of attraction; (b) instantaneous input power, solid line: $(x_0, y_0) = (1, 0)$ and dashed line: $(x_0, y_0) = (-1, 0)$.

To illustrate, Figure 4.3(a) shows a plot of basins of attraction for the system with $\alpha = 1.0, \beta = 0.1, \xi = 0.01, f = 0.1$, and with the excitation frequency $\omega = 1.1$, locating between C and D in Figure 4.2(a). The initial displacement and velocity of the system are represented by x_0 and y_0, respectively. With these settings, Figure 4.2 has shown that there are three possible values of amplitude $r = 0.52, 1.37, 1.86$, and correspondingly $\bar{p}_{in} = 190.44\text{dB}, 207.09\text{dB}, 212.42\text{dB}$. The white region of Figure 4.3(a) represents initial conditions leading to a larger r of 1.86 and larger $\bar{p}_{in}$ of 212.42dB , whereas the black region denotes initial conditions leading to $r = 0.52$ and $\bar{p}_{in} = 190.44\text{dB}$. The intermediate values of $r = 1.37$ and $\bar{p}_{in} = 207.09\text{dB}$ correspond to an unstable motion which is not physically realisable. Crossing the boundary of the basins, a slight change in the initial conditions will cause significant variations in TAIP. Figure 4.3(b) shows the time series of the input power p_{in} with prescribed parameters but with two sets of initial conditions of $(x_0, y_0) = (1, 0)$ and $(x_0, y_0) = (-1, 0)$. The former locates in the white region of Figure 4.3(a) while the latter in the black. Correspondingly, Figure 4.3(b) shows that the amplitude of p_{in} changes significantly. This clearly demonstrates the sensitivity of a nonlinear system's power flows to the initial conditions.

Effects of nonlinear stiffness parameter β on power flows

In Figure 4.4, the effects of parameter β on $\bar{p}_{in}$ and K_{max} are examined with other parameters fixed as $\xi = 0.01, \alpha = 1.0, f = 0.1$. The system changes from Case I with a softening stiffness ($\beta = -0.1, -0.01$) , to linear ($\beta = 0$), and then Case II ($\beta = 0.5$) with a hardening stiffness. From the figure, the following power flow characteristics are observed.

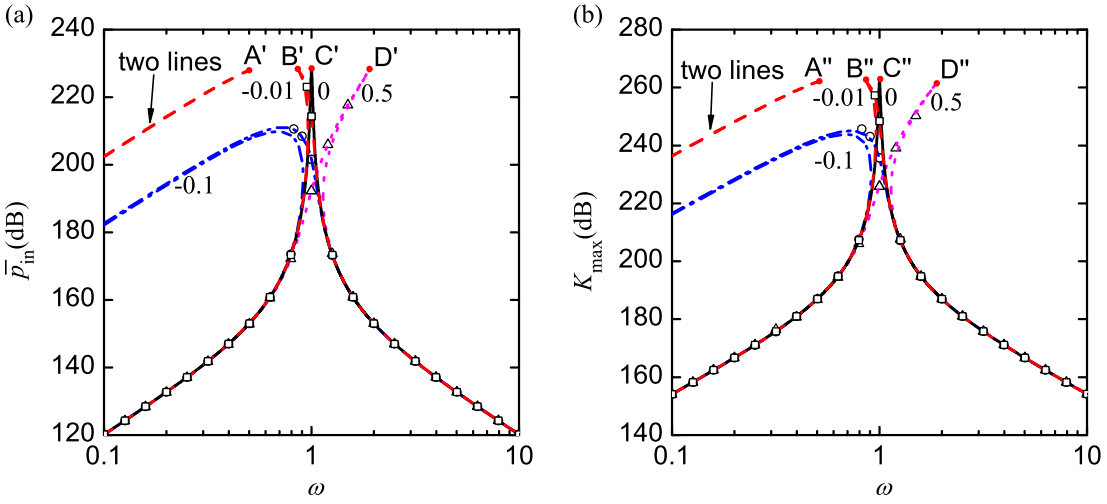

FIGURE 4.4: Effects of the nonlinear stiffness coefficient β on (a) $\bar{p}_{in}$ and (b) K_{max} . First-order HB approximations: dash-dot line ($\beta = -0.1$), dashed line ($\beta = -0.01$), solid line ($\beta = 0$) and dotted line ($\beta = 0.5$). Numerical simulation results: circles ($\beta = -0.1$), squares ($\beta = -0.01$) and triangles ($\beta = 0.5$)

- The power flow curves bend to the low frequencies for the softening stiffness system with a negative β but to the high frequencies for the hardening stiffness system with β being positive.

- The nonlinear parameter β has a strong influence on power flows when the excitation frequency is close to the resonance frequency. When the excitation frequency ω is far away from the resonance frequency, the power flow variables are not sensitive to variations in β as the curves coincide.

- For the softening, linear and hardening stiffness systems with $\beta = -0.01, 0$ and 0.5, the peaks in $\bar{p}_{in}$ and K_{max} curves are of the same height. However, the peak value for the softening system with $\beta = -0.1$ is much smaller. Using the analysis results in Section 4.2.1, it can be shown that the upper bound of power flows can be realised for the former three cases, but not for the latter with $\beta = -0.1$ for which $\Delta_1 = -26 < 0$. This characteristic suggests an approach to reduce the peak power flow values by adding a nonlinear softening stiffness into a linear isolator (see, Yang et al. (2013)).

- The figure shows that at points A', A'' and B', B''on the curves of $\beta = -0.01$, as well as at points D' and D on the curves of $\beta = 0.5$, there are two values of $\bar{p}_{in}$ and K_{max} at each corresponding frequency. Similar to the case shown previously, bifurcation occurs at these critical bifurcation points with possible jumps in the values of $\bar{p}_{in}$ and K_{max} when the excitation frequency changes.

- A nonlinear stiffness of $\beta \neq 0$ introduces a wide frequency band with a larger $\bar{p}_{in}$, compared with the linear system. This feature can be used for broadband vibration

energy harvesting (see, for example, Ramlan et al. (2010)). However, due to the existence of non-unique solutions, proper initial conditions have to be chosen such that they locate in the basin of attraction of the large amplitude motion.

Effects of linear stiffness parameter α on power flows

In Figure 4.5, the effects of the coefficient of the linear restoring force term α on the power flow variables are examined with the other parameters set as $\xi = 0.01, f = 0.1, \beta = 0.5$. In this way, the system changes from Case II when $\alpha = 5, 3$ or 1 to Case III when $\alpha = -1$. When $\alpha > 0$, it shows that an increase in α shifts the power flow curves to the higher frequencies. This is due to the fact that parameter α determines the natural frequency of the linearized system. At low frequencies, both $\bar{p}_{in}$ and K_{max} increase as α reduces from 5 to 1. However, at frequencies higher than the resonance frequency, a larger α results in larger power flows into the hardening stiffness system. This figure again demonstrates that there is a uniform upper bound (peak value) for both $\bar{p}_{in}$ and K_{max} of the system as α varies from 5 to 1.

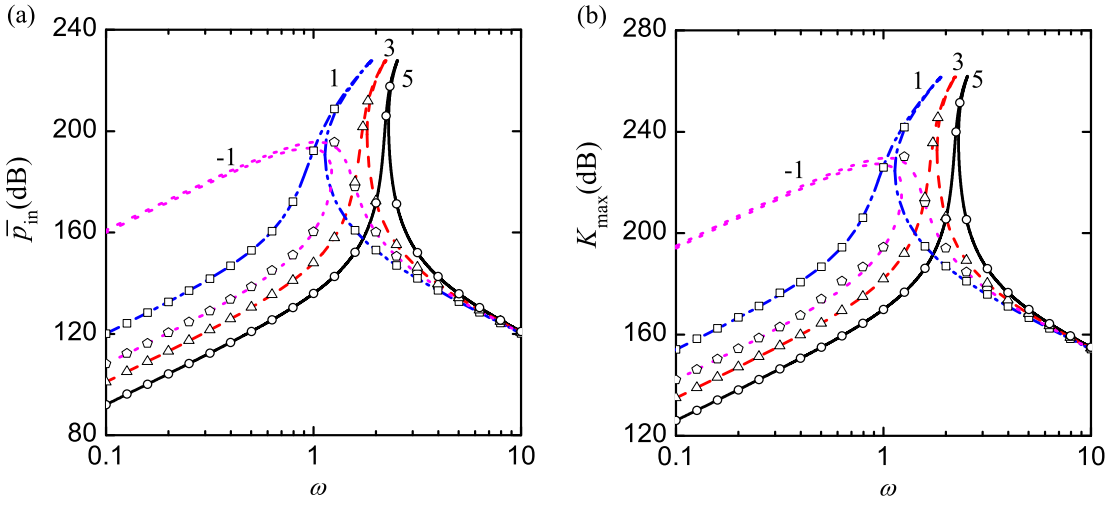

FIGURE 4.5: Effects of the linear stiffness coefficient α on (a) $\bar{p}_{in}$ and (b) K_{max} . First-order HB approximations: solid line ($\alpha = 5$), dashed line ($\alpha = 3$), dash-dot line ($\alpha = 1$) and dotted line ($\alpha = -1$). Numerical simulation results: circles ($\alpha = 5$), triangles ($\alpha = 3$), squares ($\alpha = 1$) and pentagons ($\alpha = -1$).

For the case with $\alpha = -1$, numerical simulation results indicate that the system exhibits Type-2 oscillations in one of the potential wells. Therefore, Eq. (4.22) is used to obtain the analytical approximations of power flows. The results in Figure 4.5 show that the corresponding power flow curves bend towards the low frequencies, which is similar to the characteristics of the softening stiffness system (Case I). Also, using the results obtained previously, it can be shown that upper bound of $\bar{p}_{in}$ cannot be reached as correspondingly we have $\Delta_2 = -734 < 0$. The figure also shows that as ω increases

towards high frequencies, the power flow curves of different α values tend to merge with each other. This demonstrates the basic Characteristics 3 of power flow listed previously.

Effects of damping and the excitation amplitude on power flows

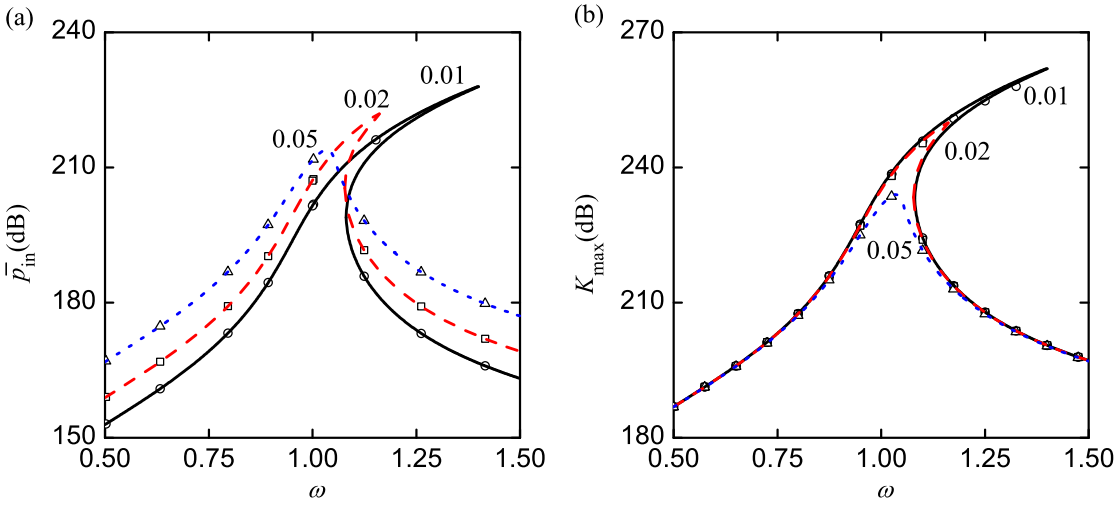

FIGURE 4.6: Effects of the damping coefficient ξ (a) $\bar{p}_{in}$ and (b) K_{max}. First-order HB approximations: solid line ($\xi = 0.01$), dashed line ($\xi = 0.02$) and dotted line ($\xi = 0.05$). Numerical simulation results: circles ($\xi = 0.01$), squares ($\xi = 0.02$) and triangles ($\xi = 0.05$).

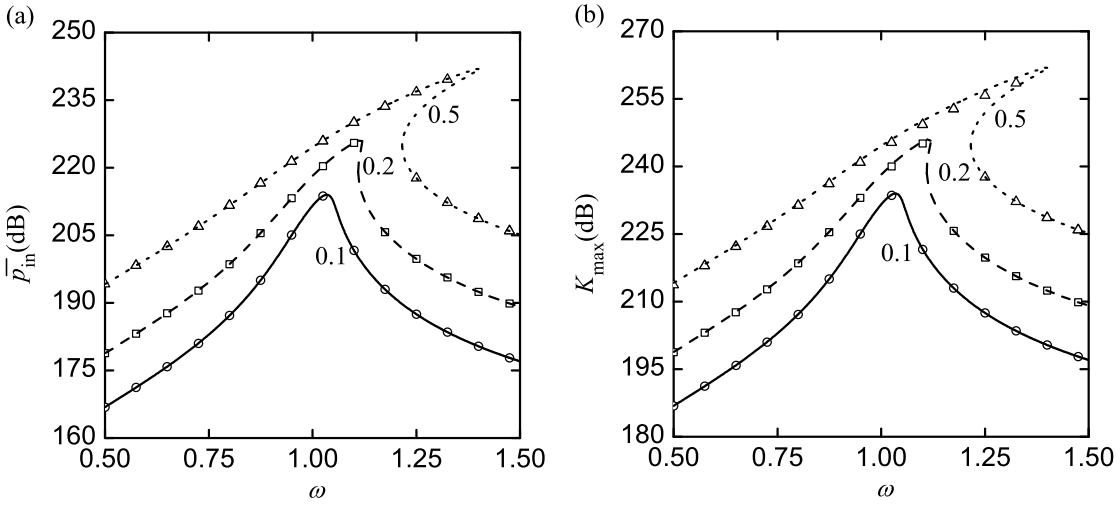

FIGURE 4.7: Effects of the excitation amplitude f on (a) $\bar{p}_{in}$ and (b) K_{max} . First-order HB approximations: solid line ($f = 0.1$), dashed line ($f = 0.2$) and dotted line ($f = 0.5$). Numerical simulation results: circles ($f = 0.1$), squares ($f = 0.2$) and triangles ($f = 0.5$).

Figures 4.6 and 4.7 show the influences of the damping coefficient ξ and the excitation amplitude f on power flows of the Case II systems. Their effects on Case I and III systems can be analysed in a similar way, so the corresponding results are not provided

here. With the other parameters set as $\alpha = 1.0, \beta = 0.1, f = 0.1$, Figure 4.6 shows that the peak values in both $\bar{p}_{in}$ and K_{max} decrease with an increasing ξ. As ξ reduces from 0.05 to 0.01, the power flow curves bend further to the higher frequency range. Away from the resonance region, the effects of damping on TAIP and the maximum kinetic energy are different, with $\bar{p}_{in}$ increasing with damping, but K_{max} not sensitive to it. Figure 4.7 shows that input power increases with the excitation amplitude f when the other parameters are set as $\alpha = 1.0, \beta = 0.1, \xi = 0.05$. It is also seen that as the f increases from 0.1 to 0.5, the nonlinear effects become stronger and the curves bend towards the high frequencies.

4.2.2 A second-order approximation

In first-order HB approximations, only the primary response component with the same frequency as the excitation is considered. However, for a nonlinear system, other frequency components may become large and dominant. To reveal this phenomenon, a second-order HB approximation is adopted to obtain more accurate solutions of power flow variables.

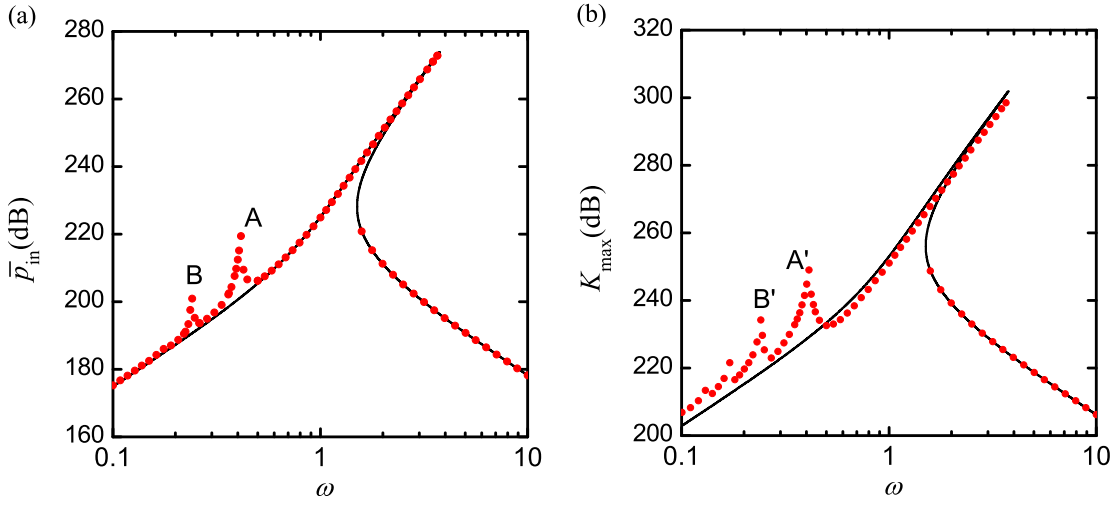

FIGURE 4.8: Effects of super-harmonic resonances on (a) $\bar{p}_{in}$ and (b) K_{max} . Solid lines: first-order HB approximations; dots: numerical simulation results. Parameters are set as $\alpha = 1.0, \beta = 0.1, \xi = 0.02, f = 2$.

Super-harmonic resonances

For the system with $\alpha = 1.0, \beta = 0.1, \xi = 0.02, f = 2$, Figure 4.8 compares the first-order HB approximations of $\bar{p}_{in}$ and K_{max} with those obtained using numerical integrations. In the low-frequency region, local peaks are found at points A and B in $\bar{p}_{in}$ and at A' and B' in K_{max} , resulting from the occurrences of super-harmonic resonances.

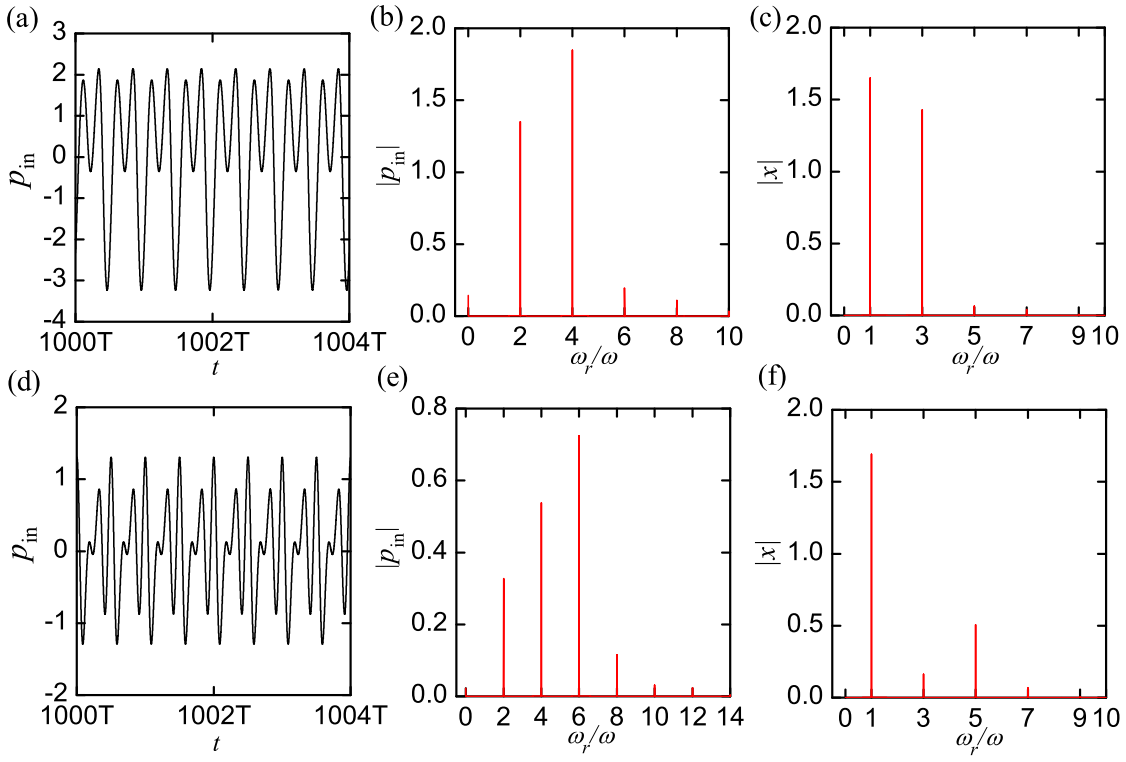

FIGURE 4.9: Power flows of the system when super-harmonic resonances occur ($\alpha = 1.0, \beta = 0.1, \xi = 0.02, f = 2.0$):(a)-(c), $\omega = 0.41$; (d)-(f), $\omega = 0.24$. (a, d) Instantaneous input power; (b, e) frequency spectra of p_{in} ; (c, f) frequency spectra of displacements.

Figures 4.9(a) and (d) show the time histories of p_{in} when the excitation frequency locates at peaks A and B in Figure 4.8, respectively. The frequency spectra ω_r of the instantaneous input power and the displacement response are presented in Figures 4.9(b, c) and 4.9(e, f). When $\omega = 0.41$, Figure 4.9(c) shows that apart from the primary response component at $\omega_r = \omega$, there is a large super-harmonic component at $\omega_r = 3\omega$. As a result, there are significant signatures in p_{in} at 2ω and 4ω. Similarly, when $\omega = 0.24$, Figure 4.9(f) shows that major response components locate at ω, 3ω, 5ω and 7ω. Consequently, the input power p_{in} is dominated by components at 2ω, 4ω, 6ω and 8ω.

To reveal the effects of super-harmonic resonances on power flows, we use a second-order HB approximation containing two frequency components ω_1 and $3\omega_1$:

$$x = \hat{x}_1 \cos\omega_1 t + \hat{x}_2 \sin\omega_1 t + \hat{x}_5 \cos 3\omega_1 t + \hat{x}_6 \sin 3\omega_1 t, \tag{4.33a}$$

$$\dot{x} = -\omega_1 \hat{x}_1 \sin\omega_1 t + \omega_1 \hat{x}_2 \cos\omega_1 t - 3\omega_1 \hat{x}_5 \sin 3\omega_1 t + 3\omega_1 \hat{x}_6 \cos 3\omega_1 t, \tag{4.33b}$$

where ω_1 equals the excitation frequency ω. Then, the nonlinear term x^3 is expressed with harmonic functions using Eqs. (4.10) and (4.11). A second-order harmonic balance

condition of Eq. (4.1) yields:

$$(\alpha-\omega_1^2)\hat{x}_1 = f - 2\xi\omega_1\hat{x}_2 - \frac{3}{4}\beta\Big(\hat{x}_1^3+\hat{x}_1\hat{x}_2^2+(\hat{x}_1^2-\hat{x}_2^2)\hat{x}_5+2\hat{x}_1\hat{x}_2\hat{x}_6+2(\hat{x}_5^2+\hat{x}_6^2)\hat{x}_1\Big), \tag{4.34a}$$

$$(\alpha-\omega_1^2)\hat{x}_2 = 2\xi\omega_1\hat{x}_1 - \frac{3}{4}\beta\Big(\hat{x}_2^3+\hat{x}_1^2\hat{x}_2+(\hat{x}_1^2-\hat{x}_2^2)\hat{x}_6-2\hat{x}_1\hat{x}_2\hat{x}_5+2(\hat{x}_5^2+\hat{x}_6^2)\hat{x}_2\Big), \tag{4.34b}$$

$$(\alpha-9\omega_1^2)\hat{x}_5 = -6\xi\omega_1\hat{x}_6 - \frac{1}{4}\beta\Big(\hat{x}_1^3-3\hat{x}_1\hat{x}_2^2+6(\hat{x}_1^2+\hat{x}_2^2)\hat{x}_5+3\hat{x}_5^3+3\hat{x}_5\hat{x}_6^2\Big), \tag{4.34c}$$

$$(\alpha-9\omega_1^2)\hat{x}_6 = 6\xi\omega_1\hat{x}_5 - \frac{1}{4}\beta\Big(-\hat{x}_2^3-3\hat{x}_1^2\hat{x}_2+6(\hat{x}_1^2+\hat{x}_2^2)\hat{x}_6+3\hat{x}_6^3+3\hat{x}_5^2\hat{x}_6\Big). \tag{4.34d}$$

A Newton-Raphson technique is used to solve this set of nonlinear equations (see, for example, Press et al. (1992)). Subsequently, TAIP is obtained from $\bar{p}_{in} = 0.5f\omega_1\hat{x}_2$. The results for TAIP agree well with those shown in Figure 4.8 around peak A.

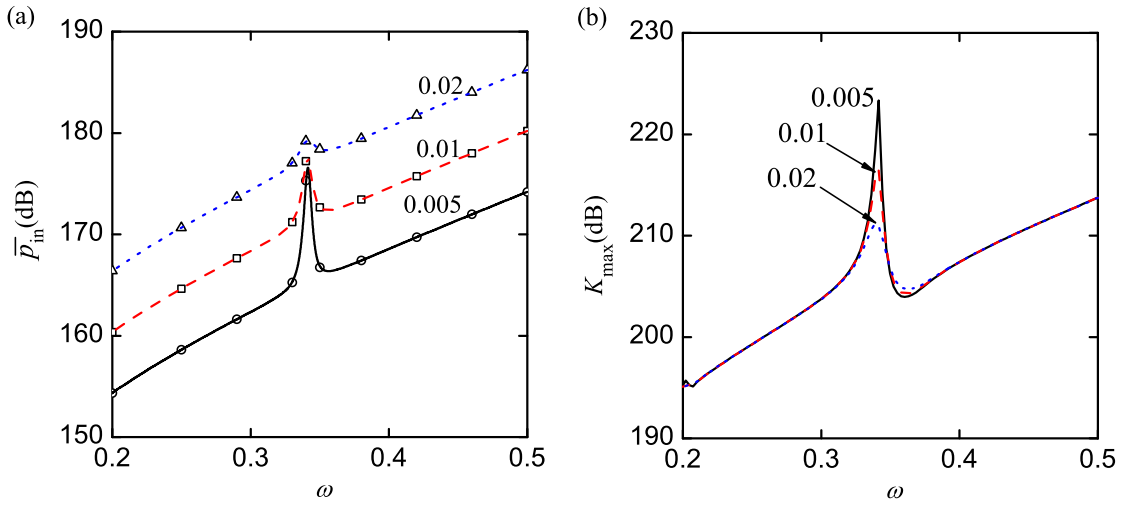

FIGURE 4.10: Effects of damping on (a) $\bar{p}_{in}$ and (b) K_{max} , in super-harmonic resonance region. Numerical simulation results: solid line ($\xi = 0.005$), dashed line ($\xi = 0.01$) and dotted line ($\xi = 0.02$). Second-order HB approximations: circles ($\xi = 0.005$), squares ($\xi = 0.01$) and triangles ($\xi = 0.02$).

Figures 4.10, 4.11 and 4.12 examine the effects of damping, nonlinearity and the excitation amplitude on the system's power flows in the super-harmonic region. They show that the numerical simulation results agree well with the second-order HB approximations. Figure 4.10 shows that for a system with $\alpha = 1, \beta = 0.1, f = 0.5$, large damping increases TAIP but suppresses the corresponding super-harmonic response peaks. The value of K_{max} is also reduced by increasing damping at the super-harmonic peak, but becomes insensitive to it when ω is away from the peak region.

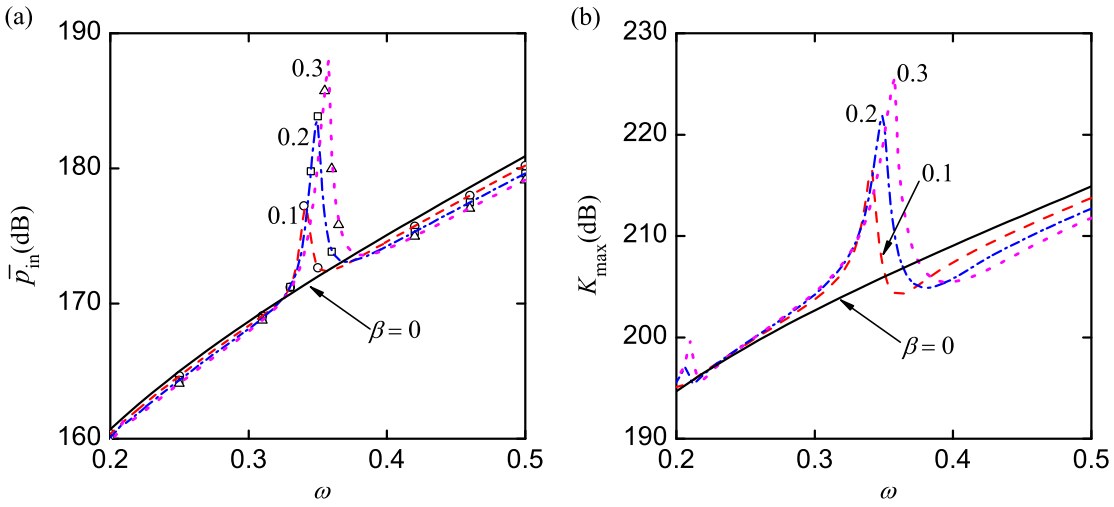

FIGURE 4.11: Effects of nonlinear parameter β on (a) $\bar{p}_{in}$ and (b) K_{max} , in super-harmonic resonance region. Numerical simulation results: solid line ($\beta = 0$), dashed line ($\beta = 0.1$), dash-dot line ($\beta = 0.2$) and dotted line ($\beta = 0.3$). Second-order HB approximations: circles ($\beta = 0.1$), squares ($\beta = 0.2$) and triangles ($\beta = 0.3$).

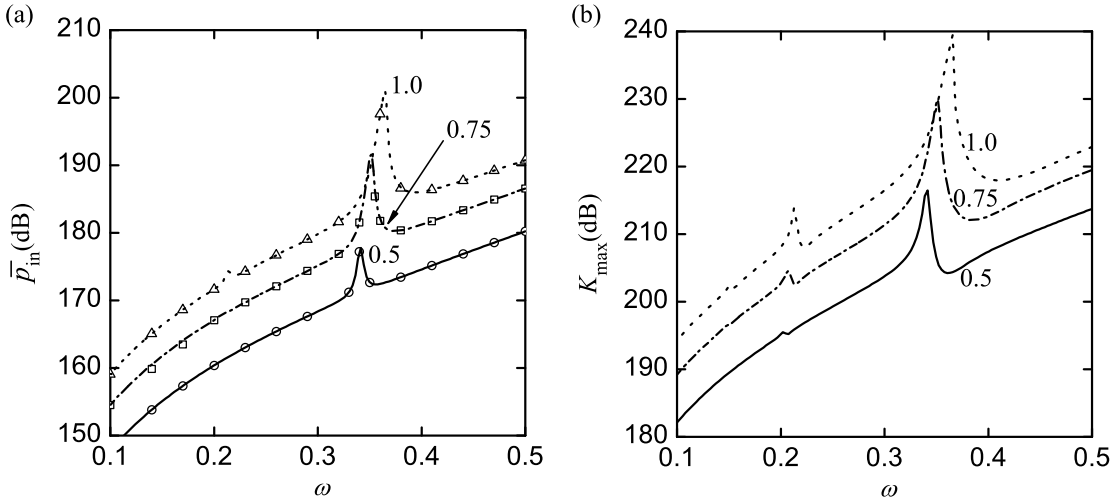

FIGURE 4.12: Effects of the excitation amplitude f on (a) $\bar{p}_{in}$ and (b) K_{max} , in super-harmonic resonance region. Numerical simulation results: solid line ($f = 0.5$), dashed line ($f = 0.75$) and dotted line ($f = 1.0$). Second-order HB approximations: circles ($f = 0.5$), squares ($f = 0.75$) and triangles ($f = 1.0$).

Figure 4.11 shows the effects of parameter β on both $\bar{p}_{in}$ and K_{max} for a system with $\xi = 0.01, \alpha = 1.0, f = 0.5$. The peak values of both $\bar{p}_{in}$ and K_{max} increase as the system nonlinearity becomes stronger. Away from the peaks, the influence of nonlinearity on $\bar{p}_{in}$ is small, but K_{max} reduces with an increasing β when $0.4 < \omega < 0.5$. Figure 4.12 shows that an increase in the excitation amplitude f generally leads to larger $\bar{p}_{in}$ and K_{max}. Two local peaks are found in each kinetic energy curve. Also, with an increase

in the excitation amplitude, the peaks become higher and the curve shifts to higher frequencies.

Sub-harmonic resonances

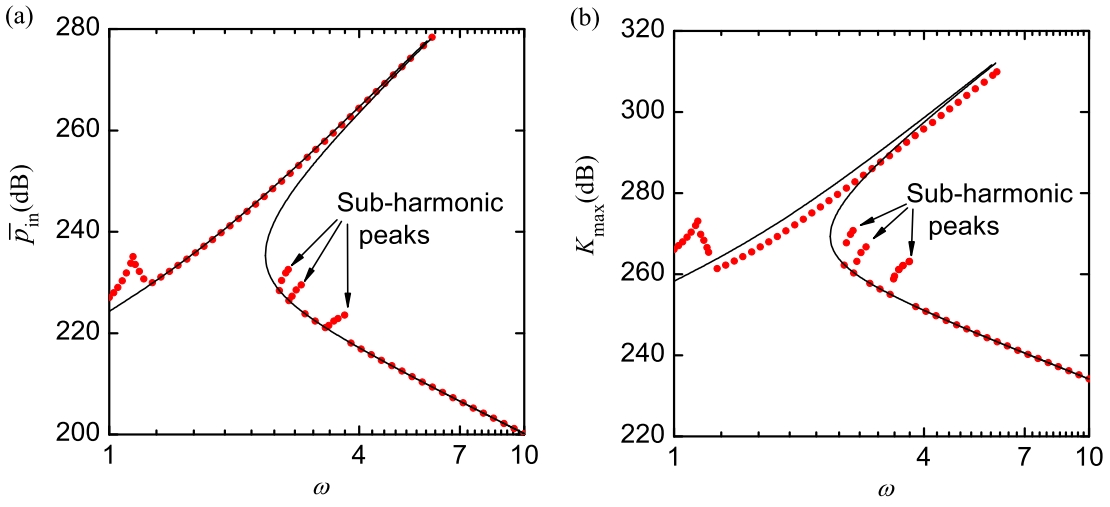

FIGURE 4.13: Effects of sub-harmonic resonances on (a) $\bar{p}_{in}$ and (b) K_{max} . Solid lines: first-order HB approximations; dots: numerical simulation results. Parameters are set as $\alpha = 1.0, \beta = 0.2, \xi = 0.02, f = 10$.

For a system subject to strong excitations, sub-harmonic resonances may appear when the excitation frequency is larger than the natural frequency of the linearized system (see Nayfeh and Mook (1979)). Thus, it is necessary to study their effects to obtain full power flow information for effective designs of passive nonlinear vibration isolators (see Yang et al. (2013)).

Figure 4.13 shows the variations of $\bar{p}_{in}$ and K_{max} with the excitation frequency for a system with $\alpha = 1.0, \beta = 0.2, \xi = 0.02, f = 10$. The results are obtained by both the RK method and a first-order HB method. There are local peaks in the lower branches of $\bar{p}_{in}$ and K_{max} obtained by numerical simulations, with the local peak values much larger than the first-order HB predictions. Therefore, to obtain a better analytical approximation, the dominant sub-harmonic components should be included in the HB model. The figure also shows a super-harmonic peak in the numerical results at $\omega = 1.14$, with a strong super-harmonic component in the response.

Figure 4.14 shows the time histories as well as frequency spectra of input power and displacement at two excitation frequencies of $\omega = 3.5$ and $\omega = 2.8$. Figures 4.14(a)-(c) for $\omega = 3.5$ show a large sub-harmonic response component at $\omega_r = \omega/3$ and a primary one at $\omega_r = \omega$. Correspondingly, significant components in p_{in} exist at $2\omega/3$, $4\omega/3$ and 2ω. When $\omega = 2.8$, there is a large sub-harmonic component at $\omega/2$, as shown in Figure

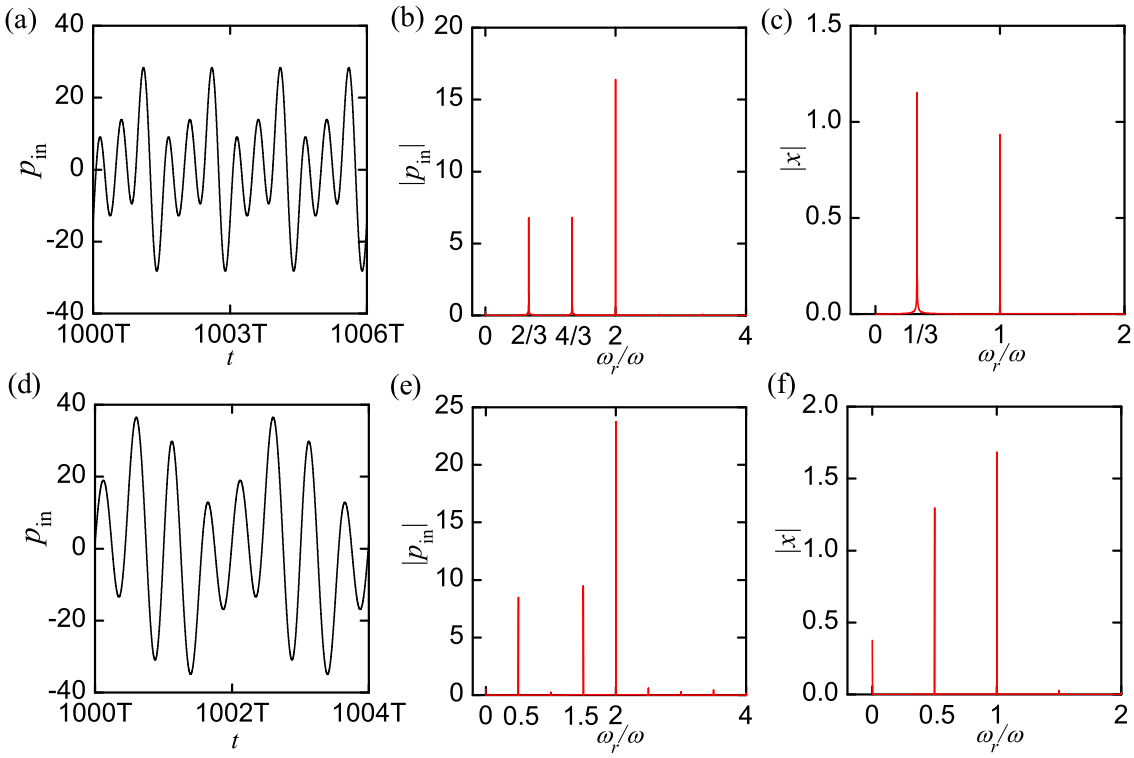

FIGURE 4.14: Power flows of the system when sub-harmonic resonances occur ($\alpha = 1.0, \beta = 0.2, \xi = 0.01, f = 10$):(a)-(c), $\omega = 3.5$; (d)-(f), $\omega = 2.8$. (a, d) Instantaneous input power; (b, e) frequency spectra of p_{in} ; (c, f) frequency spectra of displacements.

4.14(f). As a result, the input power is dominated by components at $\omega/2$, $3\omega/2$ and 2ω. Clearly, sub-harmonic resonances occur in both cases.

Again, a second-order HB method can be used to approximate TAIP of the system exhibiting sub-harmonic resonances. Considering two frequency components of ω and $\omega/3$, Figure 4.15 shows that the second-order HB approximations agree well with numerical simulations results. The value of $\bar{p}_{in}$ increases considerably at $\omega = 3.38$ but reduces significantly at $\omega = 3.69$. Sub-harmonic resonances occur between these critical frequencies, resulting in a larger amount of input power. Similarly, the power flows of the system with ($\alpha = 1.0, \beta = 0.2, \xi = 0.01, f = 10, \omega = 2.8$) can also be approximated using a second-order HB model considering frequency components ω and $\omega/2$.

4.3 Power flow behaviour associated with bifurcations and chaos

The previous section studied the power flows of the system with periodic responses containing discrete frequency components. However, chaotic motions may be encountered for the Case III systems, containing a broadband frequency signature. The corresponding power flow behaviour of the system is of great interest and investigated herein.

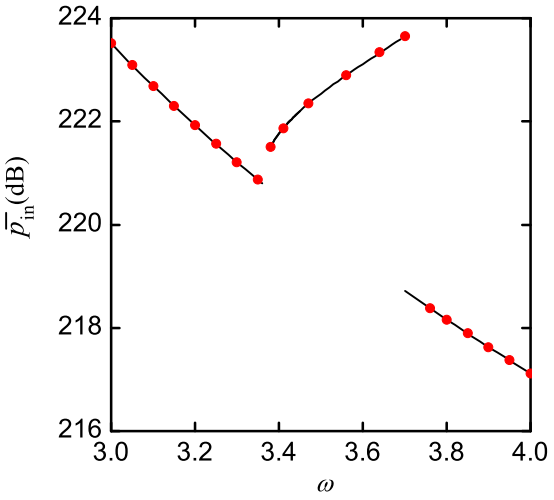

FIGURE 4.15: TAIP of the system with sub-harmonic resonances ($\alpha = 1.0, \beta = 0.2, \xi = 0.01, f = 10$). Solid line: numerical simulations; dots: second-order HB approximations.

4.3.1 Effects of bifurcations

To reveal the dynamic characteristics of the system over a frequency range, a bifurcation diagram provides a useful tool. To plot it, numerical simulations are conducted for each value of ω. The sampling displacement $x_s(t_s)$ at sampling time $t_s = t_i + (n-1)T, (n = 1, 2, \cdots,)$ is recorded, starting from t_i and using the excitation period $T = 2\pi/\omega$ as the sampling interval. In this way, for a period-1 response with a period of T, the samplings coincide at one point for a specific value of ω. Similarly, for a period-q response with its period being qT, there are q points shown for a single value of ω. If the motion is not periodic, i.e., quasi-periodic or chaotic, theoretically, there will be infinite points shown for a particular ω. The corresponding Lyapunov exponents (see, Wolf et al. (1985)) can be used to identify chaotic motions. Bifurcation occurs at frequencies where there is a sudden change in the number of shown sampling points. Similar sampling diagrams for instantaneous input power $p_s = p_{in}(t_s)$ at time t_s can be plotted to investigate input power behaviour.

For the system with $\alpha = -1, \beta = 1, \xi = 0.01, f = 0.5$ with $t_i = 500T$, Figures 4.16 and 4.17 provide bifurcation diagrams by sampling x and p_{in} , as well as variations of TAIP based on averaging time $t_p = 1000T$. To reveal different power flow solution branches, continuations are used by varying the excitation frequency from 0.1 to 10 (Figure 4.16), and from 10 to 0.1 (Figure 4.17), respectively. First-order HB approximations of TAIP are also shown in the figures for comparisons. Comparing these figures, it is seen that different stable motions co-exist when $1.58 < \omega < 4.21$. In this situation, the TAIP will be dependent on the initial conditions. Investigating the variations of p_s and TAIP with references of the bifurcation diagrams X_s, the following power flow characteristics are observed:

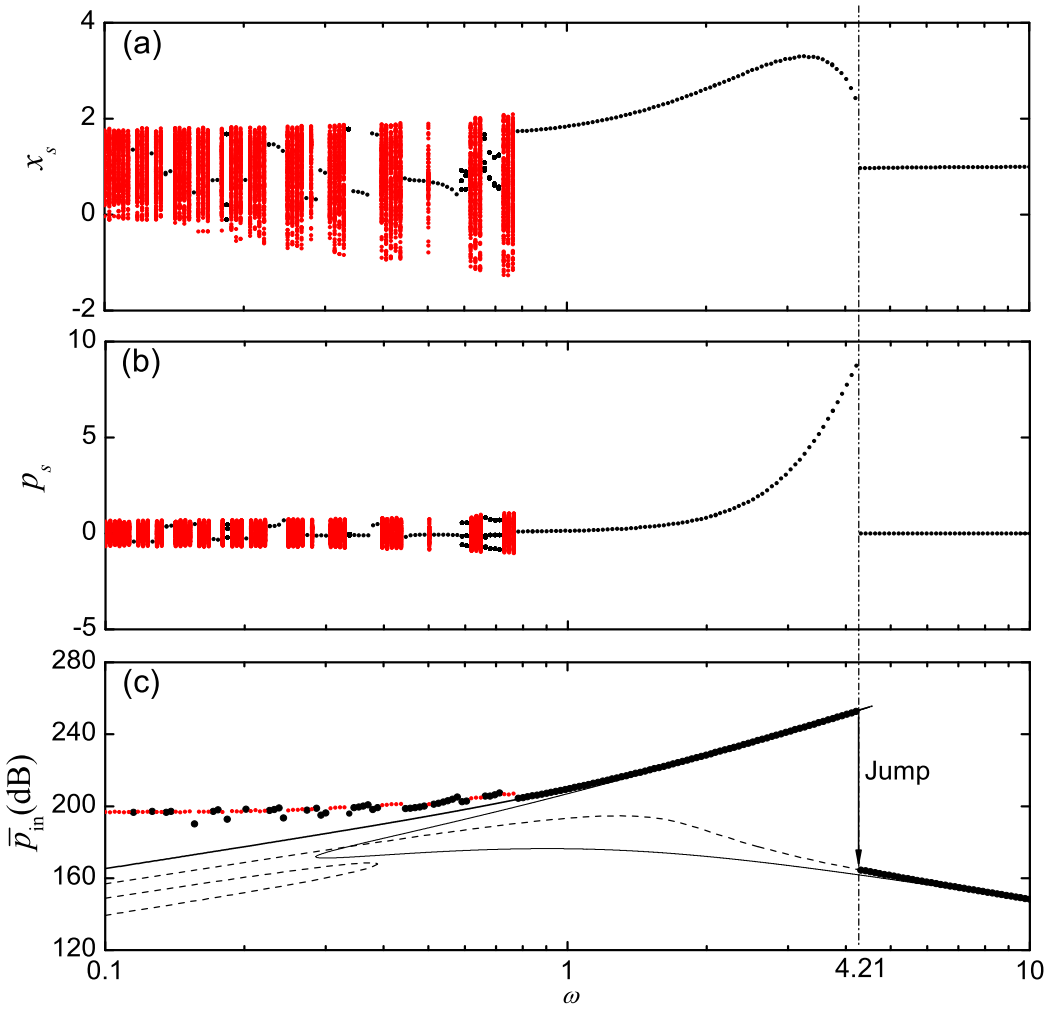

FIGURE 4.16: Effects of bifurcation on TAIP when varying ω from low to high frequencies. (a) Bifurcation diagram, (b) sampling points p_s and (c) TAIP. First-order HB approximations: solid line (Type-1 oscillations); dashed line (Type-2 oscillations). Numerical simulation results: dots.

Feature 1: At a specific excitation frequency, there is the same number of sampling points shown for X_s and p_s, so that the sampling diagram for instantaneous input power can play the same role as the conventional bifurcation diagram for identifications of periodic/non-periodic motions as well as occurrence of bifurcations.

Feature 2: In the high-frequency range, bifurcations can cause significant jumps of TAIP.

As shown in Figure 4.16, bifurcation from Type-1 (solid line) to Type-2 (dashed line) oscillations leads to a substantial jump-down in the numerical value of $\bar{p}_{in}$ at critical frequency $\omega = 4.21$. To examine the reason, Figures 4.18(a) and (d) present the variations of displacement and dissipated power at $\omega = 4.21$ and 4.22, respectively. It's shown that the former type of oscillation is of large amplitude around the point $x = 0$, while the latter case with $\omega = 4.22$ yields only a small-amplitude vibration in a single potential

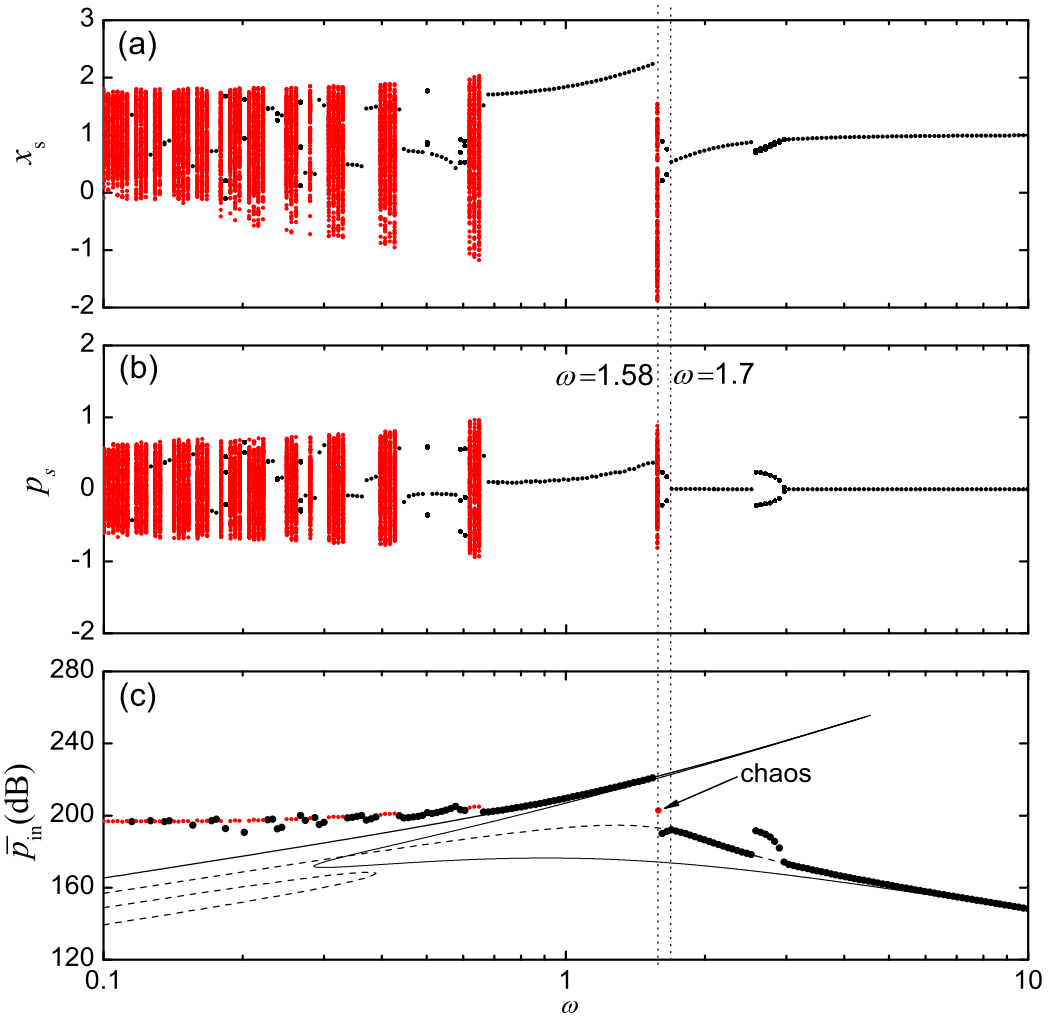

FIGURE 4.17: Effects of bifurcation on TAIP when varying ω from high to low frequencies. (a) Bifurcation diagram, (b) sampling points p_s and (c) TAIP. First-order HB approximations: solid line (Type-1 oscillations); dashed line (Type-2 oscillations). Numerical simulation results: dots.

well. Therefore, there is more power dissipation in the Type-1 oscillation than in the Type-2 oscillation and a substantial change in TAIP due to the bifurcation is observed.

Similarly in Figure 4.17, when sweeping from high to low frequencies, the system bifurcates from a period-2 oscillation to a chaotic motion at $\omega = 1.58$, and then to a Type-1 oscillation at $\omega = 1.56$. Correspondingly, TAIP increases significantly as a result of these bifurcations. As shown in Figures 4.18(b) and (e), the period-2 oscillation at $\omega = 1.60$ is in a single potential well, whereas the chaotic motion at $\omega = 1.58$ oscillates in both wells with larger amplitude, so that more power is dissipated in the latter case. Moreover, Figure 4.18(c) shows that the amplitude of Type-1 oscillation at $\omega = 1.56$ is larger than that of the chaotic motion at $\omega = 1.58$. Also, the Type-1 motion moves across two potential wells more frequently than the chaotic motion, and thus requires more energy dissipation, as shown in Figure 4.18(f).

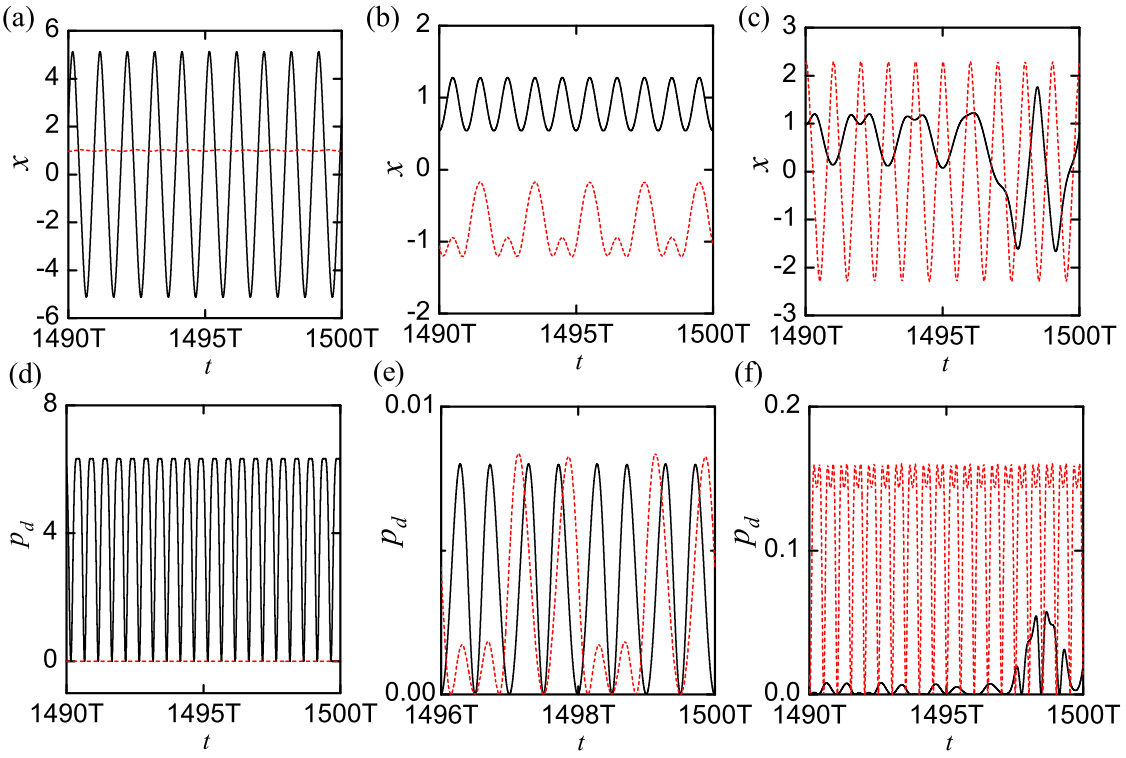

FIGURE 4.18: Bifurcations at high frequencies ($\alpha = -1, \beta = 1, \xi = 0.01, f = 0.5$). (a) and (d): solid line: $\omega = 4.21$ and dotted line: $\omega = 4.22$; (b) and (e): solid line $\omega = 1.70$ and dotted line $\omega = 1.60$; (c) and (f): solid line $\omega = 1.58$ and dotted line $\omega = 1.56$. (a)-(c): displacement response, (d)-(f): dissipated power.

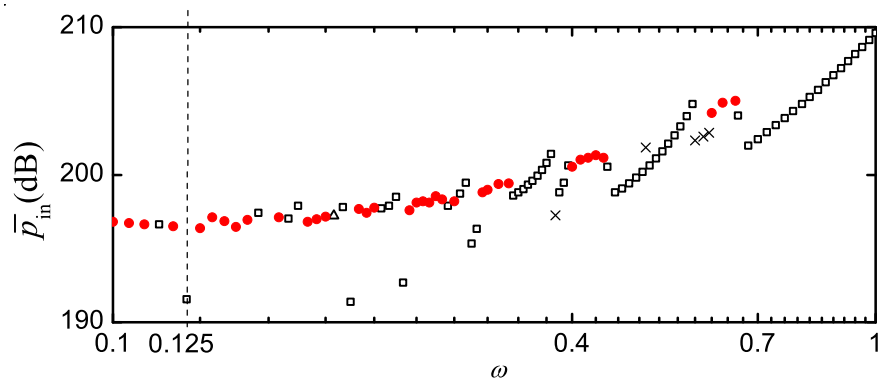

FIGURE 4.19: Variations of TAIP at low excitation frequencies using a low-to-high frequency sweep ($\alpha = -1, \beta = 1, \xi = 0.01, f = 0.5$). Dots: chaotic motions; squares: period-1 motions; triangles: period-2 motions and crosses: period-3 motions.

Feature 3: In the low-frequency range, the changes in TAIP due to bifurcations are smaller than those at high frequencies described in Feature 2.

Figure 4.19 provides an enlarged and more detailed view of the variations of TAIP in the low-frequency range for better clarity. This figure shows that TAIP of chaotic motions indicated by the dots only varies slightly with the excitation frequency. In

contrast, the TAIP corresponding to period-1 motions marked by squares changes more abruptly at some frequencies due to bifurcations. For example, the response changes from a chaotic motion at $\omega = 0.12$ to a period-1 motion at $\omega = 0.125$, and then resumes being chaotic at $\omega = 0.13$. Correspondingly, TAIP for the period-1 motion is smaller than that for the chaotic motions. Figure 4.20 shows the frequency components in the input power at these three excitation frequencies. Figure 4.20(b) shows that the period-1 motion contains discrete frequency signatures, but both chaotic motions with the largest Laypunov exponent being positive contain broadband frequency spectra, as shown by Figure 4.20(a) and (c).

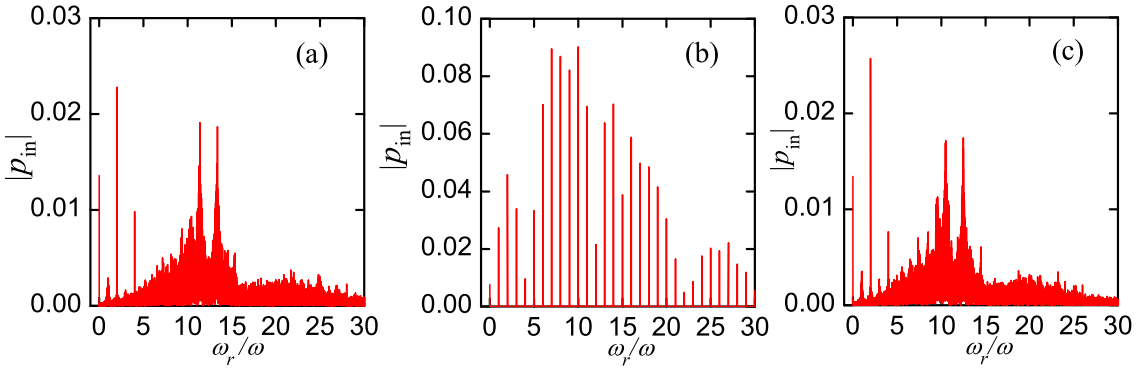

FIGURE 4.20: Frequency spectra at low excitation frequencies ($\alpha = -1, \beta = 1, \xi = 0.01, f = 0.5$). (a) $\omega = 0.120$ with the largest Lyapunov exponent: 0.039, (b) $\omega = 0.125$, period-1 motion and (c) $\omega = 0.130$ with the largest Lyapunov exponent: 0.04.

4.3.2 Effects of chaotic responses

Here we focus on the effects of chaotic motion on both the instantaneous and time-averaged input power of the system. Figures 4.16 and 4.17 reveal the following behaviour of power flows due to the occurrences of chaotic motions.

Chaos effect 1: Given an infinite sampling time span, there would be infinite sampling points for input power $p_s(t_s)$ when a chaotic motion occurs as the input power becomes non-periodic.

Chaos effect 2: Compared with the corresponding HB approximation of TAIP for the Type-1 oscillations, the numerical results show larger TAIP at low excitation frequencies, but smaller when the excitation frequency is large.

To explain this characteristic, Figure 4.21 compares the power flows of the system with $\alpha = -1, \beta = 1, \xi = 0.01, f = 0.5$, excited at $\omega = 0.13$ and $\omega = 1.58$, respectively. For the former case, as shown in Figures 4.21 (a)-(c), the HB approximation underestimates power flow levels as it neglects the power dissipation caused by super-harmonic oscillations in the potential wells. This is in contrast to the latter case with a larger excitation

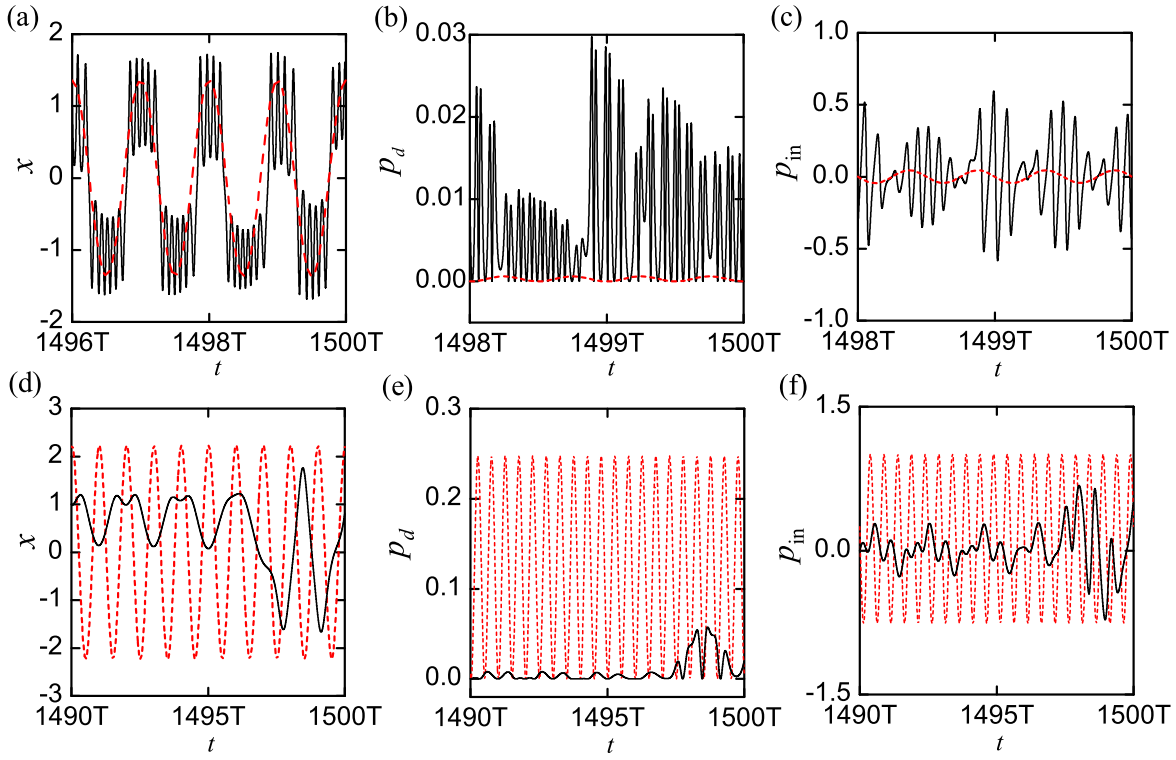

FIGURE 4.21: Comparisons of power flows for chaotic motions with the corresponding HB approximations. (a)-(c): $\omega = 0.13$ and (d)-(f): $\omega = 1.58$. (a) and (d): displacement; (b) and (e): dissipated power; (c) and (f): input power. Solid line: chaotic motions; dashed line: first-order HB approximations..

frequency of $\omega = 1.58$. As shown in Figures 4.21(d)-(f), the system moves around the unstable equilibrium at $x = 0$ less frequently with smaller amplitude than the HB approximation. Correspondingly, the dissipated and input powers are much lower than the HB predictions.

When the system displays chaotic motions, the influences of averaging time t_p on TAIP should be clarified. To examine this, we set t_p as N cycles of the excitation, i.e., $t_p = NT$ and plot the variations of $\bar{p}_{in}$ against t_p in Figure 4.22. For a chaotic response with the largest Lyapunov exponent of 0.07, the figure shows that the variations in $\bar{p}_{in}$ are smaller than 4dB when $10 < N < 100$. When $N > 100$, the value of TAIP remains in between 200dB and 202dB. Moreover, as N increases, the fluctuation becomes smaller and $\bar{p}_{in}$ tends asymptotically to 200.6dB. This suggests a conclusion as follows.

Chaos effect 3: For a chaotic response, there exists an asymptotic value of TAIP as the averaging time increases. The asymptotical behaviour of TAIP may be an important characteristic of chaotic motions of a system. As we have learnt, for periodic vibrations, TAIP based on $t_p = NT$ (N is a positive integer) is constant, independent of N. A chaotic motion could be considered as a periodic one with an infinite period, and also by definition it is bounded in space, so that its TAIP tends to a constant with increasing averaging time.

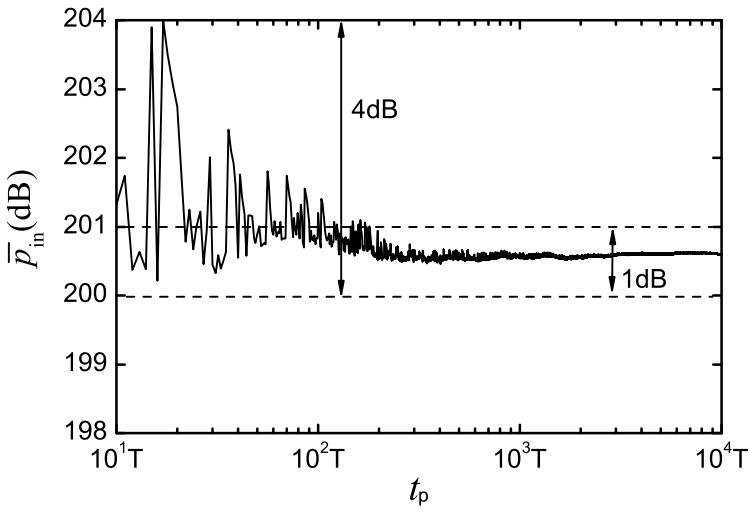

FIGURE 4.22: Effects of averaging time on time-averaged input power of a chaotic response ($\alpha = -1, \beta = 1, \xi = 0.01, f = 0.1, \omega = 0.4$). The initial conditions are set as $(x_0, y_0) = (0, 0)$.

Chaos effect 4: The TAIP for chaotic motions is not sensitive to initial conditions if the averaging time is large enough.

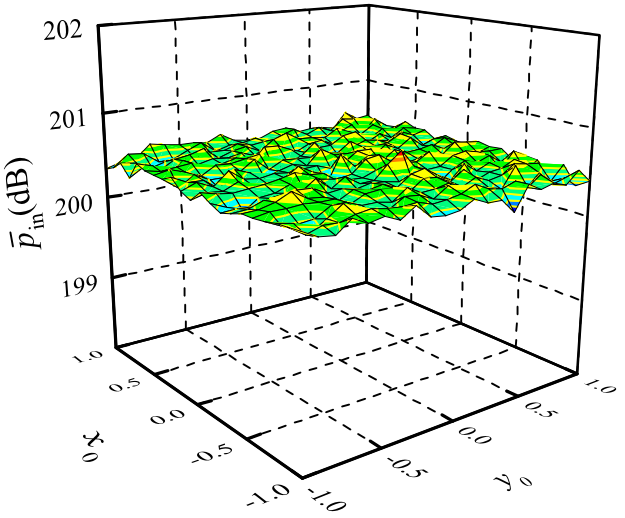

FIGURE 4.23: Effects of initial conditions, on time-averaged input power of chaotic motions ($\alpha = -1, \beta = 1, \xi = 0.01, f = 0.1, \omega = 0.4$).

To examine the effects of initial conditions on TAIP of a chaotic response, Figure 4.23 provides the numerical results of TAIP, averaged from $t_i = 500T$ using averaging time $t_p = 1000T$. With the initial displacement x_0 and velocity y_0 varying between -1 and 1, it shows that the variations in TAIP are smaller than 1dB. It should be noted that the chaotic motion considered here is the only stable solution in the examined region of

initial conditions. Otherwise, the value of TAIP may change significantly if the system response evolves to other stable solutions.

4.4 Conclusions

The Duffing oscillator was investigated in this chapter to explore its intrinsic power flow behaviour due to the stiffness nonlinearity. The effects of different nonlinear phenomena, such as sub-/super- harmonic resonances, bifurcation and chaos on power flows were investigated. The influences of different parameters, initial conditions and averaging time on the time-averaged input power (TAIP) were examined. Both the instantaneous and time-averaged power flow characteristics of the system were analysed. The HB (Harmonic balance) method was used to obtain approximate analytical solutions of power flow variables while the numerical simulations based on the Runge-Kutta method were used to provide more accurate results associated with periodic/chaotic motions. Based on the study, the following conclusions are drawn:

- If the system exhibits periodic motions, only the in-phase velocity component with the same frequency as the excitation contributes to the TAIP averaged over the response period;
- Using a first-order HB approximation, the TAIP is proportional to the maximum kinetic energy K_{max} of the system if the damping coefficient remains unchanged. Also, there exist upper bounds (peak values) for both TAIP and K_{max}, independent of the coefficients α and β. The upper bound values increase with the excitation amplitude and decrease with an increasing damping coefficient. Moreover, the TAIP and K_{max} are not sensitive to parameters α and β when the excitation frequency is large. The nonlinear parameter β has a significant influence on TAIP of the hardening/softening systems ($\alpha > 0$) near the resonance frequency. When the excitation frequency is away from the resonance, TAIP is not sensitive to variations in β. Similarly, variations in α with a fixed positive β affect TAIP mainly when the excitation frequency is close to or smaller than the primary resonance frequency;
- The TAIP may be non-unique and exhibits sensitivity to the initial conditions. The basins of attraction can be examined to identify different regions of initial conditions corresponding to varying power flow levels. Crossing the boundary of different basins, the TAIP may change significantly;
- When the system exhibits sub-/super- harmonic resonances, there will be large sub-/super- components in the input power, and also a potentially significant increase in its time-averaged value. HB formulations of different orders can be used for analytical approximations;

- Bifurcations of different types of motions can cause large jumps in the TAIP. This is especially true for the double-well potential system when the motion bifurcates from oscillations in a single potential well to be in both potential wells;
- In the low-frequency range, the numerical results of TAIP of a double well potential system were shown to be larger than the first-order HB approximations, resulting from large super-harmonic components. Compare with that, the numerical value of TAIP corresponding to chaotic motion at high frequencies was smaller than the HB approximation;
- When the system exhibits chaotic motion, the corresponding TAIP tends to an asymptotic value with increasing averaging time. Also, the TAIP is not sensitive to the initial conditions when there is a single chaotic attractor in the region;
- The TAIP provides a uniform index to assess the dynamic performance of different types of the Duffing system, exhibiting periodic/chaotic motions.

Chapter 5

Power flow analysis of the Van der Pol oscillator

In this chapter, the power flow behaviour of the Van der Pol (VDP) oscillator is investigated to examine the effects of nonlinear damping on the system's power flows. This oscillator is a typical dynamical system characterised by possible negative damping and has been shown to exhibit complex nonlinear behaviour. It was firstly proposed about a century ago to model the limit cycle oscillation (LCO) of currents in electrical circuits with a triode valve (see, Van der Pol (1920)). Ever since then, the model has been frequently used to reveal the dynamics of various systems in many scientific and industrial fields. For example, in biology, it provided a good model for the gastric mill central pattern generator in lobsters (see, for example, Rowat and Selverston (1993)). In seismology, the Van der Pol equation was used to develop a model of the interaction between two plates in geological fault (see Cartwright et al. (1999)). Similar oscillations that are exhibited by the VDP oscillator were also encountered in aero-elastic systems, such as in-flow bluff bodies (see Dowell (1981)). The essential nonlinearity in damping gives rise to complicated nonlinear phenomena, the effects of which on power flows have not been thoroughly addressed and are studied herein.

5.1 Power flow formulations

The general governing equation of a harmonically excited Van der Pol oscillator can be expressed as

$$\ddot{x} + \alpha(x^2 - 1)\dot{x} + \beta x = f\cos\omega t, \tag{5.1}$$

where f and ω denote the amplitude and frequency of the harmonic excitation force, respectively; parameter α is assumed to be positive throughout this chapter.

The nonlinearity of this oscillator is demonstrated by the damping term, i.e.,

$$f_d = \alpha(x^2 - 1)\dot{x}, \tag{5.2}$$

This equation and Figure 5.1(a) show that the damping coefficient $\alpha(x^2 - 1)$ is positive when $|x| > 1$, i.e., the displacement is large. It becomes zero when $|x| = 1$ and negative when the absolute value of displacement x is smaller than unity.

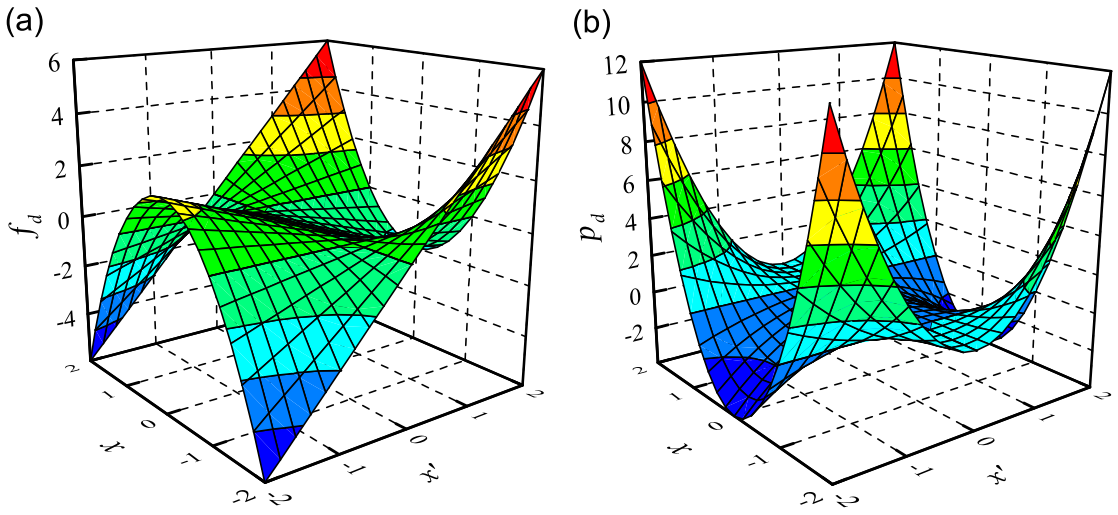

FIGURE 5.1: Variations of (a) nonlinear damping force and (b) dissipated power, with respect to displacement and velocity ($\alpha = 1$).

Multiplying by velocity $\dot{x}$ on both sides of Eq. (5.1), the equation of power balance is obtained, i.e.,

$$\ddot{x}\dot{x} + \alpha(x^2 - 1)\dot{x}\dot{x} + \beta x\dot{x} = \dot{x} f \cos\omega t, \tag{5.3}$$

which may alternatively be written as

$$\dot{K} + \dot{U} + p_d = p_{in}, \tag{5.4}$$

where

$$\dot{K} = \ddot{x}\dot{x}, \tag{5.5a}$$

$$\dot{U} = \beta x\dot{x}, \tag{5.5b}$$

$$p_d = \alpha(x^2 - 1)\dot{x}\dot{x}, \tag{5.5c}$$

$$p_{in} = \dot{x} f \cos\omega t \tag{5.5d}$$

are the instantaneous rates of change of kinetic and potential energies and instantaneous dissipated and input powers, respectively. It can be seen that the dissipated power p_d is positive when $|x| > 1$ and $x \neq 0$, as shown in Eq. (5.5c) as well as Figure 5.1(b). When

the displacement is large, the damping term in the oscillator dissipates vibration energy, similar to the effects of conventional linear viscous damping. However, when $|x| < 1$ and $\dot{x} \neq 0$, the value of p_d would be negative, indicating net energy input by damping. In other words, the damping force plays the role of energy supply when the displacement is small. This feature of the van der Pol oscillator differs greatly from linear vibration systems and has a significant impact on the system's dynamic behaviour.

Assuming that the displacement and velocity at $t = t_i$ are x_i and $\dot{x}_i$, respectively, and become x and $\dot{x}$ at $t = t_i + t_p$, an integration of Eq. (5.3) over the time span yields the equation of energy balance, i.e.,

$$\Delta K + \Delta U + E_d = E_{in}, \tag{5.6}$$

where

$$\Delta K = \frac{\dot{x}^2 - \dot{x_i}^2}{2}, \tag{5.7a}$$

$$\Delta U = \int_{t_i}^{t_i+t_p} \beta x \dot{x} \, \mathrm{d}t = \frac{\beta(x^2 - x_i^2)}{2}, \tag{5.7b}$$

$$E_d = \int_{t_i}^{t_i+t_p} \alpha(x^2 - 1)\dot{x}^2 \, \mathrm{d}t, \tag{5.7c}$$

$$E_{in} = \int_{t_i}^{t_i+t_p} \dot{x} f \cos \omega t \, \mathrm{d}t, \tag{5.7d}$$

which represent the net changes in kinetic and potential energies and total dissipated and input energies, respectively. Time-averaged input and dissipated powers using averaging time t_p are formulated as

$$\bar{p}_d = \frac{E_d}{t_p} = \frac{1}{t_p} \int_{t_i}^{t_i+t_p} \alpha(x^2 - 1)\dot{x}^2 \, \mathrm{d}t, \tag{5.8a}$$

$$\bar{p}_{in} = \frac{E_{in}}{t_p} = \frac{1}{t_p} \int_{t_i}^{t_i+t_p} \dot{x} f \cos \omega t \, \mathrm{d}t. \tag{5.8b}$$

For a linear system, the net changes in potential and kinetic energies of the system will vanish over a cycle of oscillation. Correspondingly, the time-averaged dissipated and input powers will be equal. However, this may not be the case for the current nonlinear system, as the steady-state motion may become non-periodic.

To obtain the response and subsequently power flow variables of the oscillator, analytical approximations based on the harmonic balance or the averaging methods can be used. Numerical simulations, although computationally more expensive, provide a valuable approach for verifications of analytical formulations. For the implementation, Eq. (5.1)

is firstly written in a form of two first-order differential equations in the phase space:

$$\dot{x} = y, \tag{5.9a}$$

$$\dot{y} = -\alpha(x^2 - 1)\dot{x} - \beta x + f\cos\omega t. \tag{5.9b}$$

Then numerical techniques, such as the fourth-order Runge-Kutta method, are available to obtain the solutions. In the remaining content of this chapter, the power flow behaviour of the unforced and the forced oscillators will be studied separately using analytical approximations as well as numerical methods.

5.2 Power flow characteristics of the unforced system

5.2.1 Limit cycle oscillations

The unforced Van der Pol oscillator ($f = 0$) is characterised by limit cycle oscillations, i.e., a free vibration of the unforced system arising from an initial disturbance $(x_0, y_0) \neq (0, 0)$ will not decay with time but evolve to a stable periodic motion. This is in contrast to conventional unforced, damped linear systems, which will eventually rest at static equilibrium positions as the initial energy input will be dissipated by damping. Using the fourth-order Runge-Kutta method, limit cycle oscillations of an unforced VDP oscillator with $\alpha = 0.5, \beta = 1, f = 0$ are shown in Figure 5.2(a), which suggests the steady-state motion of the system starting either from point B with $(x_0, y_0) = (1, 0)$ or point C with $(x_0, y_0) = (3, 0)$ corresponds to an enclosed curve in phase plane. When the dissipated power p_d is added to the phase portrait as another coordinate, the two-dimensional limit cycle can be transformed to a three-dimensional form, as shown in Figure 5.2(b).

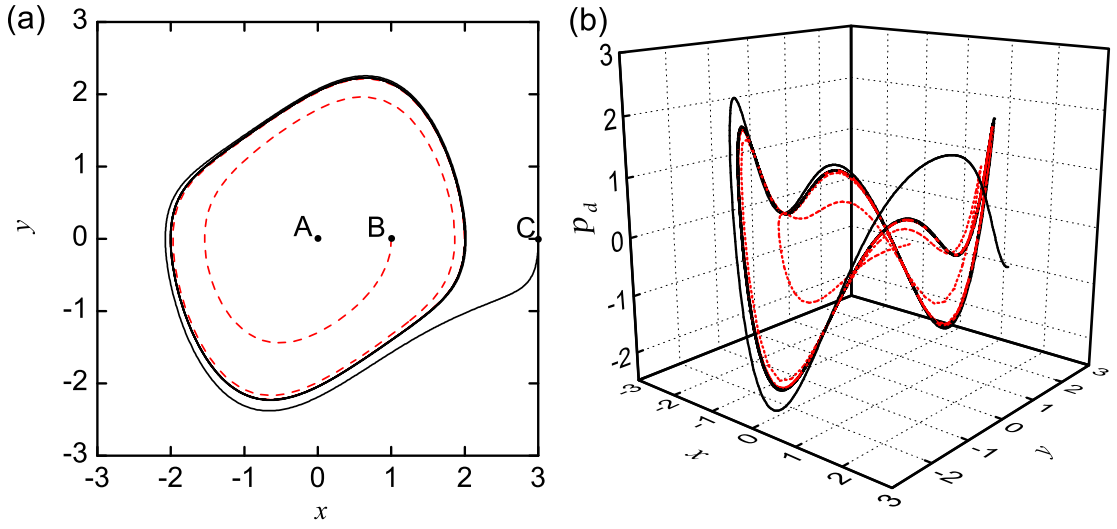

FIGURE 5.2: Phase portraits. (a) Two-dimensional and (b) three-dimensional forms.

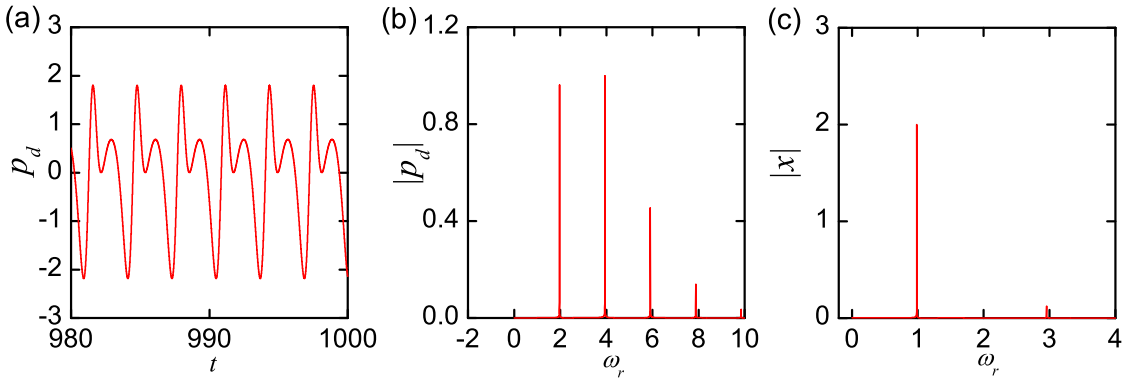

FIGURE 5.3: Power flows of the unforced system. (a) Time histories of p_d, (b) frequency spectrum of p_d and (c) frequency spectrum of displacement. Parameters $\alpha = 0.5, \beta = 1, f = 0$ and initial condition $(x_0, y_0) = (1, 0)$.

For an unforced Van der Pol oscillator, there will be no input power by the excitation. However, the instantaneous dissipated power may not be zero, as shown in Figure 5.2(b), though its time-averaged value over an oscillation cycle will vanish such that the power balance condition is satisfied. Figure 5.3 shows the time histories of the dissipated power of an unforced system with $\alpha = 0.5, \beta = 1$. Using a Fourier transformation of the time histories, the dominant frequencies in the dissipated power and the displacement are found and shown in Figures 5.3(b) and (c), respectively. It is shown that the response contains a large component at $\omega_r = \omega_p \approx 0.985$ and a small one at $\omega_r = 3\omega_p \approx 2.954$. Correspondingly, there are frequency signatures in dissipated power at $2\omega_p, 4\omega_p, 6\omega_p, 8\omega_p$ and $10\omega_p$.

5.2.2 Analytical approximations

As an alternative to the numerical investigations, analytical harmonic balance (HB) approximations can be used to reveal the power flow behaviour of the unforced system. Note that when it exhibits periodic motions, the displacement response may be represented by a truncated Fourier series, i.e.,

$$x(t) = \sum_{n=1}^{N} (\hat{z}_{2n-1} \cos n\omega_p t + \hat{z}_{2n} \sin n\omega_p t), \tag{5.10}$$

where ω_p is assumed to be the unknown fundamental frequency of the oscillation; $z_j (j = 1, 2, \cdots, 2N)$ are the coefficients of the harmonic functions. A differentiation of the displacement with respect to time yields the velocity of the system:

$$\dot{x}(t) = \sum_{n=1}^{N} (-n\omega_p \hat{z}_{2n-1} \sin n\omega_p t + n\omega_p \hat{z}_{2n} \cos n\omega_p t). \tag{5.11}$$

The nonlinear term in Eq. (5.1) can be expanded as

$$x^2\dot{x} = \hat{q}_0 + \sum_{n=1}^{N}(\hat{q}_{2n-1}\cos n\omega_p t + \hat{q}_{2n}\sin n\omega_p t), \tag{5.12}$$

where the coefficients of the components are

$$\hat{q}_0 = \frac{\omega_p}{2\pi}\int_0^{\frac{2\pi}{\omega_p}} x^2\dot{x}\,\mathrm{d}t, \tag{5.13a}$$

$$\hat{q}_{2n-1} = \frac{\omega_p}{\pi}\int_0^{\frac{2\pi}{\omega_p}} x^2\dot{x}\cos n\omega_p t\,\mathrm{d}t, \tag{5.13b}$$

$$\hat{q}_{2n} = \frac{\omega_p}{\pi}\int_0^{\frac{2\pi}{\omega_p}} x^2\dot{x}\sin n\omega_p t\,\mathrm{d}t. \tag{5.13c}$$

Inserting the expanded expressions into the governing equation (5.1) and balancing the coefficients of the corresponding harmonic terms, a total number of $2N$ equations can be established. Note that a phase condition can be used by setting $\hat{z}_2 = 0$ so that there are $2N$ unknowns in total (See, for example, Liu et al. (2007)). By solving these equations, the natural frequency, the coefficients of harmonic terms and subsequently the power flow variables are found.

To illustrate, a first-order approximation of the unforced response is assumed, i.e.,

$$x = \hat{z}_1\cos\omega_p t, \tag{5.14a}$$

$$\dot{x} = -\hat{z}_1\omega_p\sin\omega_p t, \tag{5.14b}$$

where $\hat{z}_2 = 0$ by using a phase condition. Using Eqs. (5.12), (5.13) and (5.14), the nonlinear term is approximated by

$$x^2\dot{x} = -\omega_p\hat{z}_1^3\cos\omega_p^2 t\sin\omega_p t. \tag{5.15}$$

Substituting Eqs. (5.14) and (5.15) into Eq. (5.1) and further simplifying, it follows that

$$(\beta-\omega_p^2)\hat{z}_1\cos\omega_p t - \frac{1}{4}\alpha\omega_p\hat{z}_1^3(\sin\omega_p t + \sin 3\omega_p t) + \alpha\omega_p\hat{z}_1\sin\omega_p t = 0. \tag{5.16}$$

Equating the coefficients of the first-order terms in Eq. (5.16), we obtain

$$(\beta-\omega_p^2)\hat{z}_1 = 0, \tag{5.17a}$$

$$\frac{1}{4}\alpha\omega_p\hat{z}_1(4-\hat{z}_1^2) = 0, \tag{5.17b}$$

from which the natural frequency and the response amplitude are found to be $\omega_p = \sqrt{\beta}, \hat{z}_1 = 2$, respectively. It suggests that the natural frequency ω_p is a monotonically

increasing function of β and the response amplitude keeps constant regardless of variations in the parameters α and β. With reference to Eq. (5.5c), the instantaneous dissipated power is approximated by

$$p_d \approx 4\alpha\beta\big(4\cos^2(\sqrt{\beta}t) - 1\big)\sin^2(\sqrt{\beta}t) = 2\alpha\beta\Big(\cos(2\sqrt{\beta}t) - \cos(4\sqrt{\beta}t)\Big), \tag{5.18}$$

which suggests the existence of two frequency components in the dissipated power. Using a first-order approximation, the maximum kinetic energy of the unforced system is

$$K_{max} \approx \frac{1}{2}\hat{z}_1^2\omega_p^2 = 2\beta, \tag{5.19}$$

which indicates the maximum kinetic energy is a monotonically increasing function of the stiffness coefficient β.

As has been shown in Figure 5.3, the unforced response contains more than one frequency component. Therefore, possible improvements to the accuracy of the above first-order approximations of power flows can be made by including the frequency component at 3Ω in the analytical model:

$$x = \hat{z}_1\cos\omega_p t + \hat{z}_5\cos 3\omega_p t + \hat{z}_6\sin 3\omega_p t, \tag{5.20a}$$

$$\dot{x} = -\hat{z}_1\omega_p\sin\omega_p t - 3\omega_p\hat{z}_5\sin 3\omega_p t + 3\omega_p\hat{z}_6\cos 3\omega_p t. \tag{5.20b}$$

Using Eqs. (5.13), the Fourier coefficients of the nonlinear term may be expressed as

$$\hat{q}_1 = \frac{\omega_p\hat{z}_1^2\hat{z}_6}{4}, \tag{5.21a}$$

$$\hat{q}_2 = \frac{-\omega_p\hat{z}_1(\hat{z}_1^2 + \hat{z}_1\hat{z}_5 + 2\hat{z}_5^2 + 2\hat{z}_6^2)}{4}, \tag{5.21b}$$

$$\hat{q}_5 = \frac{3\omega_p(2\hat{z}_1^2 + \hat{z}_5^2 + \hat{z}_6^2)\hat{z}_6}{4}, \tag{5.21c}$$

$$\hat{q}_6 = -\frac{\omega_p\hat{z}_1^3}{4} - \frac{3\omega_p(2\hat{z}_1^2 + \hat{z}_5^2 + \hat{z}_6^2)\hat{z}_5}{4}. \tag{5.21d}$$

Inserting the expanded expression of responses as well as the nonlinear term back into Eq. (5.1) and balancing the coefficients of the corresponding harmonic terms leads to

$$(\beta - \omega_p^2)\hat{z}_1 + \alpha q_1 = 0, \tag{5.22a}$$

$$\alpha(q_2 + \omega_p\hat{z}_1) = 0, \tag{5.22b}$$

$$(\beta - 9\omega_p^2)\hat{z}_5 + \alpha(q_5 - 3\omega_p\hat{z}_6) = 0, \tag{5.22c}$$

$$(\beta - 9\omega_p^2)\hat{z}_6 + \alpha(q_6 + 3\omega_p\hat{z}_5) = 0. \tag{5.22d}$$

Once the values of α and β are set, a Newton-Raphson method (see, for example, Press et al. (1992)) may be employed to solve the nonlinear algebraic equations (5.22). The

natural frequency, amplitudes of the first harmonic term $\rho_1(=\hat{z}_1)$ and the third $\rho_3(=\sqrt{\hat{z}_5^2+\hat{z}_6^2})$ can be obtained. The results for $\beta=1$ shown in Figure 5.4 indicate that the natural frequency of the unforced system decreases as the nonlinear damping parameter α increases. On the contrary, the amplitudes of the first and the third harmonic terms both increase with α.

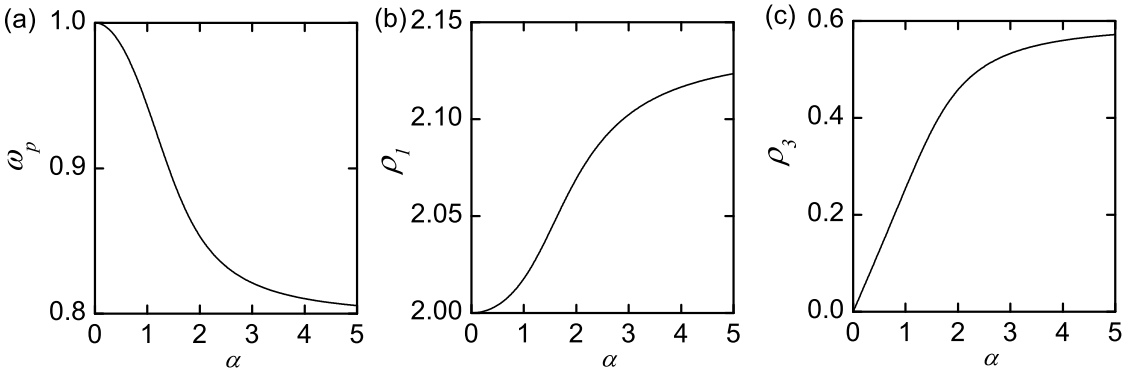

FIGURE 5.4: Second-order HB approximations of the unforced response. (a) Natural frequency, (b) ρ_1 and (c) ρ_3.

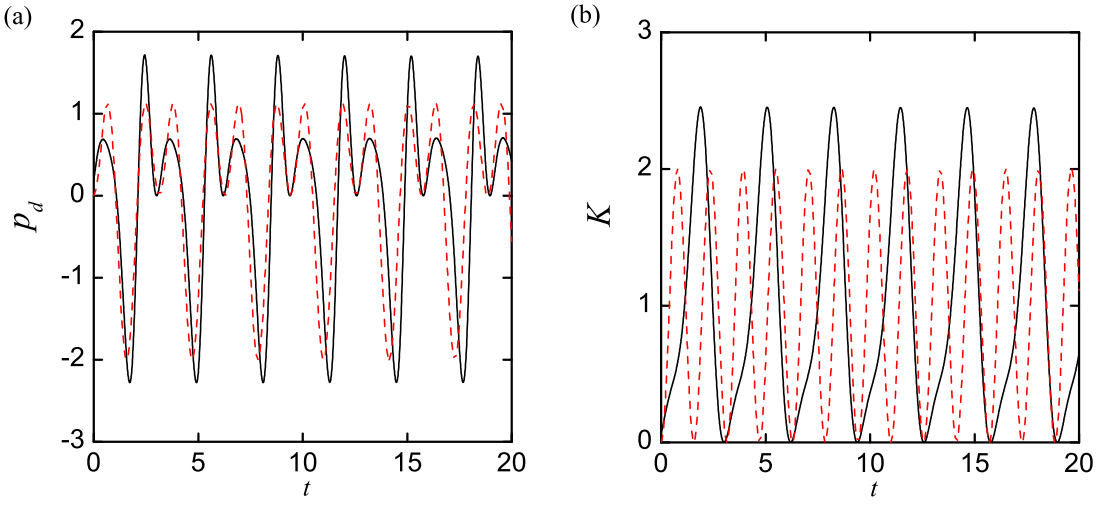

FIGURE 5.5: HB approximations of the (a) dissipated power and (b) kinetic energy. Solid line: second-order approximation and dashed line: first-order approximation.

Once the approximate solution to the displacement and velocity of the system is obtained, power flow variables, such as the instantaneous dissipated power and kinetic energy, can be calculated using Eqs. (5.5), (5.7) and (5.8). For the previously studied unforced system with $\alpha=0.5,\beta=1$, the natural frequency of the system is found to be $\omega_p=0.9846$ and the steady-state displacement is approximated by

$$x(t)=2.0041\cos(0.9849t)-0.02391\cos(2.9547t)-0.1236\sin(2.9547t).$$

The variations of dissipated power and kinetic energy are shown in Figure 5.5(a) and (b), respectively. Compared with Figure 5.3(a), it can be seen that the second-order harmonic balance model provides a good approximation of the dissipated power as the predicted magnitude, periodic and variation patterns are close to the numerical simulation results. Figure 5.5(b) provides the analytical approximations of the time histories of kinetic energy, which shows the second-order HB model predicts a larger peak in kinetic energy than the first-order approximation.

5.3 Power flow characteristics of the forced system

5.3.1 Effects of bifurcations

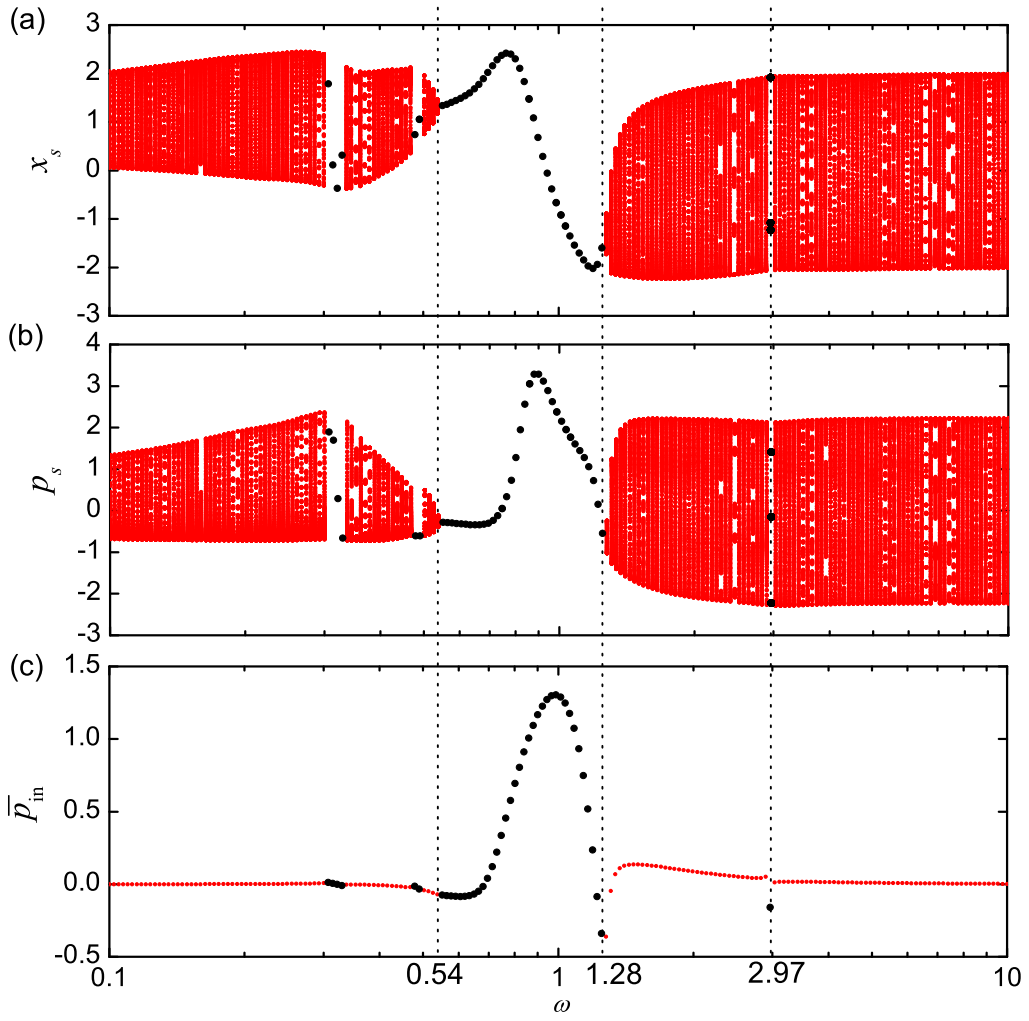

FIGURE 5.6: Effects of bifurcation on power flows. (a) Bifurcation diagram, (b) samplings of input power p_s and (c) time-averaged input power. Parameters are set as $\alpha = 0.5, \beta = 1, f = 1$.

To examine the power flow characteristics of the forced system over a large range of excitation frequencies, useful tools such as bifurcation diagrams can be used. Again, plotting such a diagram with ω as the bifurcation parameter requires numerical simulations at each interested excitation frequency. Sampling displacement x_s at sampling time $t_s = t_i + (n-1)T, n = 1, 2, \cdots$, are recorded, where t_i is the starting time while $T = 2\pi/\omega$ is the sampling interval. In this way, by examining the number of sampling points that are shown at each excitation frequency, the frequency ranges of periodic/non-periodic motions can be identified. Bifurcation occurs at critical frequencies where the number of shown sampling points changes. Correspondingly, the associated power flow behaviour arising from bifurcation can be identified by plotting the samplings of the instantaneous input power p_s and the time-averaged input power against the bifurcation parameter ω.

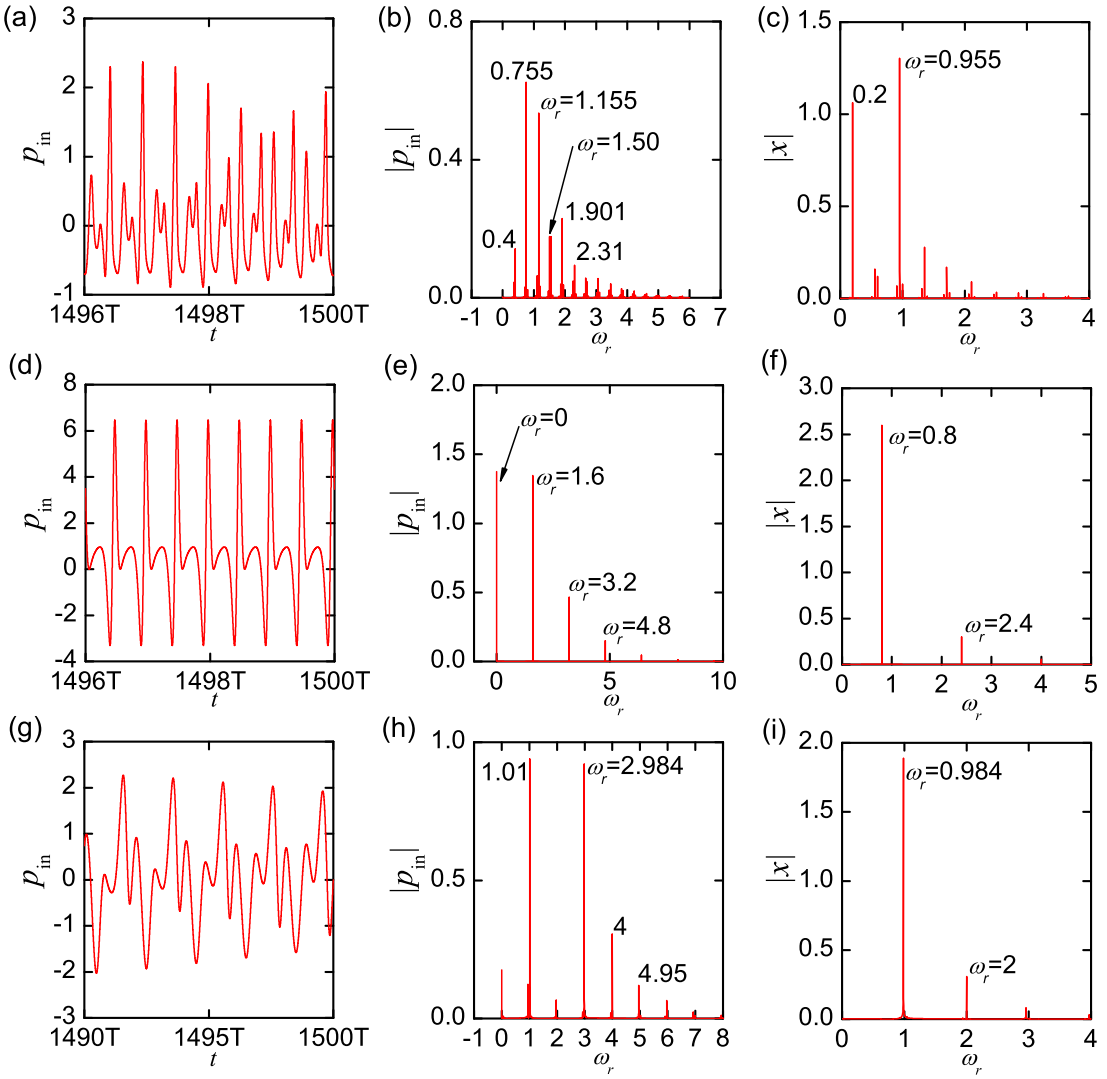

FIGURE 5.7: Time histories and spectra of power flows of the system ($\alpha = 0.5, \beta = 1.0, f = 1.0$): (a-c) $\omega = 0.2$; (d-f) $\omega = 0.8$ and (g-i) $\omega = 2$. (a,d,g) Instantaneous input power; (b,e,g) frequency spectra of p_{in} ; (c,f,i) frequency spectra of displacements.

For a system with parameters set as $\alpha = 0.5, \beta = 1, f = 1$, Figures 5.6(a)-(c) show a bifurcation diagram, the samplings of instantaneous input power and the variations of the time-averaged input power with the excitation frequency, respectively. It's shown that the system bifurcates from periodic to non-periodic motions when the excitation frequency is located at 0.54 or 1.28. In between these two critical frequencies, the system exhibits periodic motion. The peak value of the time-averaged input power is also encountered in this frequency range. It is also observed that the value of $\bar{p}_{in}$ may become negative at some excitation frequencies.

For more detailed information of the periodic/non-periodic responses of the system with $\alpha = 0.5, \beta = 1, f = 1$, Figure 5.7 shows the frequency spectra of the input power and the displacement at three locations of excitation frequencies. When $\omega = 0.8$, Figures 5.7(d)-(f) show that the system displays periodic motion with the frequency components commensurate with each other. However, for non-periodic motions, the displacement response contains frequency components that are not commensurate with the excitation frequency. For example, when the system is excited at a low excitation frequency of $\omega = 0.2$, the steady-state displacement contains a large component at $\omega_{r1} = 0.955$, apart from the one at $\omega_{r2} = \omega$, as shown in Figure 5.7(c). As a result, the input power p_{in} contains large signatures at $\omega_r = m\omega_{r1} \pm n\omega_{r2}$ (m and n are integer) and its time-histories become non-periodic, as suggested in Figure 5.7(a) and (b). Similarly, with a larger excitation frequency of $\omega = 2$, the displacement response is dominated by components at $\omega_{r1} = \omega$ and $\omega_{r2} = 0.984$. These figures indicates the quasi-periodic responses contain a forced vibration component with the excitation frequency ω and a free vibration component with the natural frequency ω_p.

To analytically approximate the power flow variables when the system displays periodic motions, the response can be assumed to be with the same frequency as the excitation. In contrast, for analytical approximations of power flows associated with non-periodic motions, the free vibration limit cycle oscillation component should also be included in the analytical model. In the following content, approximations of power flows will be made separately for these two types of motions.

5.3.2 Periodic motions

For periodic motions of the forced system, the displacement and velocity responses are assumed to be harmonic with the same frequency as that of the excitation, i.e.,

$$x = r_1 \cos(\omega t + \phi), \tag{5.23a}$$

$$y = -\omega r_1 \sin(\omega t + \phi). \tag{5.23b}$$

The method of averaging is employed herein to find the relationship between the response amplitude and system parameters such that the stability of solutions can be easily

assessed (Guckenheimer and Holmes (1983)). To implement the method, Eqs. (5.9) are firstly transformed into

$$\begin{pmatrix} \cos(\omega t+\phi) & -r_1\sin(\omega t+\phi) \\ -\omega\sin(\omega t+\phi) & -r_1\omega\cos(\omega t+\phi) \end{pmatrix} \begin{pmatrix} \dot{r}_1 \\ \dot{\phi} \end{pmatrix} = \begin{pmatrix} 0 \\ f_1 \end{pmatrix}, \tag{5.24}$$

where

$$f_1 = f\cos\omega t + \alpha\omega r_1\sin(\omega t+\phi)(r_1^2\cos^2(\omega t+\phi)-1) + r_1(\omega^2-\beta)\cos(\omega t+\phi). \tag{5.25}$$

A manipulation of Eq. (5.24) yields the following expressions of the derivatives of the amplitude and phase angle:

$$\dot{r}_1 = -\frac{f_1}{\omega}\sin(\omega t+\phi), \tag{5.26a}$$

$$\dot{\phi} = -\frac{f_1}{r_1\omega}\cos(\omega t+\phi). \tag{5.26b}$$

Based on the assumptions of the averaging method, the right hand sides of Eqs. (5.26) are approximated by their average values over an excitation cycle:

$$\dot{r}_1 = -\frac{\omega}{2\pi}\int_0^{\frac{2\pi}{\omega}} \frac{f_1}{\omega}\sin(\omega t+\phi)\,\mathrm{d}t, \tag{5.27a}$$

$$\dot{\phi} = -\frac{\omega}{2\pi}\int_0^{\frac{2\pi}{\omega}} \frac{f_1}{r_1\omega}\cos(\omega t+\phi)\,\mathrm{d}t. \tag{5.27b}$$

Completing the integrations in Eqs. (5.27) with reference to Eq. (5.25) leads to

$$\dot{r}_1 = -\frac{1}{2\omega}(f\sin\phi + \alpha\omega r_1(\frac{r_1^2}{4}-1)), \tag{5.28a}$$

$$\dot{\phi} = -\frac{1}{2\omega r_1}(f\cos\phi + r_1(\omega^2-\beta)). \tag{5.28b}$$

In steady-state motion, we have $\dot{r}_1 = \dot{\phi} = 0$ so that

$$f\sin\phi + \alpha\omega r_1(\frac{r_1^2}{4}-1) = 0, \tag{5.29a}$$

$$f\cos\phi + r_1(\omega^2-\beta) = 0. \tag{5.29b}$$

A further simplification of Eqs. (5.29) to eliminate the sine and cosine terms yields

$$f^2 = (\alpha\omega r_1)^2(\frac{r_1^2}{4}-1)^2 + r_1^2(\omega^2-\beta)^2. \tag{5.30}$$

It should be noted that a solution to the nonlinear algebraic Eq. (5.30) may not be stable. To examine its stability, the corresponding Jacobian matrix A of Eqs. (5.28) can

be studied:

$$A = \begin{pmatrix} \frac{\alpha}{2}(1-\frac{3}{4}r_1^2) & -\frac{f\cos\phi}{2\omega} \\ \frac{\beta-\omega^2}{2\omega r_1} & \frac{f\sin\phi}{2\omega r_1} \end{pmatrix} = \begin{pmatrix} \frac{\alpha}{2}(1-\frac{3}{4}r_1^2) & -\frac{r_1(\beta-\omega^2)}{2\omega} \\ \frac{\beta-\omega^2}{2\omega r_1} & \frac{\alpha}{2}(1-\frac{1}{4}r_1^2) \end{pmatrix}, \tag{5.31}$$

where Eqs. (5.29) were used to replace the trigonometric functions. For a stable solution, the real part of the eigenvalues of the corresponding matrix A must be negative, i.e., a negative trace and a positive determinant of A are required:

$$\mathrm{Tr}(A) = \frac{\alpha}{2}(1-\frac{3}{4}r_1^2) + \frac{\alpha}{2}(1-\frac{1}{4}r_1^2) = \alpha(1-\frac{1}{2}r_1^2) < 0, \tag{5.32a}$$

$$\det(A) = \frac{\alpha^2}{4}(1-\frac{3}{4}r_1^2)(1-\frac{1}{4}r_1^2) + \frac{(\beta-\omega^2)^2}{4\omega^2} > 0. \tag{5.32b}$$

The inequality (5.32a) suggests that a stable solution requires that $r_1 > \sqrt{2}$ when $\alpha > 0$. Using Eq. (5.30), the expression (5.32b) can be transformed to

$$\det(A) = \frac{\alpha^2}{4}(1-\frac{3}{4}r_1^2)(1-\frac{1}{4}r_1^2) + \frac{f^2-(\alpha\omega r_1)^2(1-\frac{r_1^2}{4})^2}{4\omega^2 r_1^2} = -\frac{\alpha^2 r_1^2}{8}(1-\frac{r_1^2}{4}) + \frac{f^2}{4\omega^2 r_1^2}, \tag{5.33}$$

which indicates that a solution with $r_1 \geq 2$ will always be stable.

Using Eqs. (5.8) and (5.23), first-order approximations of the time-averaged input power (TAIP) and the time-averaged dissipated power (TADP) of the system over an excitation cycle ($T = 2\pi/\omega$) are formulated as

$$\bar{p}_{in} = -\frac{1}{T}\int_0^T \omega r_1 f\cos\omega t\sin(\omega t+\phi)\,\mathrm{d}t = -\frac{\omega r_1 f}{2}\sin\phi, \tag{5.34a}$$

$$\bar{p}_d = \frac{1}{T}\int_0^T \alpha\omega^2 r_1^2(r_1^2\cos^2(\omega t+\phi)-1)\sin^2(\omega t+\phi)\,\mathrm{d}t = \frac{1}{8}\alpha\omega^2 r_1^2(r_1^2-4), \tag{5.34b}$$

respectively. With reference to Eq. (5.29a), the time-averaged input power is expressed by

$$\bar{p}_{in} = \frac{1}{8}\alpha\omega^2 r_1^2(r_1^2-4), \tag{5.35}$$

which is identical with the expression (5.34b) for the time-averaged dissipated power, in accordance with the principle of power balance. It also shows that when $r_1^2 < 4$, i.e., the amplitude r_1 is smaller than 2, both time-averaged input and dissipated powers become negative.

The maximum kinetic energy K_{max} of the system corresponds to the maximum velocity of $\dot{x}_{max} = \omega r_1$ and is given by

$$K_{max} = \frac{1}{2}\omega^2 r_1^2. \tag{5.36}$$

5.3.3 Quasi-periodic responses

In the above approximation of the system's power flows associated with periodic motions, only the response component with the same frequency as the excitation is considered. However, as shown in Figures 5.6 and 5.7, the system can display quasi-periodic motion over a large frequency range. For analytical approximations of the corresponding power flows, the displacement and velocity responses are assumed to contain both the natural frequency ω_p for the free vibration component and the excitation frequency ω for the forced vibration component:

$$x(t) = \hat{z}_1 \cos \omega_p t + \hat{z}_2 \sin \omega_p t + \hat{x}_1 \cos \omega t + \hat{x}_2 \sin \omega t, \tag{5.37a}$$

$$\dot{x}(t) = -\omega_p \hat{z}_1 \sin \omega_p t + \omega_p \hat{z}_2 \cos \omega_p t - \omega \hat{x}_1 \sin \omega t + \omega \hat{x}_2 \cos \omega t. \tag{5.37b}$$

The nonlinear term is expressed in a truncated Fourier form. Inserting the resultant expression as well as Eqs. (5.37) to the governing equation (5.1) and applying the harmonic balancing conditions yield the following equations

$$(\beta - \omega_p^2)\hat{z}_1 - \alpha\omega_p\hat{z}_2 + \frac{1}{4}\alpha\omega_p\hat{z}_2(\hat{z}_1^2 + \hat{z}_2^2 + 2\hat{x}_1^2 + 2\hat{x}_2^2) = 0, \tag{5.38a}$$

$$(\beta - \omega_p^2)\hat{z}_2 + \alpha\omega_p\hat{z}_1 - \frac{1}{4}\alpha\omega_p\hat{z}_1(\hat{z}_1^2 + \hat{z}_2^2 + 2\hat{x}_1^2 + 2\hat{x}_2^2) = 0, \tag{5.38b}$$

$$(\beta - \omega^2)\hat{x}_1 - \alpha\omega\hat{x}_2 + \frac{1}{4}\alpha\omega\hat{x}_2(2\hat{z}_1^2 + 2\hat{z}_2^2 + \hat{x}_1^2 + \hat{x}_2^2) = f, \tag{5.38c}$$

$$(\beta - \omega^2)\hat{x}_2 + \alpha\omega\hat{x}_1 - \frac{1}{4}\alpha\omega\hat{x}_1(2\hat{z}_1^2 + 2\hat{z}_2^2 + \hat{x}_1^2 + \hat{x}_2^2) = 0. \tag{5.38d}$$

Letting $\rho_1 = \sqrt{\hat{z}_1^2 + \hat{z}_2^2}$ and $r_1 = \sqrt{\hat{x}_1^2 + \hat{x}_2^2}$ and simplifying Eqs. (5.38a) and (5.38b) leads to

$$(\beta - \omega_p^2)\rho_1^2 = 0, \tag{5.39a}$$

$$\frac{1}{4}\alpha\omega_p\rho_1^2(4 - \rho_1^2 - 2r_1^2) = 0. \tag{5.39b}$$

Also, a manipulation of Eqs. (5.38c) and (5.38d) yields

$$(\beta - \omega^2)r_1^2 = f\hat{x}_1, \tag{5.40a}$$

$$\frac{1}{4}\alpha\omega r_1^2(2\rho_1^2 + r_1^2 - 4) = f\hat{x}_2. \tag{5.40b}$$

When $r_1^2 > 2$, Eq. (5.39b) requires that $\rho_1^2 = 0$, i.e., the response contains no free vibration component and the motion will be periodic with the same frequency as the excitation. This case has been analysed earlier and the time-averaged power flow variables are formulated in Eqs. (5.34) and (5.35).

When $r_1^2 < 2$, previous analysis has shown that the periodic motion will be unstable and

consequently there will be positive solutions of ω_p and ρ_1^2 to Eqs. (5.39a) and (5.39b), i.e.,

$$\omega_p = \sqrt{\beta}, \tag{5.41a}$$

$$\rho_1^2 = 4 - 2r_1^2. \tag{5.41b}$$

In this situation, the system will exhibit quasi-periodic motion containing both the free vibration component with a fixed frequency of $\omega_p = \sqrt{\beta}$ and the forced vibration component with frequency ω. Note that Eqs. (5.40) and (5.41) can be simplified further by eliminating $\hat{x}_1$, $\hat{x}_2$ and ρ_1^2 into the form:

$$(\beta - \omega^2)^2 r_1^2 + \frac{\alpha^2 \omega^2 r_1^2}{16}(4 - 3r_1^2)^2 = f^2. \tag{5.42}$$

Setting parameters as $\alpha = 0.5, \beta = 1, f = 1.0$ and solving Eqs. (5.30) and (5.42), the periodic as well as quasi-periodic responses are shown in Figure 5.8. The figure shows that there will be no free vibration limit cycle oscillation component when the excitation frequency is closed to the natural frequency of the linearised system, which agrees with the numerical results shown in Figure 5.6. Away from the resonant peak, it is shown that the value of r_1 changes little using either the frequency response relation (5.30) for periodic motion or Eq. (5.42) for quasi-periodic motions. In contrast, the magnitude ρ_1 of free vibration component decreases with the excitation frequency at low frequencies but increases to approach 2 at high excitation frequencies.

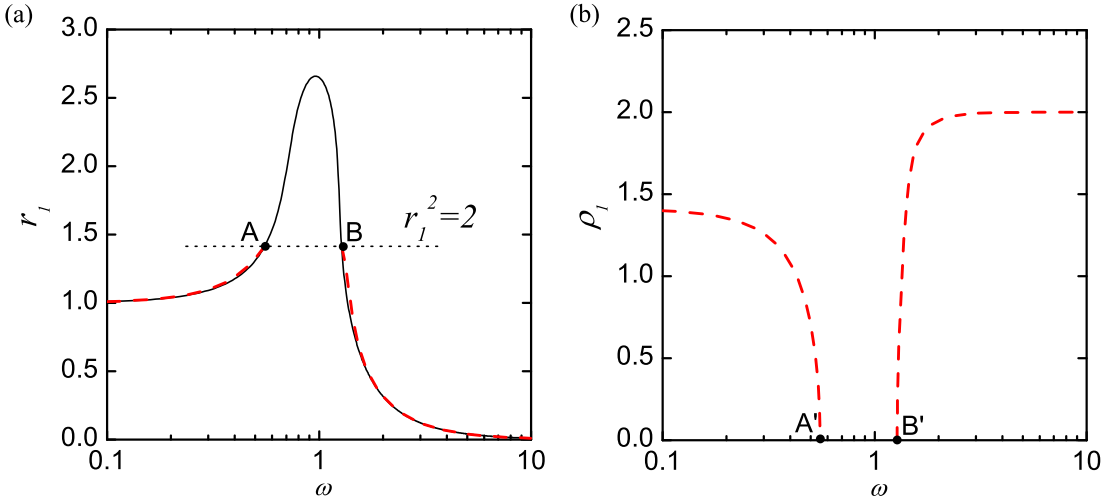

FIGURE 5.8: Analytical approximations of the magnitudes of response components ($\alpha = 0.5, \beta = 1, f = 1$). (a) Forced vibration component and (b) free vibration limit cycle oscillation component. Solid line: periodic motions; dashed line: quasi-periodic motions.

Using Eqs. (5.5d) and (5.37b), the instantaneous input power corresponding to quasi-periodic responses can be approximated by

$$p_{in} = f\cos\omega t(-\omega_p\hat{z}_1\sin\omega_p t + \omega_p\hat{z}_2\cos\omega_p t - \omega\hat{x}_1\sin\omega t + \omega\hat{x}_2\cos\omega t), \tag{5.43}$$

which contains frequency components at $\omega \pm \omega_p$, 0 and 2ω. When the averaging time is set much larger than the periods of the response components, only the stationary component of p_{in} will contribute to the time-averaged input power. Thus

$$\bar{p}_{in} \approx \frac{\omega\hat{x}_2 f}{2} = \frac{1}{8}\alpha\omega^2 r_1^2(4 - 3r_1^2). \tag{5.44}$$

where Eqs. (5.40b) and (5.41b) were used for simplifications.

For a system with $\alpha = 0.5, \beta = 1, f = 1.0$, Figure 5.9 shows the corresponding time-averaged input power obtained by using analytical approximations and numerical simulations. For the latter, the averaging time is taken as 240 excitation cycles, which is found to be sufficiently large. It shows that the numerical results agree well with analytical approximations for periodic motion when the excitation frequency ω is close to the peak frequency. Away from the resonant frequency range, analytical formulations for quasi-periodic motion provide better estimations of power flows. It shows that the analytical approximation curves for periodic and quasi-periodic motions intersect at points A'' and B'', corresponding to points A and B in Figure 5.8. This is because at these points, r_1 equals $\sqrt{2}$, so that derived value of $\bar{p}_{in}$ is the same using either Eq. (5.34) or Eq. (5.44).

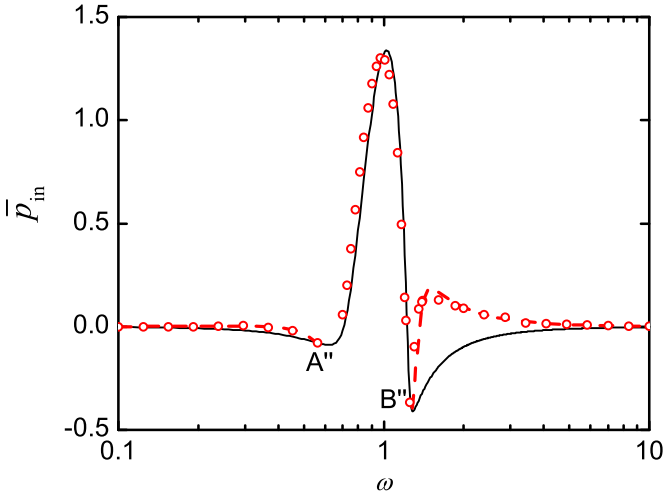

FIGURE 5.9: Verifications of the time-averaged input power ($\alpha = 0.5, \beta = 1, f = 1.0$). Solid line represents analytical approximation of periodic motions; dashed lines denote analytical approximations of quasi-periodic motions; circles indicate numerical results.

5.3.4 On negative time-averaged input power

Due to the damping nonlinearity in the oscillator, it has been shown previously in Section 5.1 that the instantaneous dissipated power of the system may become negative when the displacement is small. Similarly, for time-averaged power flows, Figures 5.6 and 5.9 as well as Eq. (5.34b) suggest that the time-averaged dissipated power $\bar{p}_d$ may become negative at some excitation frequencies. It would be of interest to investigate the frequency ranges where $\bar{p}_{in} = \bar{p}_d < 0$ using the analytical formulations. Note that from Eqs. (5.34b), (5.35) and (5.44), for negative values of $\bar{p}_{in}$ and $\bar{p}_d$, it requires

$$2 < r_1^2 < 4 \tag{5.45}$$

for stable periodic motions, and

$$\frac{3}{4} < r_1^2 \leq 2 \tag{5.46}$$

for quasi-periodic motions. When the corresponding frequency-response relations described by Eqs. (5.30) and (5.42) are used, expressions (5.45) and (5.46) are transformed into

$$\frac{f^2}{4} < (\omega^2 - \beta)^2 < \frac{3f^2}{4}, \tag{5.47}$$

which is equivalent to

$$\beta - \frac{\sqrt{3}f}{2} < \omega^2 < \beta - \frac{f}{2} \quad \text{or} \quad \beta + \frac{f}{2} < \omega^2 < \beta + \frac{\sqrt{3}f}{2}. \tag{5.48}$$

It indicates that the location of frequency range for negative time-averaged input/dissipated power is only a function of the excitation amplitude f and stiffness parameter β, independent of damping parameter α.

The inequalities (5.45) and (5.46) also suggest the value of $\bar{p}_{in}$ will be negative at the bifurcation point (with $r_1^2 = 2$) where the system response bifurcates from periodic to quasi-periodic motions. For both types of the motions, the power flow variables at the bifurcation frequency are calculated as

$$\bar{p}_{in} = \bar{p}_d = -\frac{1}{2}\alpha\omega^2. \tag{5.49}$$

where Eq. (5.34b), (5.35) and (5.44) are used. Clearly when a first-order analytical approximation is used, the variations of $\bar{p}_{in}$ and $\bar{p}_d$ at the bifurcation point will be smooth without jumps.

5.3.5 Effects of different parameters

Using the derived analytical formulations and numerical simulations, the effects of parameters β, f and α on the time-averaged input power (TAIP) are examined in this

section. For clarity, the unstable branches of analytical approximation of periodic motions with $r_1^2 < 2$ are not shown in the figures. For a system with $\alpha = 0.5, f = 1.0$, Figure 5.10 shows an increase in the stiffness coefficient β shifts the peak in each curve to the higher-frequency range. Also, the peak value of $\bar{p}_{in}$ increases with β while the minimum value decreases with an increasing β. A growing difference between analytical and numerical results is observed as β increases. In the high-frequency range, the time-averaged input power becomes less sensitive to variations of β.

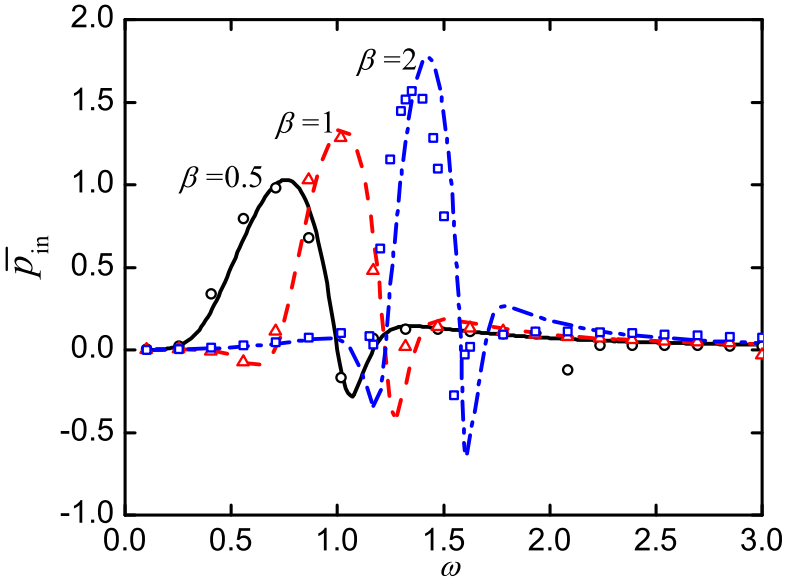

FIGURE 5.10: Effects of parameter β on time-averaged input power ($\alpha = 0.5, f = 1.0$). HB approximations: solid line ($\beta = 0.5$), dashed line ($\beta = 1$) and dash-dot line ($\beta = 2$). Numerical simulation results: circles ($\beta = 0.5$), triangles ($\beta = 1$) and squares ($\beta = 2$).

Figure 5.11 investigates the effects of the excitation amplitude f on time-averaged input power. It shows that a larger f leads to a higher peak of TAIP. However, the minimum value of TAIP becomes smaller with the increase of amplitude f. As the excitation frequency increases to be larger than 2, the curves become flatter.

The effects of damping parameter α on time-averaged input power of the system are investigated and the results are shown in Figure 5.12. It shows that the peak in the curve of $\bar{p}_{in}$ is suppressed by increasing α. However, in the high-frequency range, there is a larger amount of input power when α is large. Also, as α increases, there is an increasing discrepancy between the first-order HB approximations and the numerical simulation results. The reason is that natural frequency of the system decreases with α, as shown in Figure 5.4(a). As a result, a first-order HB approximation of quasi-periodic motion by assuming the natural frequency as a constant, as indicated in Eq. (5.41a), is not suitable when α becomes large and the nonlinearity is strong.

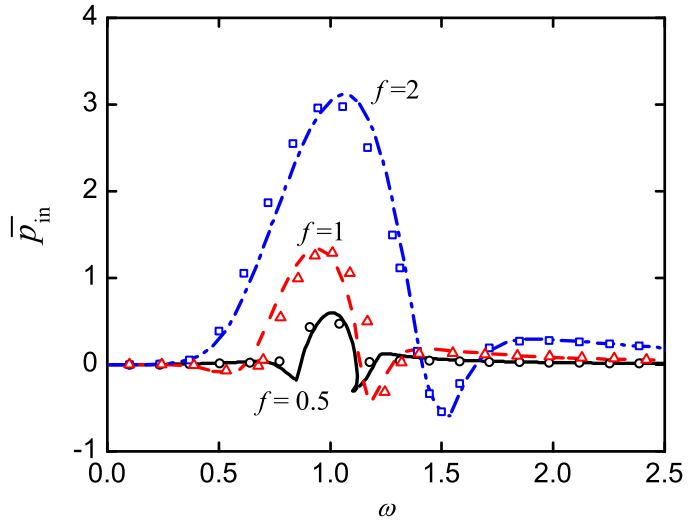

FIGURE 5.11: Effects of excitation amplitude f on time-averaged input power ($\alpha = 0.5, \beta = 1.0$). HB approximations: solid line ($f = 0.5$), dashed line ($f = 1$) and dash-dot line ($f = 2$). Numerical simulation results: circles ($f = 0.5$), triangles ($f = 1$) and squares ($f = 2$).

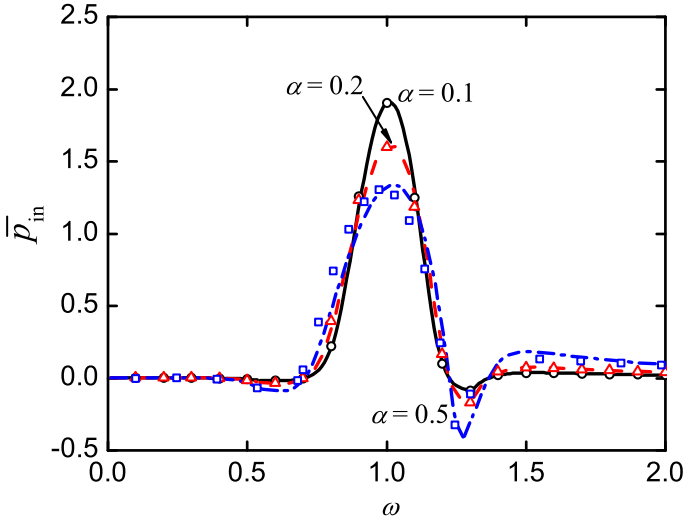

FIGURE 5.12: Effects of nonlinear parameter α on time-averaged input power ($\beta = 1, f = 1$). HB approximations: solid line ($\alpha = 0.1$), dashed line ($\alpha = 0.2$) and dash-dot line ($\alpha = 0.5$). Numerical simulation results: circles ($\alpha = 0.1$), triangles ($\alpha = 0.2$) and squares ($\alpha = 0.5$).

5.4 Conclusions

This chapter studied the power flow characteristics of unforced and forced Van der Pol oscillator to address the effects of nonlinearity in damping on power flows. The system was investigated using both analytical approximations and numerical simulations. For

the former, the method of harmonic balance and the method of averaging were employed while the latter was based on the fourth-order Runge-Kutta method. The influences of different system parameters on time-averaged input power of the system were examined. Based on this study, it was found that

- The dissipated power is negative at small deflections and positive when the displacement is large;
- The limit cycle oscillations of the unforced system are associated with the balance of vibration energy input and dissipation by the damping force. The method of harmonic balance of different orders can be used to estimate the instantaneous dissipated power and kinetic energy of the unforced system;
- The forced system may either exhibit periodic motion when the excitation frequency ω is close to the natural frequency of the corresponding linear system, or quasi-periodic motion when ω is located in the high or low frequency ranges. It was shown that the associated time-averaged input and dissipated powers can be formulated analytically using the method of harmonic balance or the method of averaging;
- Analytical results suggested that time-averaged input power can become negative in a band of excitation frequencies. Analytical formulation showed that the band is only a function of the excitation amplitude f and the stiffness parameter β. independent of the damping parameter α;
- It was also analytically and numerically shown that bifurcations from periodic to quasi-periodic motions may not lead to jumps in time-averaged input/dissipated power curves at some bifurcation points.

Chapter 6

Power flow analysis of a two-DOF nonlinear system for vibration isolation

In this chapter, the power flow behaviour of a two degrees-of-freedom nonlinear system with a nonlinear vibration isolator is investigated. Single degree-of-freedom (SDOF) models are usually used to assess the performance of passive/active/hybrid isolators in attenuating vibration transmission from an excited source to a receiving structure (see, for example, Den Hartog (1934); Rivin (2003)). Such simplified models assume a rigid foundation on which a mass is mounted. However, many practical mounting bases, such as those commonly encountered in automobiles, aeroplanes and ships, are not rigid but flexible, and there exist strong coupling effects between the isolator and the base structure (see Sciulli and Inman (1999); Xiong et al. (2005a)). Under these circumstances, research findings using the rigid base assumption may not be valid. In addition, to improve the effectiveness of linear vibration isolators, different configurations of nonlinear vibration isolation systems have been proposed by introducing nonlinear stiffness or damping elements (see, for example, Ibrahim (2008)). To evaluate their isolation efficiency, force or displacement transmissibility is often used as the performance indicator, which may not reflect the actual vibration transmission. Investigations on power flow characteristics of coupled nonlinear vibration isolation systems are very limited. To addresses these issues, a two degrees-of-freedom (2DOF) nonlinear dynamical system is studied in this chapter from a viewpoint of vibrational power flows. The vibration power generation, transmission and dissipation behaviour arising from damping and stiffness nonlinearities in the isolator will be studied and revealed for better designs of nonlinear vibration isolators.

6.1 Mathematical model

As shown in Figure 6.1, a coupled two-DOF nonlinear vibration isolation system contains a one-DOF base of a mass m_1, a linear spring with stiffness coefficient k_1 and a linear viscous damper with coefficient c_1, to model a mode of an elastic structure. A machine with mass m_2 is mounted on the base structure via a nonlinear isolator with nonlinearities in both damping and stiffness. The oscillating mass m_2 is subjected to a harmonic excitation of amplitude f and frequency ω. The static equilibrium position, where the dynamic deflections $x_1 = x_2 = 0$, is taken as the reference position where the dynamic restoring forces of the springs vanish. It is assumed that the damping force $G(\dot{\delta})$ of the isolator is a cubic function of the relative velocity of the mass m_2 and m_1, while the restoring force $F(\delta)$ of the isolator is a nonlinear function of the relative displacement:

$$G(\dot{\delta}) = c_2\dot{\delta}(1 + \alpha\dot{\delta}^2), \tag{6.1a}$$

$$F(\delta) = k_2\delta(1 + \beta\delta^2), \tag{6.1b}$$

where $\delta = x_2 - x_1$ is the dynamic deflection of the isolator; α is the nonlinear damping parameter; β is the nonlinear stiffness parameter with $\beta = 0$, $\beta > 0$ and $\beta <$ corresponding to linear, hardening and softening springs, respectively.

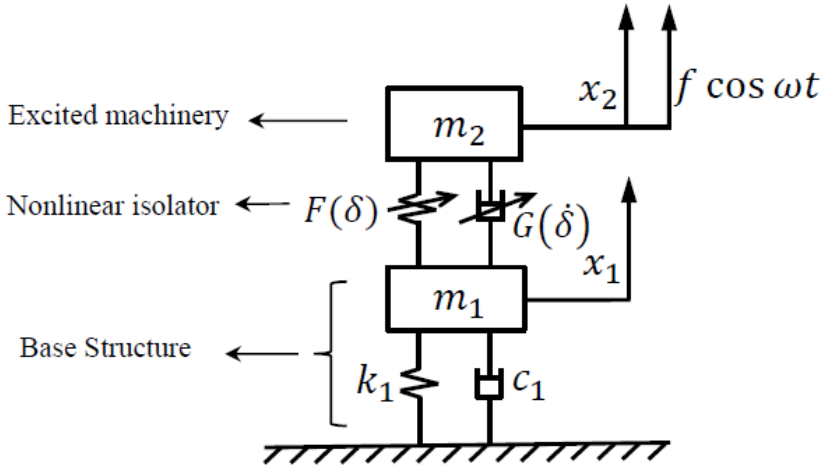

FIGURE 6.1: A schematic representation of a two-DOF nonlinear system with a nonlinear isolator and a linear one-DOF base.

Using the Newton's law of motion, the dynamic governing equations of the system are obtained as

$$m_1\ddot{x}_1 + c_1\dot{x}_1 + k_1x_1 - c_2\dot{\delta}(1 + \alpha\dot{\delta}^2) - k_2\delta(1 + \beta\delta^2) = 0, \tag{6.2}$$

$$m_2\ddot{x}_2 + c_2\dot{\delta}(1 + \alpha\dot{\delta}^2) + k_2\delta(1 + \beta\delta^2) = f\cos\omega t. \tag{6.3}$$

Introducing the following non-dimensional parameters:

$$x_0 = \frac{m_1 g}{k_1}, \quad \mu = \frac{m_2}{m_1}, \quad \omega_1 = \sqrt{\frac{k_1}{m_1}}, \quad \omega_2 = \sqrt{\frac{k_2}{m_2}},$$

$$\gamma = \frac{\omega_2}{\omega_1}, \quad \xi_1 = \frac{c_1}{2m_1\omega_1}, \quad \xi_2 = \frac{c_2}{2m_2\omega_2}, \quad \eta = \alpha\omega_1^2 x_0^2, \quad \epsilon = \beta x_0^2,$$

$$f_0 = \frac{f}{k_1 x_0}, \quad y = \frac{\delta}{x_0}, \quad x = \frac{x_1}{x_0}, \quad \Omega = \frac{\omega}{\omega_1}, \quad \tau = \omega_1 t,$$

the governing equations (6.2) and (6.3) are transformed into a non-dimensional form

$$x'' + 2\xi_1 x' + x - \mu\gamma\big(2\xi_2 y'(1+\eta y'^2) + \gamma y + \epsilon\gamma y^3\big) = 0, \tag{6.4}$$

$$\mu y'' + \mu\gamma\big(2\xi_2 y'(1+\eta y'^2) + \mu\gamma y + \epsilon\gamma y^3\big) = -\mu x'' + f_0\cos\Omega\tau, \tag{6.5}$$

where the primes denote differentiations with respect to the non-dimensional time τ.

To assist further analysis, these non-dimensional equations are written in a form of phase space representation, i.e.,

$$\begin{pmatrix} x' \\ z' \\ y' \\ u' \end{pmatrix} = \begin{pmatrix} z \\ -2\xi_1 z - x + \mu\gamma\big(2\xi_2 u(1+\eta u^2) + \gamma y + \epsilon\gamma y^3\big) \\ u \\ \frac{f_0}{\mu}\cos\Omega\tau + 2\xi_1 z + x - (\mu+1)\gamma\big(2\xi_2 u(1+\eta u^2) + \gamma y + \epsilon\gamma y^3\big) \end{pmatrix}. \tag{6.6}$$

In order to reveal the vibration power flow characteristics of the system, it is essential to solve the nonlinear equations (6.6) so that the dynamic response can be obtained. There is no accurate analytical solution to these equations, but tools are available for approximations either by adopting analytical methods or by numerical simulations. The former usually consider a few discrete frequencies in the response and have the advantages of less computational cost and the ability to address both stable and unstable solutions. In comparison, the latter predict the response more accurately incorporating many more response frequency components, but cost more computational power. In this chapter, the method of averaging will be used to find the relationship between power flow variables and the parameters. Direct numerical solutions based on the fourth-order Runge-Kutta method will also be employed to verify the analytical approximations.

6.2 Analytical approximations

6.2.1 Frequency-response relations

The method of averaging has been widely used for first-order approximations of the periodic responses of nonlinear vibrating systems (see, Nayfeh and Mook (1979)). For

the current system in steady-state motions, the displacement and velocity responses of mass m_1 and the isolator may be assumed to be harmonic with the same frequency as that of the excitation, i.e,

$$x = a\cos(\Omega\tau + \phi), \tag{6.7a}$$

$$x' = -a\Omega\sin(\Omega\tau + \phi), \tag{6.7b}$$

$$y = b\cos(\Omega\tau + \theta), \tag{6.7c}$$

$$y' = -b\Omega\sin(\Omega\tau + \theta), \tag{6.7d}$$

where a and b represent response amplitudes while ϕ and θ are phase angles. Using the averaging formulations outlined in Section 3.2.2 with references to Eqs. (6.6) and (6.7), we have

$$a'\cos(\Omega\tau + \phi) - a\phi'\sin(\Omega\tau + \phi) = 0, \tag{6.8a}$$

$$-a'\Omega\sin(\Omega\tau + \phi) - a\Omega\phi'\cos(\Omega\tau + \phi) = f_1, \tag{6.8b}$$

$$b'\cos(\Omega\tau + \theta) - b\theta'\sin(\Omega\tau + \theta) = 0, \tag{6.8c}$$

$$-b'\Omega\sin(\Omega\tau + \theta) - b\Omega\theta'\cos(\Omega\tau + \theta) = f_2, \tag{6.8d}$$

where

$$f_1 = a(\Omega^2 - 1)\cos(\Omega\tau + \phi) + 2\xi_1 a\Omega\sin(\Omega\tau + \phi) + \mu\gamma\Delta, \tag{6.9a}$$

$$f_2 = \frac{f_0}{\mu}\cos\Omega\tau + b\Omega^2\cos(\Omega\tau + \theta) + a'\Omega\sin(\Omega\tau + \phi) + (a\Omega^2 + a\Omega\phi')\cos(\Omega\tau + \phi) - \gamma\Delta, \tag{6.9b}$$

$$\Delta = -2\xi_2 b\Omega\sin(\Omega\tau + \theta)\big(1 + \eta b^2\Omega^2\sin^2(\Omega\tau + \theta)\big) + \gamma b\cos(\Omega\tau + \theta) + \epsilon\gamma b^3\cos^3(\Omega\tau + \theta). \tag{6.9c}$$

Solutions of Eqs. (6.8) yield the following expressions of the time change rates of response amplitudes and phase angles, i.e.,

$$a' = -\frac{1}{\Omega}f_1\sin(\Omega\tau + \phi), \tag{6.10a}$$

$$\phi' = -\frac{1}{a\Omega}f_1\cos(\Omega\tau + \phi), \tag{6.10b}$$

$$b' = -\frac{1}{\Omega}f_2\sin(\Omega\tau + \theta), \tag{6.10c}$$

$$\theta' = -\frac{1}{b\Omega}f_2\cos(\Omega\tau + \theta). \tag{6.10d}$$

According to the averaging method, the derivatives of amplitudes and phase angles can be approximated by their average values over a cycle of the excitation:

$$a' \approx -\frac{1}{2\pi}\int_0^{\frac{2\pi}{\Omega}} f_1 \sin(\Omega\tau+\phi)\,\mathrm{d}\tau, \tag{6.11a}$$

$$\phi' \approx -\frac{1}{2\pi a}\int_0^{\frac{2\pi}{\Omega}} f_1 \cos(\Omega\tau+\phi)\,\mathrm{d}\tau, \tag{6.11b}$$

$$b' \approx -\frac{1}{2\pi}\int_0^{\frac{2\pi}{\Omega}} f_2 \sin(\Omega\tau+\theta)\,\mathrm{d}\tau, \tag{6.11c}$$

$$\theta' \approx -\frac{1}{2\pi b}\int_0^{\frac{2\pi}{\Omega}} f_2 \cos(\Omega\tau+\theta)\,\mathrm{d}\tau. \tag{6.11d}$$

Using Eqs. (6.9) to substitute f_1 and f_2 and then completing the integrations in Eqs. (6.11), it follows that

$$a' = -\frac{1}{\Omega}\Big(\xi_1 a\Omega + \mu\gamma b\big(-\xi_2\Omega(1+\frac{3}{4}\eta b^2\Omega^2)\cos(\phi-\theta) + \frac{\gamma}{2}(1+\frac{3}{4}\epsilon b^2)\sin(\phi-\theta)\big)\Big), \tag{6.12a}$$

$$\phi' = -\frac{1}{a\Omega}\Big(\frac{1}{2}a(\Omega^2-1) + \mu\gamma b\big(\xi_2\Omega(1+\frac{3}{4}\eta b^2\Omega^2)\sin(\phi-\theta) + \frac{\gamma}{2}(1+\frac{3}{4}\epsilon b^2)\cos(\phi-\theta)\big)\Big), \tag{6.12b}$$

$$b' = -\frac{1}{\Omega}\Big(\frac{f_0}{2\mu}\sin\phi + \frac{a'\Omega}{2}\cos(\phi-\theta) - \frac{a\Omega^2+a\Omega\phi'}{2}\sin(\phi-\theta) + \gamma\xi_2 b\Omega(1+\frac{3}{4}\eta b^2\Omega^2)\Big), \tag{6.12c}$$

$$\theta' = -\frac{1}{b\Omega}\Big(\frac{f_0}{2\mu}\cos\phi + \frac{b\Omega^2}{2} + \frac{a'\Omega}{2}\sin(\phi-\theta) + \frac{a\Omega^2+a\Omega\phi'}{2}\cos(\phi-\theta) - \frac{\gamma^2 b}{2}(1+\frac{3}{4}\epsilon b^2)\Big). \tag{6.12d}$$

Note that in steady-state motion, the changes in response amplitudes and phase angles vanish, i.e., $a' = \phi' = b' = \theta' = 0$, using which Eqs. (6.12) are transformed into

$$2\xi_1 a\Omega + \mu\gamma b\big(-2\xi_2\Omega(1+\frac{3}{4}\eta b^2\Omega^2)\cos(\phi-\theta) + \gamma(1+\frac{3}{4}\epsilon b^2)\sin(\phi-\theta)\big) = 0, \tag{6.13a}$$

$$a(\Omega^2-1) + \mu\gamma b\big(2\xi_2\Omega(1+\frac{3}{4}\eta b^2\Omega^2)\sin(\phi-\theta) + \gamma(1+\frac{3}{4}\epsilon b^2)\cos(\phi-\theta)\big) = 0, \tag{6.13b}$$

$$\frac{f_0}{2\mu}\sin\phi - \frac{a\Omega^2}{2}\sin(\phi-\theta) + \gamma\xi_2 b\Omega(1+\frac{3}{4}\eta b^2\Omega^2) = 0, \tag{6.13c}$$

$$\frac{f_0}{2\mu}\cos\phi + \frac{a\Omega^2}{2}\cos(\phi-\theta) + \frac{b}{2}\Big(\Omega^2 - \gamma^2(1+\frac{3}{4}\epsilon b^2)\Big) = 0. \tag{6.13d}$$

From Eqs. (6.13a) and (6.13b), we have

$$\cos(\phi-\theta)=\frac{4\xi_1\xi_2 a\Omega^2(1+\frac{3}{4}\eta b^2\Omega^2)-\gamma a(\Omega^2-1)(1+\frac{3}{4}\epsilon b^2)}{\mu\gamma b\big(\gamma^2(1+\frac{3}{4}\epsilon b^2)^2+(2\xi_2\Omega)^2(1+\frac{3}{4}\eta b^2\Omega^2)^2\big)}, \tag{6.14a}$$

$$\sin(\phi-\theta)=\frac{-2\xi_2 a\Omega(\Omega^2-1)(1+\frac{3}{4}\eta b^2\Omega^2)-2\xi_1\gamma a\Omega(1+\frac{3}{4}\epsilon b^2)}{\mu\gamma b\big(\gamma^2(1+\frac{3}{4}\epsilon b^2)^2+(2\xi_2\Omega)^2(1+\frac{3}{4}\eta b^2\Omega^2)^2\big)}. \tag{6.14b}$$

Substituting Eqs. (6.14a) and (6.14b) back into Eqs. (6.13a) and (6.13b) and simplifying the resultant expressions, it follows that

$$a^2\big((\Omega^2-1)^2+(2\xi_1\Omega)^2\big)=(\mu\gamma b)^2\big(\gamma^2(1+\frac{3}{4}\epsilon b^2)^2+(2\xi_2\Omega)^2(1+\frac{3}{4}\eta b^2\Omega^2)^2\big). \tag{6.15}$$

Similarly, using Eqs. (6.14a) and (6.14b) to eliminate the trigonometric functions $\sin(\phi-\theta)$ and $\cos(\phi-\theta)$ in Eqs. (6.13c) and (6.13d), we obtain

$$\begin{aligned}\frac{f_0^2}{4\mu^2}=\;&(\gamma\xi_2 b\Omega)^2(1+\tfrac{3}{4}\eta b^2\Omega^2)+\frac{a^2\Omega^2\big((\mu+2)\Omega^2-2\big)}{4\mu}+\frac{b^2}{4}\big(\Omega^2-\gamma^2(1+\tfrac{3}{4}\epsilon b^2)\big)^2\\&+\frac{a^2\Omega^4\big(4\xi_1\xi_2\Omega^2(1+\frac{3}{4}\eta b^2\Omega^2)-\gamma(\Omega^2-1)(1+\frac{3}{4}\epsilon b^2)\big)}{2\mu\gamma\big(\gamma^2(1+\frac{3}{4}\epsilon b^2)^2+(2\xi_2\Omega)^2(1+\frac{3}{4}\eta b^2\Omega^2)^2\big)}.\end{aligned} \tag{6.16}$$

Eqs. (6.15) and (6.16) provide the relationship between steady-state response amplitudes and the system parameters. It should be noted that in these equations, the nonlinear stiffness parameter ϵ and the nonlinear damping parameter η only appear in the terms $1+\frac{3}{4}\epsilon b^2$ and $1+\frac{3}{4}\eta b^2\Omega^2$, respectively. If the absolute values of $\frac{3}{4}\epsilon b^2$ and $\frac{3}{4}\eta b^2\Omega^2$ are much smaller than unity, the effects of the stiffness and damping nonlinearities on the solutions of these two equations, i.e., response amplitudes, may be small.

It should be noted that a manipulation of Eq. (6.15) can lead to an expression for a^2 as a function of b^2 and other parameters. A substitution of this function into Eq. (6.16) to replace a^2 yields an equation of b^2, which can be solved using a bisection algorithm (see, Press et al. (1992)). Subsequently, the response amplitude a^2 as well as the phase angles is obtained using equations (6.13), (6.14) and (6.15). For a nonlinear system with parameters set as $\xi_1=\xi_2=0.01, \mu=0.5, \gamma=1, \epsilon=0.5, \eta=0.5, f_0=0.1$, Figure 6.2 shows that the analytical approximations of response amplitudes (denoted by solid lines) agree well with those obtained using numerical simulations (represented by dots), verifying the averaging formulations. The figure also shows different response branches, the stability of which is assessed using the stability analysis to be discussed in the next section.

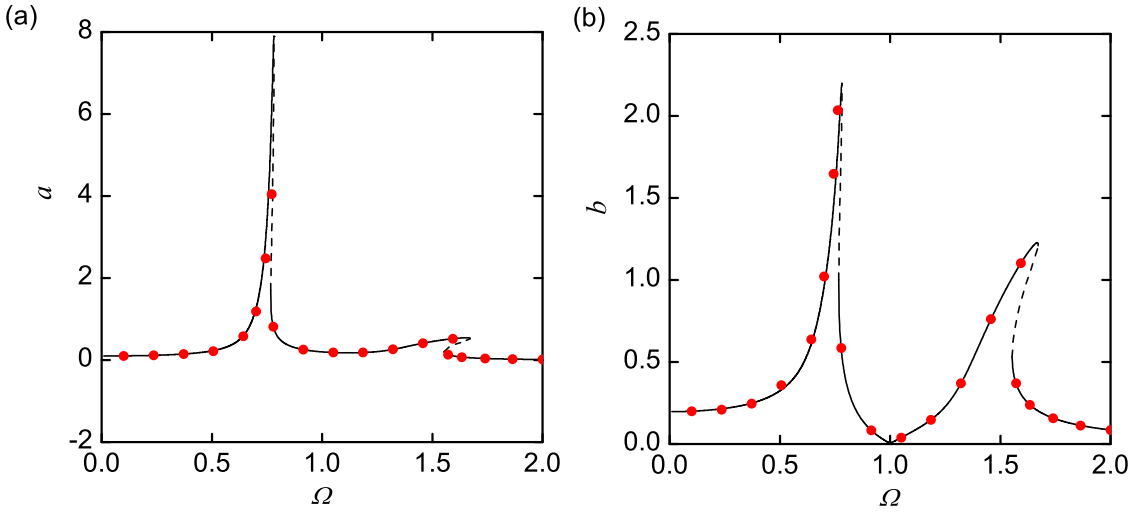

FIGURE 6.2: Verification of averaging formulations. Solid and dashed lines represent stable and unstable analytical solutions, respectively; dots denote numerical results

6.2.2 Stability analysis

Figure 6.2 shows that in the frequency range near the second resonance peak, there exist multiple solutions of a and b at a single frequency Ω. As they correspond to either stable or unstable responses, it is useful to assess the associated stability as only the stable ones are physically realisable. For the clarity of the derivation process, Eqs. (6.12) are rewritten as

$$a' = u_1' = g_1(a, \phi, b, \theta), \tag{6.17a}$$
$$\phi' = u_2' = g_2(a, \phi, b, \theta), \tag{6.17b}$$
$$b' = u_3' = g_3(a, \phi, b, \theta), \tag{6.17c}$$
$$\theta' = u_4' = g_4(a, \phi, b, \theta), \tag{6.17d}$$

where

$$g_1 = -\frac{1}{\Omega}\Big(\xi_1 a\Omega + \mu\gamma b\big(-\xi_2\Omega(1+\frac{3}{4}\eta b^2\Omega^2)\cos(\phi-\theta) + \frac{\gamma}{2}(1+\frac{3}{4}\epsilon b^2)\sin(\phi-\theta)\big)\Big),$$

$$g_2 = -\frac{1}{a\Omega}\Big(\frac{1}{2}a(\Omega^2-1) + \mu\gamma b\big(\xi_2\Omega(1+\frac{3}{4}\eta b^2\Omega^2)\sin(\phi-\theta) + \frac{\gamma}{2}(1+\frac{3}{4}\epsilon b^2)\cos(\phi-\theta)\big)\Big),$$

$$g_3 = -\frac{1}{\Omega}\Big(\frac{f_0}{2\mu}\sin\phi + \frac{g_1\Omega}{2}\cos(\phi-\theta) - \frac{a\Omega^2 + a\Omega g_2}{2}\sin(\phi-\theta) + \gamma\xi_2 b\Omega(1+\frac{3}{4}\eta b^2\Omega^2)\Big),$$

$$g_4 = -\frac{1}{b\Omega}\Big(\frac{f_0}{2\mu}\cos\phi + \frac{b\Omega^2}{2} + \frac{g_1\Omega}{2}\sin(\phi-\theta) + \frac{a\Omega^2 + a g_2\Omega}{2}\cos(\phi-\theta) - \frac{\gamma^2 b}{2}(1+\frac{3}{4}\epsilon b^2)\Big).$$

The stability of a solution $(a_0, b_0, \phi_0, \theta_0)$ can be assessed by examining the real parts of the corresponding eigenvalues of the characteristic matrix, which is

$$A = \begin{pmatrix} a_{11} & a_{12} & a_{13} & a_{14} \\ a_{21} & a_{22} & a_{23} & a_{24} \\ a_{31} & a_{32} & a_{33} & a_{34} \\ a_{41} & a_{42} & a_{43} & a_{44} \end{pmatrix}, \tag{6.18}$$

where $a_{ij} = \frac{\partial g_i}{\partial u_j}, (i, j = 1, 2, 3, 4)$ for which the detailed expressions not provided here. In the derivations of a_{ij}, it may be noted that at each solution point $(a_0, b_0, \phi_0, \theta_0)$ of a response curve, we have $g_i = 0, (i = 1, 2, 3, 4)$. If a solution which is stable, the corresponding eigenvalues of A must all have negative real parts. On the other hand, if one or more eigenvalues of A has a positive real part, the corresponding solution will be unstable. Based on the criteria, the stability of a solution can be determined. Based on the criteria, the stability of different response curves of the system with $\xi_1 = \xi_2 = 0.01, \mu = 0.5, \gamma = 1, \epsilon = 0.5, \eta = 0.5, f_0 = 0.1$ was examined and indicated in Figure 6.2 by solid or dashed lines.

6.3 Power flow formulations

6.3.1 Input power

The non-dimensional instantaneous input power into the system is the product of excitation with the corresponding velocity. In this system, there is only one external force acting on the mass m_2, so that the total instantaneous input power is

$$p_{in} = f_0 v_2 \cos \Omega\tau, \tag{6.19}$$

where $v_2 = x' + y'$ is the non-dimensional velocity of mass m_2. When a first-order approximation is sought, the velocity can be formulated as

$$v_2 = x' + y' = -a\Omega \sin(\Omega\tau + \phi) - b\Omega \cos(\Omega\tau + \theta), \tag{6.20}$$

and the time-averaged input power over an excitation cycle $T = 2\pi/\Omega$ becomes

$$\bar{p}_{in}(\Omega) = \frac{1}{T} \int_0^T p_{in} \, \mathrm{d}\tau = -\frac{f_0 a \Omega}{2} \sin\phi - \frac{f_0 b \Omega}{2} \sin\theta. \tag{6.21}$$

Using the relations in Eqs. (6.13) and (6.14) to replace the trigonometric functions in Eq. (6.21), a first-order approximation of the time-averaged input power is obtained as

$$\bar{p}_{in}(\Omega) = \xi_1 a^2 \Omega^2 + \mu\gamma\xi_2 b^2 \Omega^2 (1 + \frac{3}{4}\eta b^2 \Omega^2). \tag{6.22}$$

6.3.2 Dissipated power

In the system, vibration energy is dissipated by the damping in the isolator as well as that in the base. Power dissipated by each damper is the product of the damping force with the corresponding velocity. Therefore, the total instantaneous dissipated power is expressed by

$$p_d = f_{d1}x' + f_{d2}y', \tag{6.23}$$

where $f_{d1} = 2\xi_1 x'$ and $f_{d2} = 2\mu\gamma\xi_2 y'$ are the damping forces in the base structure and in the isolator, respectively.

The time-averaged value of the dissipated power using an excitation cycle as the averaging time is formulated by

$$\bar{p}_t(\Omega) = \frac{1}{T}\int_0^T p_d \,\mathrm{d}\tau. \tag{6.24}$$

Expressing p_d with a first-order approximation and evaluating Eq. (6.24), it follows that

$$\bar{p}_d(\Omega) = \xi_1 a^2\Omega^2 + \mu\gamma\xi_2 b^2\Omega^2(1 + \frac{3}{4}\eta b^2\Omega^2). \tag{6.25}$$

Comparing this equation with Eq. (6.22), it is clearly seen that the expressions of $\bar{p}_{in}$ and $\bar{p}_d$ are identical, i.e., the input power is all dissipated by damping over an oscillation cycle. This is in accordance with the principle of energy balance, as correspondingly for periodic motions, the net change in the kinetic and potential energies of the system will vanish over a cycle of oscillation.

6.3.3 Transmitted power

Transmitted power between sub-systems provides a valuable measure of the flow of vibration energy in dynamical systems and thus is of interest in vibration isolation. The instantaneous power transmitted from the excited mass m_2, through the nonlinear isolator to the base is the product of the corresponding transmitted force to the mass m_1 and its velocity, i.e.,

$$p_t = f_t x', \tag{6.26}$$

where $f_t = \mu\gamma\big(2\xi_2 y'(1+\eta y'^2) + \gamma y + \epsilon\gamma y^3\big)$ is the transmitted force and x' is the velocity of the primary mass m_1.

The time-averaged transmitted power over an excitation period T is

$$\bar{p}_t(\Omega) = \frac{1}{T}\int_0^T p_t \,\mathrm{d}\tau. \tag{6.27}$$

Again, using a first-order approximation of p_t and completing the integration in Eq. (6.27) leads to

$$\bar{p}_t(\Omega) = \mu\gamma a\Omega\big(\xi_2 b\Omega(1+\frac{3}{4}\eta b^2\Omega^2)\cos(\phi-\theta) - \frac{\gamma b}{2}(1+\frac{3}{4}\epsilon b^2)\sin(\phi-\theta)\big), \tag{6.28}$$

which is further simplified using Eq. (6.13a) into

$$\bar{p}_t(\Omega) = \xi_1 a^2\Omega^2. \tag{6.29}$$

It shows that the time-averaged transmitted power to the base equals the time-averaged dissipated power by damper c_1. It is reasonable, as the kinetic and potential energies of the base structure will remain the same after an oscillation cycle and the energy transmitted must all be dissipated by damper c_1.

6.3.4 Maximum kinetic energies

In the applications of vibration control devices, the squared values of velocity amplitudes or the kinetic energy of a structure are often used as cost functions to measure the control effectiveness (see, for example, Jenkins et al. (1993); Xiong et al. (2003)). For the current system in steady-state motion, the maximum kinetic energy of the mass m_1 is represented as

$$K_1 = \frac{1}{2}(|x'|_{max})^2 \approx \frac{1}{2}a^2\Omega^2, \tag{6.30}$$

where a first-order approximation of the velocity $x' = -a\Omega\sin(\Omega\tau+\phi)$ was used, so that its amplitude $|x'|_{max} = a\Omega$. Comparing this equation with Eq. (6.29), it is seen that the kinetic energy of base is proportional to the time-averaged power transmitted to the base if there is a positive and fixed damping coefficient ξ_1.

For the kinetic energy of the excited mass, note that from Eq. (6.20), the amplitude of the velocity of mass m_2 is

$$|v_2|_{max} = \Omega\sqrt{(a^2+b^2)+2ab\cos(\phi-\theta)}. \tag{6.31}$$

Using Eq. (6.14a) to replace $\cos(\phi-\theta)$, the maximum kinetic energy of the excited mass m_2 is

$$K_2 = \frac{1}{2}\mu(a^2+b^2)\Omega^2 + a^2\Omega^2\frac{4\xi_1\xi_2\Omega^2(1+\frac{3}{4}\eta b^2\Omega^2) - \gamma(\Omega^2-1)(1+\frac{3}{4}\epsilon b^2)}{\gamma\Big(\gamma^2(1+\frac{3}{4}\epsilon b^2)^2 + (2\xi_2\Omega)^2(1+\frac{3}{4}\eta b^2\Omega^2)^2\Big)}. \tag{6.32}$$

6.4 Case studies for the isolator performance

6.4.1 The isolator with stiffness nonlinearity

Here, a special case of a nonlinear isolator with nonlinear stiffness ($\epsilon \neq 0$) but linear viscous damping ($\eta = 0$) is considered. The response amplitudes and power flow variables of the system are obtained using the analytical approximation as well as numerical simulations. The dB reference for the power flow variables is set as 10^{-12} throughout this chapter. In the following figures of this chapter, the lines represent analytical approximate solutions while the symbols denote numerical solutions using the fourth-order Runge-Kutta method.

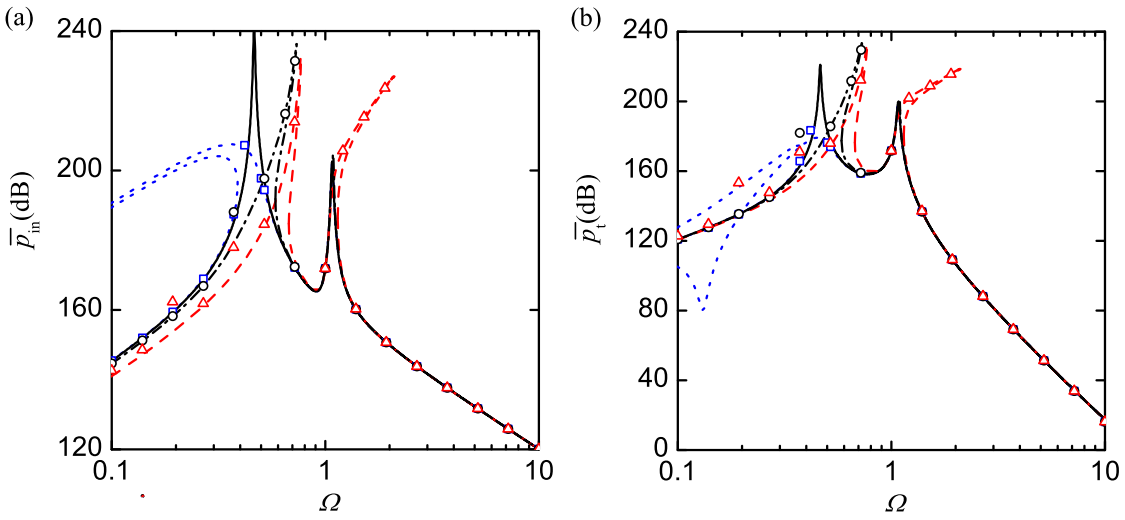

FIGURE 6.3: Time-averaged (a) input and (b) transmitted powers of the systems with different nonlinear stiffness coefficient. Solid line: $\epsilon = 0$, linear isolator; dotted line or squares: $\epsilon = -0.01$; dash-dot line or circles: $\epsilon = 0.1$; dashed line or triangles: $\epsilon = 0.5$.

Figures 6.3 and 6.4 show the effects of nonlinear stiffness parameter ϵ of the isolator on power flows as well as the kinetic energies of the system with $\xi_1 = \xi_2 = 0.01, \mu = 0.5, \gamma = 0.5, \eta = 0, f_0 = 0.1$. The value of ϵ changes from $\epsilon = -0.01$ indicating a softening stiffness isolator, to $\epsilon = 0$, corresponding to a linear isolator, and then to 0.1 and 0.5 for hardening stiffness isolators. The figures show numerical and analytical approximate results agree well with each other over a large frequency range, verifying the averaging formulations of power flow variables.

By comparing with the results of the linear case $\epsilon = 0$, some power flow characteristics due to the stiffness nonlinearity in the isolator are observed:

- A softening stiffness of $\epsilon = -0.01$ bends the first peak in the curve of time-averaged input/transmitted powers to the low-frequency band with significant reductions of

the corresponding peak value. In comparison, a hardening stiffness with $\epsilon = 0.1$ bends the first peak to the higher frequencies while the second peaks in $\bar{p}_{in}$ and $\bar{p}_t$ curves remain almost unchanged. When the nonlinear parameter ϵ increases to 0.5, the hardening stiffness becomes stronger and both peaks in each power flow curve are twisted significantly to the higher frequencies. For the hardening stiffness cases, the first peak in $\bar{p}_{in}$ is reduced slightly by adding the nonlinearity, but the second peak value in $\bar{p}_{in}$ and both peaks in transmitted power $\bar{p}_t$ may become higher than those of the linear case.

- Associated with the twisting of curves due to the stiffness nonlinearity, non-unique solution branches of power flows, indicating different power flow paths, are encountered in the low-frequency range for the softening stiffness isolator and in the high-frequency range for the hardening stiffness isolator. In these frequency ranges, the time-averaged power flow of the system will be dependent on the initial conditions.

- When the excitation frequency is far away from the peak frequencies, the power flow variables of the system are not sensitive to the stiffness parameter ϵ as the curves of different examined cases coincide.

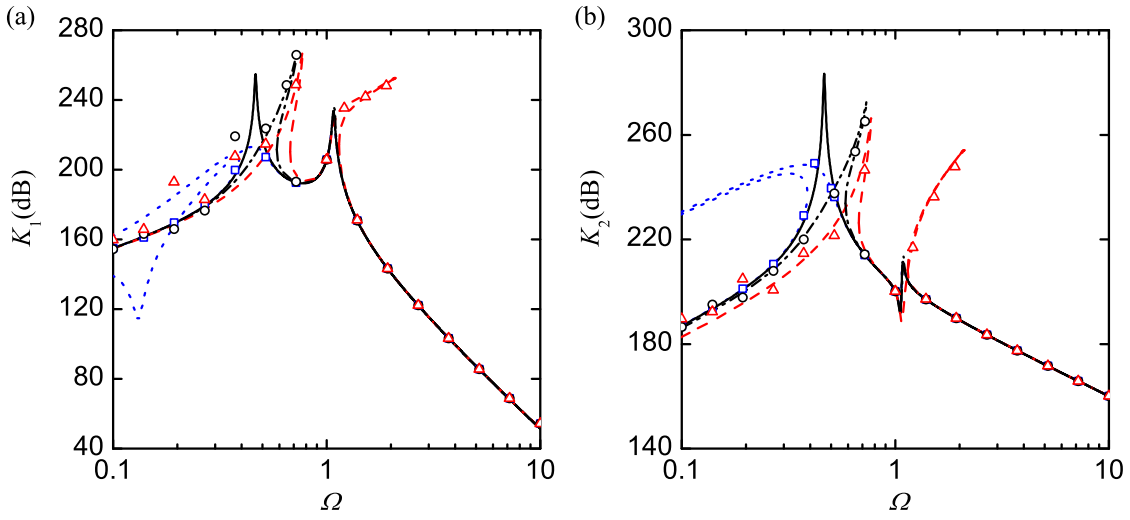

FIGURE 6.4: Kinetic energies (a) K_1 and (b) K_2 of the systems with different nonlinear stiffness coefficient. Solid line: $\epsilon = 0$, linear isolator; dotted line or squares: $\epsilon = -0.01$; dash-dot line or circles: $\epsilon = 0.1$; dashed line or triangles: $\epsilon = 0.5$.

Similar with the variations of power flow variables, Figure 6.4 shows the curves of kinetic energies of the masses bend to a lower-frequency range when the isolator is of a softening stiffness and to the high frequencies when there is a hardening stiffness. It shows that introducing a softening stiffness can greatly reduce the first peak values. A hardening stiffness, in contrast, results in an increase in the first peak value of the kinetic energy K_1 of the base structure, but a reduction in that of K_2. The second peak value in the

kinetic energy curves remains almost unchanged when $\epsilon = -0.01, 0$ or 0.1, but increases significantly when $\epsilon = 0.5$.

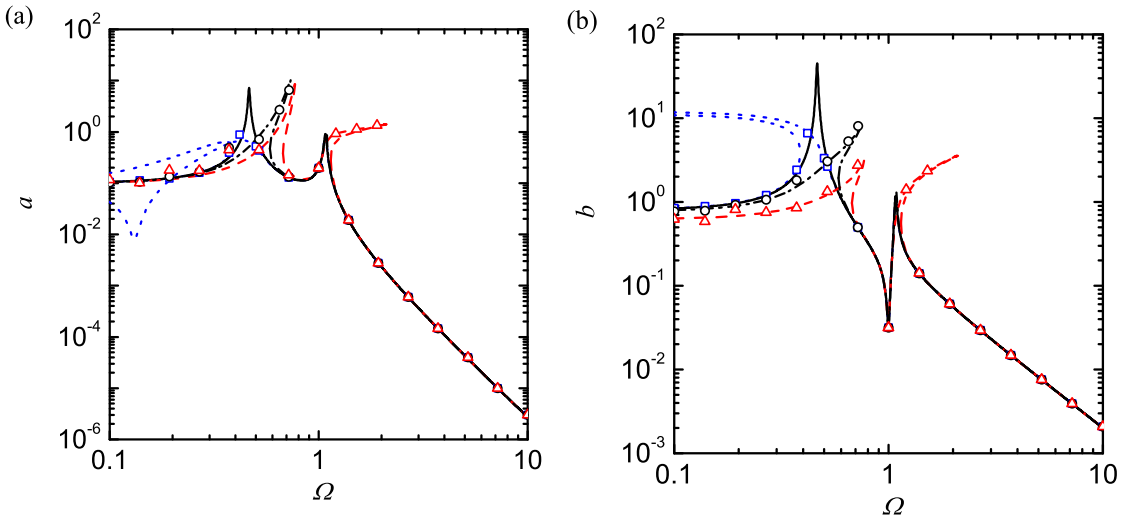

FIGURE 6.5: Response amplitudes (a) a and (b) b of the systems with different nonlinear stiffness coefficient. Solid line: $\epsilon = 0$, linear isolator; dotted line or squares: $\epsilon = -0.01$; dash-dot line or circles: $\epsilon = 0.1$; dashed line or triangles: $\epsilon = 0.5$.

To understand the underlying cause of the insensitivity of power flows to the stiffness nonlinearity of the isolator in the non-resonant region, Figure 6.5 shows the variations of response amplitudes against the excitation frequency. It is observed that the stiffness nonlinearity mainly affects response amplitudes locally when Ω is close to the resonant peak frequencies and the value of b is larger than unity. As mentioned previously, for a significant influence of the nonlinear stiffness on the response amplitudes, the value of b has to be sufficiently large such that the contribution of the nonlinear parameter ϵ to the term $1 + \frac{3}{4}\epsilon b^2$ in Eqs. (6.15) and (6.16) cannot be ignored. When the excitation frequency is far away from the peaks, b is so small that $\frac{3}{4}\epsilon b^2 \ll 1$. Correspondingly, the response amplitudes, time-averaged power flows and kinetic energies of the system are little affected by the variations of the stiffness nonlinearity.

6.4.2 The isolator with damping nonlinearity

The effects of nonlinear damping in the isolator on vibration power flows are investigated here by assuming a linear stiffness. With some parameters fixed as $\xi_1 = \xi_2 = 0.01, \mu = 0.5, \gamma = 0.5, f_0 = 0.1, \epsilon = 0$, the nonlinear damping coefficient η changes from zero for a isolator with linear viscous damping to 0.1 and then 1, both suggesting a combination of linear and cubic damping forces. The variations of time-averaged power flows, kinetic energies as well as response amplitudes with the excitation frequency are shown in Figures 6.6, 6.7 and 6.8 respectively. It is observed that:

- The nonlinear damping may have large influences on the peak values of time-averaged power flows as well as the kinetic energies. As seen in Figures 6.6 and 6.7, increasing the nonlinear damping parameter η from 0 to 0.1 and then to 1 results in substantial reductions in the first peak values of the curves. In comparison, there is much smaller change in the second peak values;

- Unlike the influences of the nonlinear stiffness, there is no bending or twisting of the peaks and the time-averaged power flow variables remain single-valued at a single excitation frequency;

- When the excitation frequency Ω is away from the peaks, the power flow quantities shown in these figures are not sensitive to the variations of the nonlinear damping parameter η.

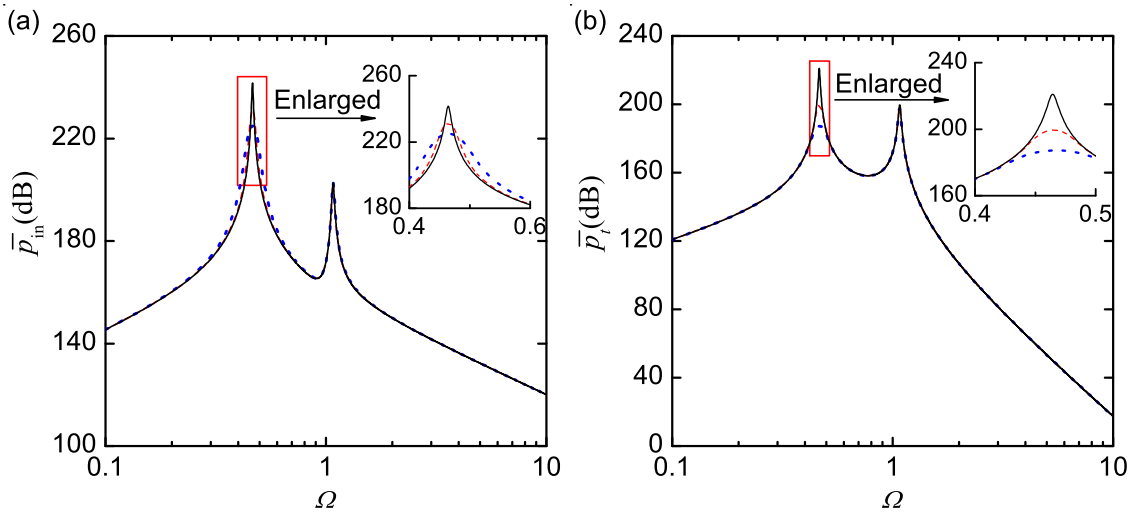

FIGURE 6.6: Time-averaged (a) input and (b) transmitted powers of the systems with different nonlinear damping coefficient. Solid line: $\eta = 0$; dashed line: $\eta = 0.1$ and dotted line: $\eta = 1$.

These power flow characteristics show that adding the cubic damping nonlinearity to the isolator provides benefits for vibration isolation as the peak values are reduced while at the same time multiple solutions are avoided. For more detailed information of the nonlinear damping effects on power flows, Figure 6.8 shows the corresponding curves of the response amplitudes for different η values. When the excitation frequency is close to the first peak, the value of b is large. Consequently, the changes of η from 0 to 1 yield large variations of the term $1 + \frac{3}{4}\eta b^2\Omega^2$ so that the response amplitudes governed by Eqs. (6.15) and (6.16) are greatly affected. In contrast, when Ω moves away from the first resonant frequency, the value b is small so that the responses amplitudes are not sensitive to η as $\frac{3}{4}\eta b^2\Omega^2 \ll 1$ and $1 + \frac{3}{4}\eta b^2\Omega^2 \approx 1$. As a result, the kinetic energies as well as time-averaged power flow quantities $\bar{p}_{in}$ and $\bar{p}_t$ are not sensitive to the nonlinear damping when away from the resonance frequencies.

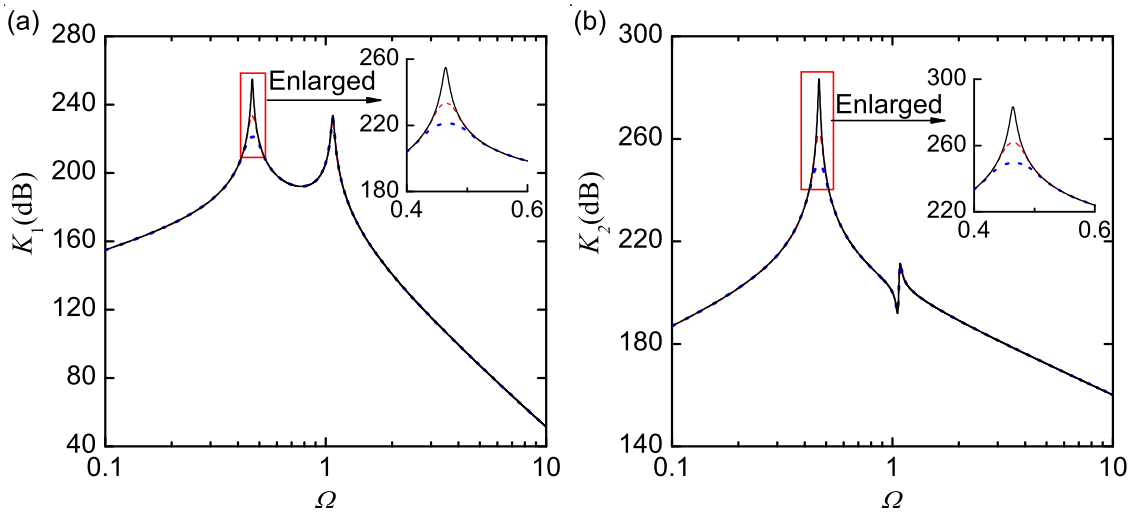

FIGURE 6.7: Kinetic energies (a) K_1 and (b) K_2 of the systems with different nonlinear damping coefficient. Solid line: $\eta = 0$; dashed line: $\eta = 0.1$ and dotted line: $\eta = 1$.

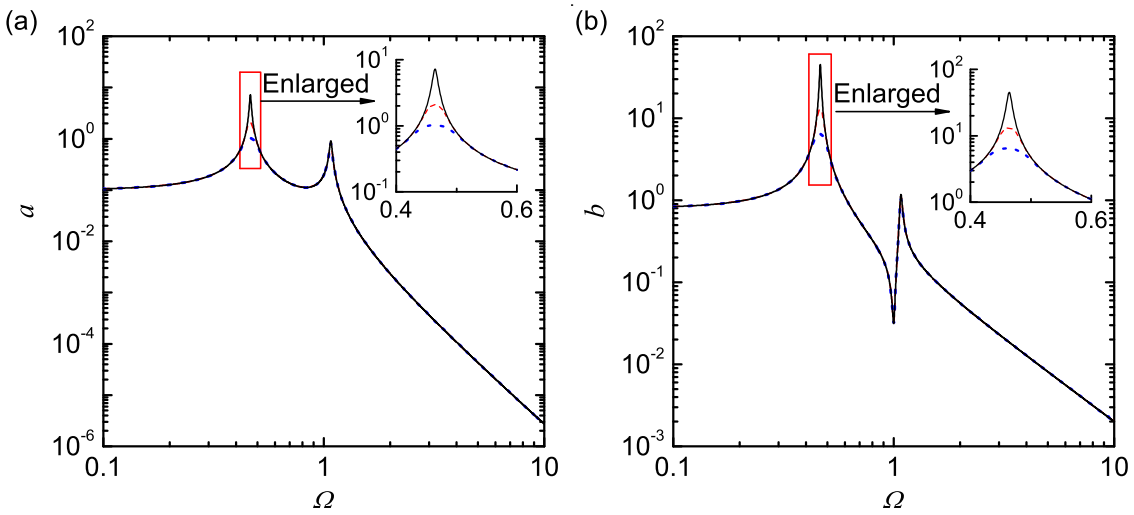

FIGURE 6.8: Response amplitudes (a) a and (b) b of the systems with different nonlinear damping coefficient. Solid line: $\eta = 0$; dashed line: $\eta = 0.1$ and dotted line: $\eta = 1$.

6.4.3 The isolator with stiffness and damping nonlinearities

In previous sections, the nonlinearity only exists in the stiffness or the damping of the isolator. Here, both damping and stiffness nonlinearities in the isolator are considered. The nonlinear stiffness coefficient ϵ is fixed as 0.5 while the nonlinear damping coefficient η changes from 0 to 0.1 and then to 0.5. Other parameters are set as $\xi_1 = \xi_2 = 0.01, \mu = 0.5, \gamma = 0.5, f_0 = 0.1$. The variations of time-averaged power flows and kinetic energies of the system with the excitation frequency are shown in Figures 6.9 and 6.10, respectively. The effects of the hardening nonlinear stiffness are again demonstrated by the bending of the peaks in the curves to the high-frequency range. Similar to the nonlinear stiffness

system studied in Section 6.4.1, multiple solution branches of power flow variables are encountered. An increase in the nonlinear damping parameter η from 0 to 0.5 results in a narrower frequency band for non-unique power flows. Also, introducing the damping nonlinearity in the isolator assists in a reduction of the second peak value of the time-averaged power flow curve.

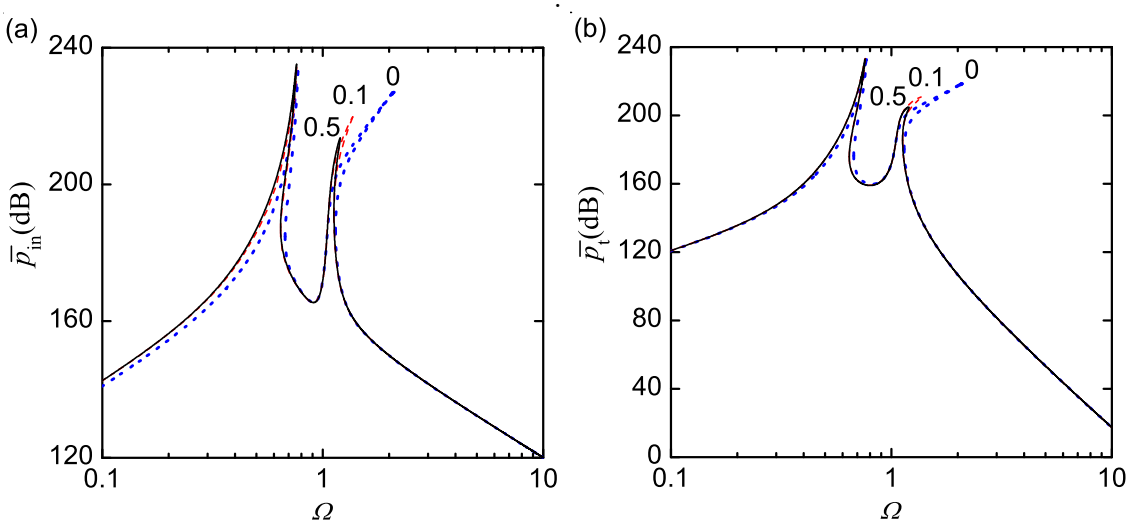

FIGURE 6.9: Time-averaged (a) input and (b) transmitted powers of the systems with a fixed nonlinear stiffness coefficient but different nonlinear damping coefficient. Solid line: $\eta = 0.5$; dashed line: $\eta = 0.1$ and dotted line: $\eta = 0$.

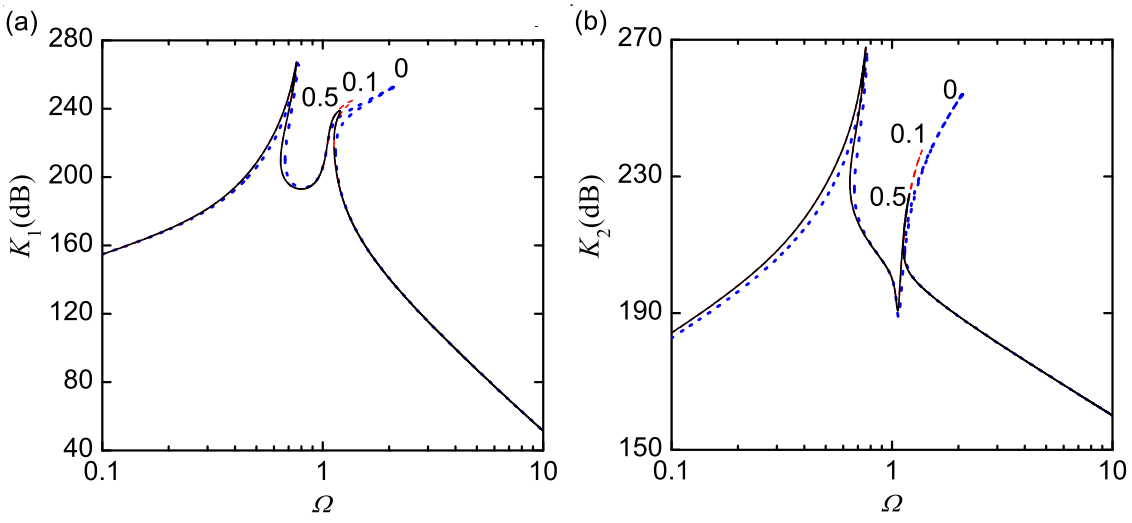

FIGURE 6.10: Kinetic energies (a) K_1 and (b) K_2 of the systems with fixed a nonlinear stiffness coefficient but different nonlinear damping coefficient. Solid line: $\eta = 0.5$; dashed line: $\eta = 0.1$ and dotted line: $\eta = 0$.

Figure 6.11 examines the corresponding response characteristics of the system. It is shown that introducing nonlinear damping in the hardening stiffness isolator lowers the

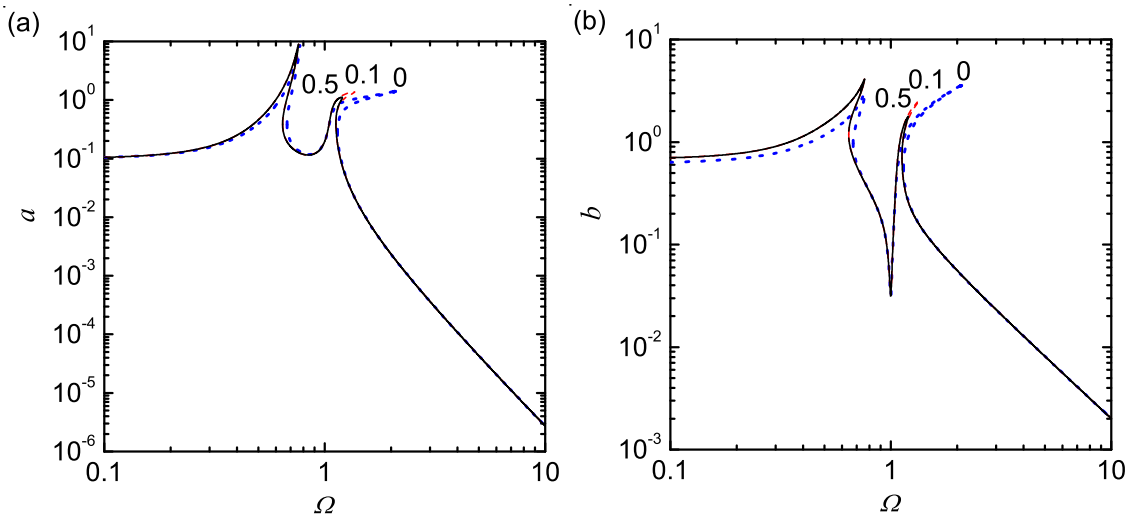

FIGURE 6.11: Response amplitudes (a) a and (b) b of the systems with fixed a nonlinear stiffness coefficient but different nonlinear damping coefficient. Solid line: $\eta = 0.5$; dashed line: $\eta = 0.1$ and dotted line: $\eta = 0$.

second resonance peak. However, the values of power flow variables at other excitation frequencies are little affected. This is again due to the fact that the value of $\frac{3}{4}\eta b^2\Omega^2$ is much smaller than 1 in the frequency range away from the second resonance. Consequently, $1+\frac{3}{4}b^2\eta\Omega^2 \approx 1$ in the frequency response relations and the response amplitudes and time-averaged power flows vary little with η in a wide frequency range.

6.4.4 Effects of other parameters

In this section, the effects of other parameters, including the mass ratio μ, the frequency ratio γ, damping parameters ξ_1 and ξ_2, as well as the excitation magnitude f_0 on the power flows and kinetic energies of the system are examined. For brevity, the isolator is considered to be with hardening stiffness. Systems with softening isolators can be investigated in a similar way and thus the results are not provided here.

For a system with $\xi_1 = \xi_2 = 0.01, \gamma = 1, \epsilon = 1, \eta = 1, f_0 = 0.1$, Figures 6.12 shows the effects of mass ratio μ on time-averaged input and transmitted powers, kinetic energies and the response amplitudes, respectively. It shows that the mass ratio μ influences the time-averaged input power significantly over a wide frequency range, whereas the time-averaged transmitted power varies substantially only when the excitation frequency locates close to or in between two resonant peak frequencies. It is observed that a small mass ratio of $\mu = 0.2$ leads to larger amount of input power in a wide range of excitation frequencies. Also, as the value of μ decreases from 1 to 0.5 and then to 0.2, the second peak value of $\bar{p}_{in}$ increases whereas the peak values of $\bar{p}_t$ remain almost unchanged. A large difference between the analytical and numerical results is observed at point B (and B') in Figure 6.12 with the excitation frequency Ω being

approximately 0.27. Further examination of the corresponding response suggests the existence of large super-harmonic components at $\Omega_r = 3\Omega$ and $\Omega_r = 5\Omega$, as shown in Figure 6.13. Clearly, super-harmonic resonance occurs and thus the first-order averaging approximation underestimated time-averaged power flow levels.

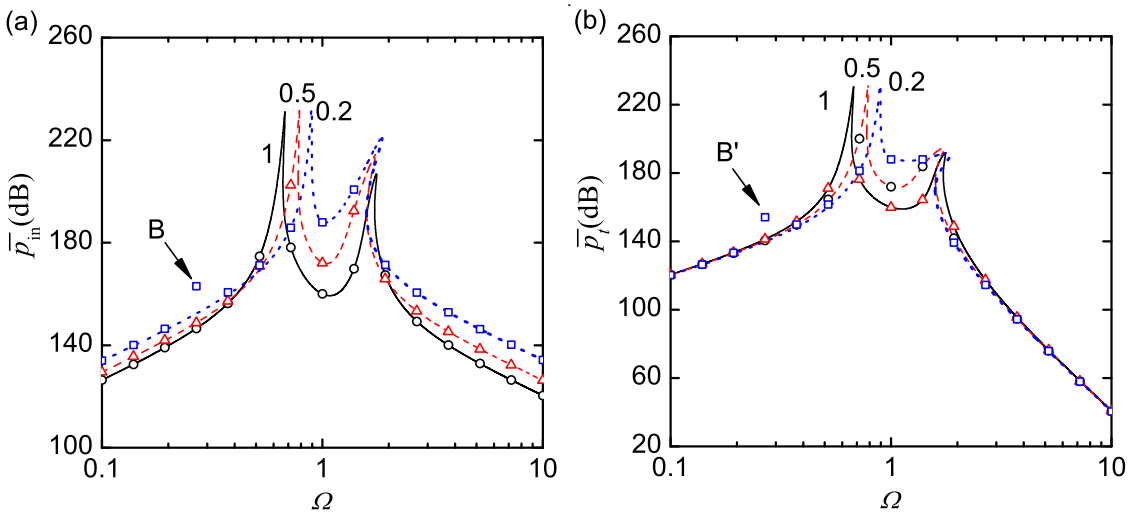

FIGURE 6.12: Time-averaged (a) input and (b) transmitted powers of the systems with different mass ratio μ. Solid line or circles: $\mu = 1$; dashed line or triangles: $\mu = 0.5$; dotted line or squares: $\mu = 0.2$.

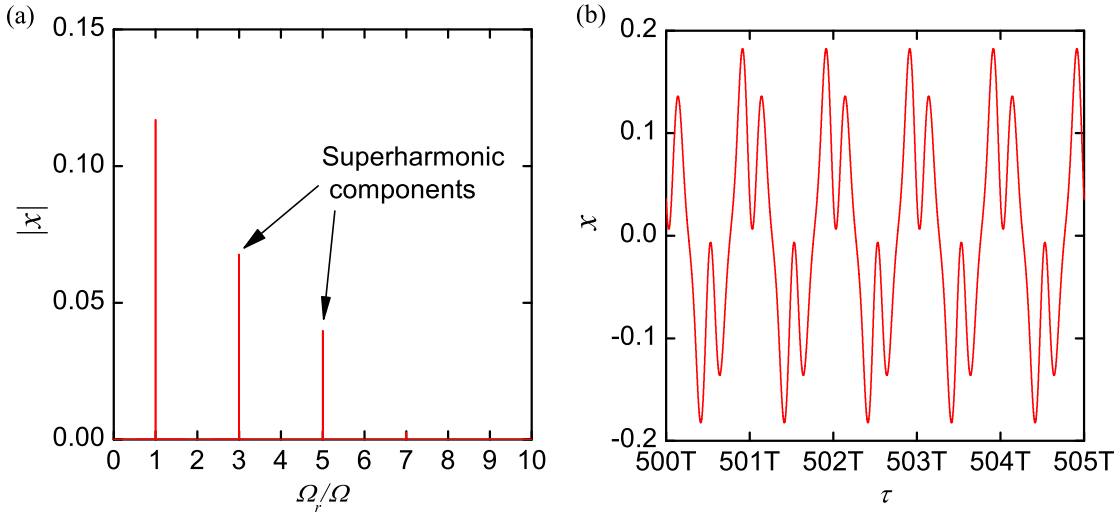

FIGURE 6.13: Occurrence of super-harmonic resonances ($\xi_1 = \xi_2 = 0.01, \gamma = 1, \mu = 0.2, \epsilon = 1, \eta = 1, f_0 = 0.1, \Omega = 0.27$). (a) Frequency spectrum and (b) time histories.

Figure 6.14(a) shows that the influences of μ on the kinetic energy K_1 of the base are similar to those on the time-averaged transmitted power shown in Figure 6.12(b). In the low-frequency range, the maximum kinetic energy of the excited mass m_2 is not sensitive to the mass ratio μ, but in the high-frequency range, K_2 increases significantly as μ reduces from 1 to 0.2. It shows that that the first peak in the curves of K_2 increases

with μ, but the second peak value of K_2 is suppressed by increasing μ. Figure 6.15 shows the response amplitude a of the base structure is sensitive to variations of μ when the excitation frequency Ω is close to or locates in between two peak frequencies, but not sensitive to it in other frequency ranges. In comparison, the relative deflection b of the isolator generally decreases when mass ratio μ increases.

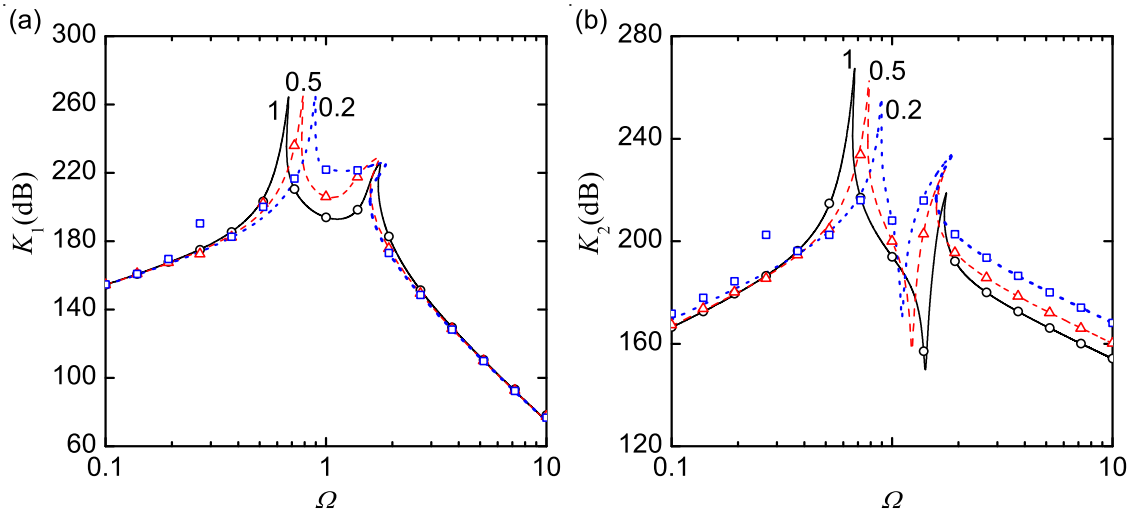

FIGURE 6.14: Kinetic energies (a) K_1 and (b) K_2 of the systems with different mass ratio μ. Solid line or circles: $\mu = 1$; dashed line or triangles: $\mu = 0.5$; dotted line or squares: $\mu = 0.2$.

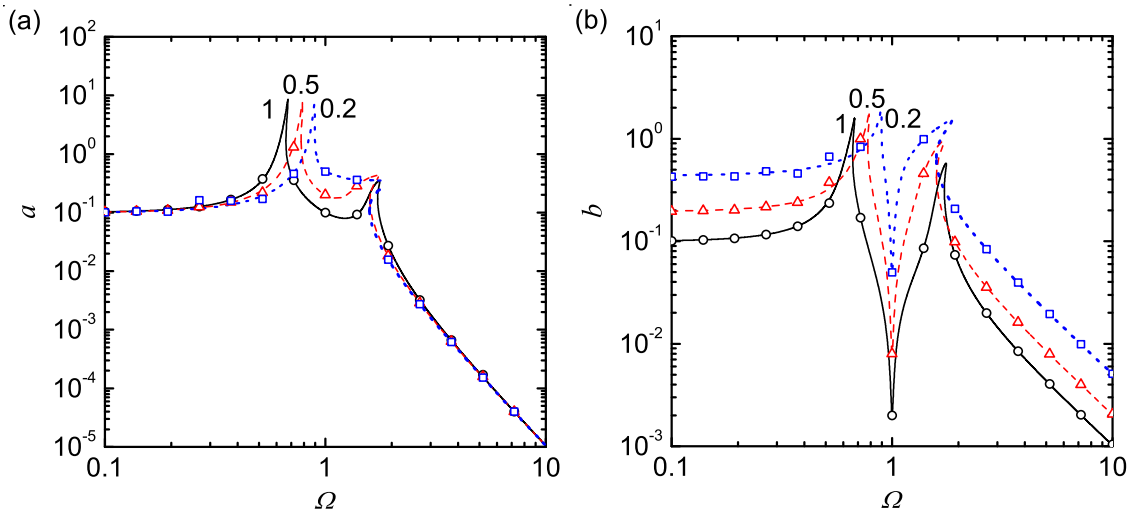

FIGURE 6.15: Response amplitudes (a) a and (b) b of the systems with different mass ratio μ. Solid line or circles: $\mu = 1$; dashed line or triangles: $\mu = 0.5$; dotted line or squares: $\mu = 0.2$.

Figure 6.16, 6.17 and 6.18 show the influences of the frequency ratio γ on system's power flows, kinetic energies and response amplitudes, respectively. When the parameters are

set as $\xi_1 = \xi_2 = 0.01, \mu = 1, \epsilon = 0.5, \eta = 0.1, f_0 = 0.1$, Figure 6.16 shows that an increase in γ shifts both peaks in each power flow curve towards the high-frequency range. The first peak frequency increases slightly, but the second one grows significantly. The amount of time-averaged input power $\bar{p}_{in}$ increases with γ in the high-frequency range. In contrast, in the low-frequency range, there is less power input as γ increases from 0.5 to 2 . The time-averaged transmitted power shows a similar dependence on γ in the high-frequency range, but is less sensitive to it when Ω is small.

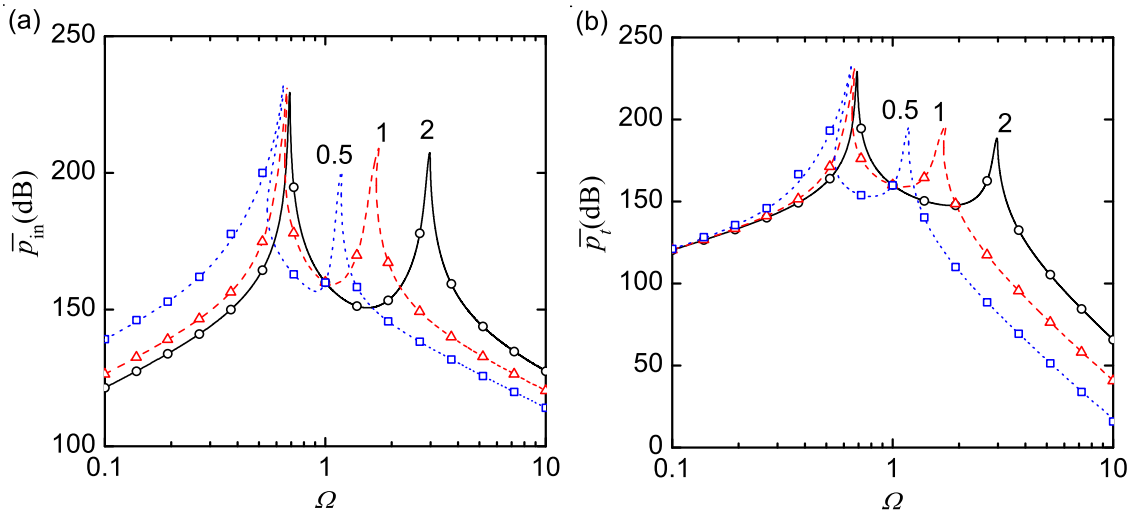

FIGURE 6.16: Time-averaged (a) input and (b) transmitted powers of the systems with different frequency ratio γ. Solid line or circles: $\gamma = 2$; dashed line or triangles: $\gamma = 1$; dotted line or squares: $\gamma = 0.5$.

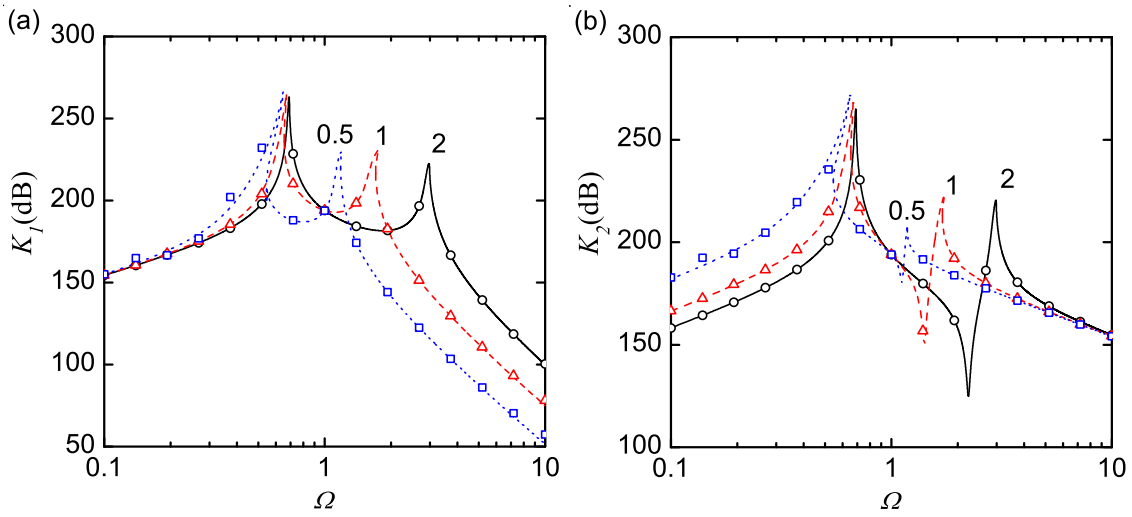

FIGURE 6.17: Kinetic energies (a) K_1 and (b) K_2 of the systems with different frequency ratio γ. Solid line or circles: $\gamma = 2$; dashed line or triangles: $\gamma = 1$; dotted line or squares: $\gamma = 0.5$.

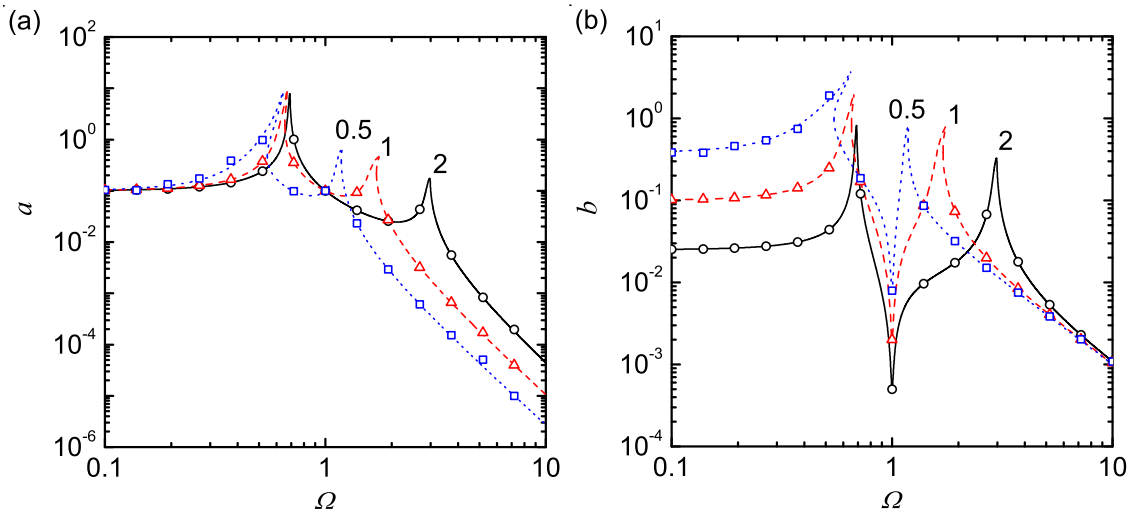

FIGURE 6.18: Response amplitudes (a) a and (b) b of the systems with different frequency ratio γ. Solid line or circles: $\gamma = 2$; dashed line or triangles: $\gamma = 1$; dotted line or squares: $\gamma = 0.5$.

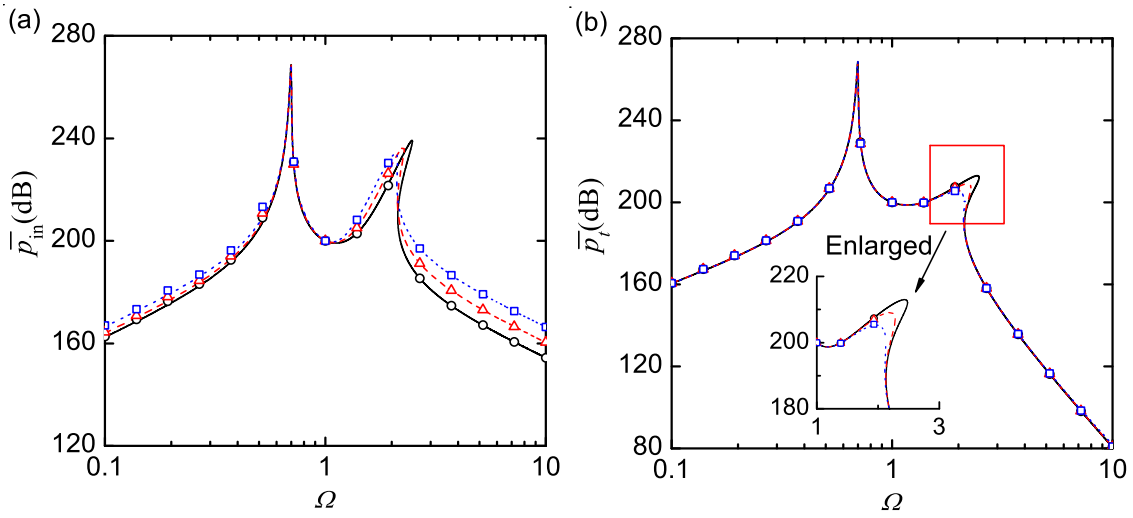

FIGURE 6.19: Time-averaged (a) input and (b) transmitted powers of the systems with different linear damping in the isolator. Solid line or circles: $\xi_2 = 0.005$; dashed line or triangles: $\xi_2 = 0.01$; dotted line or squares: $\xi_2 = 0.02$.

The patterns of kinetic energy curves shown in Figure 6.17(a) are similar to those shown in Figure 6.16(b) as the transmitted power $\bar{p}_t$ and the kinetic energy of the base K_1 is proportional when the damping parameter ξ_1 is fixed. In comparison, the kinetic energy K_2 of mass m_2 shows its strong dependence on γ at low excitation frequencies. However, when the excitation frequency becomes large, the value of K_2 becomes less sensitive to the frequency ratio γ. The variations of the response amplitudes are shown in Figure 6.18, which suggests the response amplitude of the base structure is sensitive to frequency ratio γ at high excitation frequencies with its value increasing with γ. As

Ω reduces to lower frequencies, the curves of amplitude a tend to merge with each other. On the contrary, the dynamic deflection of the isolator b depends more on γ in the low-frequency range, but changes less with it in the high-frequency range.

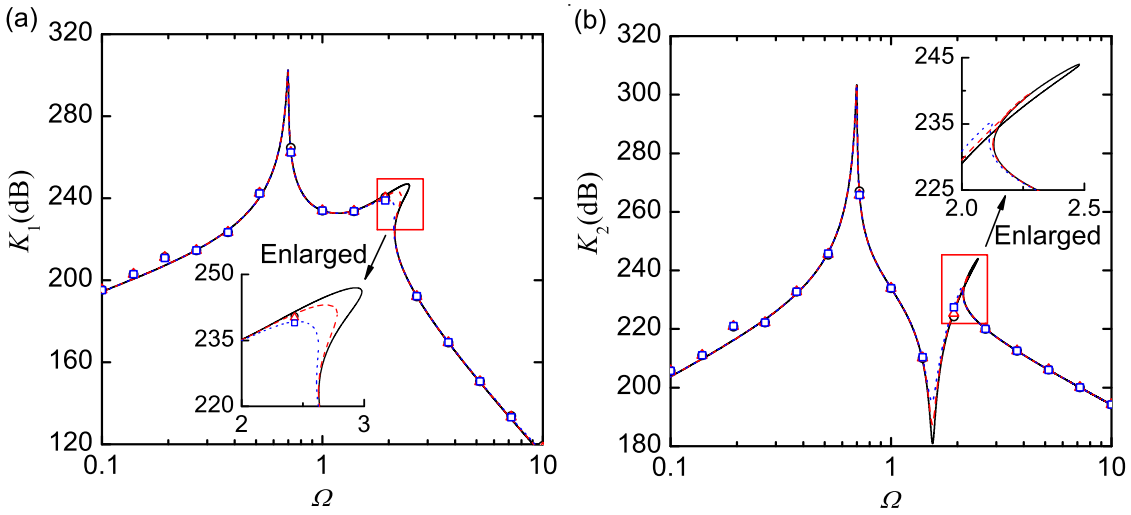

FIGURE 6.20: Kinetic energies (a) K_1 and (b) K_2 of the systems with different linear damping in the isolator. Solid line or circles: $\xi_2 = 0.005$; dashed line or triangles: $\xi_2 = 0.01$; dotted line or squares: $\xi_2 = 0.02$.

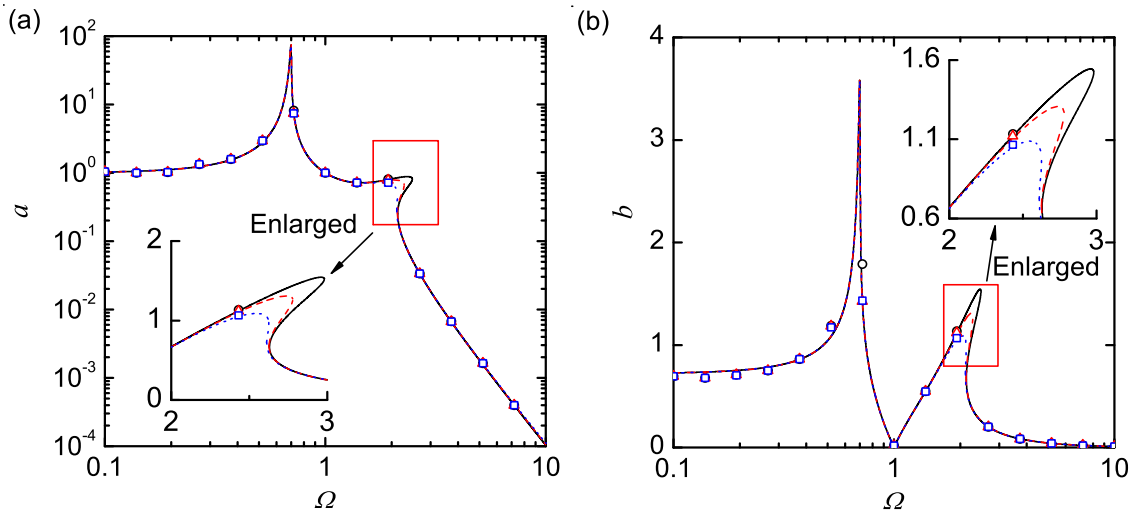

FIGURE 6.21: Response amplitudes (a) a and (b) b of the systems with different linear damping in the isolator. Solid line or circles: $\xi_2 = 0.005$; dashed line or triangles: $\xi_2 = 0.01$; dotted line or squares: $\xi_2 = 0.02$.

In Figures 6.19, 6.20 and 6.21, the effects of damping parameter ξ_2 of the isolator on power flows, kinetic energies as well as response amplitudes are investigated. For the considered system with $\xi_1 = 0.01, \mu = 1, \gamma = 1, \epsilon = 1, \eta = 1, f_0 = 1$, Figures 6.19(b) and 6.20 show that the second peak in the time-averaged transmitted power as well as the

kinetic energies curves is suppressed by increasing ξ_2. When Ω locates far away from the second peak frequency, there is little change in the values of transmitted power and kinetic energies as ξ_2 varies. In comparison, the change in input power is more significant due to variations of ξ_2. Its value increases with ξ_2 in the low/high-frequency range when Ω is away from the peak frequencies. Figure 6.21 shows that the second resonance peak is also reduced by increasing damping. As ξ_2 increases, the peak bends less to the high-frequency range and there is a smaller frequency band for multiple solutions. Away from the peak frequencies, the values of a and b remain almost unchanged when the value of ξ_2 changes from 0.005, to 0.01 and then to 0.02.

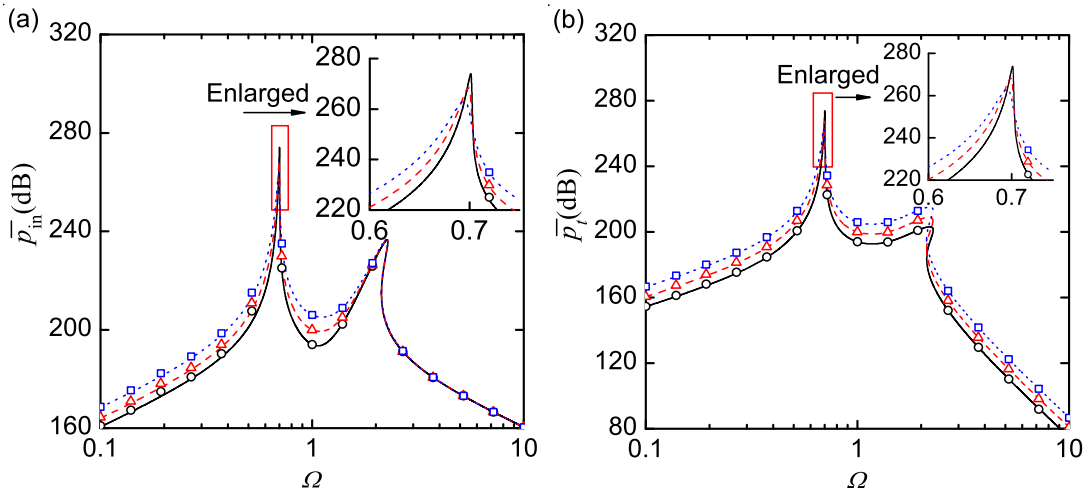

FIGURE 6.22: Time-averaged (a) input and (b) transmitted powers of the systems with different damping in the base structure. Solid line or circles: $\xi_1 = 0.005$; dashed line or triangles: $\xi_1 = 0.01$; dotted line or squares: $\xi_1 = 0.02$.

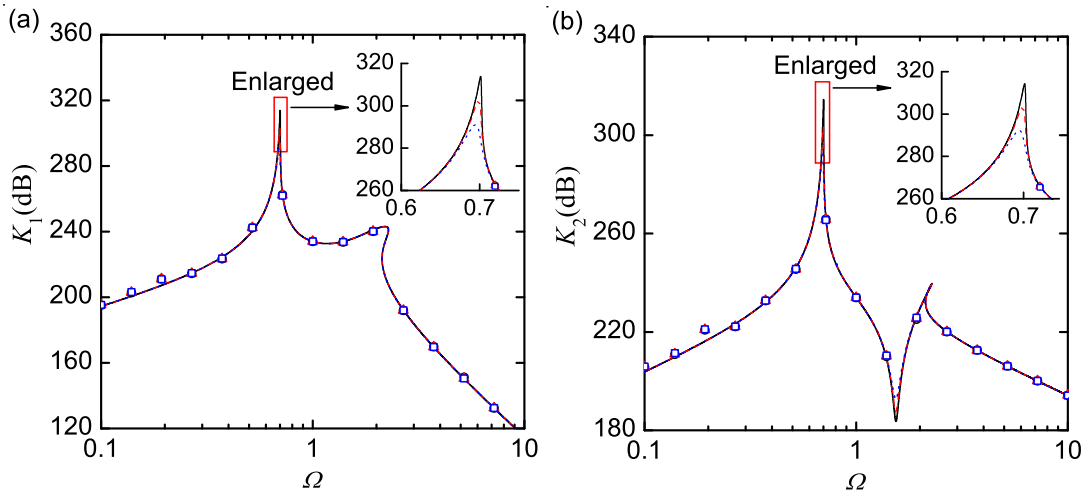

FIGURE 6.23: Kinetic energies (a) K_1 and (b) K_2 of the systems with different damping in the base structure. Solid line or circles: $\xi_1 = 0.005$; dashed line or triangles: $\xi_1 = 0.01$; dotted line or squares: $\xi_1 = 0.02$.

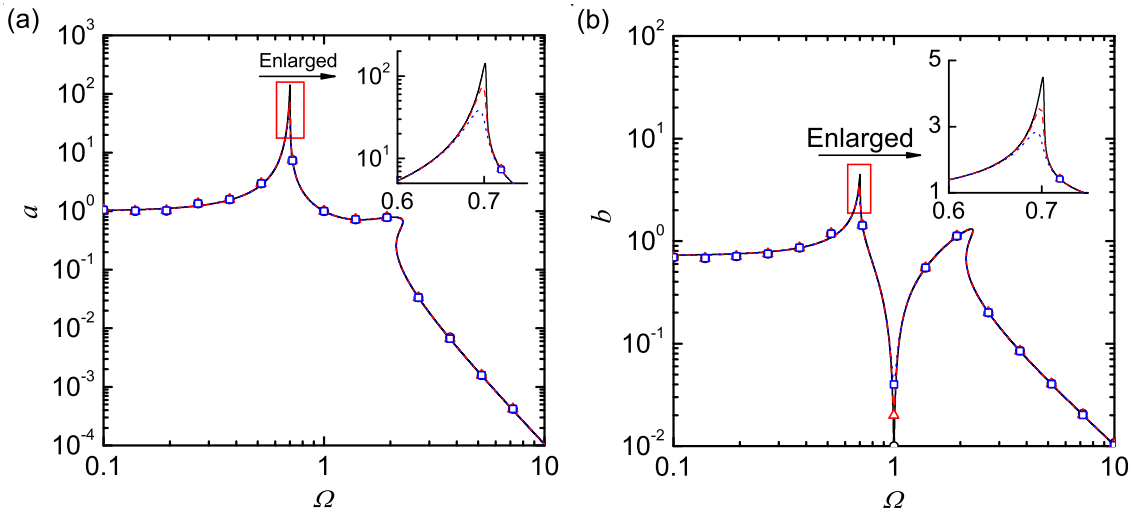

FIGURE 6.24: Response amplitudes (a) a and (b) b of the systems with different damping in the base structure. Solid line or circles: $\xi_1 = 0.005$; dashed line or triangles: $\xi_1 = 0.01$; dotted line or squares: $\xi_1 = 0.02$.

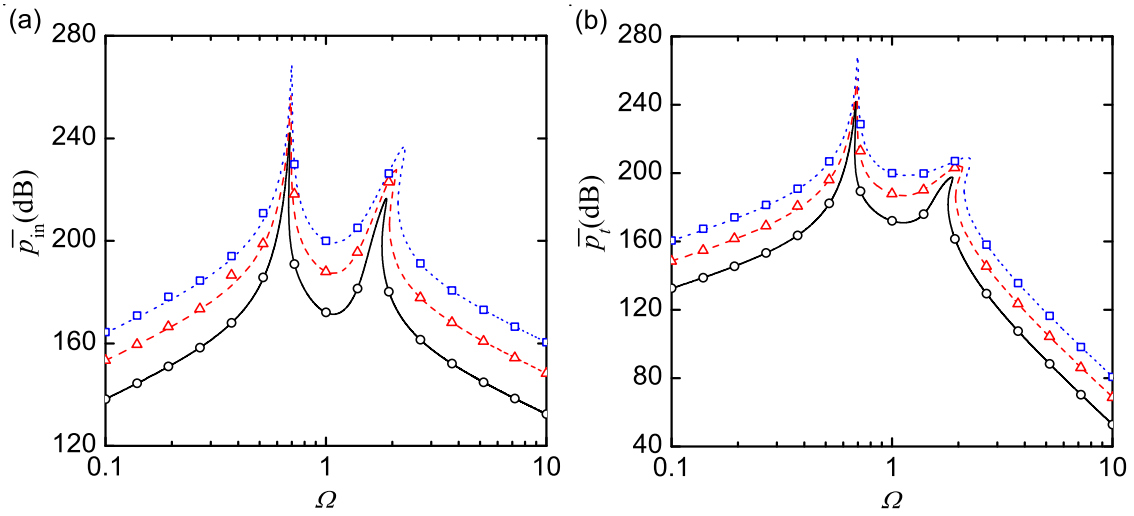

FIGURE 6.25: Time-averaged (a) input and (b) transmitted powers of the systems under different force amplitude f_0. Solid line or circles: $f_0 = 0.2$; dashed line or triangles: $f_0 = 0.5$; dotted line or squares: $f_0 = 1$.

Figures 6.22, 6.23 and 6.24 show the influences of damping in the base structure on power transmission, kinetic energies and response amplitudes, respectively. It is shown that a change in ξ_1 causes large variations of time-averaged input power when the excitation frequency Ω locates in the low-frequency range, with its value increasing with ξ_1. However, in the high-frequency range, the amount of time-averaged input power changes little when varying ξ_1. In contrast, the time-averaged power transmission is sensitive to the damping in the base over the examined region of frequencies. It is shown that heavier damping in the base can result in more power to be transmitted and dissipated.

Figure 6.22 also shows that the first peak values of $\bar{p}_{in}$ and $\bar{p}_t$ are moderately suppressed by damping as their values decrease with an increasing ξ_1. Similarly, Figure 6.23 and 6.24 show the first resonant peaks in the curves of the kinetic energies and response amplitudes are greatly attenuated by adding a heavier damping in the base structure. At other frequencies, the variable values show a small dependence on ξ_1.

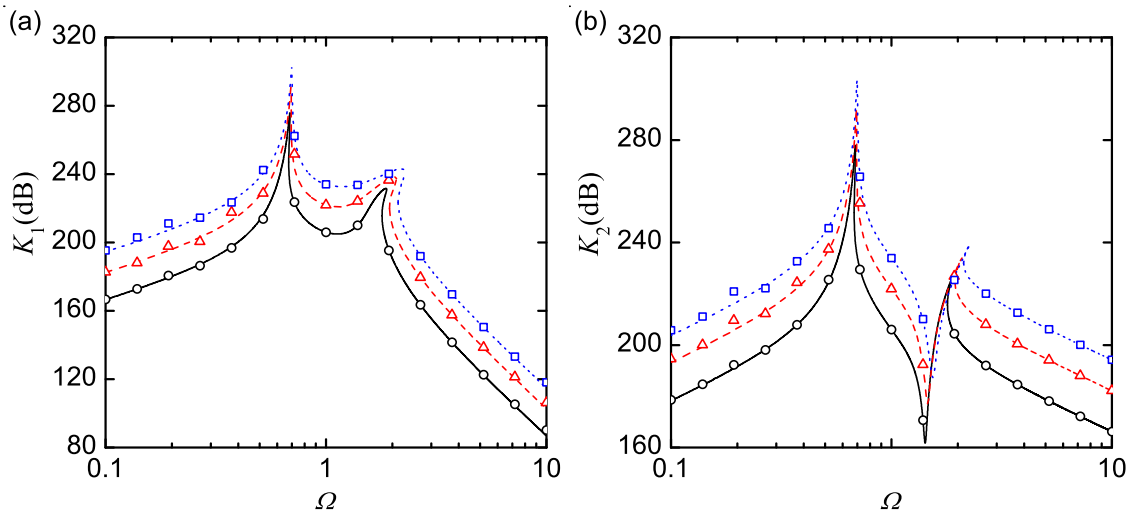

FIGURE 6.26: Kinetic energies (a) K_1 and (b) K_2 of the systems under different force amplitude f_0. Solid line or circles: $f_0 = 0.2$; dashed line or triangles: $f_0 = 0.5$; dotted line or squares: $f_0 = 1$.

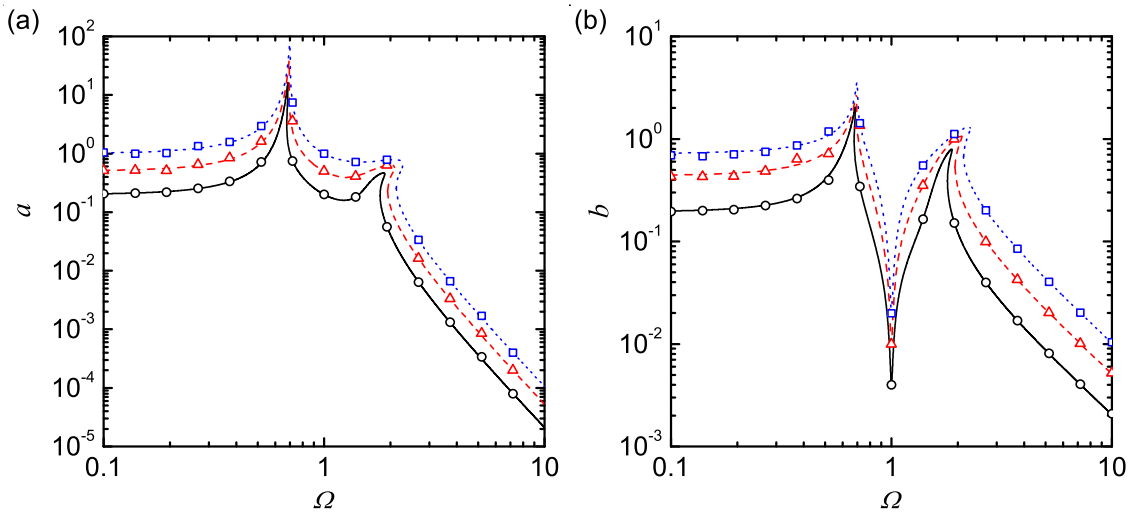

FIGURE 6.27: Response amplitudes (a) a and (b) b of the systems under different force amplitude f_0. Solid line or circles: $f_0 = 0.2$; dashed line or triangles: $f_0 = 0.5$; dotted line or squares: $f_0 = 1$.

Figures 6.25,6.26 and 6.27 show the effects of the excitation amplitude f_0 on the power flows, kinetic energies as well as response amplitude, respectively. The figures suggest that a larger excitation amplitude generally results in larger amount of time-averaged

power flows as well as increases in kinetic energies. Moreover, as f_0 increases from 0.2, to 0.5 and then to 1, the response amplitudes a and b also increase. The nonlinear stiffness effects of the isolator become stronger and consequently the second peak in the curves of power flows and kinetic energies bends further towards the high-frequency range.

6.5 Conclusions

This chapter studied the vibrational power flow behaviour of a two degrees-of-freedom nonlinear vibration isolation system. The model consisted of an excited mass, mounted on a linear SDOF base structure via a nonlinear isolator with nonlinearities in both damping and stiffness. The coupling effects between the isolator and the flexible base were examined from the power flow perspective. The performance of the isolator with different nonlinearities was assessed by investigating the levels time-averaged power flows as well as kinetic energies. As a first-order approximation, the averaging method was used to formulate power flow quantities. Numerical simulations based on the Runge-Kutta method were also carried out for verification of the analytical approximations. Based on the investigation, the following conclusions may be drawn.

- Introducing softening stiffness in the isolator can provide benefits for vibration isolation by bending the peaks in the curves of time-averaged power flows as well as kinetic energies to the low-frequency range and reducing the peak values. In contrast, adding hardening stiffness in the isolator bends the peaks to the high-frequency range and can result in higher peaks in power transmission, which are not desirable for vibration isolation.
- Introduction of a cubic nonlinear damping force in the isolator is beneficial in suppressing the peak values of time-averaged power flows while narrowing the frequency band of multiple solutions.
- Analytical approximation showed that the time-averaged transmitted power is proportional to the maximum kinetic energy of the base if its damping coefficient is fixed. Moreover, the time-averaged transmitted power is found to be identical to the averaged dissipated power by base damping.
- Parameter study showed that variations of the mass ratio μ results in significant changes in the time-averaged transmitted power when the excitation frequency located between the peak frequencies. In comparison, the amount of transmitted power is more sensitive to the frequency ratio γ in the high-frequency range.
- The time-averaged transmitted power exhibits strong dependence on the linear damping coefficient ξ_1 of the base structure over a large range of excitation frequencies. In contrast, it is sensitive to the linear damping coefficient ξ_2 of the isolator only when the excitation frequency Ω is close to the peak frequencies.

Chapter 7

Power flow analysis of a two-DOF nonlinear system for vibration absorption

In this chapter, the power flow characteristics of a two degrees-of-freedom (DOF) nonlinear system with a linear/nonlinear absorber attached to a linear/nonlinear primary structure are investigated. The use of linear dynamic vibration absorbers for vibration mitigation of linear structures has been extensively investigated. Early such studies were reported by Frahm (1911) as well as Den Hartog (1934) who proposed the addition of a linear attachment to a linear oscillator to suppress its vibration. It was shown that if the natural frequency of the absorber is tuned to that of the primary system, effective vibration attenuation can be achieved when the excitation frequency is the same as the natural frequency of the primary system. To widen the frequency band for effective functioning of vibration absorbers, the feasibility of using nonlinear vibration absorbers have been explored (see, Roberson (1952); Pipes (1953); Arnold (1955); Hunt and Nissen (1982)). More recently, some researchers adopted the concepts of passive targeted energy transfer in vibration absorption and qualitatively studied the functioning form of nonlinear vibration absorbers when the primary structure is subject to impact load (see, for example, Viguié and Kerschen (2009, 2010)). Xiong and Cao (2011) investigated the power flows in a two-DOF system with a nonlinear absorber attached to a linear oscillator. The possibility of using a linear vibration absorber to reduce the primary resonance of a nonlinear system was considered by Ji and Zhang (2010). However, the displacement response, instead of power flow quantities, was usually used as performance index of vibration absorbers. This chapter addresses the issue by studying a system with a nonlinear primary structure and a nonlinear absorber from the vibrational power flow perspective. Time-averaged power flows, as well as kinetic energies will be investigated to examine the effectiveness of nonlinear absorbers.

7.1 Mathematical model

Figure 7.1 shows a schematic representation of a two-DOF vibration absorption system, in which a vibrating primary structure, subject to a harmonic excitation of amplitude f and frequency ω, is modelled by a single DOF system consisting of a mass m_1, a linear/nonlinear spring with restoring force $G(x_1)$ and a linear viscous damper with damping coefficient c_1. To attenuate its vibration, a light-weight mass m_2 is attached to the main structure through a linear/nonlinear spring with restoring force $F(\delta)$ and a linear viscous damper with damping coefficient c_2. It is assumed that the masses only have vertical displacement and their static equilibrium positions where the dynamical deflections $x_1 = x_2 = 0$, are taken as the reference. The relationships between restoring forces and the corresponding dynamic deflections of the linear/nonlinear springs are described by

$$G(x_1) = k_1 x_1 (1 + \alpha x_1^2), \tag{7.1a}$$

$$F(\delta) = k_2 \delta (1 + \beta \delta^2), \tag{7.1b}$$

respectively, where k_1 and k_2 are positive, representing the linear stiffness; α and β are the nonlinear stiffness parameters; x_1 and $\delta = x_2 - x_1$ denote the dynamic deflections of the springs of the primary structure and the absorber, respectively. A positive α (or β) corresponds to a hardening spring with the stiffness increasing with the deflection whereas a negative α (or β) denotes a softening spring with its stiffness being a monotonically decreasing function of the corresponding deflection.

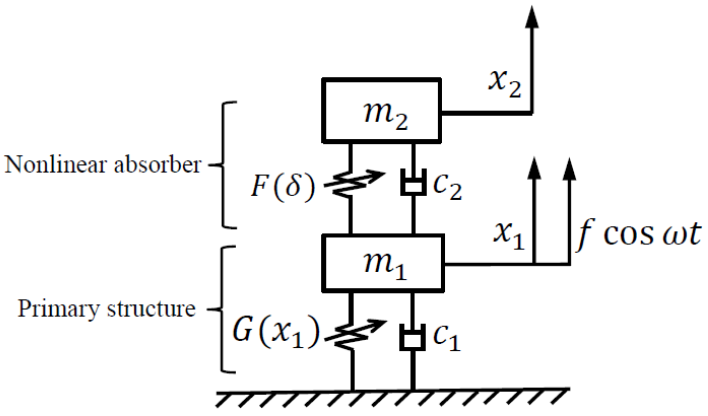

FIGURE 7.1: A schematic representation of a two-DOF system with a nonlinear vibration absorber and a nonlinear primary structure.

The governing equations of motion of the system are obtained as

$$m_1 \ddot{x}_1 + c_1 \dot{x}_1 + k_1 x_1 (1 + \alpha x_1^2) - c_2 \dot{\delta} - k_2 \delta (1 + \beta \delta^2) = f \cos \omega t, \tag{7.2}$$

$$m_2\ddot{x}_2 + c_2\dot{\delta} + k_2\delta(1+\beta\delta^2) = 0. \tag{7.3}$$

By introducing the following non-dimensional parameters:

$$x_0 = \frac{m_1 g}{k_1}, \quad \mu = \frac{m_2}{m_1}, \quad \omega_1 = \sqrt{\frac{k_1}{m_1}}, \quad \omega_2 = \sqrt{\frac{k_2}{m_2}},$$

$$\gamma = \frac{\omega_2}{\omega_1}, \quad \xi_1 = \frac{c_1}{2m_1\omega_1}, \quad \xi_2 = \frac{c_2}{2m_2\omega_2}, \quad \eta = \alpha x_0^2, \quad \epsilon = \beta x_0^2,$$

$$f_0 = \frac{f}{k_1 x_0}, \quad y = \frac{\delta}{x_0}, \quad x = \frac{x_1}{x_0}, \quad \Omega = \frac{\omega}{\omega_1}, \quad \tau = \omega_1 t,$$

the governing equations are written in a non-dimensional form

$$x'' + 2\xi_1 x' + x + \eta x^3 - \mu\gamma(2\xi_2 y' + \gamma y + \epsilon\gamma y^3) = f_0 \cos\Omega\tau, \tag{7.4}$$

$$y'' + \gamma(2\xi_2 y' + \gamma y + \epsilon\gamma y^3) = -x'', \tag{7.5}$$

where the primes denote differentiations with respect to the non-dimensional time τ.

To facilitate further numerical and analytical investigations of power flow characteristics, Eqs. (7.4) and (7.5) are transformed into a set of four first-order differential equations

$$\begin{pmatrix} x' \\ z' \\ y' \\ u' \end{pmatrix} = \begin{pmatrix} z \\ f_0\cos\Omega\tau - 2\xi_1 z - x - \eta x^3 + \mu\gamma(2\xi_2 u + \gamma y + \epsilon\gamma y^3) \\ u \\ -f_0\cos\Omega\tau + 2\xi_1 z + x + \eta x^3 - (\mu+1)\gamma(2\xi_2 u + \gamma y + \epsilon\gamma y^3) \end{pmatrix}. \tag{7.6}$$

For performance assessment of nonlinear dynamic absorbers based on vibrational power flows, it is essential to solve Eqs. (7.6) so that the response and power flow characteristics can be obtained. However, they are a set of nonlinear equations when $\eta \neq 0$ and/or $\epsilon \neq 0$, for which exact analytical solutions are not available. As an alternative, approximate solutions are sought using analytical methods or numerical simulations. In this chapter, the averaging method will be used for first-order analytical approximations of power flow variables while at the same time numerical results are also provided for verifications.

7.2 Analytical solutions

7.2.1 Frequency-response relations

The averaging method (see, for example, Nayfeh and Mook (1979)) is used herein for a first-order approximation of the displacement responses and power flow quantities. For its implementation, the steady-state responses of the primary structure and the absorber

are assumed to be harmonic with the same frequency as the excitation, i.e.,

$$x = a\cos(\Omega\tau + \phi), \tag{7.7a}$$

$$x' = -a\Omega\sin(\Omega\tau + \phi), \tag{7.7b}$$

$$y = b\cos(\Omega\tau + \theta), \tag{7.7c}$$

$$y' = -b\Omega\sin(\Omega\tau + \theta), \tag{7.7d}$$

where a, b, ϕ and θ are unknown response amplitudes or phase angles. Using the assumptions of the averaging method, Eqs. (7.6) are transformed into

$$a'\cos(\Omega\tau + \phi) - a\phi'\sin(\Omega\tau + \phi) = 0, \tag{7.8a}$$

$$-a'\sin(\Omega\tau + \phi) - a\phi'\cos(\Omega\tau + \phi) = \frac{f_1}{\Omega}, \tag{7.8b}$$

$$b'\cos(\Omega\tau + \theta) - b\theta'\sin(\Omega\tau + \theta) = 0, \tag{7.8c}$$

$$-b'\sin(\Omega\tau + \theta) - b\theta'\cos(\Omega\tau + \theta) = \frac{f_2}{\Omega}, \tag{7.8d}$$

where

$$f_1 = a(\Omega^2 - 1)\cos(\Omega\tau + \phi) - \eta a^3\cos^3(\Omega\tau + \phi) + f_0\cos\Omega\tau + 2\xi_1 a\Omega\sin(\Omega\tau + \phi) + \mu\gamma\Delta, \tag{7.9a}$$

$$f_2 = b\Omega^2\cos(\Omega\tau + \theta) + a'\Omega\sin(\Omega\tau + \phi) + (a\Omega^2 + a\Omega\phi')\cos(\Omega\tau + \phi) - \gamma\Delta, \tag{7.9b}$$

$$\Delta = -2\xi_2 b\Omega\sin(\Omega\tau + \theta) + \gamma b\cos(\Omega\tau + \theta) + \epsilon\gamma b^3\cos^3(\Omega\tau + \theta). \tag{7.9c}$$

The expressions of time change-rates of response amplitudes and phase angles are found by solving Eqs. (7.8), i.e.,

$$a' = -\frac{1}{\Omega}f_1\sin(\Omega\tau + \phi), \tag{7.10a}$$

$$\phi' = -\frac{1}{a\Omega}f_1\cos(\Omega\tau + \phi), \tag{7.10b}$$

$$b' = -\frac{1}{\Omega}f_2\sin(\Omega\tau + \theta), \tag{7.10c}$$

$$\theta' = -\frac{1}{b\Omega}f_2\cos(\Omega\tau + \theta). \tag{7.10d}$$

Assuming that the response amplitudes and phase angles are slowing-varying variables of time, the left hand sides of Eqs. (7.10) can be approximated by their average value

over an excitation cycle, i.e.,

$$a' \approx -\frac{1}{2\pi}\int_0^{\frac{2\pi}{\Omega}} f_1 \sin(\Omega\tau+\phi)\,\mathrm{d}\tau, \tag{7.11a}$$

$$\phi' \approx -\frac{1}{2\pi a}\int_0^{\frac{2\pi}{\Omega}} f_1 \cos(\Omega\tau+\phi)\,\mathrm{d}\tau, \tag{7.11b}$$

$$b' \approx -\frac{1}{2\pi}\int_0^{\frac{2\pi}{\Omega}} f_2 \sin(\Omega\tau+\theta)\,\mathrm{d}\tau, \tag{7.11c}$$

$$\theta' \approx -\frac{1}{2\pi b}\int_0^{\frac{2\pi}{\Omega}} f_2 \cos(\Omega\tau+\theta)\,\mathrm{d}\tau. \tag{7.11d}$$

Replacing f_1 and f_2 using expressions (7.9a), (7.9b) and (7.9c), then evaluations of the integrations in Eqs. (7.11) lead to

$$a' = -\frac{1}{\Omega}\Big(\frac{f_0}{2}\sin\phi + \xi_1 a\Omega + \mu\gamma b\big(-\xi_2\Omega\cos(\phi-\theta) + \frac{\gamma}{2}(1+\frac{3}{4}\epsilon b^2)\sin(\phi-\theta)\big)\Big), \tag{7.12a}$$

$$\phi' = -\frac{1}{a\Omega}\Big(\frac{f_0}{2}\cos\phi + \frac{1}{2}a(\Omega^2-1-\frac{3}{4}\eta a^2) + \mu\gamma b\big(\xi_2\Omega\sin(\phi-\theta) + \frac{\gamma}{2}(1+\frac{3}{4}\epsilon b^2)\cos(\phi-\theta)\big)\Big), \tag{7.12b}$$

$$b' = -\frac{1}{\Omega}\Big(\frac{a'\Omega}{2}\cos(\phi-\theta) - \frac{a\Omega^2+a\Omega\phi'}{2}\sin(\phi-\theta) + \gamma\xi_2 b\Omega\Big), \tag{7.12c}$$

$$\theta' = -\frac{1}{b\Omega}\Big(\frac{b\Omega^2}{2} + \frac{a'\Omega}{2}\sin(\phi-\theta) + \frac{a\Omega^2+a\Omega\phi'}{2}\cos(\phi-\theta) - \frac{\gamma^2 b}{2}(1+\frac{3}{4}\epsilon b^2)\Big). \tag{7.12d}$$

In steady-state motion, the derivatives of response amplitudes and phase angles vanish, i.e., $a' = \phi' = b' = \theta' = 0$, so that Eqs. (7.12) are transformed into

$$\frac{f_0}{2}\sin\phi + \xi_1 a\Omega + \mu\gamma b\big(-\xi_2\Omega\cos(\phi-\theta) + \frac{\gamma}{2}(1+\frac{3}{4}\epsilon b^2)\sin(\phi-\theta)\big) = 0, \tag{7.13a}$$

$$\frac{f_0}{2}\cos\phi + \frac{1}{2}a(\Omega^2-1-\frac{3}{4}\eta a^2) + \mu\gamma b(\xi_2\Omega\sin(\phi-\theta) + \frac{\gamma}{2}(1+\frac{3}{4}\epsilon b^2)\cos(\phi-\theta)) = 0, \tag{7.13b}$$

$$-\frac{a\Omega^2}{2}\sin(\phi-\theta) + \gamma\xi_2 b\Omega = 0, \tag{7.13c}$$

$$\frac{a\Omega^2}{2}\cos(\phi-\theta) + \frac{b\Omega^2}{2} - \frac{\gamma^2 b}{2}(1+\frac{3}{4}\epsilon b^2) = 0. \tag{7.13d}$$

Simplifying (7.13c) and (7.13d) to eliminate the phase angles, we obtain

$$a^2\Omega^4 = (2\gamma\xi_2 b\Omega)^2 + b^2(\gamma^2 - \Omega^2 + \frac{3}{4}\epsilon\gamma^2 b^2)^2. \tag{7.14}$$

Similarly, substituting the terms with phase angles in Eqs. (7.13a) and (7.13b) by using Eqs. (7.13c) and (7.13d), we have

$$f_0^2 a^2 = 4\Omega^2(\gamma\mu\xi_2 b^2+\xi_1 a^2)^2+\Big(a^2(\Omega^2+\mu\Omega^2-1-\frac{3}{4}\eta a^2)+\mu b^2(\gamma^2+\frac{3}{4}\epsilon\gamma^2 b^2-\Omega^2)\Big)^2. \quad (7.15)$$

Thus, the relationship between steady-state response amplitudes of the systems and different parameters is governed by Eqs. (7.14) and (7.15), which are nonlinear algebraic equations. Note that the unknown a^2 can be expressed in terms of b^2 and other parameters using Eq. (7.14). A substitution of the resultant expression into Eq. (7.15) to replace a^2 yields a nonlinear equation of b^2, which can be solved by using a bisection algorithm (see, for example, Press et al. (1992)). The solutions provide first-order approximations of the response amplitudes.

For a nonlinear system with parameters set as $\xi_1 = \xi_2 = 0.01, \eta = 0.01, \epsilon = 0.1, f = 0.2, \mu = 0.1, \gamma = 1.0$, Figure 7.2 compares the fourth-order Runge-Kutta numerical results of the response amplitudes with those obtained using the averaging method. A good agreement of these results is shown, which verifies the averaging formulations. In the figure, the stability of different solution branches is also shown. The procedure for stability analysis is provided in the following section.

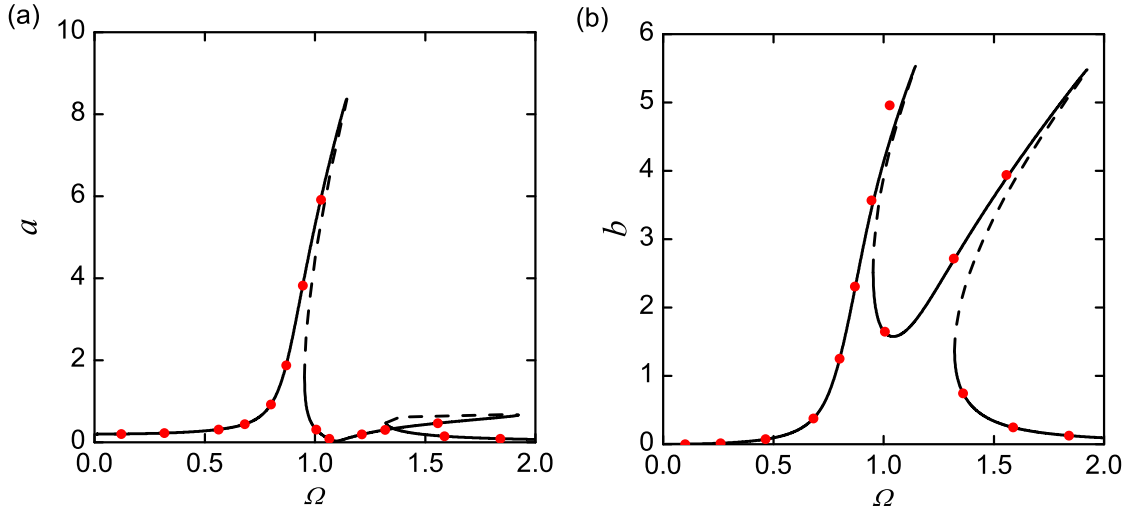

FIGURE 7.2: Verification of averaging formulations. Solid and dashed lines represent stable and unstable analytical solutions, respectively; dots denote numerical results.

7.2.2 Stability analysis

As shown in Figure 7.2, at some excitation frequencies, there may be more than one solution to Eqs. (7.14) and (7.15), i.e., non-unique steady-state responses may be encountered. In this situation, it is useful to perform stability analysis of the solutions as

only the stable ones are physically realisable and generally of more interest to engineering applications. To show the analysing process, Eqs. (7.12) are rewritten as

$$a' = u_1' = g_1(a, \phi, b, \theta), \tag{7.16a}$$

$$\phi' = u_2' = g_2(a, \phi, b, \theta), \tag{7.16b}$$

$$b' = u_3' = g_3(a, \phi, b, \theta), \tag{7.16c}$$

$$\theta' = u_4' = g_4(a, \phi, b, \theta), \tag{7.16d}$$

where

$$g_1 = -\frac{1}{\Omega}\Big(\frac{f_0}{2}\sin\phi + \xi_1 a\Omega + \mu\gamma b\big(-\xi_2\Omega\cos(\phi-\theta) + \frac{\gamma}{2}(1+\frac{3}{4}\epsilon b^2)\sin(\phi-\theta)\big)\Big), \tag{7.17a}$$

$$g_2 = -\frac{1}{a\Omega}\Big(\frac{f_0}{2}\cos\phi + \frac{1}{2}a(\Omega^2 - 1 - \frac{3}{4}\eta a^2) + \mu\gamma b\big(\xi_2\Omega\sin(\phi-\theta) + \frac{\gamma}{2}(1+\frac{3}{4}\epsilon b^2)\cos(\phi-\theta)\big)\Big), \tag{7.17b}$$

$$g_3 = -\frac{1}{\Omega}\Big(\frac{g_1\Omega}{2}\cos(\phi-\theta) - \frac{a\Omega^2 + ag_2\Omega}{2}\sin(\phi-\theta) + \gamma\xi_2 b\Omega\Big), \tag{7.17c}$$

$$g_4 = -\frac{1}{b\Omega}\Big(\frac{b\Omega^2}{2} + \frac{g_1\Omega}{2}\sin(\phi-\theta) + \frac{a\Omega^2 + ag_2\Omega}{2}\cos(\phi-\theta) - \frac{\gamma^2 b}{2}(1+\frac{3}{4}\epsilon b^2)\Big). \tag{7.17d}$$

Then the corresponding characteristic matrix of a solution $(a_s, \phi_s, b_s, \theta_s)$ to the frequency response relations (7.14) and (7.15) is

$$A = \begin{pmatrix} a_{11} & a_{12} & a_{13} & a_{14} \\ a_{21} & a_{22} & a_{23} & a_{24} \\ a_{31} & a_{32} & a_{33} & a_{34} \\ a_{41} & a_{42} & a_{43} & a_{44} \end{pmatrix}, \tag{7.18}$$

where $a_{ij} = \dfrac{\partial g_i}{\partial u_j}, (i, j = 1, 2, 3, 4)$. In the derivation process, the property that for any solution point $(a_s, \phi_s, b_s, \theta_s)$ the value of $g_i = 0 (i = 1, 2, 3, 4)$ can be used. The stability of the solution is then identified by examining the corresponding eigenvalues of the matrix A. If the eigenvalues all have negative real part, the solution will be stable. On the other hand, one of the eigenvalues is with a positive real part, the corresponding solution becomes unstable. Based on these, the stability of different solution branches for the system with $\xi_1 = \xi_2 = 0.01, \eta = 0.01, \epsilon = 0.1, f = 0.2, \mu = 0.1, \gamma = 1.0$ was assessed and indicated by different lines in Figure 7.2.

7.3 Power flow formulations

To assess the vibration absorption performance, the effects of the stiffness nonlinearity in the primary structure as well as in the absorber on the vibration power generation, dissipation, transmission and absorption should be clarified. In the following content, power flow variables as well kinetic energies of the system will be formulated using the previous averaging formulations.

7.3.1 Input power

The non-dimensional instantaneous input power into the system is the product of excitation with the corresponding velocity. In this system, there is only one excitation acting on mass m_1, so that we have

$$p_{in} = f_0 v_1 \cos\Omega\tau, \tag{7.19}$$

where v_1 is instantaneous velocity of the primary structure. When a first-order harmonic response is assumed, we have $v_1 = -a\Omega\sin(\Omega\tau+\phi)$. Consequently, the time-averaged input power is formulated by

$$\bar{p}_{in}(\Omega) = \frac{1}{T}\int_0^T p_{in}\,\mathrm{d}\tau \approx -\frac{f_0 a\Omega}{2}\sin\phi, \tag{7.20}$$

where the averaging time T was taken as $2\pi/\Omega$, a cycle of excitation. Replacing the trigonometric function $\sin\phi$ in Eq. (7.20) using the relations in Eqs. (7.13) and further simplifying, the time-averaged input power is expressed by

$$\bar{p}_{in}(\Omega) = \xi_1 a^2\Omega^2 + \mu\gamma\xi_2 b^2\Omega^2. \tag{7.21}$$

7.3.2 Transmitted power

It is useful to clarify the power transmission paths in the system. The power injected by the external excitation is partly transmitted downwards and dissipated by the damper c_1, while the rest is transmitted upwards through the nonlinear spring and damper c_2 to mass m_2. The instantaneous power transmitted to mass m_2 is product of the force acting upon it and the corresponding velocity, i.e.,

$$p_t = f_t v_2, \tag{7.22}$$

where $f_t = \mu\gamma(2\xi_2 y' + \gamma y + \epsilon\gamma y^3)$ is the transmitted force and $v_2 = x' + y'$ is the velocity of mass m_2. The time-averaged transmitted power to mass m_2 over an excitation cycle

is formulated by

$$\bar{p}_t(\Omega) = \frac{1}{T}\int_0^T p_t \, \mathrm{d}\tau. \tag{7.23}$$

Replacing the variables in the expressions of f_t and v_2 with their first-order analytical approximations and evaluating the integration in Eq. (7.23) yields

$$\bar{p}_t(\Omega) = \mu\gamma(\xi_2 ab\Omega^2 \cos(\phi-\theta) - \frac{\gamma ab\Omega}{2}(1+\frac{3}{4}\epsilon b^2)\sin(\phi-\theta) + \xi_2 b^2\Omega^2). \tag{7.24}$$

Using the relationships given by Eqs. (7.13) to eliminate the trigonometric functions, it can be shown that

$$\bar{p}_t(\Omega) = 0. \tag{7.25}$$

This expression indicates that there will be no net time-averaged power transmission to mass m_2 over a period of motion. This is accounted for by the fact that the mass is considered as a rigid body with no internal damping. Also, over an oscillation cycle, there will be no net change in its kinetic energy. According to the principle of energy balance, the total transmitted energy into mass m_2 should be zero in the time span.

7.3.3 Dissipated power

The dissipated power refers to the rate change of energy that turned into heat by damping. For the system under investigation, the total instantaneous dissipated power is

$$p_d = f_{d1}x' + f_{d2}y', \tag{7.26}$$

where $f_{d1} = 2\xi_1 x'$ and $f_{d2} = 2\mu\gamma\xi_2 y'$ are the damping forces of dampers c_1 and c_2, respectively. The first term in the equation represents power dissipated by the primary structure while the second denotes power dissipated by the absorber.

The time-averaged dissipated power over an excitation cycle is

$$\bar{p}_d(\Omega) = \frac{1}{T}\int_0^T p_d \, \mathrm{d}\tau. \tag{7.27}$$

Replacing velocities x' and y' with their first-order approximations described by Eqs. (7.7b) and (7.7d), the instantaneous dissipated power can be expressed in a first-order form, using which to complete the integration in Eq. (7.27) leads to

$$\bar{p}_d(\Omega) = \xi_1 a^2\Omega^2 + \mu\gamma\xi_2 b^2\Omega^2. \tag{7.28}$$

Comparing this equation with Eq. (7.21), it is clear that the expressions for $\bar{p}_{in}$ and $\bar{p}_d$ are exactly the same. This agrees with the principle of energy balance, i.e., over a cycle of oscillation, the input energy by the external excitation is all dissipated by damping while the system's kinetic and potential energies keep unchanged.

7.3.4 Absorbed power

The power absorbed by the dynamic vibration absorber equals the power dissipated by its damper c_2, and thus can be expressed by

$$p_a = f_{d2} y'. \tag{7.29}$$

Using averaging approximations, the time-averaged absorbed power over a cycle of oscillation is

$$\bar{p}_a(\Omega) = \frac{1}{T}\int_0^T p_a \, \mathrm{d}\tau = \mu\gamma\xi_2 b^2\Omega^2. \tag{7.30}$$

For efficient vibration absorption, the value of $\bar{p}_a(\Omega)$ needs to be large, compared the time-averaged input power.

7.3.5 Maximum kinetic energies

In steady-state motion, the maximum kinetic energy of mass m_1 corresponds to the maximum velocity

$$K_1 = \frac{1}{2}(|v_1|_{max})^2 \approx \frac{1}{2}a^2\Omega^2. \tag{7.31}$$

where a first-order approximation of the velocity $v_1 = -a\Omega\sin(\Omega\tau + \phi)$ was used with its amplitude being $|v_1|_{max} = a\Omega$.

Referring to Eqs. (7.7b) and (7.7d), the velocity of the absorber mass m_2 is expressed as

$$v_2 = x' + y' = -a\Omega\sin(\Omega\tau + \phi) - b\Omega\sin(\Omega\tau + \theta), \tag{7.32}$$

and its amplitude is

$$|v_2|_{max} = \Omega\sqrt{(a^2 + b^2) + 2ab\cos(\phi - \theta)}. \tag{7.33}$$

The trigonometric term $\cos(\phi - \theta)$ in Eq. (7.33) may be replaced using relations in Eq. (7.13d), by which the expression for the maximum kinetic energy of mass m_2 is found to be

$$K_2 = \frac{1}{2}\mu(|v_2|_{max})^2 = \frac{1}{2}\mu(a^2 - b^2)\Omega^2 + \mu\gamma^2 b^2(1 + \frac{3}{4}\epsilon b^2). \tag{7.34}$$

As its fundamental role of a vibration absorber is to reduce the steady-state response of the primary structure, its kinetic energy K_1 may be used as a criteria for performance assessment of the nonlinear vibration absorbers.

7.4 Case studies for the absorber performance

7.4.1 A nonlinear absorber attached to a linear primary structure

Here, vibration mitigation of a harmonically-excited linear primary structure ($\eta = 0$) by using a nonlinear absorber with $\epsilon \neq 0$ is considered. To examine the effects of the stiffness nonlinearity in the dynamic absorber on vibration power input and absorption, the nonlinear coefficient ϵ varies from -0.01 indicating softening stiffness, to 0.5, for a hardening stiffness absorber. The results for the linear absorber case of $\epsilon = 0$ are also provided for comparison. Other system parameters are set as $\xi_1 = 0.01, \xi_2 = 0.01, \eta = 0, \mu = 0.1, \gamma = 1.0, f_0 = 0.2$ and power flow quantities are shown in a decibel scale with the dB reference set as 10^{-12} throughout this chapter. Also, in the remaining figures of this chapter, the lines represent analytical approximate results while the symbols denote numerical solutions based on the fourth-order Runge-Kutta method. Figures 7.3, 7.4 and 7.5 show the variations of time-averaged input and absorbed powers, the kinetic energies as well as the response amplitudes. Some influences of the introduced stiffness nonlinearity in the absorber on power flows of the system are observed:

- Nonlinear stiffness in the absorber results in bending of the peaks in the curves of time-averaged power flows as well as kinetic energies. As shown in Figures 7.3 and 7.4, the peaks are bent either towards the low-frequency range when the absorber processes a softening stiffness with $\epsilon < 0$, or towards the high frequencies when the stiffness is of a hardening type ($\epsilon > 0$). This characteristic may reduce the effectiveness of vibration absorbers as the amount of time-averaged power flow at the expected functioning frequency $\Omega = 1$ of the absorber may become multiple-valued and large.

- Associated with the bending of the curves, there are changes in the peak values of time-averaged power flows as well as kinetic energies. For the softening absorber case of $\epsilon = -0.01$, the second peak encountered at a high excitation frequency in time-averaged input power $\bar{p}_{in}$ and in the kinetic energy K_1 becomes much higher than that of corresponding linear system. However, the other peaks in the curves are suppressed. For the hardening absorber case of $\epsilon = 0.5$, the first peak values in the curves of $\bar{p}_{in}$ and K_1 are larger than those of the corresponding linear system. In contrast, the second peak values in $\bar{p}_{in}$ and K_1 and both the peaks in $\bar{p}_a$ and K_2 are reduced from the linear case.

- The twisting of curves also results in non-unique branches in some frequency ranges, indicating possible multiple solutions of power flows at a single excitation frequency.

- When the excitation frequency is away from the peak regions, the curves that correspond to different types of absorbers coincide with each other and the time-averaged power flows are not sensitive to variations of ϵ. It indicates that the stiffness nonlinearity has local but not global effects on the system's power flows.
- Adding a strong hardening stiffness of $\epsilon = 0.5$ can shift the local minimum point in the curves of $\bar{p}_{in}$ and K_1 to higher frequency range, which need to be taken into consideration in the application of nonlinear absorbers.

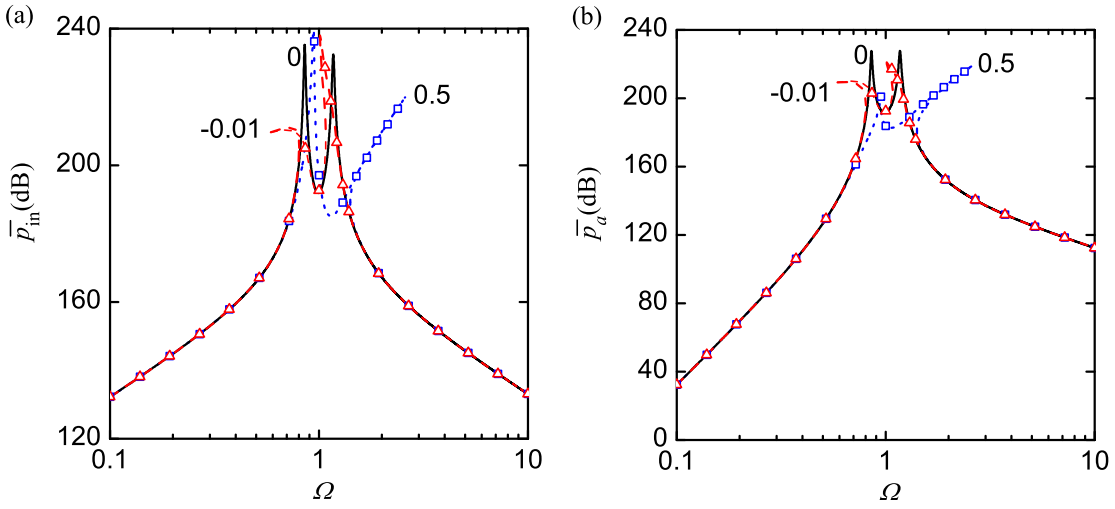

FIGURE 7.3: Time-averaged (a) input and (b) absorbed powers for system with a linear primary structure and an absorber with different nonlinear stiffness. Solid line: $\epsilon = 0$; dash line or triangles: $\epsilon = -0.01$; dotted line or squares: $\epsilon = 0.5$.

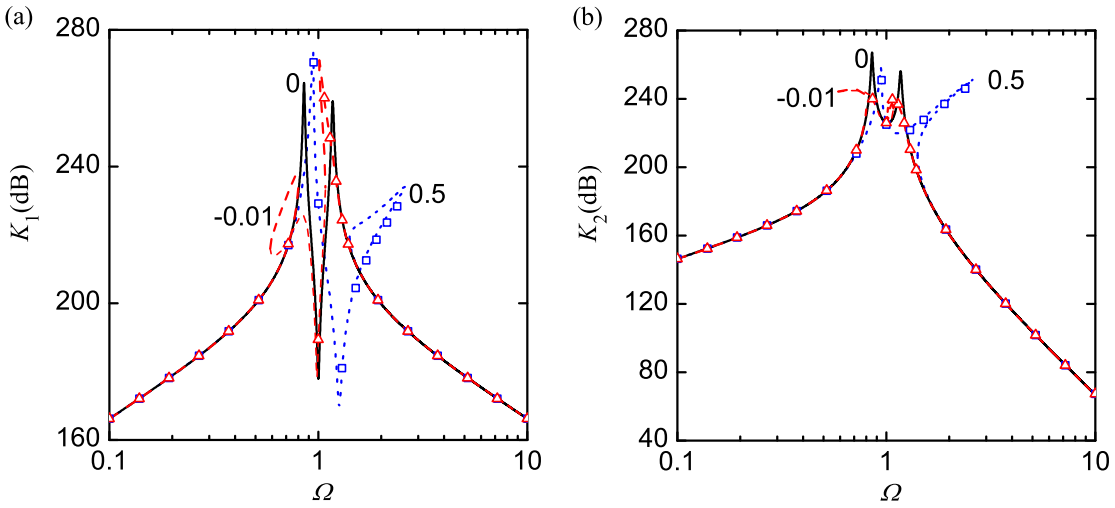

FIGURE 7.4: Kinetic energies (a) K_1 and (b) K_2 of systems with a linear primary structure and an absorber with different nonlinear stiffness. Solid line: $\epsilon = 0$; dash line or triangles: $\epsilon = -0.01$; dotted line or squares: $\epsilon = 0.5$.

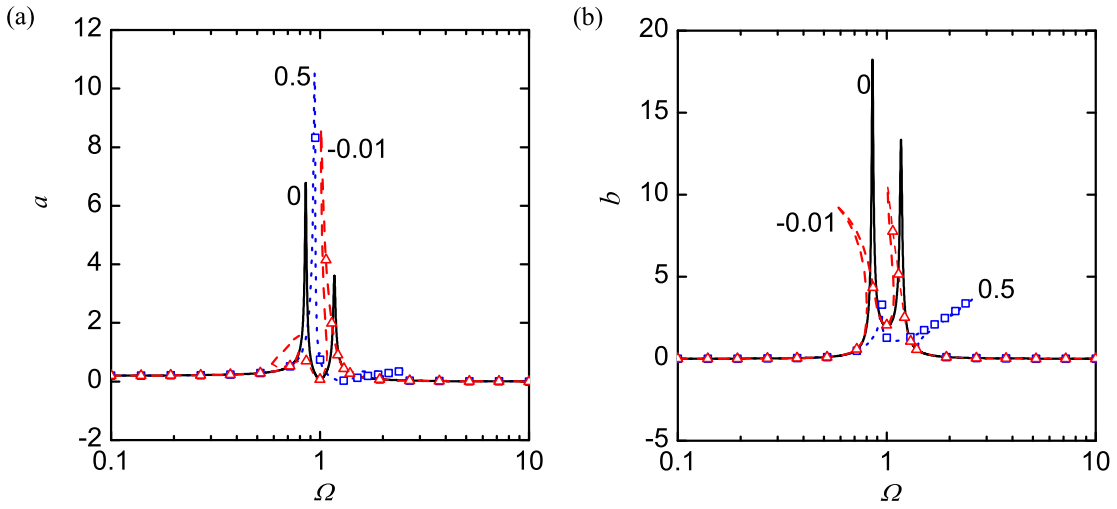

FIGURE 7.5: Response amplitudes (a) a and (b) b of systems with a linear primary structure and an absorber with different nonlinear stiffness. Solid line: $\epsilon = 0$; dash line or triangles: $\epsilon = -0.01$; dotted line or squares: $\epsilon = 0.5$.

Figure 7.5 shows that the response peaks are also bent towards either low or high frequencies, depending on the type of stiffness nonlinearities in the absorber. It shows that the addition of the softening stiffness absorber suppresses the first resonant peak of the primary structure. However, it leads to a higher second peak at a higher excitation frequency. A hardening stiffness of $\epsilon = 0.5$ reduces the second response peak of the primary structure, but its first peak value becomes larger than that of the corresponding linear system. Away from the peak regions, the response amplitudes are not sensitive to the variations of ϵ. This may arise from the fact that the response amplitudes are small in the non-resonant frequency ranges, so that the value of $\frac{3}{4}\epsilon b^2$ is much smaller than unity and can be neglected in Eqs. (7.14) and (7.15).

7.4.2 A linear absorber attached to a nonlinear primary structure

In engineering practice, vibrating devices are usually assumed to be functioning in the linear region, and on this basis linear vibration absorbers are designed and attached. Problems may arise from this design methodology when the primary structure actually contains significant nonlinearity. To address this, a special case of attaching a linear absorber with $\epsilon = 0$ to a nonlinear primary system is studied herein to reveal the effectiveness of the former when different types of stiffness nonlinearity exists in the primary structure. In Figures 7.6, 7.7 and 7.8, the nonlinear stiffness parameter of the base varies from $\eta = -0.05$ indicating a softening characteristic, to zero for a linear structure and then becomes $\eta = 0.1$ suggesting a structure of a hardening stiffness. The other parameters of the system are set as $\xi_1 = \xi_2 = 0.01, \mu = 0.1, \gamma = 1, f_0 = 0.2$.

Compared with the previous case of adding a nonlinear absorber to a linear primary structure, Figures 7.6 and 7.7 show that:

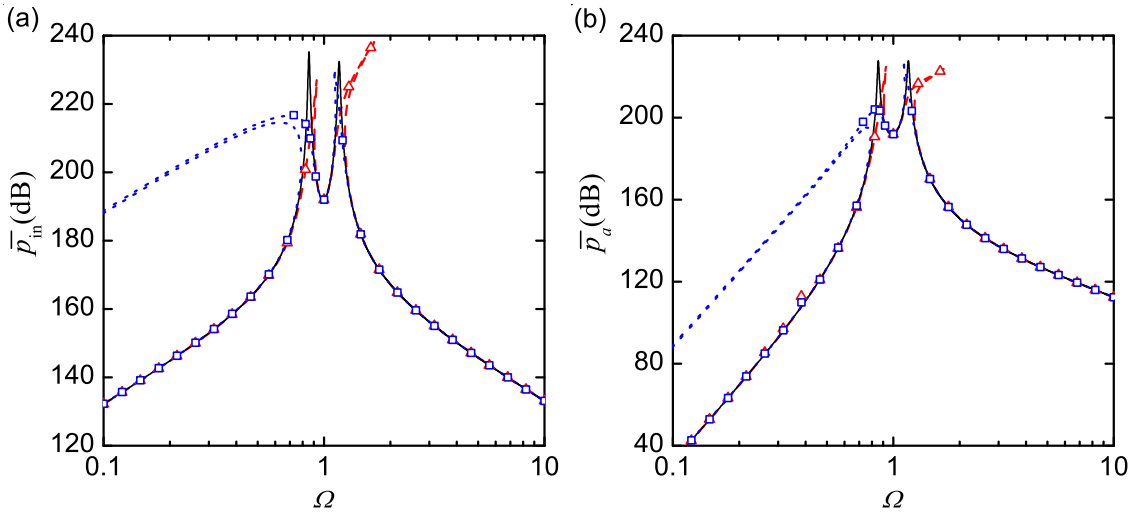

FIGURE 7.6: Time-averaged (a) input and (b) absorbed powers for systems with a linear absorber and a primary structure with different nonlinear stiffness. Solid line: $\eta = 0$; dashed line or triangles: $\eta = 0.1$; dotted line or squares: $\eta = -0.05$.

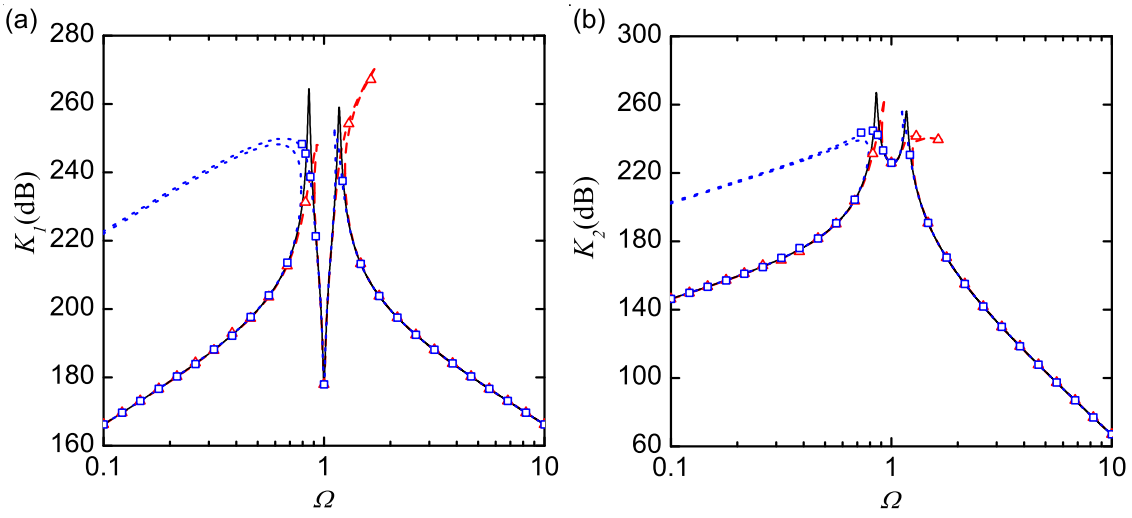

FIGURE 7.7: Kinetic energies (a) K_1 and (b) K_2 of systems with a linear absorber and a primary structure with different nonlinear stiffness. Solid line: $\eta = 0$; dashed line or triangles: $\eta = 0.1$; dotted line or squares: $\eta = -0.05$.

- Both peaks in each curve of time-averaged power flows and kinetic energies bend towards the same direction, either to the low or to the high frequency ranges, similar with the previous case shown in Figures 7.3 and 7.4.

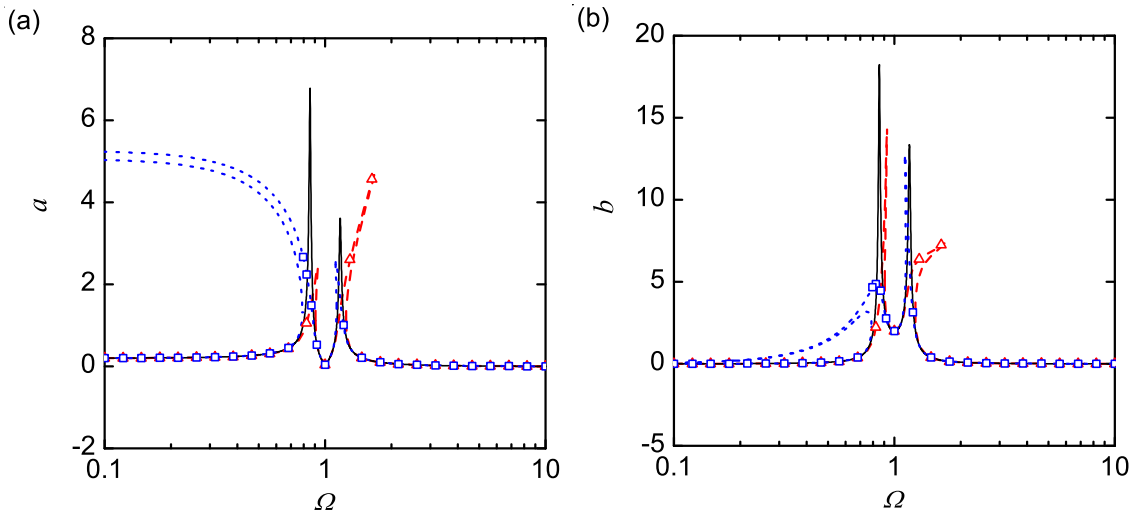

FIGURE 7.8: Response amplitudes (a) a and (b) b of systems with a linear absorber and a primary structure with different nonlinear stiffness. Solid line: $\eta = 0$; dashed line or triangles: $\eta = 0.1$; dotted line or squares: $\eta = -0.05$.

- In the low-frequency range, a softening stiffness in the primary structure can greatly reduce the first peaks in power flow and kinetic energy curves. A hardening stiffness can assist in attenuations of the first peaks, but may lead to higher second peak values in $\bar{p}_{in}$ and K_1.
- When the excitation frequency is far away from the peak regions, the time-averaged power flows and kinetic energies vary little with η.
- The bending of curves results in multiple solutions. More importantly, if nonlinearity is strong enough, at the desired function frequency $\Omega = 1$ of the absorber, there may be non-unique and potentially high levels of power flows. This will jeopardize effective vibration absorption of the primary structure.

The variations of response amplitudes are shown in Figure 7.8. It's seen that the response amplitudes near the peak frequencies are significantly altered by the nonlinearity, but remain almost unchanged for different values of η in other frequency ranges. Again, this is due to small-amplitude oscillations in these frequency ranges, as the corresponding terms with the nonlinear stiffness parameter η can be neglected in the frequency-response relations, described by Eqs. (7.14) and (7.15).

7.4.3 Nonlinear absorbers attached to a softening primary structure

The previous two cases in Sections 7.4.1 and 7.4.2 considered existence of stiffness nonlinearity either in the primary system or the absorber. Since the motions of the two masses are coupled, it is necessary to examine the interaction effects of stiffness nonlinearity

in the absorber and that in the primary structure. The outcome of such investigations may provide guidance for a proper design of the absorber's nonlinearity, with respect to the existing nonlinearity in the primary structure. For clarity, this section considers a softening primary structure attached with a hardening/softening nonlinear absorber, while the next section will focus on vibration absorption of a hardening stiffness primary structure using nonlinear absorbers.

Figures 7.9, 7.10 and 7.11 show the variations of time-averaged power flows, kinetic energies and response amplitudes of a system with $\xi_1 = \xi_2 = 0.01, \mu = 0.1, \gamma = 1, f_0 = 0.2, \eta = -0.02$. The primary structure is of softening stiffness while the absorber possesses softening stiffness when $\epsilon = -0.01$ or hardening stiffness when $\epsilon = 0.1$. The results for a linear absorber case with $\epsilon = 0$ are also provided for comparison.

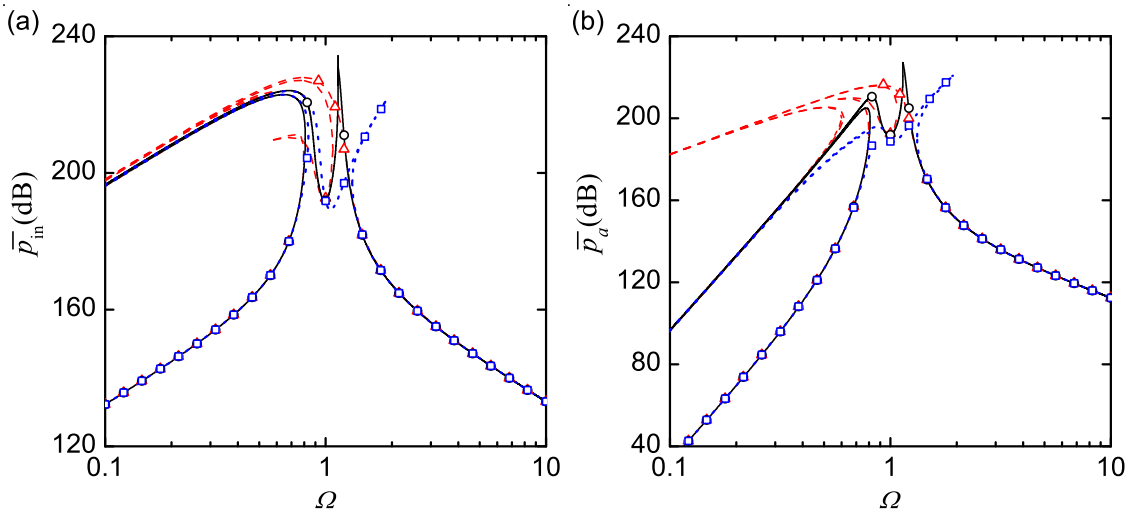

FIGURE 7.9: Time-averaged (a) input and (b) absorbed powers for systems with a softening primary structure and a nonlinear absorber. Solid line or circles: $\epsilon = 0$; dashed line or triangles: $\epsilon = -0.01$; dotted line or squares: $\epsilon = 0.1$.

The figures show that the first peak in each curve of the linear absorber case bends significantly to the low-frequency range. Compared with that, attaching the softening stiffness absorber of $\epsilon = -0.01$ to the softening stiffness primary structure strengthens the overall softening nonlinearity of the system, demonstrated by the further twisting of both peaks to the low-frequency range. This also results in multiple solutions of power flow variables over a larger range of excitation frequencies, including the original tuning frequency $\Omega = 1$ of a linear absorber. Thus, for reducing the vibrations of a softening primary structure, the use of softening stiffness absorbers may be undesirable. In contrast, adding a hardening stiffness absorber of $\epsilon = 0.1$ to the softening primary structure bends the second peak in the power flow curves to the high-frequency range while keeping the first peak extended to the low-frequency range. The second peak values in time-averaged power flows and kinetic energies are greatly reduced. Also, the power

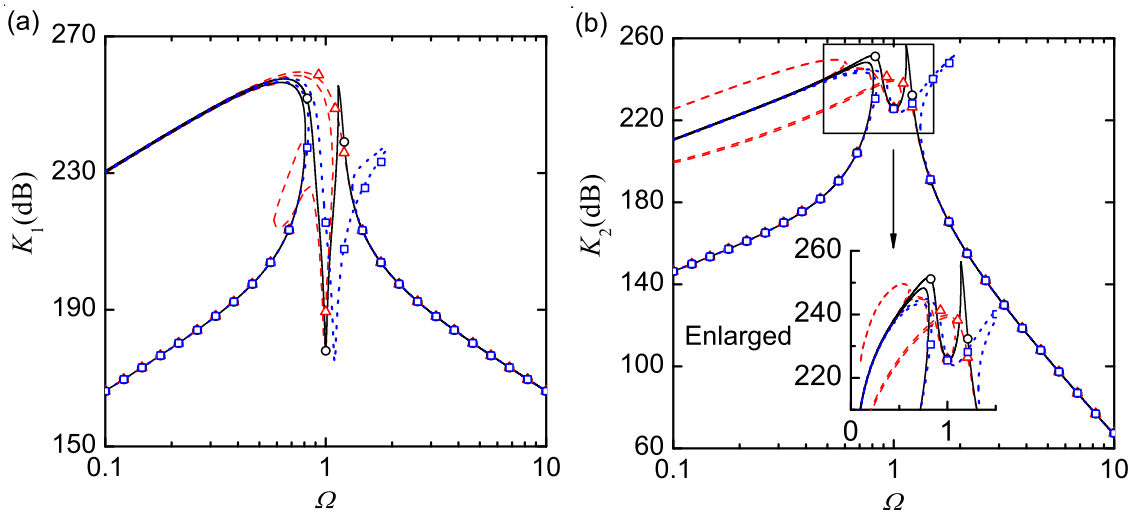

FIGURE 7.10: Kinetic energies (a) K_1 and (b) K_2 of systems with a softening primary structure and a nonlinear absorber. Solid line or circles: $\epsilon = 0$; dashed line or triangles: $\epsilon = -0.01$; dotted line or squares: $\epsilon = 0.1$.

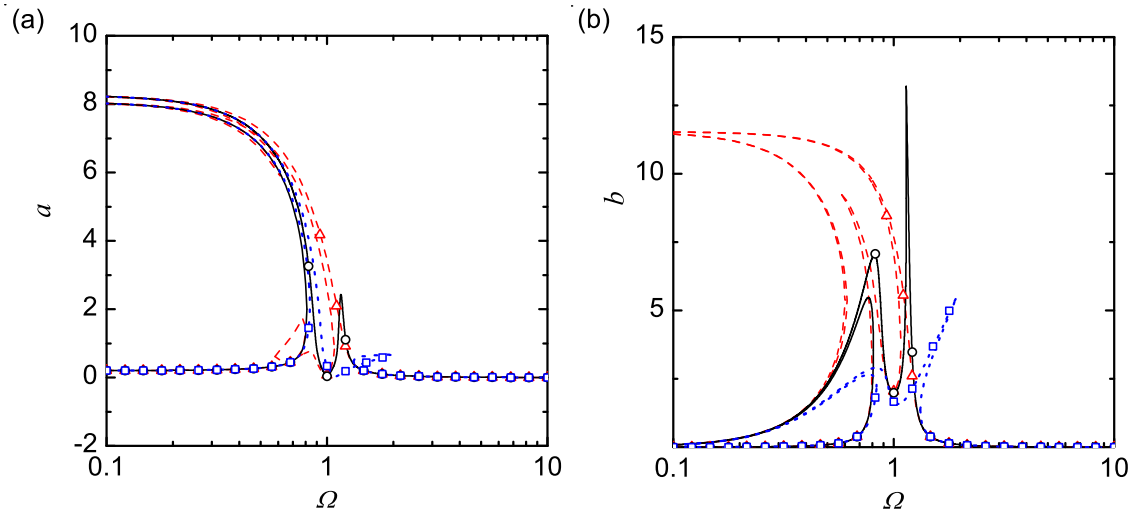

FIGURE 7.11: Response amplitudes (a) a and (b) b of systems with a softening primary structure and a nonlinear absorber. Solid line or circles: $\epsilon = 0$; dashed line or triangles: $\epsilon = -0.01$; dotted line or squares: $\epsilon = 0.1$.

flow variables and kinetic energies are single-valued and small at the tuning frequency $\Omega = 1$. Thus, hardening stiffness absorbers may be used for vibration absorption of softening primary structures.

Figure 7.11 shows the corresponding variations of response amplitudes. It is observed that adding a softening absorber to the softening primary structure can deteriorate vibration absorption by introducing multiple solutions at $\Omega = 1$. A hardening stiffness absorber, however, greatly reduces the second response peak of the primary structure.

7.4.4 Nonlinear absorbers attached to a hardening primary structure

In this section, the performance of different types of nonlinear absorbers in suppressing the vibrations of a hardening primary structure is investigated. For a system with $\xi_1 = \xi_2 = 0.01, \mu = 0.1, \gamma = 1, f_0 = 0.2, \eta = 0.05$, the nonlinear stiffness parameter ϵ of the absorber is set as -0.01 for a softening stiffness absorber and 0.1 for a hardening stiffness absorber. The variations of power flow variables, kinetic energies and response amplitudes are shown in Figures 7.12, 7.13 and 7.14, respectively. For comparison, the results for the system with a linear absorber with $\epsilon = 0$ attached to the hardening primary structure are also provided in the figures.

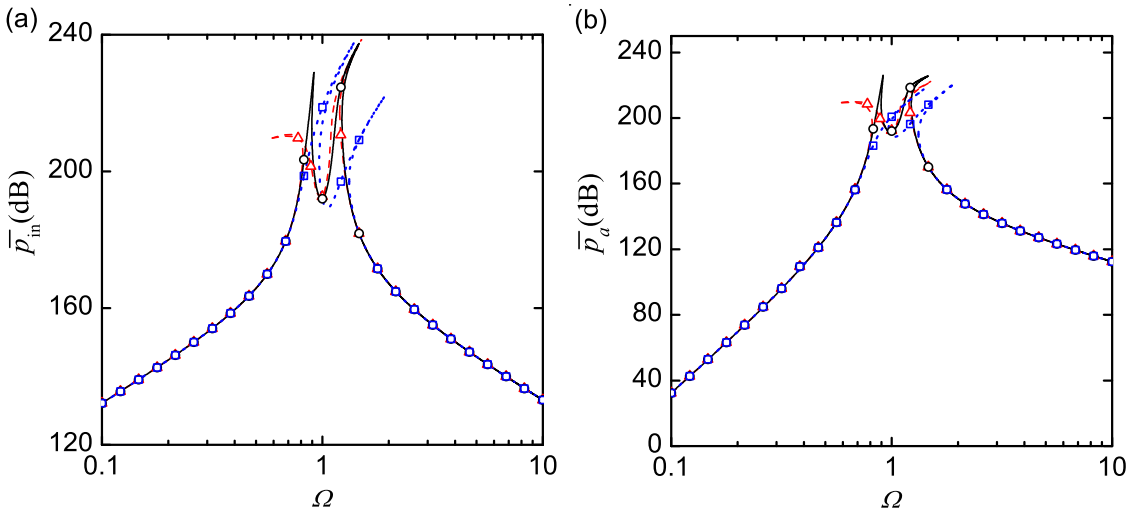

FIGURE 7.12: Time-averaged (a) input and (b) absorbed powers for systems with a hardening primary structure and a nonlinear absorber. Solid line or circles: $\epsilon = 0$; dashed line or triangles: $\epsilon = -0.01$; dotted line or squares: $\epsilon = 0.1$.

The figures show that the peaks in the corresponding curves of the linear absorber case bend slightly to the high-frequency range. In comparison, an introduction of a hardening stiffness absorber to the hardening primary structure yields further bending of the peaks to the higher frequencies. The figures show that multiple solutions exist in a larger range of excitation frequencies, including the tuning frequency $\Omega = 1$ of the corresponding linear absorber. This characteristic is not desirable for the application of vibration absorbers. It's shown that the first peaks in time-averaged input power $\bar{p}_{in}$ and kinetic energy K_1 curves are much higher than those of the linear absorber case. The second peaks values in the curves become lower.

The use of the softening stiffness absorber to the hardening primary structure, however, bends first peaks towards the low-frequency range. The second peaks remain bent to the high frequencies. In this way, the dynamic responses of the system, including power flow variables and kinetic energies, remain single-valued at the tuning frequency of $\Omega = 1$.

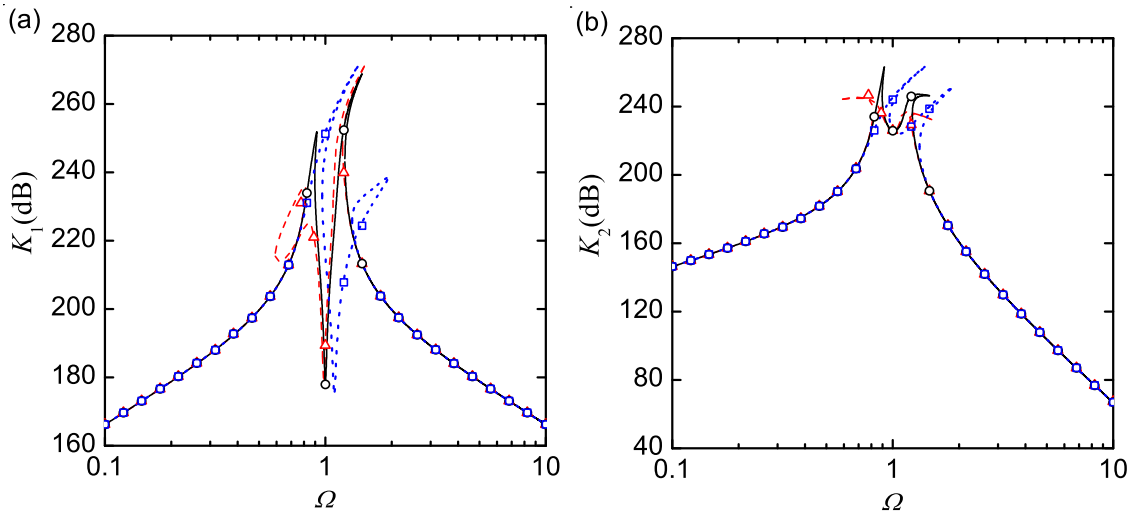

FIGURE 7.13: Kinetic energies (a) K_1 and (b) K_2 of systems with a hardening primary structure and a nonlinear absorber. Solid line or circles: $\epsilon = 0$; dashed line or triangles: $\epsilon = -0.01$; dotted line or squares: $\epsilon = 0.1$.

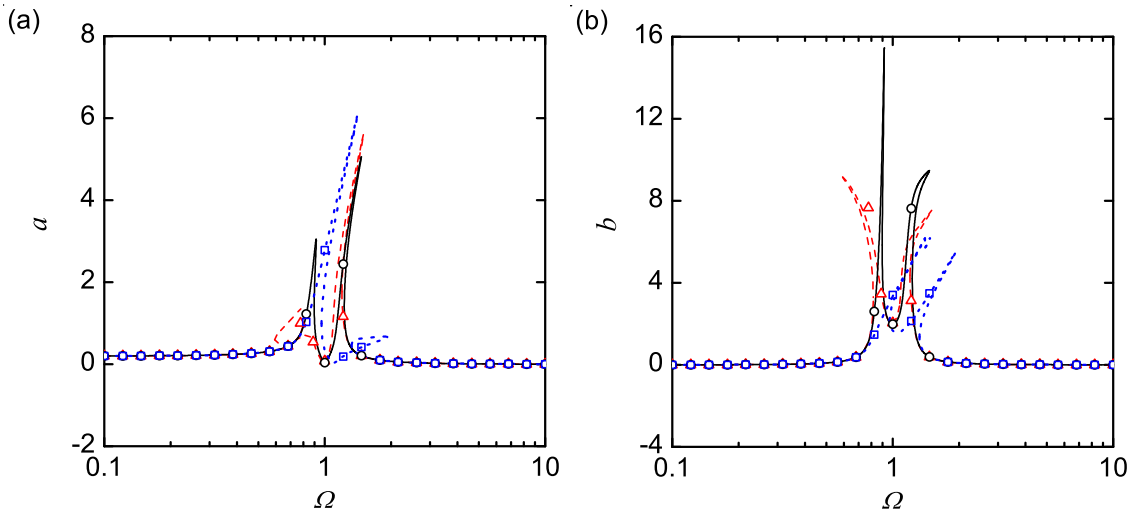

FIGURE 7.14: Response amplitudes (a) a and (b) b of systems with a hardening primary structure and a nonlinear absorber. Solid line or circles: $\epsilon = 0$; dashed line or triangles: $\epsilon = -0.01$; dotted line or squares: $\epsilon = 0.1$.

It is also observed that the first peaks of the curves are suppressed, creating a larger frequency band of effective vibration absorption. These characteristics clearly demonstrate the benefits of using a softening stiffness absorber when the primary structure is of a hardening stiffness.

Figure 7.14 provides the corresponding variations of the response amplitudes, subject to changes of the nonlinear stiffness parameter of the absorber. It shows that a hardening stiffness absorber can assist in suppression of the second response peak, while a softening stiffness absorber significantly alleviates the first response peak value.

7.4.5 Effects of other parameters

In this section, the influences of different parameters including the mass ration μ, frequency ratio γ and the linear damping coefficient ξ_2 of the absorber, on power flow characteristics of the two-DOF vibration absorption system are investigated.

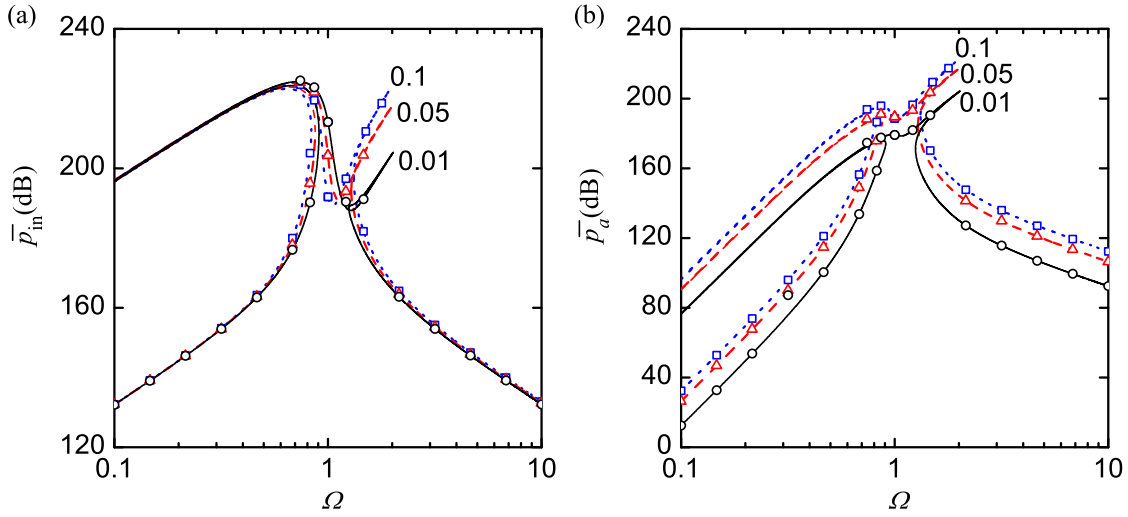

FIGURE 7.15: Time-averaged (a) input and (b) absorbed powers for systems with different mass ratio μ. Solid line or circles: $\mu = 0.01$; dashed line or triangles: $\mu = 0.05$; dotted line or squares: $\mu = 0.1$.

For a system with parameters set as $\xi_1 = \xi_2 = 0.01, \epsilon = 0.1, \eta = -0.02, \gamma = 1, f_0 = 0.2$, i.e., a softening primary structure attached with a hardening absorber, Figures 7.15, 7.16 and 7.17 show the influences of mass ratio μ on power flows, kinetic energies as well as the response amplitudes. It is observed that as μ increases from 0.01 to 0.05 and then to 0.1, the time-averaged input power is mainly affected in a small band of excitation frequencies close to the second peak with the peak value increasing with μ. However, there are large variations of the time-averaged absorbed power over a large range of excitation frequencies, with its value increasing with μ.

Figure 7.16(a) shows that there are substantial changes in kinetic energy K_1 of the primary structure when the excitation frequency locates in between the first and the second peak frequencies. Its second peak value increases with the mass ratio μ. Figure 7.16(b) shows that the variations of the absorber's kinetic energy K_2 are of a similar pattern with the time-averaged power absorption, with the kinetic energy increasing with μ over a large frequency range.

Figure 7.17 shows the response amplitudes are also affected by the mass ratio in a small range of excitation frequencies close to or in between the resonant peaks. It is seen that the second response peak of the primary structure increases with μ. When the

excitation frequency is close to unity, the response amplitudes increase as the mass ratio μ decreases.

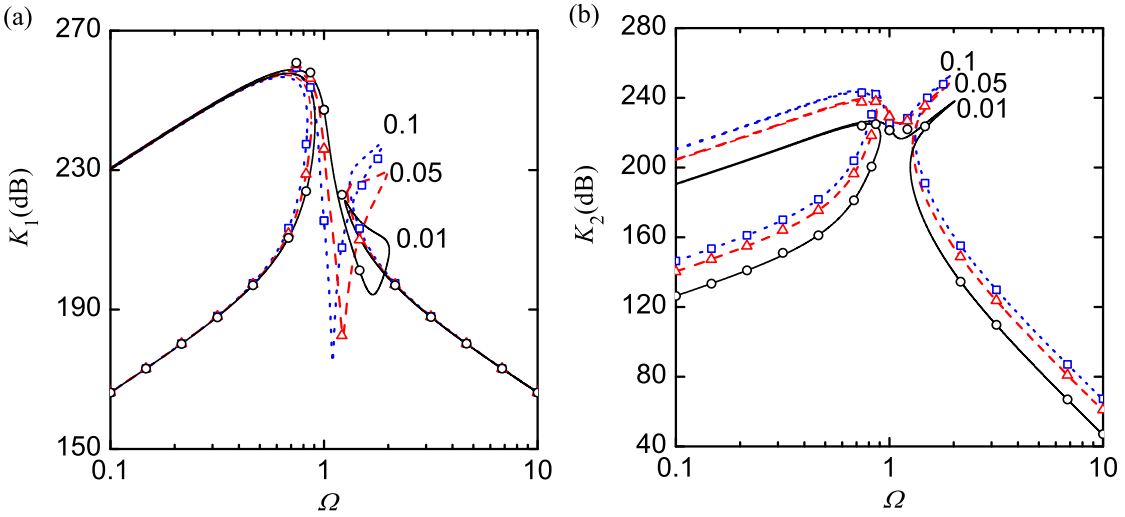

FIGURE 7.16: Kinetic energies (a) K_1 and (b) K_2 of systems with different mass ratio μ. Solid line or circles: $\mu = 0.01$; dashed line or triangles: $\mu = 0.05$; dotted line or squares: $\mu = 0.1$.

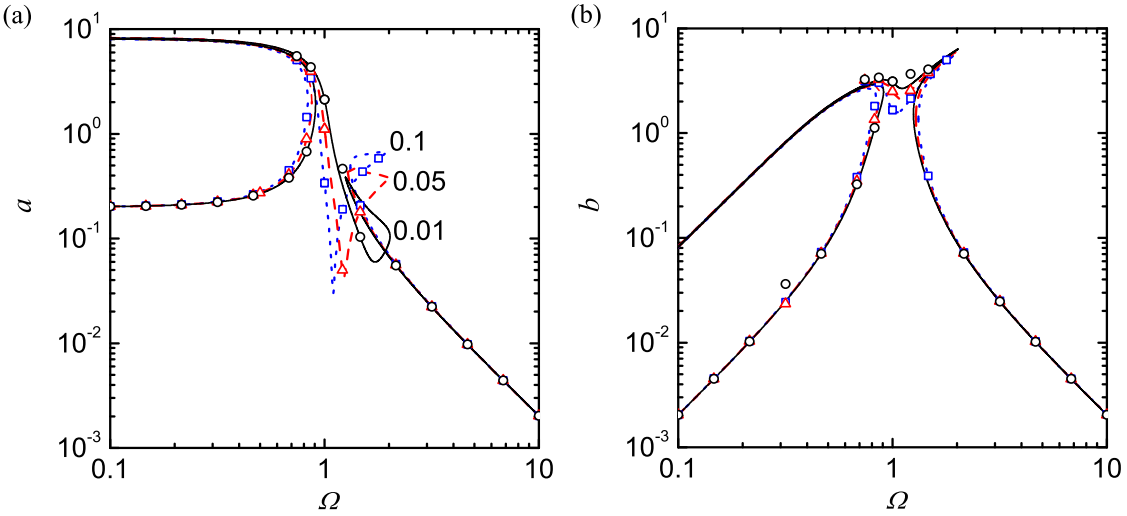

FIGURE 7.17: Response amplitudes (a) a and (b) b of systems with different mass ratio μ. Solid line or circles: $\mu = 0.01$; dashed line or triangles: $\mu = 0.05$; dotted line or squares: $\mu = 0.1$.

Figures 7.18, 7.19 and 7.20 examine the effects of the frequency ratio γ by setting the other parameters as $\xi_1 = \xi_2 = 0.01, \mu = 0.1, \eta = -0.02, \epsilon = 0.1, f_0 = 0.2$ for a system with a softening stiffness primary structure and a hardening stiffness absorber. The results show that decreasing the frequency ratio γ can shift the local minimum point in the curves of time-averaged power flows and kinetic energies to lower frequencies. It

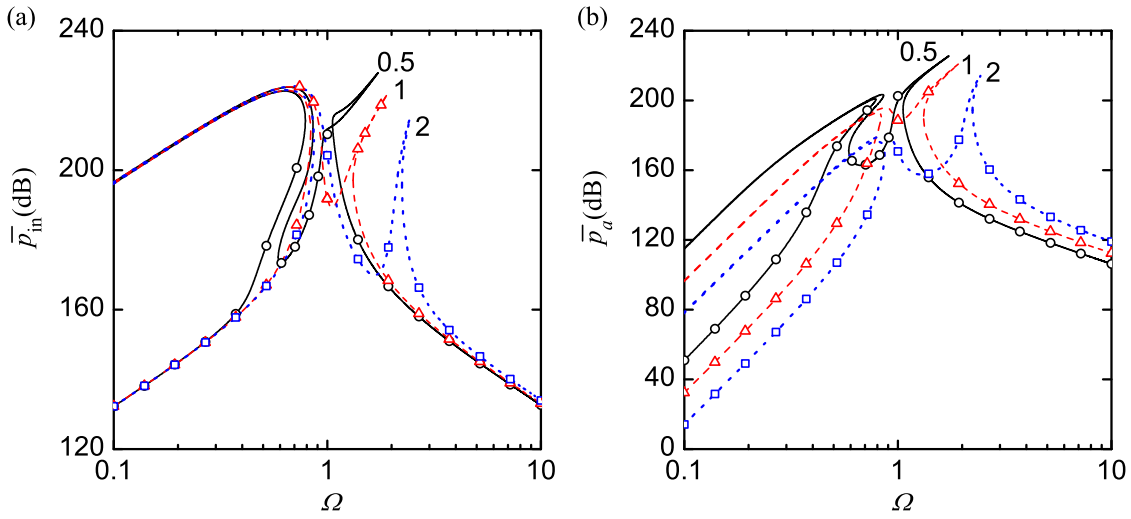

FIGURE 7.18: Time-averaged (a) input and (b) absorbed powers for systems with different frequency ratio γ. Solid line or circles: $\gamma = 0.5$; dashed line or triangles: $\gamma = 1$; dotted line or squares: $\gamma = 2$.

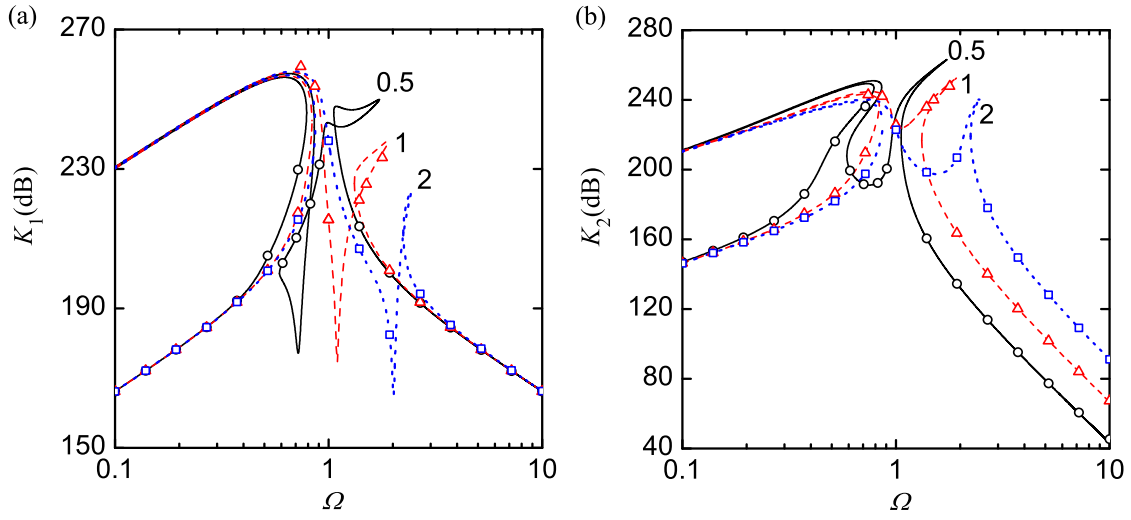

FIGURE 7.19: Kinetic energies (a) K_1 and (b) K_2 of systems with different frequency ratio γ. Solid line or circles: $\gamma = 0.5$; dashed line or triangles: $\gamma = 1$; dotted line or squares: $\gamma = 2$.

is observed that the variations in γ have a strong influence on $\bar{p}_{in}$ and K_1 when the excitation frequency is close to the peak frequencies. It's seen that the second peak values of time-averaged power flows and kinetic energies decrease with an increasing γ. The level of power absorption changes significantly over the examined frequency range. At high excitation frequencies, the value of $\bar{p}_a$ increases with the frequency ratio. However, in the low-frequency range, it decreases with as γ changes from 0.5 to 1, and then to 2. Figure 7.19 (b) shows that the kinetic energy K_2 of the absorber increases with γ, but becomes not sensitive to its variation in the low-frequency range.

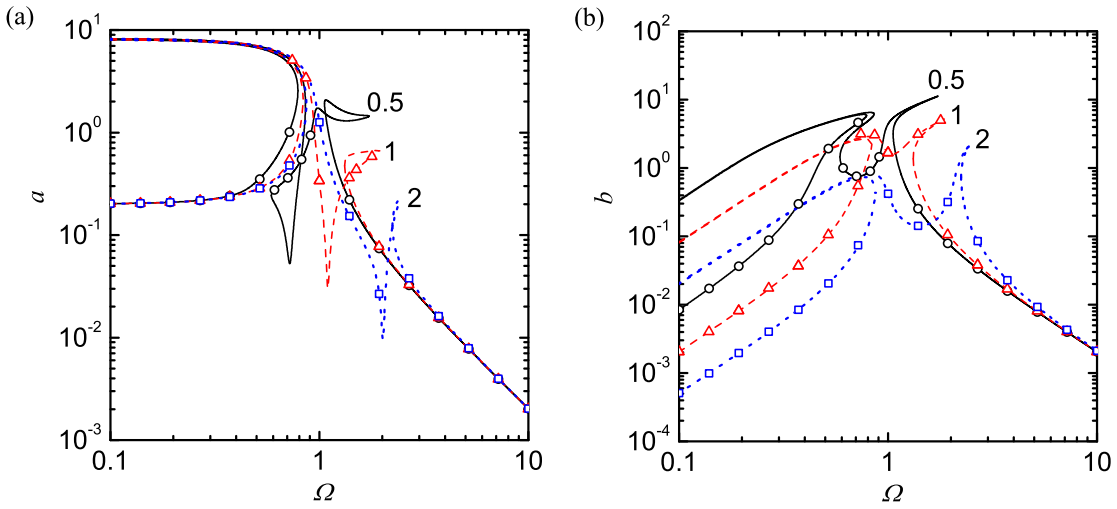

FIGURE 7.20: Response amplitudes (a) a and (b) b of systems with different frequency ratio γ. Solid line or circles: $\gamma = 0.5$; dashed line or triangles: $\gamma = 1$; dotted line or squares: $\gamma = 2$.

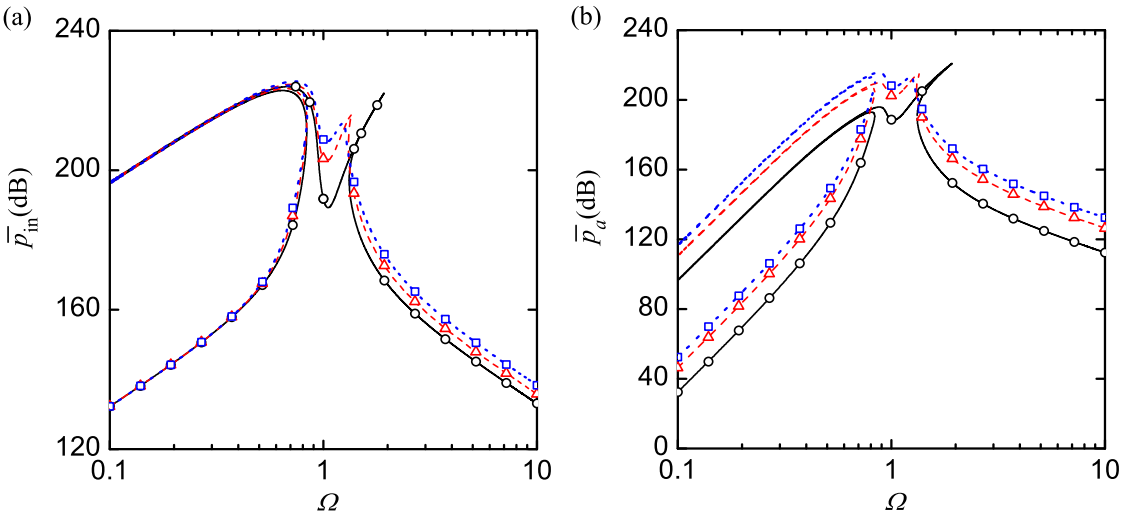

FIGURE 7.21: Time-averaged (a) input and (b) absorbed powers for systems with different absorber linear damping. Solid line or circles: $\xi_2 = 0.01$; dashed line or triangles: $\xi_2 = 0.05$; dotted line or squares: $\xi_2 = 0.1$.

Figure 7.20(a) shows that the response amplitude a of the primary structure is sensitive to the frequency ratio when the excitation frequency Ω is close to the resonant frequencies. In the high or low frequency range, its value changes little irrespective of the variations in γ. In comparison, Figure 7.20(b) shows that the relative response amplitude b of the absorber changes significantly in the low-frequency range. When the excitation frequency is large, the value of b becomes much less sensitive to γ, as the curves for different cases tend to emerge.

In Figures 7.21,7.22 and 7.23, the influences of the damping coefficient ξ_2 of the absorber

on time-averaged power flows, kinetic energies as well as response amplitudes are investigated. The examined system with $\xi_1 = 0.01, \epsilon = 0.1, \eta = -0.02, \mu = 0.1, \gamma = 1, f_0 = 0.2$ possesses softening stiffness in the primary structure but hardening stiffness in the absorber. The results show that although the second peak in $\bar{p}_{in}$ curve is suppressed by increasing the absorber's damping, the amount of time-averaged input power increases with ξ_2 over a wide band of frequencies. Similarly, Figure 7.21(b) suggests that there will generally be more power absorption if heavier damping exists in the nonlinear absorber.

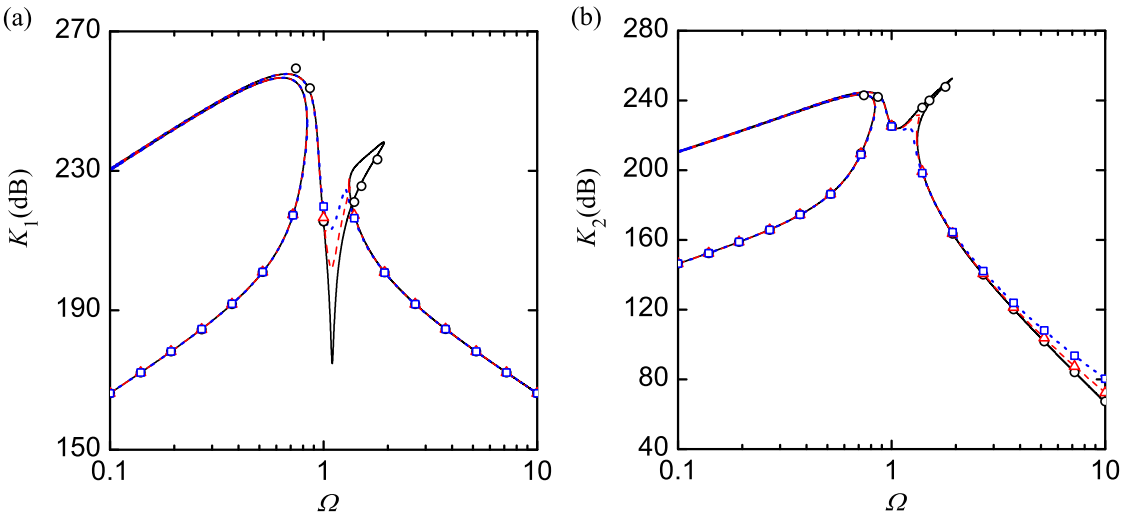

FIGURE 7.22: Kinetic energies (a) K_1 and (b) K_2 of systems with different absorber linear damping. Solid line or circles: $\xi_2 = 0.01$; dashed line or triangles: $\xi_2 = 0.05$; dotted line or squares: $\xi_2 = 0.1$.

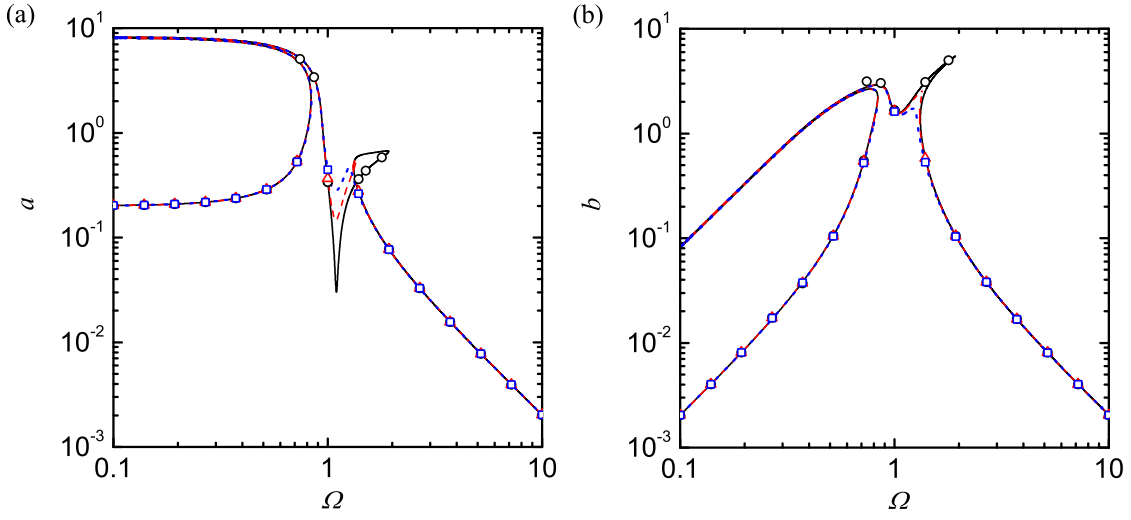

FIGURE 7.23: Response amplitudes (a) a and (b) b of systems with different absorber linear damping. Solid line or circles: $\xi_2 = 0.01$; dashed line or triangles: $\xi_2 = 0.05$; dotted line or squares: $\xi_2 = 0.1$.

For the effects of ξ_2 on kinetic energies of the system, it is shown in Figure 7.22 that the second peaks in the curves of kinetic energies K_1 and K_2 are suppressed by increasing the absorber's damping. However, between the peak frequencies, an increase in the damping also leads to larger kinetic energy K_1 of the primary structure, which is undesirable for vibration absorption. Figure 7.23 shows that there are large changes in the response amplitude a of the primary structure and relative response amplitude b of the absorber when Ω is close to the second resonant frequency. In the high or low frequency ranges away from the peak frequencies, the response amplitudes are not sensitive to the linear damping coefficient ξ_2 of the absorber.

7.5 Conclusions

The power flow behaviour of a two degrees-of-freedom nonlinear vibration absorption system has been investigated. Stiffness nonlinearity was considered to exist in the absorber and/or in the primary structure. The method of averaging was used to derive analytical approximate formulations of time-averaged power flow variables as well as kinetic energies of the system. Numerical simulations were carried out to verify the averaging approximations. Different combinations of the stiffness nonlinearity in the absorber and primary structure were investigated to examine the effectiveness of the nonlinear vibration absorbers. It was found that

- If the stiffness nonlinearity only exists either in the absorber or in the primary structure, the peaks in each time-averaged power flow curve bend towards the same frequency ranges. This behaviour may undermine the capacity of vibration absorption as there may be non-unique time-averaged power flow levels at a desired functioning frequency of the absorber;
- Adding a softening stiffness absorber to a softening stiffness primary structure may worsen the vibration absorption performance as it can result in multiple solution branches in a large band of frequencies. In comparison, attaching a hardening absorber provides benefits by creating a wide frequency range where the time-averaged power flows remain low and single-valued at each excitation frequency;
- Similarly, introducing a hardening stiffness absorber to a hardening stiffness primary structure can also create a large frequency band of multiple solutions. In contrast, a softening stiffness absorber assists in vibration mitigation by bending the peaks in time-averaged power flows towards different frequency ranges, so that effective vibration absorption can be achieved in a wider range of excitation frequencies;

- Variations of the mass ratio μ or the frequency ratio γ can result in substantial changes in the time-averaged input power over a large range of excitation frequencies. In comparison, the kinetic energy K_1 of the primary structure is sensitive to μ and γ only when the excitation frequency Ω locates close to or in between the peak frequencies.

Chapter 8

Power flow analysis of a nonlinear flapping foil energy harvesting system

As demonstrated in Chapter 5, the unforced Van der Pol oscillator is able to extract external energy at small oscillation amplitudes and dissipate energy when the displacement is large to sustain a stable limit cycle oscillation. The power flow characteristic of this nonlinear oscillator provides insights for designs of energy harvesting devices by using flow-induced vibrations. In this chapter, a nonlinear flapping foil system is proposed to harness energy from air flows. With two coupled equations governing its dynamics in heave and pitch motions, this system can absorb the flow energy to generate a bending-torsion flutter when the flow velocity exceeds a critical speed (see, for example, Bisplinghoff et al. (1955); Fung (1969)). Nonlinear stiffness models are introduced in both degrees-of-freedom of the system to avoid divergence when the flow velocity exceeds the critical speed. An electro-magnetic power generation unit is used to convert the mechanical energy imported from the air flows into electricity. To assess the energy harvesting capacity, it is necessary to clarify the associated energy input, transmission, generation and dissipation behaviour of the system. Power flow analysis provides a useful tool for the purpose and thus is performed to study this energy harvesting system.

8.1 Application background

In view of a pressing demand to deal with climate issues such as global warming, there have been a growing interest in renewable energy harvesting (see, for example, Xing et al. (2011). Flutter phenomenon, which corresponds to limit cycle oscillations of elastic bodies in flows, suggests the possibility of energy harvesting using flow-induced vibrations. Several studies on this have been reported. Wu et al. (1972) showed that an oscillating

wing in the water is capable of harvesting energy from waves. McKinney and DeLaurier (1981) presented a similar device for wind energy extraction and suggested that the efficiency of this type of energy harvesting device was comparable to the conventional wind mills. Jones and Platzer (1997) and Jones et al. (1999) used a panel method to examine the power exchange between a uniform flow and a foil undergoing prescribed pitching and heaving motions. It was shown that vibration energy can be extracted from coupled pitch-heave motions with particular phase angles. Bernitsas et al. (2008) proposed a so-called vortex induced vibration aquatic clean energy converter to harness energy from ocean or other water resources and showed that the device can extract energy with high power conversion ratio. Zhu et al. (2009) and Zhu and Peng (2009) modelled a foil energy harvester with linear supporting springs and examined its harvesting capability. The results suggested a lower energy generation efficiency of flapping foil than the conventional rotary turbines. To improve the efficiency, Shimizu et al. (2008) conducted a multi-objective parameter optimization of a flapping wing power generator and showed that the power generation can be increased up to 30%.

However, in the publications mentioned above, the supporting springs of the foils were assumed to be linear. Under this configuration, the system motion will be divergent when the flow velocity exceeds the critical flutter speed. To avoid divergence, the pitching motions were prescribed in the studies, which in turn require extra energy for motion control in a practical design. Moreover, no actual electrical generation unit was included in the designs, and thus the mechanical-electric coupling was omitted. Furthermore, the quantity used to measure the harvested power was either the input power into the foil by aerodynamic loads (see, for example, McKinney and DeLaurier (1981)), or the dissipated power by a damper (see, Zhu et al. (2009); Zhu and Peng (2009); Peng and Zhu (2009); Shimizu et al. (2008)), which may not reflect the actual energy harnessed.

In this chapter, we intend to address these issues by investigating an integrated nonlinear energy harvesting system consisting of a flapping foil and an electro-magnetic generator using the power flow analysis approach. A nonlinear energy harvesting device with a two degrees-of-freedom flapping foil supported by nonlinear springs and an electro-magnetic generator is investigated from a viewpoint of power flow. Due to the nonlinearity in stiffness in both degrees-of-freedom, possible limit cycle oscillations exist, which correspond to stable periodic oscillations that can be used for energy harvesting. Hence, there is no need to control the pitch motion and operational cost can be reduced.

The following content presents the details of the theory and methods used in the analysis. Following a description of the model for the foil-electromagnetic generator interaction system, the governing equations are derived. The aerodynamic lift and moment applied on the foil were approximated analytically based on a quasi-steady aerodynamic theory. A fourth-order Runge-Kutta method is adopted to numerically solve the obtained equations. The input, transmitted and dissipated powers are calculated using the derived power flow formulations to measure the effects of nonlinear parameters on energy

generation. The developed model and analysis procedure provide a useful approach for examining similar energy harvesting systems for applications.

8.2 Mathematical model

8.2.1 Dynamic governing equations of the foil

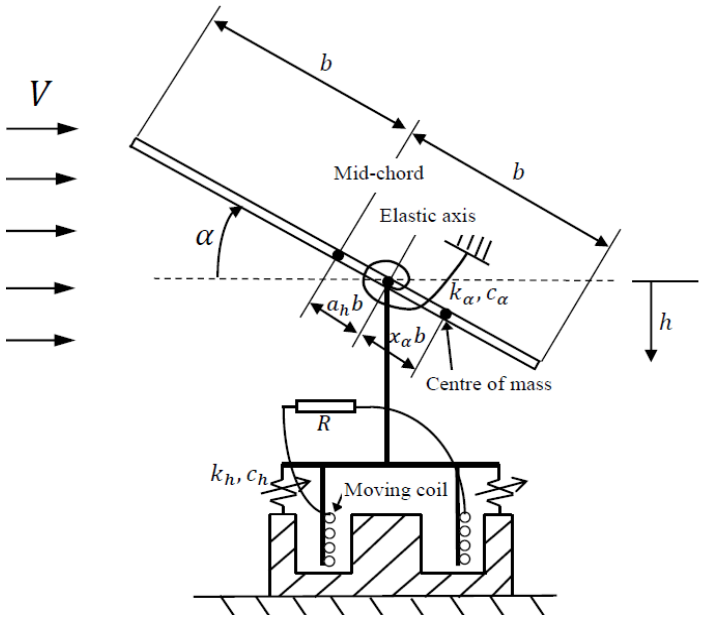

FIGURE 8.1: A schematic model of a nonlinear flapping foil energy harvesting device.

As shown in Figure 8.1, the energy harvesting system under investigation consists of a flat foil placed in a uniform air flow of velocity V and an electro-magnetic electric generator. The foil is supported at an elastic axis by nonlinear springs in both heave and pitch degrees-of-freedom, of which the stiffness are described by

$$k_h(h) = k_{h1} + k_{h2}h^2, \tag{8.1a}$$

$$k_\alpha(\alpha) = k_{\alpha 1} + k_{\alpha 2}\alpha^2, \tag{8.1b}$$

respectively. In both degrees-of-freedom, there exists linear viscous damping. It is assumed that the heaving displacement h of the foil is positive when moving downwards, whereas the pitching angle α is positive when nose up. The moving coil, located in a magnetic field, is rigidly connected to the foil at the elastic axis through a rigid, massless bar. In this way, electricity can be generated when the coil moves up and down and cuts lines of magnetic flux, according to the electromagnetic induction mechanism (see, Kittel (1967)). The location of the elastic axis, when the foil is in static equilibrium, is taken as the reference position with $h = 0$. In the figure, b denotes the half chord length;

a_h represents the non-dimensional distance from airfoil mid-chord to the elastic axis; x_α is the non-dimensional distance from elastic axis to centre of mass. In the following analysis, a foil of a unit span is considered.

The governing equations of motion of the foil are written as (see, Fung (1969))

$$m\ddot{h} + S\ddot{\alpha} + c_h\dot{h} + hk_h(h) = F - F_M, \tag{8.2}$$

$$S\ddot{h} + I_\alpha\ddot{\alpha} + c_\alpha\dot{\alpha} + \alpha k_\alpha(\alpha) = M, \tag{8.3}$$

where m is total mass of the foil and the coil; S is the mass static moment; I_α is the mass moment of inertia; c_h and c_α are the viscous damping coefficients for heave and pitch motions, respectively; F and M are aerodynamic lift and pitching moment, respectively; F_M is an electro-magnetic force.

To simplify the model, some non-dimensional parameters are defined as

$$\xi = \frac{h}{b}, \quad V^* = \frac{V}{b\omega_\alpha}, \quad \tau = \frac{Vt}{b}, \quad \omega_\xi = \sqrt{\frac{k_{h1}}{m}}, \quad \omega_\alpha = \sqrt{\frac{k_{\alpha1}}{I_\alpha}},$$

$$\bar{\omega} = \frac{\omega_\xi}{\omega_\alpha}, \quad \zeta_\xi = \frac{c_h}{2m\omega_\xi}, \quad \zeta_\alpha = \frac{c_\alpha}{2I_\alpha\omega_\alpha}, \quad \mu = \frac{m}{\pi\rho b^2},$$

$$x_\alpha = \frac{S}{mb}, \quad r_\alpha = \sqrt{\frac{I_\alpha}{mb^2}}, \quad \beta_\xi = \frac{k_{h2}b^2}{k_{h1}}, \quad \beta_\alpha = \frac{k_{\alpha2}}{k_{\alpha1}}.$$

Using those, the governing equations (8.2) and (8.3) are written in a non-dimensional form

$$\xi'' + x_\alpha\alpha'' + 2\zeta_\xi\frac{\bar{\omega}}{V^*}\xi' + (\frac{\bar{\omega}}{V^*})^2(\xi + \beta_\xi\xi^3) = -\frac{1}{\pi\mu}C_l(\tau) + \frac{F_M b}{mV^2}, \tag{8.4}$$

$$\frac{x_\alpha}{r_\alpha^2}\xi'' + \alpha'' + 2\frac{\zeta_\alpha}{V^*}\alpha' + \frac{1}{V^{*2}}(\alpha + \beta_\alpha\alpha^3) = \frac{2}{\pi\mu r_\alpha^2}C_m(\tau), \tag{8.5}$$

where a prime $'$ denotes differentiation with respect to τ ; the lift force and moment were approximated by adopting a quasi-steady aerodynamic theory (see, Fung (1969)):

$$F = -\rho bV^2C_l(\tau), \tag{8.6}$$

$$M = 2\rho bV^2C_m(\tau), \tag{8.7}$$

where $C_l(\tau)$ and $C_m(\tau)$ are non-dimensional coefficients for the lift and the pitching moment, respectively. For incompressible flows, they can be expressed by:

$$\begin{aligned} C_l(\tau) = {} & 2\pi\Big(\alpha(0) + \xi'(0) + (\frac{1}{2} - a_h)\alpha'(0)\Big)\phi(\tau) + \pi(\xi'' - a_h\alpha'' + \alpha') \\ & + 2\pi\int_0^\tau \phi(\tau - \sigma)\Big(\alpha'(\sigma) + \xi''(\sigma) + (\frac{1}{2} - a_h)\alpha''(\sigma)\Big)\,\mathrm{d}\sigma, \end{aligned} \tag{8.8}$$

$$
\begin{aligned}
C_m(\tau) = & \frac{\pi}{2} a_h (\xi'' - a_h \alpha'') - (\frac{1}{2} - a_h)\frac{\pi}{2}\alpha' - \frac{\pi}{16}\alpha'' \\
& + \pi(\frac{1}{2} + a_h)\Big(\alpha(0) + \xi'(0) + (\frac{1}{2} - a_h)\alpha'(0)\Big)\phi(\tau) \\
& + \pi(\frac{1}{2} + a_h)\int_0^\tau \phi(\tau - \sigma)\Big(\alpha'(\sigma) + \xi''(\sigma) + (\frac{1}{2} - a_h)\alpha''(\sigma)\Big)\,\mathrm{d}\sigma,
\end{aligned} \tag{8.9}
$$

where $\phi(\tau)$ is the Wagner function. For a flat foil, it may be expressed as (see, Fung (1969))

$$
\phi(\tau) = 1 - \Psi_1 e^{-\epsilon_1 \tau} - \Psi_2 e^{-\epsilon_2 \tau}, \tag{8.10}
$$

where the constants $\phi_1 = 0.165, \phi_2 = 0.335, \epsilon_1 = 0.0455$ and $\epsilon_2 = 0.3$ were determined by Jones (1940).

8.2.2 Electro-magnetic equations of the generator

Assuming that the electric power generation obeys Laplace theorem describing electro-magnetic phenomenon (see, Kittel (1967)), voltage will be induced by the moving coil in the magnetic field of flux density B. Suppose the effective length of the coil is l, then the induced voltage is obtained as

$$
e(t) = Bl\dot{h}. \tag{8.11}
$$

When the electric coil is in an electric circuit with resistance R, inductance L, a dynamic current i is introduced. By applying the Kirchhoff's voltage law, an equation governing the dynamic current is obtained

$$
L\frac{\mathrm{d}i(t)}{\mathrm{d}t} + Ri(t) - e = 0. \tag{8.12}
$$

where it was assumed that no electric capacitors exist in the circuit. Substituting Eq. (8.11) into Eq. (8.12), we obtain the following non-dimensional differential equation:

$$
i' + \frac{Rb}{LV} i - \frac{Blb}{L}\xi' = 0. \tag{8.13}
$$

When there is electric current flowing through the moving coil, an electro-magnetic force will be produced

$$
F_M = iBl. \tag{8.14}
$$

8.3 Power flow formulations

The equations of power balance are derived by multiplying Eqs. (8.2), (8.3) and (8.12) by $\dot{h}$, $\dot{\alpha}$ and i, respectively:

$$m\ddot{h}\dot{h} + S\ddot{\alpha}\dot{h} + c_h\dot{h}\dot{h} + hk_h(h)\dot{h} = F\dot{h} - F_M\dot{h}, \tag{8.15}$$

$$S\ddot{h}\dot{\alpha} + I_\alpha\ddot{\alpha}\dot{\alpha} + c_\alpha\dot{\alpha}\dot{\alpha} + \alpha k_\alpha(\alpha)\dot{\alpha} = M\dot{\alpha}, \tag{8.16}$$

$$Li\frac{\mathrm{d}i}{\mathrm{d}t} + Ri^2 - ei = 0. \tag{8.17}$$

A summation of Eqs. (8.15), (8.16) and (8.17) with references to Eqs. (8.11) and (8.14) leads to

$$m\ddot{h}\dot{h} + I_\alpha\ddot{\alpha}\dot{\alpha} + S\ddot{\alpha}\dot{h} + S\ddot{h}\dot{\alpha} + c_h\dot{h}\dot{h} + c_\alpha\dot{\alpha}\dot{\alpha} + hk_h(h)\dot{h} + \alpha k_\alpha(\alpha)\dot{\alpha} + Li\frac{\mathrm{d}i}{\mathrm{d}t} + Ri^2 = F\dot{h} + M\dot{\alpha}. \tag{8.18}$$

Alternatively, it may be written as

$$\dot{K} + p_d + \dot{U} + p_c + p_g = p_{in}, \tag{8.19}$$

where

$$\dot{K} = m\ddot{h}\dot{h} + I_\alpha\ddot{\alpha}\dot{\alpha} + S\ddot{\alpha}\dot{h} + S\ddot{h}\dot{\alpha}, \tag{8.20a}$$

$$\dot{U} = hk_h(h)\dot{h} + \alpha k_\alpha(\alpha)\dot{\alpha} \tag{8.20b}$$

represent the rate of change of kinetic and potential energies, respectively;

$$p_d = c_h\dot{h}\dot{h} + c_\alpha\dot{\alpha}\dot{\alpha} \tag{8.21}$$

denotes the instantaneous power dissipation by mechanical damping;

$$p_c = Li\frac{\mathrm{d}i}{\mathrm{d}t} \tag{8.22}$$

is rate of change of energy stored in the electric inductor;

$$p_g = Ri^2 \tag{8.23}$$

is the power consumed by the electric resistor R;

$$p_{in} = F\dot{h} + M\dot{\alpha} \tag{8.24}$$

denotes the instantaneous input power, i.e., the rate of work done by the flow on the foil. Transmitted power from the mechanical to electro-magnetic system equals the product

of the electro-magnetic force and the heaving velocity, i.e.

$$p_t = F_M \dot{h}. \tag{8.25}$$

Integrating Eq. (8.19) from $t = t_i$ to $t = t_i + t_p$ leads to an equation of energy balance in the time span

$$\Delta K + E_d + \Delta U + E_c + E_g = E_{in}. \tag{8.26}$$

where ΔK and ΔU are the net changes in kinetic and potential energies,

$$E_d = \int_{t_i}^{t_i+t_p} p_d \,\mathrm{d}t, \quad E_c = \int_{t_i}^{t_i+t_p} p_c \,\mathrm{d}t,$$

$$E_g = \int_{t_i}^{t_i+t_p} p_g, \,\mathrm{d}t \quad \text{and} \quad E_{in} = \int_{t_i}^{t_i+t_p} p_{in} \,\mathrm{d}t$$

are the total dissipated energy, the change in the energy that is stored in the electric inductor, the energy generated (consumed by the resistor) and total work done by the aerodynamic force and moment to the foil, respectively. Dividing these energy quantities by the time span t_p results in time-averaged power flow variables, which can be used to assess energy harvesting performance.

8.4 Simulation method

The integral terms in Eqs. (8.8) and (8.9) make it difficult to study the system's dynamical behaviour analytically. To assist investigations, new variables are introduced as (see, for example, Lee et al. (1999))

$$w_1 = \int_0^\tau e^{-\epsilon_1(\tau-\sigma)}\alpha(\sigma)\,\mathrm{d}\sigma, \tag{8.27a}$$

$$w_2 = \int_0^\tau e^{-\epsilon_2(\tau-\sigma)}\alpha(\sigma)\,\mathrm{d}\sigma, \tag{8.27b}$$

$$w_3 = \int_0^\tau e^{-\epsilon_1(\tau-\sigma)}\xi(\sigma)\,\mathrm{d}\sigma, \tag{8.27c}$$

$$w_4 = \int_0^\tau e^{-\epsilon_2(\tau-\sigma)}\xi(\sigma)\,\mathrm{d}\sigma. \tag{8.27d}$$

Using these expressions and Eq. (8.14), we transform Eqs. (8.4), (8.5) and (8.13) into the following form of differential equations

$$c_0\xi'' + c_1\alpha'' + c_2\xi' + c_3\alpha' + c_4\xi + c_5\xi^3 + c_6\alpha + c_7w_1 + c_8w_2 + c_9w_3 + c_{10}w_4 + c_{11}i = f(\tau), \tag{8.28}$$

$$d_0\xi'' + d_1\alpha'' + d_2\alpha' + d_3\alpha + d_4\alpha^3 + d_5\xi' + d_6\xi + d_7w_1 + d_8w_2 + d_9w_3 + d_{10}w_4 = g(\tau), \tag{8.29}$$

$$n_1\xi' + n_2i' + n_3i = 0, \tag{8.30}$$

where

$$f(\tau)=\frac{2}{\mu}\Big((\frac{1}{2}-a_h)\alpha(0)+\xi(0)\Big)(\Psi_1\epsilon_1 e^{-\epsilon_1\tau}+\Psi_2\epsilon_2 e^{-\epsilon_2\tau}), \tag{8.31}$$

$$g(\tau)=-\frac{(1+2a_h)f(\tau)}{2r_\alpha^2}. \tag{8.32}$$

The detailed expressions for coefficients in Eqs. (8.28), (8.29) and (8.30) are

$$c_0=1+\frac{1}{\mu},\quad c_1=x_\alpha-\frac{a_h}{\mu},\quad c_2=2\zeta_\xi\frac{\bar{\omega}}{V^*}+\frac{2}{\mu}(1-\Psi_1-\Psi_2),$$

$$c_3=\frac{1}{\mu}\big(1+(1-2a_h)(1-\Psi_1-\Psi_2)\big),\quad c_4=\big(\frac{\bar{\omega}}{V^*}\big)^2+\frac{2}{\mu}(\epsilon_1\Psi_1+\epsilon_2\Psi_2),$$

$$c_5=\big(\frac{\bar{\omega}}{V^*}\big)^2\beta_\xi,\quad c_6=\frac{2}{\mu}\Big((1-\Psi_1-\Psi_2)+(\frac{1}{2}-a_h)(\epsilon_1\Psi_1+\epsilon_2\Psi_2)\Big),$$

$$c_7=\frac{2}{\mu}\epsilon_1\Psi_1\big(1-\epsilon_1(\frac{1}{2}-a_h)\big),\quad c_8=\frac{2}{\mu}\epsilon_2\Psi_2\big(1-\epsilon_2(\frac{1}{2}-a_h)\big),$$

$$c_9=-\frac{2\epsilon_1^2\Psi_1}{\mu},\quad c_{10}=-\frac{2\epsilon_2^2\Psi_2}{\mu},\quad c_{11}=-\frac{Bl}{\mu\pi\rho b^3\omega_\alpha^2V^{*2}},$$

$$d_0=\frac{x_\alpha}{r_\alpha^2}-\frac{a_h}{\mu r_\alpha^2},\quad d_1=1+\frac{8a_h^2+1}{8\mu r_\alpha^2},$$

$$d_2=2\frac{\zeta_\alpha}{V^*}+\frac{1-2a_h}{2\mu r_a^2}-\frac{(1-2a_h)(1+2a_h)(1-\Psi_1-\Psi_2)}{2\mu r_\alpha^2},$$

$$d_3=\frac{1}{V^*}-\frac{1+2a_h}{2\mu r_\alpha^2}-\frac{(1-2a_h)(1+2a_h)(\Psi_1\epsilon_1+\Psi_2\epsilon_2)}{2\mu r_\alpha^2},$$

$$d_4=\frac{\beta_\alpha}{V^{*2}},\quad d_5=-\frac{(1-\Psi_1-\Psi_2)(1+2a_h)}{\mu r_\alpha^2},$$

$$d_6=-\frac{(\epsilon_1\Psi_1+\epsilon_2\Psi_2)(1+2a_h)}{\mu r_\alpha^2},\quad d_7=-\frac{\epsilon_1\Psi_1(1+2a_h)\big(1-\epsilon_1(\frac{1}{2}-a_h)\big)}{\mu r_\alpha^2},$$

$$d_8=-\frac{\epsilon_2\Psi_2(1+2a_h)\big(1-\epsilon_2(\frac{1}{2}-a_h)\big)}{\mu r_\alpha^2},\quad d_9=\frac{\epsilon_1^2\Psi_1(1+2a_h)}{\mu r_\alpha^2},\quad d_{10}=\frac{\epsilon_2^2\Psi_1(1+2a_h)}{\mu r_\alpha^2},$$

$$n_1=-\frac{Blb}{L},\quad n_2=1,\quad n_3=\frac{Rb}{LV}.$$

Introducing nine new variables

$$x_1=\alpha,\quad x_2=\alpha',\quad x_3=\xi,$$

$$x_4=\xi',\quad x_5=w_1,\quad x_6=w_2,$$

$$x_7=w_3,\quad x_8=w_4,\quad x_9=i,$$

equations (8.28), (8.29) and (8.30) are transformed into a set of nine first-order differential equations

$$\begin{pmatrix} x_1' \\ x_2' \\ x_3' \\ x_4' \\ x_5' \\ x_6' \\ x_7' \\ x_8' \\ x_9' \end{pmatrix} = \begin{pmatrix} x_2 \\ (c_0H - d_0P)/(d_0c_1 - c_0d_1) \\ x_4 \\ -(c_1H + d_1P)/(d_0c_1 - c_0d_1) \\ x_1 - \epsilon_1 x_5 \\ x_1 - \epsilon_2 x_6 \\ x_3 - \epsilon_1 x_7 \\ x_3 - \epsilon_2 x_8 \\ -(n_1x_4 + n_3x_9)/n_2 \end{pmatrix}, \tag{8.33}$$

where

$$P = c_2x_4 + c_3x_2 + c_4x_3 + c_5x_3^3 + c_6x_1 + c_7x_5 + c_8x_6 + c_9x_7 + c_{10}x_8 + c_{11}x_9 - f(\tau),$$

$$H = d_2x_2 + d_3x_1 + d_4x_1^3 + d_5x_4 + d_6x_3 + d_7x_5 + d_8x_6 + d_9x_7 + d_{10}x_8 - g(\tau).$$

Once the initial conditions of the system are set, these first-order equations can be solved using a fourth-order Runge-Kutta method. This operation yields the time histories of non-dimensional displacements and the dynamic current. Instantaneous / time-averaged power flow variables are then obtained using the formulations in Section 8.3.

8.5 Energy harvesting performance

Using the above formulations and simulation approach, the energy harvesting performance of the system is assessed in this section. When the electric generator is not included in the model, the non-dimensional flutter velocity of a system with $\bar{\omega} = 0.2$, $\omega_\alpha = 3$, $\zeta_\xi = \zeta_\alpha = 0.01$, $\mu = 100$, $x_\alpha = 0.25$, $r_\alpha = 0.5$, $a_h = -0.5$, $\beta_\xi = 1$, $\beta_\alpha = 1.5$, is calculated to be approximately 6.3. When $V^* = 6$, below the critical speed, an initial motion of the system will decay and then vanish, as shown in Figure 8.2(a) and (b). However, when the flow velocity $V^* = 6.5$, which is above the flutter speed, the system will display stable periodic oscillations shown in Figure 8.2(c) and (d).

Figure 8.3 represents the motions of the foil shown in Figure 8.2 as trajectories in the phase plane. Clearly, when below flutter velocity, the foil evolves to the static equilibrium position of $\alpha = \alpha' = \xi = \xi' = 0$. In comparison, with a larger flow velocity of $V^* = 6.5$, it exhibits limit cycle oscillations in steady state,similar to the behaviour of the unforced Van der Pol oscillator discussed in Chapter 5.

To investigate the coupling effects between the generator and the foil, Figure 8.4 compares the time histories of the displacement response, obtained with or without considerations of the electro-magnetic generator. For the former case, parameter values

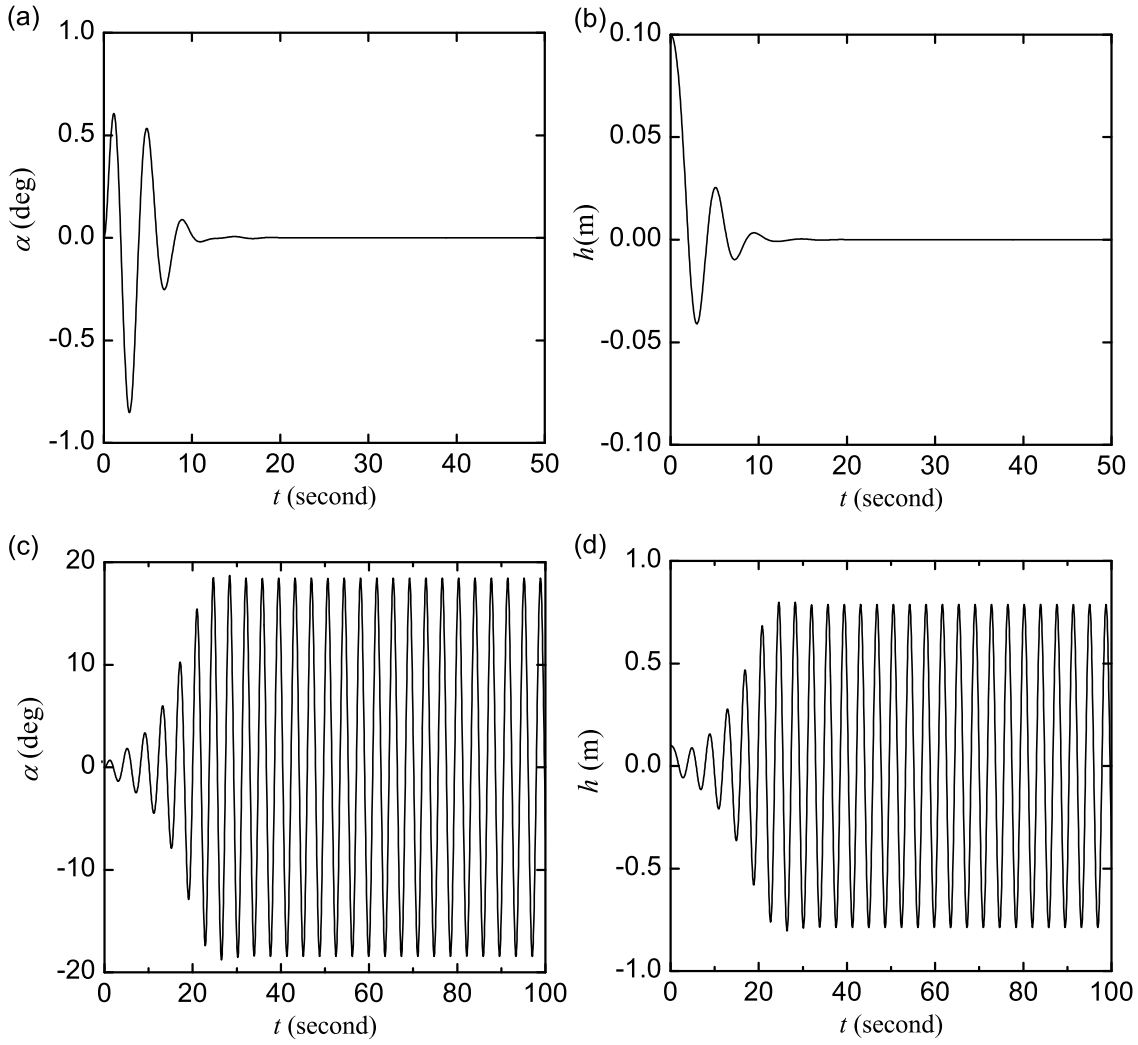

FIGURE 8.2: Time histories of the displacements. (a) and (b): $V^* = 6$, below the critical flutter velocity; (c) and (d): $V^* = 6.5$, above the critical flutter velocity. Initial conditions are set as $\alpha = \alpha' = \xi' = 0$, $\xi = 0.1$.

are set as $B = 0.5$T, $l = 20$m, $R = 1\Omega$, $L = 0.05$H, $b = 1$m, $\rho = 1.293$kg/m^3, while the others kept the same as those used in Figure 8.2. The figure shows that the incorporation of electric generator in the model results in decreases of response amplitudes in both degrees-of-freedom. While the pitching amplitude reduces slightly, the heaving amplitude decreases significantly. The reason may be that the electro-magnetic force created by the coil introduces extra resistance in the heave motion. The large differences in results between modelling with and without considering the electrical-magnetic unit demonstrate a necessity to consider interactions between electric and mechanical subsystems for effective simulations of the energy harvesting system.

With parameters set the same as those used in Figure 8.4, the time series of the dynamic current in the circuit is shown in Figure 8.5. In steady state, it varies with a constant amplitude of about 8.63 Amp. Using Eq. (8.23), the maximum instantaneous power

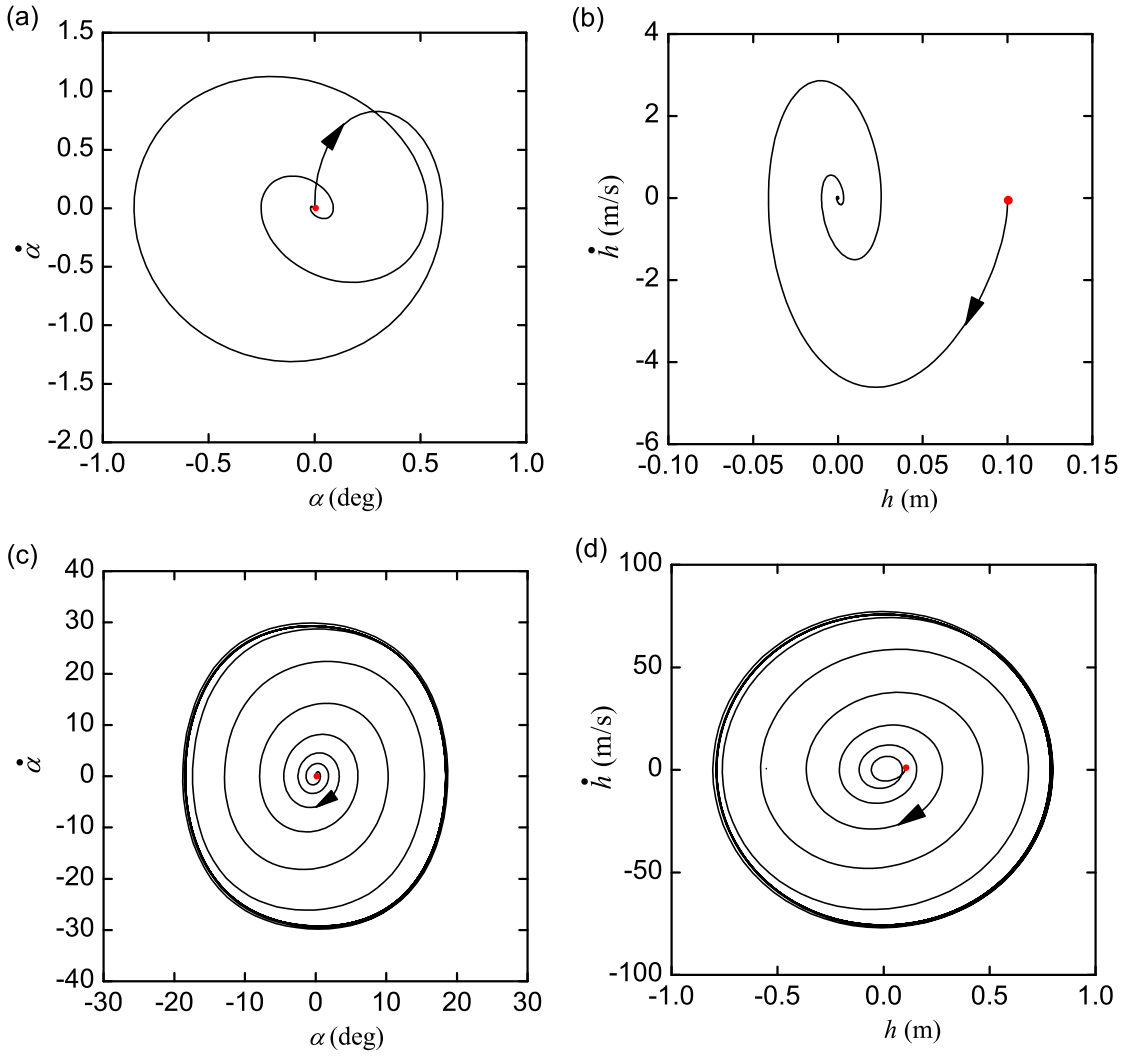

FIGURE 8.3: Phase trajectories. (a) and (b) below flutter velocity $V^* = 6$, (c) and (d) above flutter velocity $V^* = 6.5$. Other parameters are set the same as in Figure 8.2.

generation is calculated to be approximately 75.58 Watts. Correspondingly, the time-averaged generated power over an oscillation cycle is 37.79 Watts. Note that in the above simulations, a foil of a unit span is considered. If its span increases to 5 meters, the average power generation will be about 188.95 Watts.

Again, considering the same parameters values as those used for Figure 8.4, the time-averaged power flow variables over a period of oscillation of the model with generator and that without the generator are listed in Table 8.1. For the former case, the averaged rate of work done on the foil, i.e., time-averaged input power, equals the sum of time-averaged dissipated and transmitted powers. For the latter case, the time-averaged input power balances the power dissipated by mechanical damping. It is found that the average input power of the system with a generator is much larger than that without considering the electro-magnetic generator. The reason is that the electric circuit functions as a power dissipation mechanism so that more power is needed to drive the system, compared with

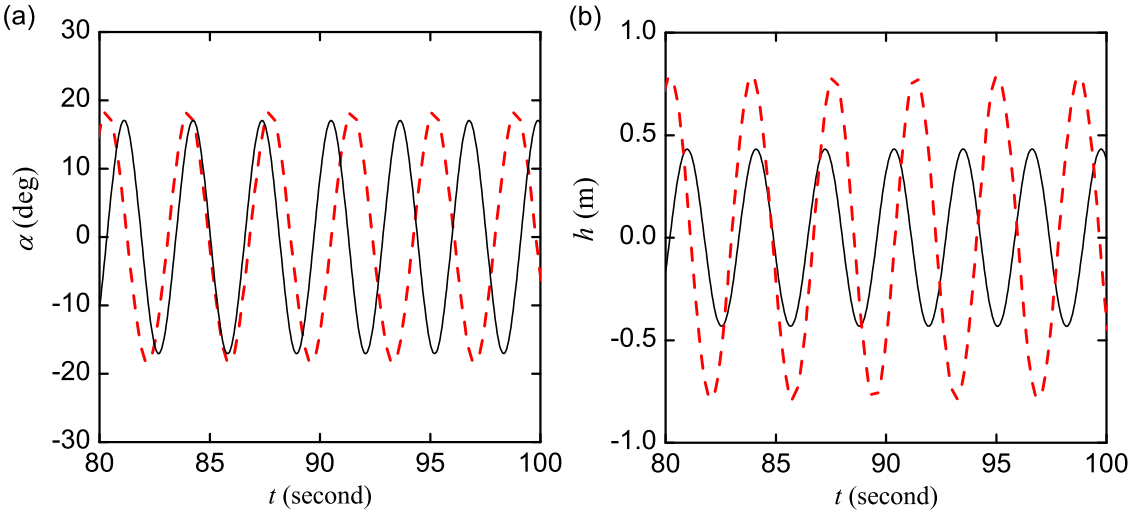

FIGURE 8.4: Comparison of displacement with (denoted by solid lines) /without (represented by dashed lines) considering the generator. (a) pitch motion and (b) heave motion. Parameters are set as $V^* = 6.5$, $\bar{\omega} = 0.2$, $\omega_\alpha = 3$, $\zeta_\xi = \zeta_\alpha = 0.01$, $\mu = 100$, $x_\alpha = 0.25$, $r_\alpha = 0.5$, $a_h = -0.5$, $\beta_\xi = 1$, $\beta_\alpha = 1.5$, $B = 0.5$T, $l = 20$m, $R = 1\Omega$, $L = 0.05$H, $b = 1$m, $\rho = 1.293$kg/m^3.

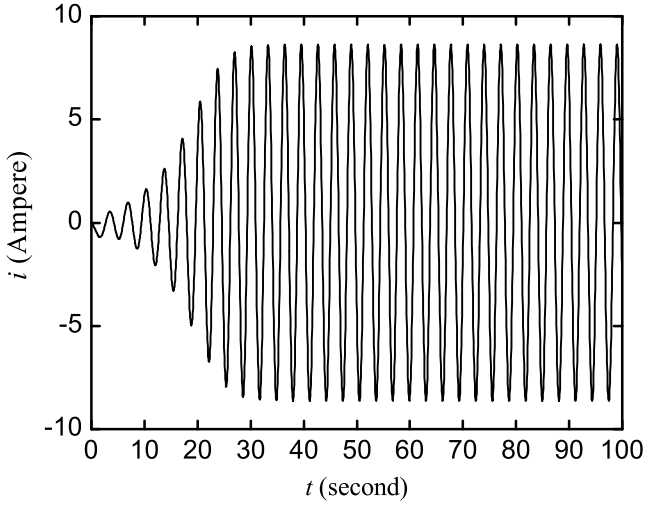

FIGURE 8.5: The time histories of dynamic current. Parameters are set the same as in Figure 8.4.

the model with no generator. Moreover, for the case with consideration of the generator, input power into the foil is largely transmitted into the electric circuit with only a small portion being dissipated by mechanical damping.

In Figure 8.6, the influence of electric resistance on the generated power is examined for the system with different configurations of stiffness nonlinearities. The peak values of the curves indicate an impedance matching, which occurs when resistance is approximately 0.065Ω. Comparing the solid line with the dashed line, it's seen that an increase in β_ξ

TABLE 8.1: Averaged power exchange (in Watts) in steady-state motion

Powers	With generator	without generator
Averaged rate of work done on the foil	40.14	5.20
Averaged dissipated power	2.90	5.20
Averaged transmitted power	37.24	Not applicable
Averaged generated power	37.24	Not applicable

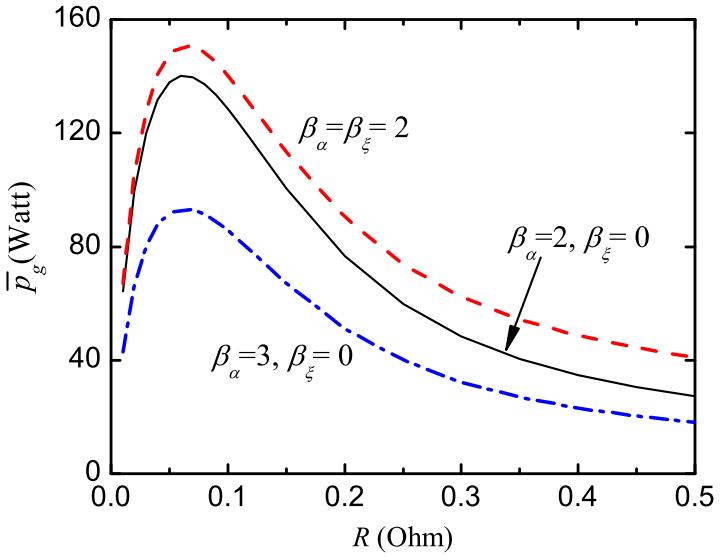

FIGURE 8.6: The effects of the electric resistance on maximum power generation under different nonlinear stiffness configurations. Solid line: $\beta_\xi = 0$, $\beta_\alpha = 2$, dashed line: $\beta_\xi = 2$, $\beta_\alpha = 2$ and dash-dot line: $\beta_\xi = 0$, $\beta_\alpha = 3$. Other parameters are set the same as in Figure 8.4.

is beneficial for improving power generation. With the considered parameter values, a smaller value of β_α is preferable for a larger power generation. However, the amplitude of pitching motion will increase accordingly with a decreasing β_α. To ensure the accuracy of the simulations results, the amplitude of the pitch motion should remain lower than a limit so that the assumptions of the adopted quasi-aerodynamic theory can be satisfied.

8.6 Conclusions

In this chapter, a nonlinear flapping foil vibration energy harvesting system was proposed to extract external energy. The foil was placed in air flows and supported by nonlinear springs in both heave and pitch degrees-of-freedom. The quasi-steady aerodynamic

theory was used for approximations of the lift force and moment. The fourth-order Runge-Kutta method was employed for numerical simulations of power transmission and generation in the system. Based on the investigation, the following conclusions can be drawn:

- Adding hardening stiffness nonlinearities with cubic restoring force in both the pitch and the heave degrees-of-freedom of the foil, its motion may be characterised by stable limit cycle oscillations (LCOs) that are similar to those exhibited by the Van der Pol oscillator;
- When the flow velocity is above the critical flutter speed, the stable LCOs can be used to extract energy from the air-flows without extra cost to control the stability of the system;
- Power flow analysis provides an effective way to quantitatively reveal the amount of power generation, dissipation and transmission in the system. It was shown that modelling the system without considering the coupling effects between the electro-magnetic generator and the foil can lead to significant inaccuracies in the predicted values of time-averaged power flows;
- Changing the coefficients of cubic restoring forces terms of the nonlinear supporting springs, the amplitude of the dynamic current and the amount of power generation will be substantially affected. For the considered cases, a larger nonlinear stiffness coefficient in the pitch motion benefited power generation, whereas smaller nonlinear stiffness in the heave motion was desirable for the same purpose.

Chapter 9

Power flow analysis of a nonlinear vibration isolation system with a negative stiffness mechanism

The needs for high-performance low-frequency vibration isolation systems arise in many scientific and industrial fields, ranging from the design of seat suspension systems for vehicles to motion isolations of optical instruments for gravitational wave detections (see, for example, Winterflood (2001); Lee et al. (2007a)). For an effective isolation using a conventional isolator, low spring stiffness is required so as to reduce its natural frequency Ω_n to be much smaller than the excitation frequency Ω. However, this leads to a large static deflection, which is not desirable in many practical designs. To solve this paradox, a negative stiffness mechanism (NSM) can be configured in parallel with a linear isolator so that a low dynamic stiffness can be achieved while ensuring a large static stiffness (see, for example, Platus (1991)). However, many NSMs are inherently nonlinear and strong nonlinearity can be introduced to the overall system (see, for example, Cao et al. (2008)). As a result, frequencies other than the excitation frequency may emerge in the dynamic response. Therefore, the traditional isolation performance index, such as force or displacement transmissibility considering only the response component at the excitation frequency, is not really suitable. Vibrational power flow variables provide better indications of the isolation performance as they can incorporate the effects of many other frequency components. In this chapter, power flow analysis is performed on a nonlinear vibration isolation system with a NSM, which is created by a pair of bars under compression forces. Both analytical and numerical approaches will be used to reveal its dynamics and power flow behaviour. Suggestions will also be provided for more effective vibration isolations using the device.

9.1 Mathematical model

As shown in Figure 9.1, the system model consists of a conventional linear mass-spring-damper system and a nonlinear negative-stiffness mechanism (NSM). The linear part is made up of a mass m subject to a harmonic excitation, a vertical linear spring of stiffness k and a viscous damper with a damping coefficient c. The NSM is created by two rigid massless bars of fixed length l, hinged together at one end with the mass while the other ends, subject to two equivalent compression forces P, are allowed to move freely in frictionless horizontal channels. It is assumed that the bars are horizontal when the unforced mass is in its static equilibrium position of $x = 0$. The motion of the system is restricted to be in the two dimensional plane. As the system is symmetric, the mass only has vertical movement.

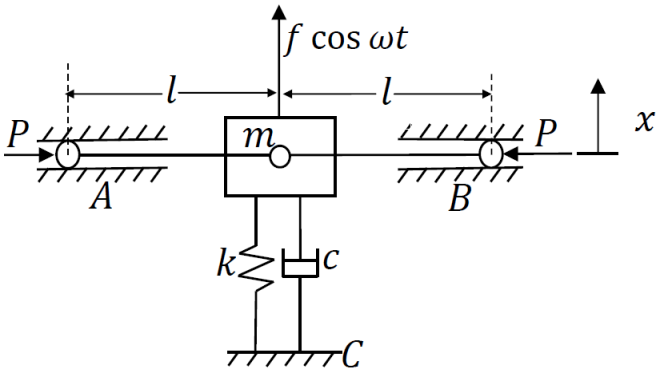

FIGURE 9.1: A schematic representation of a vibration isolation system with a negative stiffness mechanism.

If the mass reaches $x = \pm l$, the bars will be vertical and the motion cannot be maintained so that situation should be avoided. When $-l < x < l$, the equation of motion is

$$m\ddot{x} + c\dot{x} + kx - 2P\frac{x}{\sqrt{l^2 - x^2}} = f\cos\omega t, \tag{9.1}$$

where f and ω are the amplitude and frequency of the harmonic excitation force, respectively. Letting

$$\omega_0 = \sqrt{\frac{k}{m}},\ \tau = \omega_0 t,\ \xi = \frac{c}{2m\omega_0},\ \alpha = \frac{2P}{kl},\ X = \frac{x}{l},\ f_0 = \frac{f}{kl},\ \Omega = \frac{\omega}{\omega_0},$$

we obtain a non-dimensional equation of motion

$$X'' + 2\xi X' + X(1 - \frac{\alpha}{\sqrt{1 - X^2}}) = f_0\cos\Omega\tau, \quad |X| < 1, \tag{9.2}$$

where a prime denotes a differentiation with respect to τ.

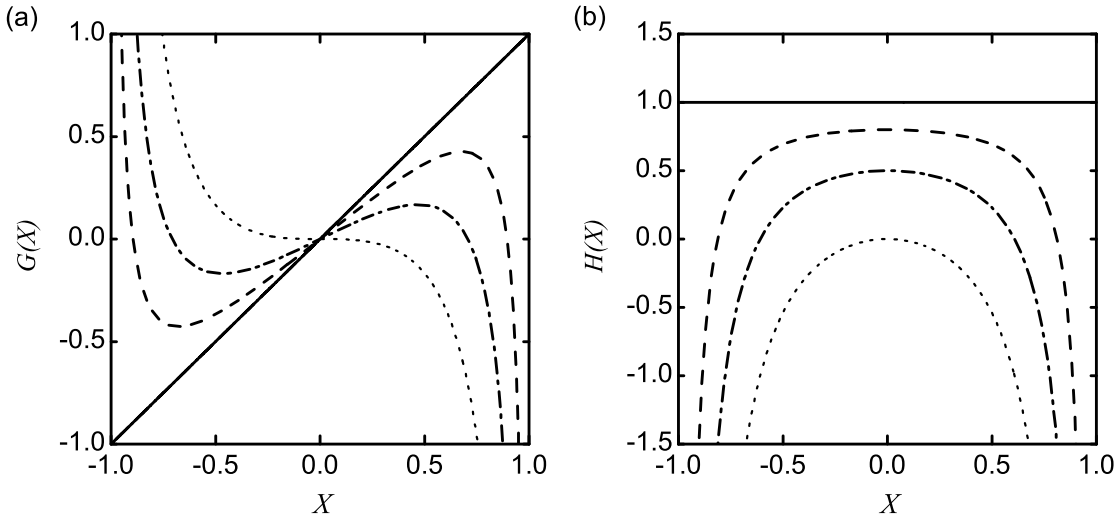

FIGURE 9.2: The variations of (a) nonlinear restoring force and (b) stiffness characteristics of the system. Solid, dashed, dash-dotted and dotted lines represent α=0, 0.2, 0.5 and 1, respectively.

The total non-dimensional restoring force from both the linear spring and the NSM is given by

$$G(X) = X(1 - \frac{\alpha}{\sqrt{1-X^2}}), \quad |X| < 1. \tag{9.3}$$

A differentiation of $G(X)$ with respect to X leads to the following expression of the non-dimensional stiffness of the system:

$$H(X) = 1 - \frac{\alpha}{(1-X^2)\sqrt{1-X^2}}, \quad |X| < 1. \tag{9.4}$$

This equation shows that nonlinear stiffness is affected by a positive α and the displacement X through a negative nonlinear term $-\alpha/(1-X^2)^{-3/2}$. Its value decreases with the increase of α and deflection $|X|$. Figures 9.2(a) and (b) respectively present the variations of $G(X)$ and $H(X)$ with displacement X, for different values of α $(0 < \alpha < 1)$. It is seen that when $\alpha \neq 0$, the largest stiffness is found at point $X = 0$. For a fixed value of α $(0 < \alpha < 1)$, the dynamic stiffness reduces from positive to zero, and then becomes negative with increasing deflection. The position $X = 0$ is a static equilibrium position, around which, for a small amplitude vibration, Eq. (9.3) can be expanded using a Taylor series

$$G(X) = X(1 - \frac{\alpha}{\sqrt{1-X^2}}) = X(1-\alpha) - \frac{\alpha}{2}X^3 + O(X^4), \tag{9.5}$$

where $O(X^4)$ represents the higher-order terms. The linearised stiffness of the system is $1-\alpha$ $(0 < \alpha < 1)$, and thus the linearised natural frequency of the system about the static equilibrium is given by

$$\Omega_n = \sqrt{1-\alpha}. \tag{9.6}$$

When α is set close to 1, this frequency will be approximately zero. Linear vibration isolation theory would suggest a wider frequency range of effective vibration isolation. However, it may not be necessarily true for the cases with NSM, since the NSM is inherently nonlinear and undesirable nonlinear effects may arise from it. A more detailed study is presented in the following sections.

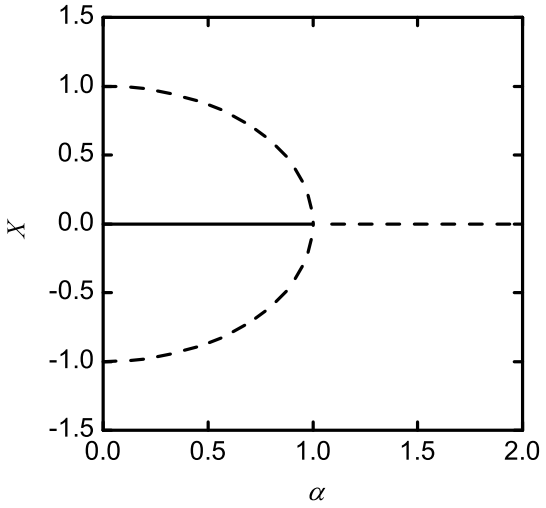

FIGURE 9.3: Bifurcation diagram of the unforced system. Solid line: stable equilibria; dashed line: unstable equilibria.

To design this isolation system, it is necessary to determine the static equilibrium points of the damped system and investigate their corresponding stabilities to choose a suitable supporting position. These can be completed by using fundamental nonlinear dynamics theories, and therefore the details are neglected in this chapter. Such investigation reveals a pitchfork bifurcation, as shown in Figure 9.3. When $0 < \alpha < 1$ there are two unstable equilibrium points $(\pm\sqrt{1-\alpha^2}, 0)$ and a stable one at $(0, 0)$. However, when $\alpha \leq 1$ there exists only an unstable one at $(0, 0)$. As a result, the value range of $0 < \alpha < 1$ is used and the point $(0, 0)$ should be employed as the static supporting point for the nonlinear isolation system studied herein.

9.2 Forced system

9.2.1 Primary resonances

Eq. (9.2) has the following form in the phase space

$$\begin{pmatrix} X' \\ Y' \end{pmatrix} = \begin{pmatrix} Y \\ f_0 \cos\Omega\tau - 2\xi Y - X(1 - \dfrac{\alpha}{\sqrt{1-X^2}}) \end{pmatrix}. \tag{9.7}$$

Using an averaging method, we assume that $X = r\cos(\Omega\tau+\phi)$ and $Y = -r\Omega\sin(\Omega\tau+\phi)$, where r and ϕ are functions of time, so that Eq. (9.7) is transformed into

$$\begin{pmatrix} \cos(\Omega\tau+\phi) & -r\sin(\Omega\tau+\phi) \\ -\Omega\sin(\Omega\tau+\phi) & -r\Omega\cos(\Omega\tau+\phi) \end{pmatrix} \begin{pmatrix} r' \\ \phi' \end{pmatrix} = \begin{pmatrix} 0 \\ f_1 \end{pmatrix}, \tag{9.8}$$

where

$$f_1 = f_0\cos\Omega\tau + 2r\xi\Omega\sin(\Omega\tau+\phi) + r\Omega^2\cos(\Omega\tau+\phi) - r\cos(\Omega\tau+\phi)\Delta, \tag{9.9a}$$

$$\Delta = 1 - \frac{\alpha}{\sqrt{1-r^2\cos^2(\Omega\tau+\phi)}}. \tag{9.9b}$$

The determinant of the coefficient matrix of Eq. (9.8) is not zero, so that by using Cramer's rule we obtain its solution

$$r' = -\frac{1}{\Omega}f_1\sin(\Omega\tau+\phi), \tag{9.10a}$$

$$\phi' = -\frac{1}{r\Omega}f_1\cos(\Omega\tau+\phi). \tag{9.10b}$$

The right hand sides of Eqs. (9.10a) and (9.10b) may be approximated by their average values over a period of the excitation load, which leads to

$$r' = -\frac{\Omega}{2\pi}\int_0^{\frac{2\pi}{\Omega}} \frac{1}{\Omega}f_1\sin(\Omega\tau+\phi)\,\mathrm{d}\tau, \tag{9.11a}$$

$$\phi' = -\frac{\Omega}{2\pi}\int_0^{\frac{2\pi}{\Omega}} \frac{1}{\Omega r}f_1\cos(\Omega\tau+\phi)\,\mathrm{d}\tau. \tag{9.11b}$$

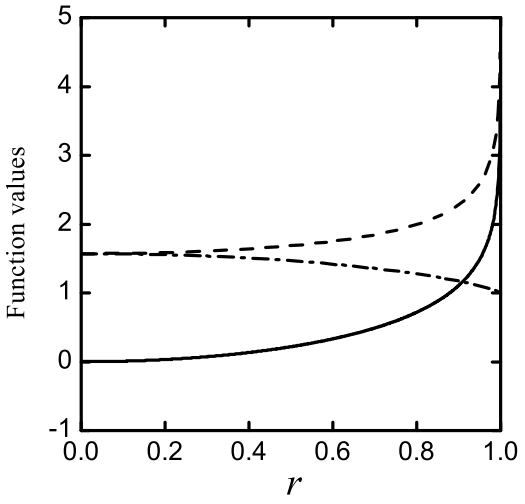

FIGURE 9.4: Elliptical integral curves. Solid line: $K(r)-E(r)$, dashed line: $K(r)$, and dash-dotted line: $E(r)$.

After completing the integrations in Eqs. (9.11), we obtain

$$r' = -\frac{1}{2\Omega} f_0 \sin\phi - r\xi, \tag{9.12a}$$

$$r\phi' = -\frac{1}{\Omega} f_0 \cos\phi - \frac{r\Omega}{2} + \frac{r}{2\Omega} - \frac{2\alpha}{\pi\Omega r}\big(K(r) - E(r)\big), \tag{9.12b}$$

where $K(r)$ and $E(r)$, shown by the curves in Figure 9.4, denote the first and second complete elliptic integrals, respectively (see, Abramowitz and Stegun (1965)).

Letting $r' = \phi' = 0$, which physically implies that the time-averaged rates of change of the response amplitude and phase angle vanish, we obtain

$$-\frac{1}{2\Omega} f_0 \sin\phi - r\xi = 0, \tag{9.13a}$$

$$-\frac{1}{\Omega} f_0 \cos\phi - \frac{r\Omega}{2} + \frac{r}{2\Omega} - \frac{2\alpha}{\pi\Omega r}\big(K(r) - E(r)\big) = 0, \tag{9.13b}$$

from which an averaged approximate relationship between the excitation frequency and the system response can be derived

$$f_0^2 = r^2\Big((2\xi\Omega)^2 + \big(\Omega^2 - 1 + \beta(r,\alpha)\big)^2\Big), \tag{9.14}$$

where

$$\beta(r,\alpha) = \frac{4\alpha}{\pi r^2}\big(K(r) - E(r)\big).$$

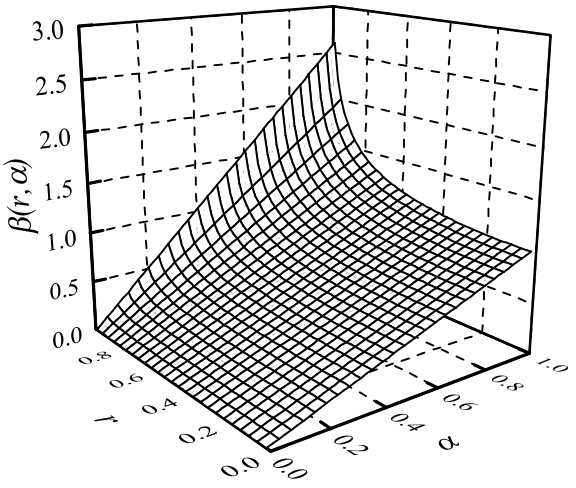

FIGURE 9.5: Variations of the nonlinear function $\beta(r,\alpha)$ with r and α.

Here, a nonlinear function $\beta(r,\alpha)$ is introduced to denote the effect of the system nonlinearity. Figure 9.5 shows a surface plot of $\beta(r,\alpha)$ as the function of the response magnitude r and the nonlinear parameter α. For a given r, its value is proportional to the parameter α. Larger values of these two variables produce a stronger nonlinearity.

A further manipulation of Eq. (9.14) gives

$$r/f_0 = \frac{1}{\sqrt{(2\xi\Omega)^2 + \left(\Omega^2 - 1 + \beta(r,\alpha)\right)^2}}. \tag{9.15}$$

The ratio r/f_0 may be defined as the nonlinear receptance function developed from the linear system, since by setting $\beta(r,\alpha) = 0$ it would give the corresponding linear receptance. It represents the response amplitude per unit amplitude of the external excitation force. However, it should be noted that this ratio varies with the response amplitude for a nonlinear system ($\alpha \neq 0$), as shown in Figure 9.6, which is different from that of the linear isolator. Note that the expression inside the square root of the denominator on the right hand side of Eq. (9.15) is a quadratic function of Ω^2. For a fixed r and α, the maximum value of r/f_0 can be found at

$$\Omega^2 = 1 - \beta - 2\xi^2, \quad \text{when } 1 - \beta - 2\xi^2 > 0, \tag{9.16a}$$

$$\Omega^2 = 0, \quad \text{when } 1 - \beta - 2\xi^2 \leq 0. \tag{9.16b}$$

Eq. (9.15) takes special forms for some given parameters. For linear ($\alpha = \beta = 0$), un-damped ($\xi = 0$) and static force ($\Omega = 0$) cases, the corresponding expressions are

$$r/f_0 = \frac{1}{\sqrt{(2\xi\Omega)^2 + (\Omega^2 - 1)^2}}, \quad r/f_0 = \frac{1}{|\Omega^2 - 1 + \beta(r,\alpha)|}, \quad r/f_0 = \frac{1}{|\beta(r,\alpha) - 1|}.$$

Figure 9.6 shows three curved surfaces of the defined receptance for different nonlinear parameter values. In each surface, there exist a peak receptance curve, which can be formulated mathematically by Eqs. (9.16a) and (9.16b). For the nonlinear isolator ($\alpha \neq 0$), an increase in the response amplitude r would bend this curve to the low frequency range. The figure shows that the nonlinear receptance ($\alpha \neq 0$) depends on response amplitude, which is in contrast to the linear case ($\alpha = 0$). When α increases to 0.7 and then 0.9, the nonlinearity becomes stronger and the peak curve would shift toward a lower-frequency range. Also, by increasing α, the value of r/f_0 increases in the lower-frequency range but decreases near the resonance frequency of the linear system. However, at excitation frequencies much larger than unity, r/f_0 is not sensitive to α.

In order to verify the averaging formulations, Figures 9.7(a) and (b) compare the static and dynamic solutions obtained by the averaging method (solid line) and those by numerical approaches (circles), respectively. The numerical solutions of the static system in Figure 9.7(a) are obtained by using a bisection method to solve the governing equation

$$X\left(1 - \frac{\alpha}{\sqrt{1 - X^2}}\right) = f_0. \tag{9.17}$$

Figure 9.7(a) shows three solution branches, namely upper, middle and lower branches for the static case when f_0 is smaller than 0.0379. In particular, the equilibrium points

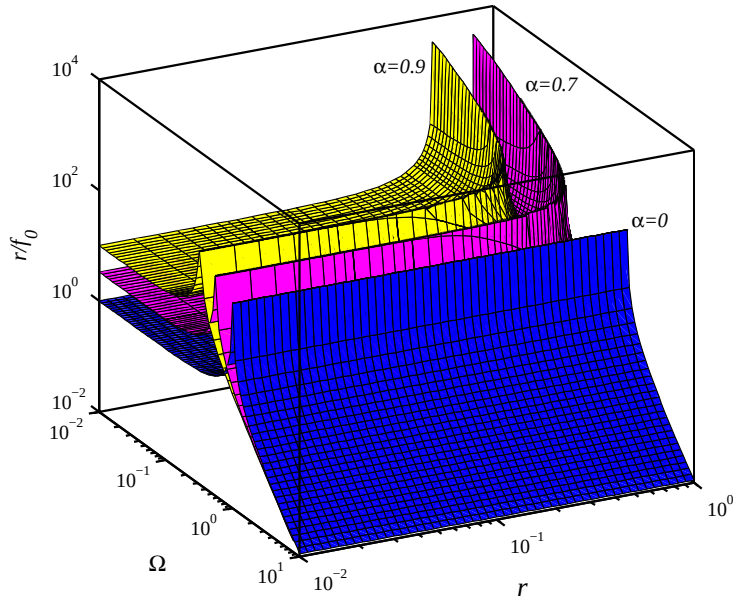

FIGURE 9.6: The receptance function surfaces ($\xi = 0.01$). The yellow, magenta and blue surfaces correspond to $\alpha = 0.9, \alpha = 0.7$ and $\alpha = 0$, respectively.

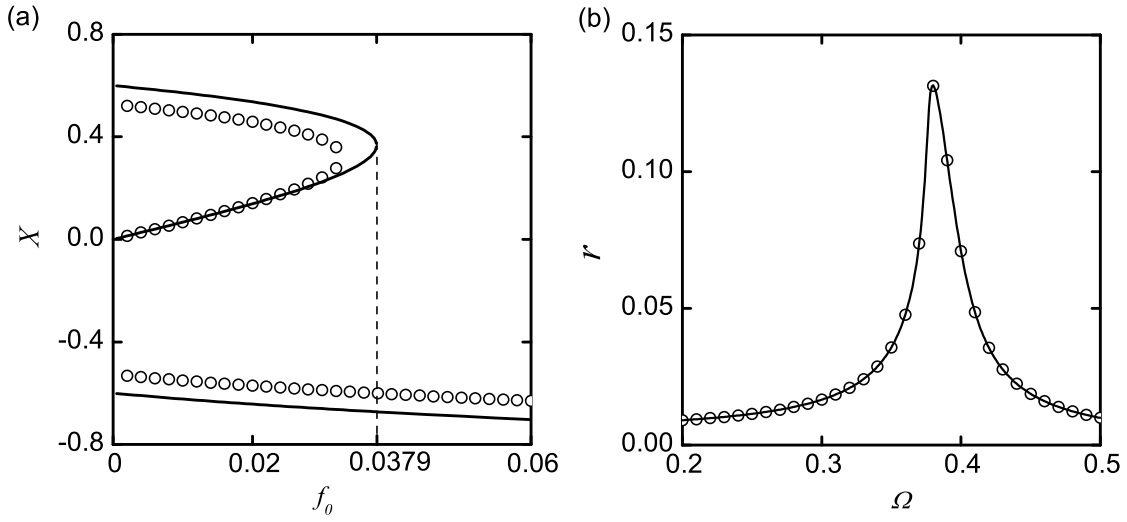

FIGURE 9.7: Verifications of the derived frequency response relationship ($\alpha = 0.85$), solid line indicates the results from the averaging method while circles mark the numerical method results: (a) static solution under constant force ($\xi = 0, \Omega = 0$); (b) dynamic solution ($\xi = 0.01, f_0 = 0.001$).

are at $X_1 = 0, X_{2,3} = \pm\sqrt{1 - 0.85^2} \approx \pm 0.53$ when $f_0 = 0$. Increasing f_0 from 0 to 0.06, the upper and middle branch curves move towards each other, merge and then disappear at $f_0 = 0.0379$. It is observed that with $\alpha = 0.85, \xi = 0, \Omega = 0$, the middle branch results obtained by both methods agree relatively well. The differences in solutions of the upper and lower branches may arise from the inefficiency of the averaging method in dealing with static systems. For the dynamic case with $\alpha = 0.85, \xi = 0.01, f_0 = 0.001$, Figure

9.7(b) compares the averaging results with those obtained using a Runge-Kutta method. The results agree well with each other and thus verify the averaging formulations.

It should be noted that the averaging method using a first-order approximation cannot provide information on frequency components other than the excitation frequency, such as sub-harmonic components in a higher frequency range. For this reason, we will further investigate the system by using a Runge-Kutta method in Section 9.2.3. This implies that the averaging formulations may be directly used in designs when the excitation frequency is close to the primary resonance frequency, but in other frequency ranges a numerical approach may be used to incorporate more response frequency components.

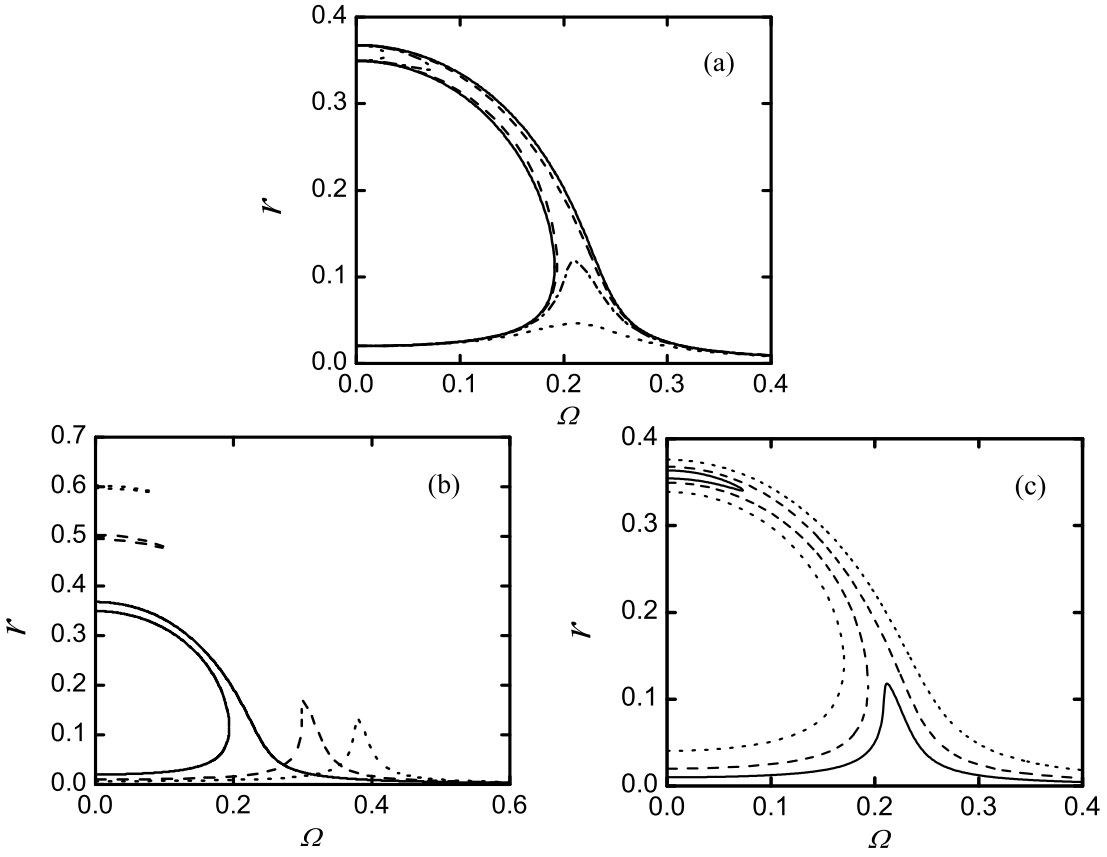

FIGURE 9.8: Frequency response curves for primary resonances. (a) The effect of damping ($\alpha = 0.95, f_0 = 0.001$): solid line, dash line, dash-dotted line and dotted line refer to $\xi = 0, 0.01, 0.02$ and 0.05, respectively; (b) the effect of parameter α ($\xi = 0.01, f_0 = 0.001$): solid line, dash line and dotted line represent the cases $\alpha = 0.95, 0.90$ and 0.85, respectively (c) the effect of excitation amplitude ($\xi = 0.01, \alpha = 0.85$): solid line, dash line and dotted line denote $f_0 = 0.0005, 0.001$ and 0.002 respectively.

To examine the influences of different parameters on the dynamic response amplitude, Figure 9.8 shows two dimensional plots. It is shown that the frequency response patterns of the nonlinear isolation system are similar to those of the Duffing oscillator with softening stiffness (see, Nayfeh and Mook (1979)). Two inherently nonlinear characteristics are shown: 1) the response curves bend to the lower frequency range with increasing

response amplitude; 2) multiple solutions exist in the low-frequency range. In Figure 9.8(a), the nonlinear parameter and the force amplitude are kept the same to show the effect of damping. Increasing the damping parameter ξ, the response amplitude decreases, which is similar to its effects on responses of linear systems. Figure 9.8(b) examines the effect of parameter α, and shows that negative stiffness by NSM increases with this parameter, so that the resonance frequency is reduced. Similarly, Figure 9.8(c) plots the influences of the force magnitude which indicates that an increase in f_0 results in a larger response amplitude.

9.2.2 Stability analysis

The stability of the approximate solutions obtained above can be studied by investigating the corresponding characteristic matrix of Eqs. (9.12), that is

$$A = \begin{pmatrix} -\xi & -\frac{1}{2\Omega} f_0 \cos\phi \\ \frac{1}{r}\Big(-\frac{\Omega}{2} + \frac{1}{2\Omega} + \frac{2\alpha}{\pi\Omega r^2}\big(K(r) - \frac{E(r)}{1-r^2}\big)\Big) & \frac{1}{2\Omega r} f_0 \sin\phi \end{pmatrix}, \tag{9.18}$$

where the following derivatives of elliptical integrals $K(r)$ and $E(r)$ were used (see, Whittaker and Watson (1996)), i.e.,

$$\frac{\mathrm{d}K(r)}{\mathrm{d}r} = \frac{E(r)}{r(1-r^2)} - \frac{K(r)}{r}, \quad \frac{\mathrm{d}E(r)}{\mathrm{d}r} = \frac{E(r) - K(r)}{r}.$$

Replacing the trigonometric functions in Eq. (9.18) using Eqs. (9.13), the characteristic matrix is rewritten as

$$A = \begin{pmatrix} -\xi & \frac{\Omega r}{2} - \frac{r}{2\Omega} + \frac{2\alpha}{\pi\Omega r}\big(K(r) - E(r)\big) \\ -\frac{\Omega}{2r} + \frac{1}{2\Omega r} + \frac{2\alpha}{\pi\Omega r^3}\big(K(r) - \frac{E(r)}{1-r^2}\big) & -\xi \end{pmatrix}. \tag{9.19}$$

The characteristic equation is

$$\lambda^2 + 2\xi\lambda + b = 0, \tag{9.20}$$

where

$$b = \Big(\frac{\Omega r}{2} - \frac{r}{2\Omega} + \frac{2\alpha}{\pi\Omega r}\big(K(r) - E(r)\big)\Big)\Big(\frac{\Omega}{2r} - \frac{1}{2\Omega r} - \frac{2\alpha}{\pi\Omega r^3}\big(K(r) - \frac{E(r)}{1-r^2}\big)\Big) + \xi^2.$$

For a stable response, the corresponding solutions of Eq. (9.20) must have negative real parts. Since $\xi > 0$ generally holds true for a physical system, it requires $b > 0$.

The stabilities of responses of the system for $\alpha = 0.90$ and 0.85 are identified and shown in Figure 9.9. In the figure, the dashed lines correspond to a negative value of b, which denote unstable solutions, while the solid lines represent stable solutions with positive

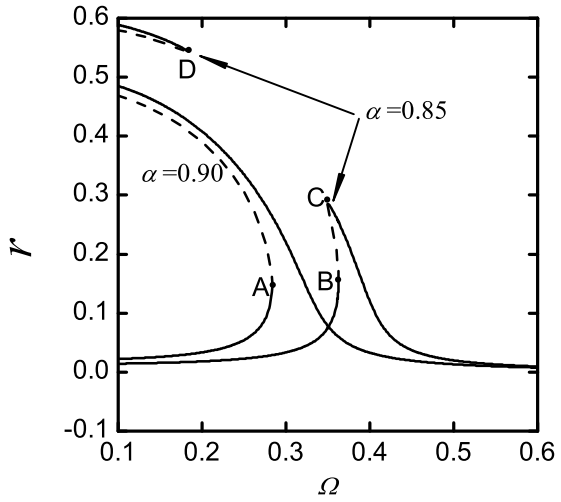

FIGURE 9.9: Stabilities of the solutions obtained by using averaging method ($\xi = 0.01, f_0 = 0.002$). Solid lines represent stable solutions; dashed lines denote unstable solutions.

b. At points A, B, C and D, the value of b is zero. These points are the critical points between the stable and unstable solutions. It can be seen that for α=0.90, there is a continuous branch of unstable solutions and two stable solution branches. However, the solution branches become discontinuous when $\alpha = 0.85$. The stabilities of solutions shown in Figure 9.8 can also be determined in a similar way.

9.2.3 Nonlinear transmissibility

To address this important issue involving the performance of a designed isolation system, we have to understand the main differences of this nonlinear isolator from its linear counterparts in the following aspects.

The first is that the configuration of the system is different from a conventional linear isolator. As shown in Figure 9.1 and mentioned in Section 9.1, the investigated nonlinear isolator consists of a linear spring-damper (k, c) unit and a NSM made up of two bars under compression forces P. The former is connected to the base point C where only a vertical reaction force is created. The bars subject to two constant forces are allowed to move freely only in the horizontal direction. Therefore, at each bar end point (A or B), a vertical reaction force and a horizontal motion are produced. Since the horizontal motions at point A or B of the bars are restricted by the length l of the rigid bars, its calculation is not necessary in practical designs. However, for an expected performance of the design, we have to investigate force transmission to the base points separately.

There are also inherent nonlinear characteristics introduced by adding NSM. Due to the nonlinearity, the response of the system does not vary linearly with excitation force

magnitude. Also, multiple frequency components exist in the steady-state response and thus the response as well as transmitted force is not time-harmonic. To reveal the force transmission behaviour accurately, detailed information on the frequency components, their magnitudes and relative phase angles in the response are needed. It is usually too complex to obtain. However, as discussed in Section 9.2.1, the averaging method provides a very good first-order approximation neglecting the effects of other response components. The derived nonlinear equation (9.15) can be directly used to estimate force transmissibility (see, Virgin et al. (2008)).

Based on the above discussions as well as the derived averaged solution (9.15), we study the force transmission to base points C and A, B in this section, but leave the study of sub-harmonic resonances to Section 9.2.4.

Force transmissibility at the vertical spring base point C

The non-dimensional transmitted force to the base point C consists of the vertical spring force and damping force, and is given by

$$f_{t1} = 2\xi X' + X. \tag{9.21}$$

When the solution $X = r\cos(\Omega T + \phi)$ is introduced, the magnitude of f_{t1} becomes

$$|f_{t1}| = r\sqrt{(2\xi\Omega)^2 + 1}. \tag{9.22}$$

Thus the force transmissibility at the vertical spring base point may be defined as

$$TR_1 = \frac{|f_{t1}|}{f_0} = \frac{r}{f_0}\sqrt{(2\xi\Omega)^2 + 1} = \frac{\sqrt{(2\xi\Omega)^2 + 1}}{\sqrt{(2\xi\Omega)^2 + \left(\Omega^2 - 1 + \beta(r,\alpha)\right)^2}}. \tag{9.23}$$

This equation indicates that the force transmissibility at the base point C relates to the receptance function shown in Eq. (9.15) by a factor $\sqrt{(2\xi\Omega)^2 + 1}$, which is the transfer function of the linear vertical spring-damper unit. The variations of force transmissibility TR_1 with the excitation frequency Ω and amplitude r are shown in Figure 9.10. Under the same Ω and r, the force transmissibility grows with α in the lower-frequency range, but remains almost the same at higher frequencies ($\Omega > 3$) where the three surfaces merge with each other. However, when the excitation frequency is near the resonant frequency $\Omega_n = 1$ of the linear isolator, TR_1 reduces significantly, which shows the benefits of introducing NSM.

Eq. (9.23) also shows that the force transmissibility TR_1 is a function of the response amplitude r when $\beta \neq 0$. Since the response amplitude depends on the force amplitude f_0, TR_1 also depends on f_0, which is of concern in the applications of nonlinear isolators. Figure 9.11(a) shows the influence of force amplitude on TR_1 by setting the parameters of the nonlinear system as $\alpha = 0.01, \beta = 0.95$ while changing f_0 from 0.001, 0.002 to

0.005, and comparing the transmissibility TR_1 with that of the corresponding linear system of $f_0 = 0.001, \xi = 0.01, \alpha = 0$. With other parameters fixed, the result suggests that the excitation magnitude affects the force transmissibility at point C only when the excitation frequency is close to or smaller than the linearised fundamental frequency Ω_n. At larger frequencies than $\Omega_n = \sqrt{1-\alpha}$ where the isolator is designed to function, the force transmissibility is not sensitive to the magnitude of the excitation force.

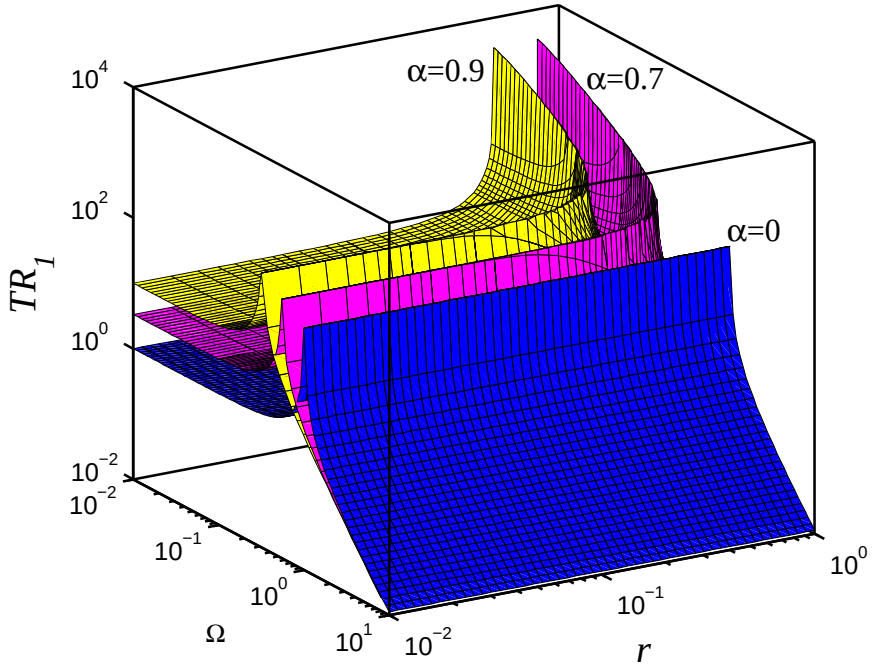

FIGURE 9.10: Force transmission to base point C ($\xi = 0.01$). The yellow, magenta and blue surfaces correspond to $\alpha = 0.9, \alpha = 0.7$ and $\alpha = 0$ respectively.

With prescribed excitation magnitude and damping coefficient, Figure 9.11(b) plots the influence of the nonlinear parameter α on TR_1. As α increases from 0 to 0.95, the corresponding peaks in the transmissibility TR_1 curves move to lower frequencies and the frequency range where $TR_1 < 1$ is enlarged, which is beneficial to vibration isolations. It shows multiple branches of transmissibility, corresponding to different solutions, in the low-frequency range where the value of TR_1 might be large. These large values of transmissibility are not desirable and should be avoided. This can be realised by choosing a suitable working frequency range in the isolation design.

Vertical force transmissibility at bar base points A and B

The total non-dimensional vertical force transmitted to these base points is

$$f_{t2} = -\alpha \frac{X}{\sqrt{1-X^2}}. \tag{9.24}$$

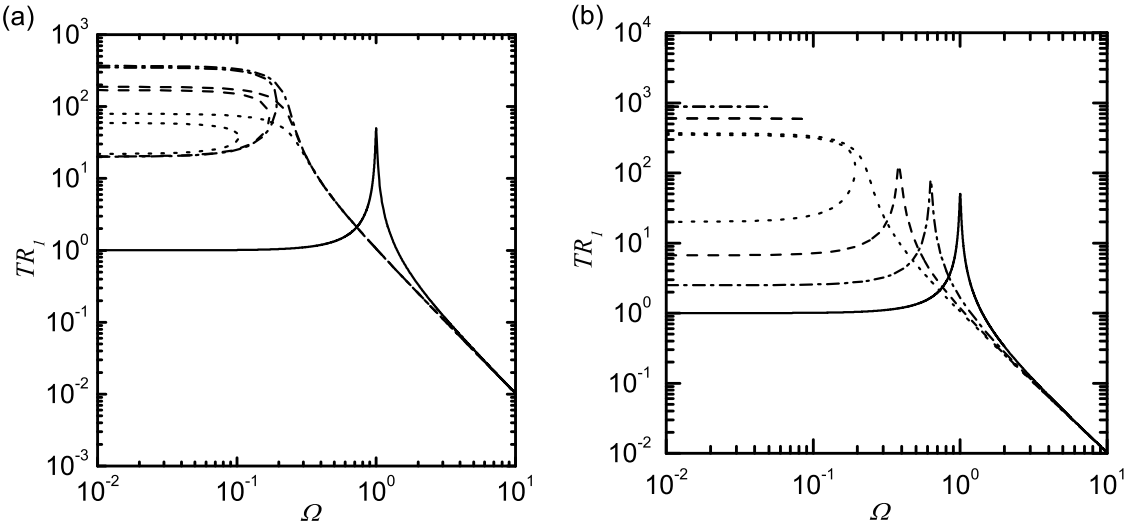

FIGURE 9.11: Influences of parameters on TR_1. (a) Varying f_0 with $\xi = 0.01$; solid line $f_0 = 0.001, \alpha = 0$, i.e., linear case; dash-dotted line, dash line and dotted line for $\alpha = 0.95$ while $f_0 = 0.001, 0.002$ and 0.005, respectively. (b) Varying α with $f_0 = 0.001, \xi = 0.01$: solid line $\alpha = 0$, i.e., linear case; dash-dotted, dashed and dotted lines for $\alpha = 0.60, 0.85$ and 0.95, respectively.

When $\alpha > 0$, f_{t2} is an odd function of X monotonically decreasing with X. Thus its absolute value becomes the largest when $X = \pm r$, which is

$$|f_{t2}|_{max} = \alpha \frac{r}{\sqrt{1-r^2}}. \tag{9.25}$$

For a given value of f_0, the maximum force transmissibility from the mass to the ends of bars is

$$TR_2 = \frac{|f_{t2}|_{max}}{f_0} = \frac{\alpha}{\sqrt{1-r^2}} \cdot \frac{r}{f_0}. \tag{9.26}$$

TR_2 is thus $\alpha/\sqrt{1-r^2}$ times the nonlinear receptance given by Eq. (9.15). Its variations with the excitation frequency and response amplitude are shown in Figure 9.12, which is of a similar pattern with Figure 9.6. One difference is that at higher frequencies, a larger nonlinear parameter would correspondingly induce slightly larger force transmissibility TR_2 and the surfaces do not merge with each other.

9.2.4 Sub-harmonic resonances

For a linear system with one degree of freedom, there is only one resonance frequency in its dynamic response. However, this is not valid for a nonlinear system. Because of nonlinearity, resonances may happen even when the excitation frequency is away from the natural frequency of the linearised system. For an effective isolation of vibrations, of special interest are sub-harmonic resonances that may occur even when the excitation frequency is well above $\sqrt{2}\Omega_n$.

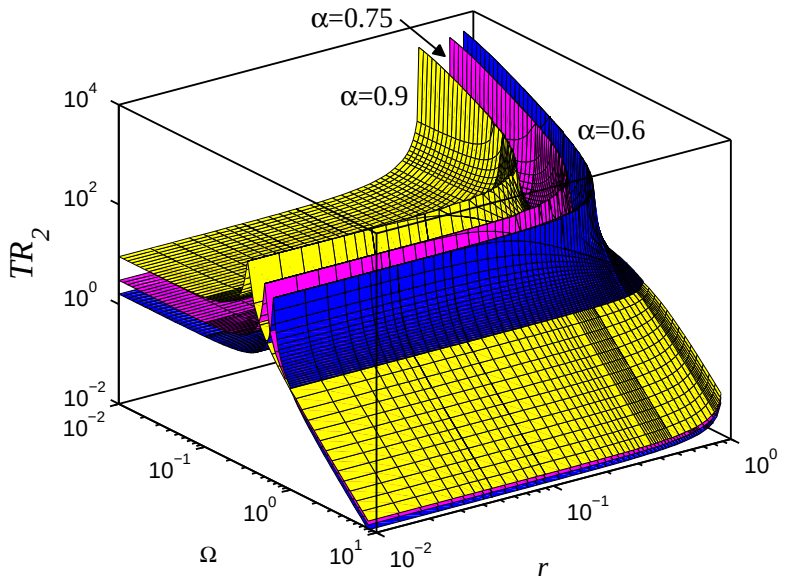

FIGURE 9.12: The variation of TR_2 with excitation frequency Ω and amplitude r ($\xi = 0.01$). The yellow, magenta and blue surfaces correspond to $\alpha = 0.9, \alpha = 0.75$ and $\alpha = 0.6$, respectively.

To reveal the sub-harmonic resonances of this nonlinear system, Eq. (9.7) was numerically integrated using a fourth-order Runge-Kutta method with initial conditions of $(X_0, Y_0) = (0, 0)$. In Figure 9.13(a), the non-dimensional displacement $X_s(\tau_s)$ of the mass at sampling time $\tau_s = \tau_0 + 2\pi(n-1)/\Omega, (n = 1, 2, \cdots)$ with $\tau_0 = 1000$, is recorded for each value of Ω. In this way, if the period of the steady state motion equals the sampling time interval $2\pi/\Omega$, X_s will remain the same for all samplings, so that there will only be a single sampling point shown in the figure for a given Ω. This is the case when $0.75 < \Omega < 0.81$ or $1.05 < \Omega < 1.2$ in Figure 9.13(a). However, when Ω lies between 0.81 and 1.05, where there are three different sampling points, which suggests occurrence of sub-harmonic resonances with the period of motion being $6\pi/\Omega$. Figure 9.13(b) plots the variations of the maximum displacement of the mass in steady state motion against the excitation frequency. It shows the maximum displacement increases significantly in the frequency band where sub-harmonic resonances occur.

Figure 9.13(c) and (d) provide detailed information of a response with a large sub-harmonic frequency component in the time domain and frequency domain, respectively. A time history of the steady-state displacement is shown in Figure 9.13(c). It is then Fourier transformed to obtain its frequency components (ω_r) in Figure 9.13(d). Clearly, a sub-harmonic resonance occurs as one of the response components is one third of the excitation frequency $\omega_r = \Omega/3$. It should be noted that in this particular case, the excitation frequency Ω lies in the functioning frequency range of the linearised system. The sub-harmonic resonances are unwanted as it reduces the effective isolation capacity. More discussion on avoiding such resonances will be given in Section 9.4.

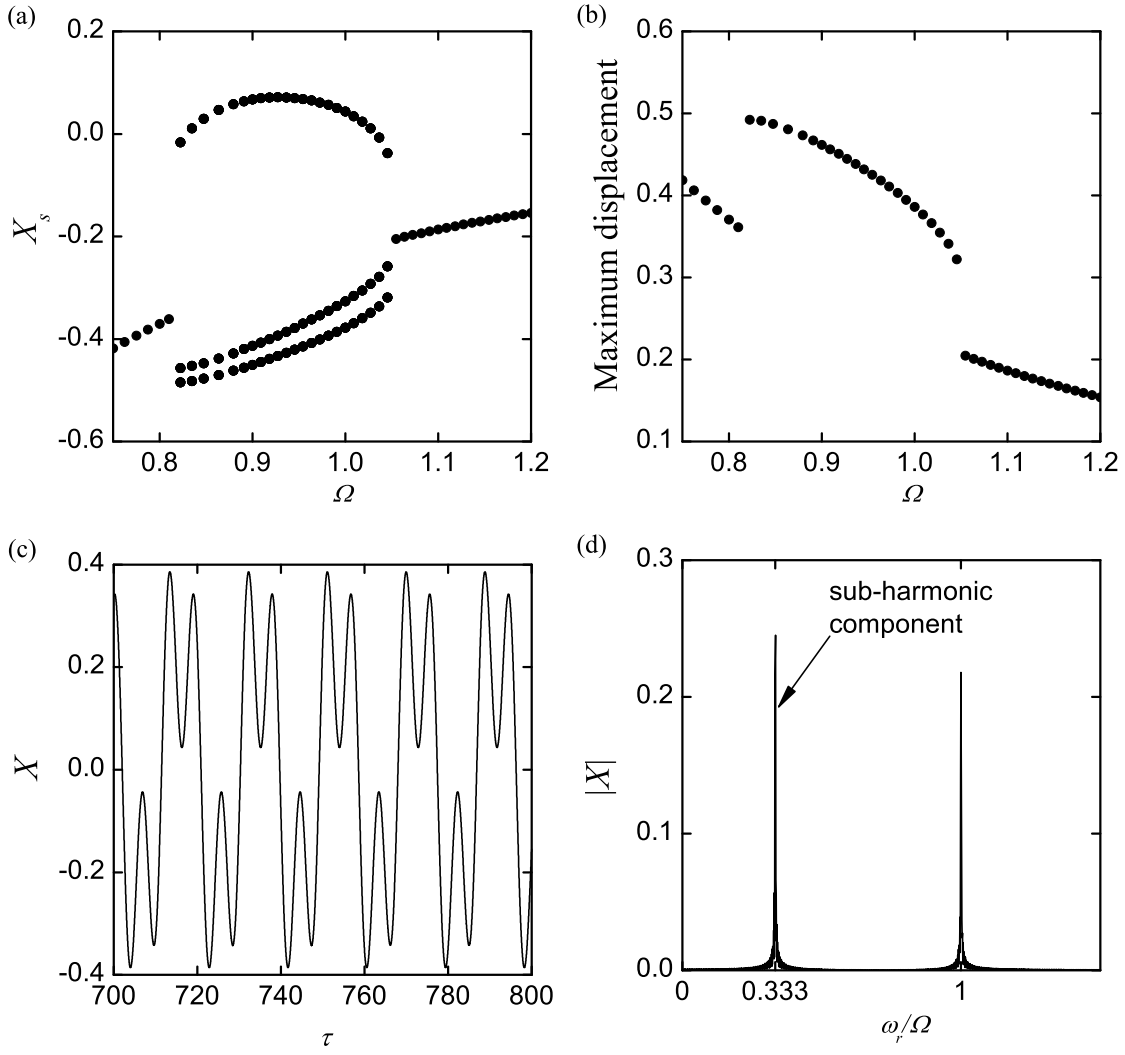

FIGURE 9.13: Sub-harmonic resonances ($\xi = 0.01, \alpha = 0.85, f_0 = 0.2$). (a) Sampling displacement; (b) maximum displacement; (c) time history of displacement ($\Omega = 1.0$) and (d) frequency components in the response ($\Omega = 1.0$).

9.3 Power flow characteristics of the system

9.3.1 Instantaneous power

The power flow equation of the system can be obtained by multiplying both sides of Eq. (9.2) by the velocity X', that is

$$X'X'' + 2\xi X'X' + X'X(1 - \frac{\alpha}{\sqrt{1 - X^2}}) = X' f_0 \cos \Omega\tau, \tag{9.27}$$

which may be further written as

$$K' + p_d + U' = p_{in}, \tag{9.28}$$

where

$$K' = X'X'', \quad p_d = 2\xi X'^2,$$
$$U' = X'X(1 - \frac{\alpha}{\sqrt{1-X^2}}), \quad p_{in} = X' f_0 \cos\Omega\tau$$

are the rate of change of kinetic energy, dissipated power, the rate of change potential energy and instantaneous input power, respectively. The rate of change of system mechanical energy can be obtained by summing K' and U'. Integrating these variables with respect to τ, we obtain

$$\Delta K = \frac{X'^2}{2}, \tag{9.29a}$$
$$E_d = \int_{\tau_i}^{\tau_i+\tau_p} 2\xi X'^2 \, \mathrm{d}\tau, \tag{9.29b}$$
$$\Delta U = \int_{\tau_i}^{\tau_i+\tau_p} X'X(1-\frac{\alpha}{\sqrt{1-X^2}}) \, \mathrm{d}\tau = \frac{X^2}{2} + \alpha\sqrt{1-X^2}, \tag{9.29c}$$
$$E_{in} = \int_{\tau_i}^{\tau_i+\tau_p} X' f_0 \cos\Omega\tau \, \mathrm{d}\tau, \tag{9.29d}$$

where ΔK and ΔU stand for the net changes in kinetic and potential energies, respectively; E_d and E_{in} are the total dissipated energy and input energy, respectively; τ_p is the time span for the integration and the system was assumed to start from $(X_0, X_0') = (0, 0)$ at $\tau = \tau_i$. The nonlinearity of the system is demonstrated by the last term in Eq. (9.29c). For a linear isolation system, the maximum potential energy corresponds to the largest deflection. However, it is not true for the current nonlinear system as U does not increase linearly with $|X|^2$. When $0 < \alpha < 1$, it is shown in Figure 9.14 that two local maximums exist at $X = \pm\sqrt{1-\alpha^2}$, which correspond to unstable equilibrium points of the unforced system.

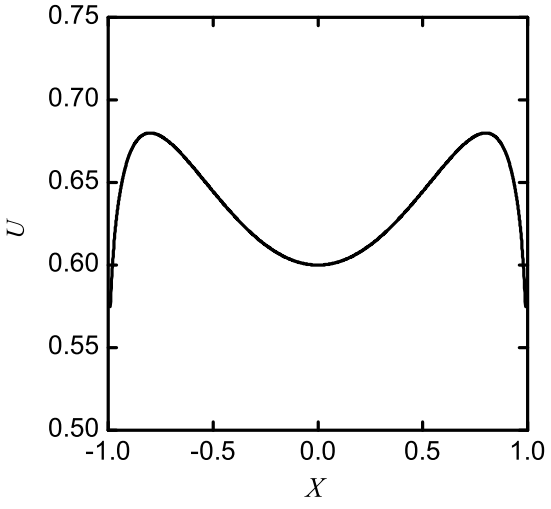

FIGURE 9.14: Variations of the potential energy with displacement ($\alpha = 0.6$).

The power flow characteristics of the system with multiple solutions are of interest. Figure 9.15 shows a time series of instantaneous input power into the system, which indicates the sensitivity of the input power to the initial conditions for a nonlinear system.

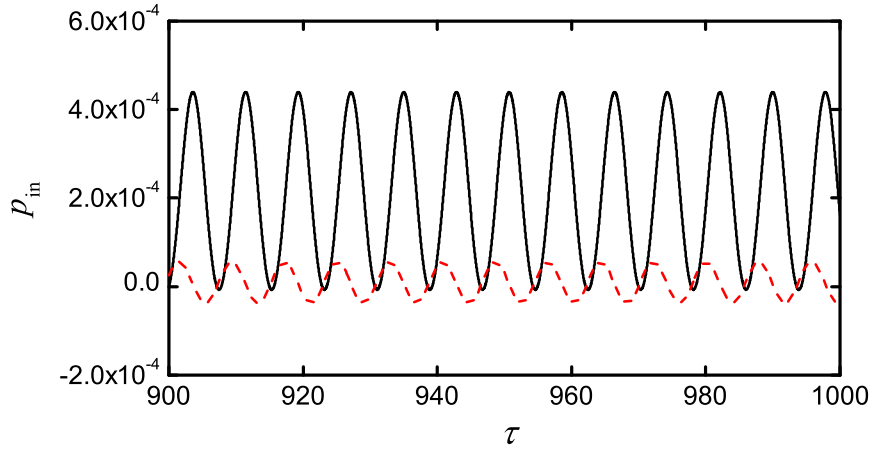

FIGURE 9.15: Sensitivity of input power to initial conditions ($\xi = 0.01, \alpha = 0.8, f_0 = 0.003, \Omega = 0.4$). Solid line for $(X_0, Y_0) = (0, 0.15)$ and dashed line for $(X_0, Y_0) = (0, 0)$.

9.3.2 Time-averaged power

Here we consider the time-averaged power flow behaviour of the nonlinear system. If the steady-state motion of the system is periodic with a period of τ_p, its maximum kinetic energy is

$$K_{max} = \frac{Y_{max}^2}{2}, \tag{9.30}$$

where Y_{max} is the maximum velocity. There will be no net changes in both kinetic and potential energy over a period of oscillation. The time-averaged input power equals the time-averaged dissipated power, and can be calculated by the integrals

$$\bar{p}_{in} = \frac{1}{\tau_p} \int_{\tau_i}^{\tau_i+\tau_p} X' f_0 \cos \Omega\tau \, \mathrm{d}\tau, \tag{9.31}$$

$$\bar{p}_d = \frac{1}{\tau_p} \int_{\tau_i}^{\tau_i+\tau_p} 2\xi X'^2 \, \mathrm{d}\tau, \tag{9.32}$$

respectively, where τ_0 is a chosen starting time and τ_p is the averaging time. For a nonlinear system, when the system or excitation parameters vary, the period of steady-state motions might also change. For instance, as discussed in Section 9.2.4, a sub-harmonic resonance may occur. Then the period of steady-state motion of the system would be three times that of excitation force so that $\tau_p = 6\pi/\Omega$. For vibration isolation designs, we aim to reduce the input energy to the system. Therefore, the time-averaged input power may be adopted as a vibration isolation performance indicator.

When a first-order approximation is applied, the relationship shown by Eq. (9.13a) might be used to derive the power flow variables. As for this case $X' = -r\sin(\Omega\tau + \phi)$, the averaged input power is expressed as

$$\bar{p}_{in} = -\frac{1}{\tau_p}\int_{\tau_i}^{\tau_i+\tau_p} r\Omega\sin(\Omega\tau+\phi) f_0\cos\Omega\tau\,\mathrm{d}\tau = -\frac{1}{2}r\Omega f_0\sin\phi, \tag{9.33}$$

where the averaging time τ_p is taken as $2\pi/\Omega$. Using Eq. (9.13a), the expression for averaged input power can be transformed to

$$\bar{p}_{in} = \xi r^2\Omega^2. \tag{9.34}$$

The maximum kinetic energy of the mass in the steady state motion is written as

$$K_{max} = \frac{Y_{max}^2}{2} = \frac{r^2\Omega^2}{2}. \tag{9.35}$$

Comparing the above two equations, it can be found that $\bar{p}_{in}$ and K_{max} are proportional when a first-order approximation of the response is considered and the damping coefficient ξ is fixed. Figures 9.16, 9.17 and 9.18 show that the results obtained from analytical solutions (indicated by the different lines) agree very well with those from numerical simulations (represented by the symbols). The power flow spectra are shown in decibel scale (dB reference:10^{-12}). There are no numerical simulation results available for unstable solutions.

In Figure 9.16, the time-averaged input power and the maximum kinetic energies for three different damping levels are plotted against the non-dimensional excitation frequency. It is shown that their peak values are found around the linearised natural frequency Ω_n. The figure indicates that a lighter damping of $\xi = 0.01$ would give a larger peak in both averaged input power and kinetic energy than the systems with $\xi = 0.02$ or $\xi = 0.05$. However, when the excitation frequency is away from resonances, the effects of damping on the two quantities are quite different. In these frequency ranges, the time-averaged input power would increase with damping while in contrast the system's maximum kinetic energy is not sensitive to it.

Figure 9.17 presents the influences of the nonlinear parameter α on time-averaged input power as well as maximum kinetic energy of the mass. It shows that with the increase of α from zero towards unity, the peaks of the curves shift to the left with possible multiple solutions at frequencies smaller than 0.1. However, the peak values remain approximately the same for different α with the considered damping and excitation magnitude. This characteristic is different from that of the force transmissibility whose peak values increase with nonlinearity, as discussed in the previous section. It also suggests that in the low-frequency range, a larger value of α will induce a higher level of power input into the system and a larger kinetic energy. In contrast, when the excitation frequency range is close to unity, which is the original natural frequency without using

NSM, the addition of NSM can greatly reduce the time averaged input power and kinetic energy. At much higher frequencies, adding NSM is shown to have only a small influence on p_{in} and K_{max} . As natural frequencies of isolators are usually designed to be lower than the excitation frequency, a large value of α is beneficial for decreasing the power input into the system and also system's kinetic energy.

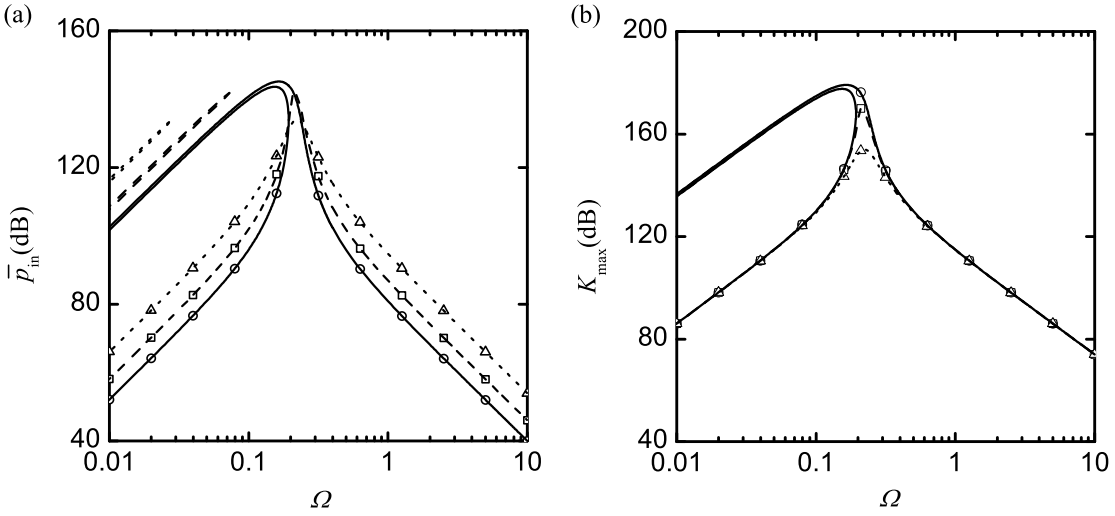

FIGURE 9.16: Influences of damping on (a) averaged input power and (b) maximum kinetic energy ($\alpha = 0.95, f_0 = 0.001$). Solid line, dash line and dotted line represent the cases $\xi = 0.01, 0.02$ and 0.05, respectively. Circles ($\xi = 0.01$), squares ($\xi = 0.02$) and triangles ($\xi = 0.05$) are the results from numerical simulations.

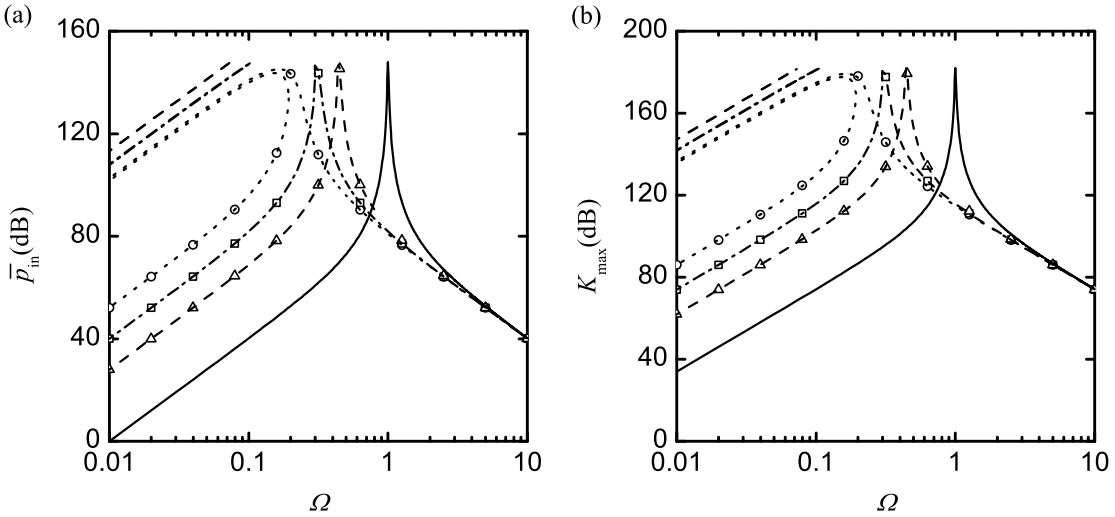

FIGURE 9.17: Influences of nonlinear parameter α on (a) averaged input power and (b) maximum kinetic energy ($\xi = 0.01, f_0 = 0.001$). Solid line, dash line, dash-dotted and dotted line refer to $\alpha = 0, 0.80, 0.90$ and 0.95 respectively. Circles ($\alpha = 0.95$), squares ($\alpha = 0.90$) and triangles ($\alpha = 0.80$) are the results from numerical simulations.

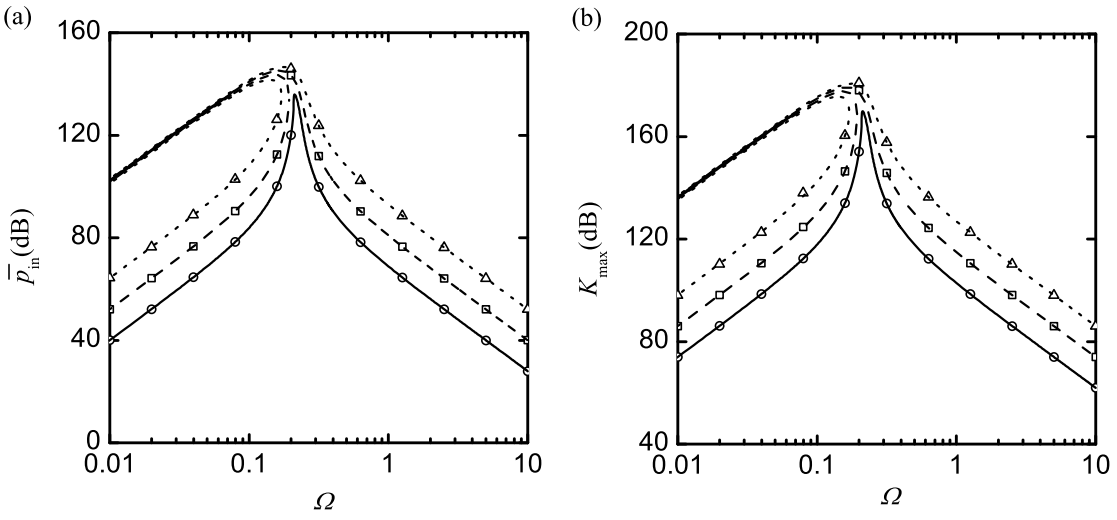

FIGURE 9.18: Influences of excitation amplitude on (a) averaged input power and (b) maximum kinetic energy ($\xi = 0.01, \alpha = 0.95$). Solid line, dashed line and dotted line refer to $f_0 = 0.0005, 0.001$ and 0.002 respectively. Circles ($f_0 = 0.0005$), squares ($f_0 = 0.001$) and triangles ($f_0 = 0.002$) are the results from numerical simulations.

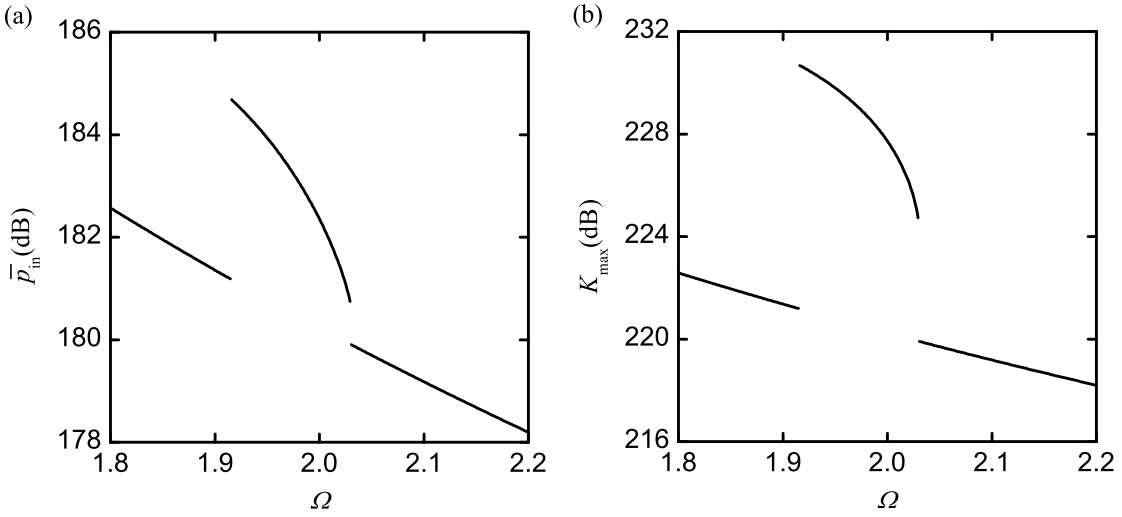

FIGURE 9.19: The plot of (a) time-averaged input power and (b) maximum kinetic energy of the system with possible sub-harmonic resonances ($\xi = 0.005, \alpha = 0.52, f_0 = 0.8$).

In Figure 9.18, the influence of the excitation magnitude on power flow is examined. It shows that with the frequency and the damping coefficient values fixed, averaged input power and kinetic energy would increase with the excitation magnitude. It is also found that an increase in excitation amplitude results in a larger maximum input power value. Moreover, with the increase of excitation amplitude, the power flow curves bend to the lower-frequency band.

Figure 9.19 shows the changes of the maximum kinetic energy and time-averaged input

power with excitation frequency when sub-harmonic resonances occur. The results are obtained by numerical simulations only as the averaging approximation is no longer valid. As stated earlier, under sub-harmonic resonances, the period of the steady-state response would be three times that of the excitation. Thus, the time span for averaging is chosen to be $6\pi/\Omega$. The plot clearly indicates a sudden jump up in both the kinetic energy and averaged input power curves when $\Omega = 1.91$ and a jump down at the higher frequency of 2.03. It can be shown that in the frequency range between the two critical frequencies, there exist sub-harmonic resonances. Obviously, in terms of minimizing kinetic energy and averaged input power, the occurrence of sub-harmonic resonances is undesirable for vibration isolation.

9.4 Suggestions for engineering applications

9.4.1 Restriction on maximum deflection

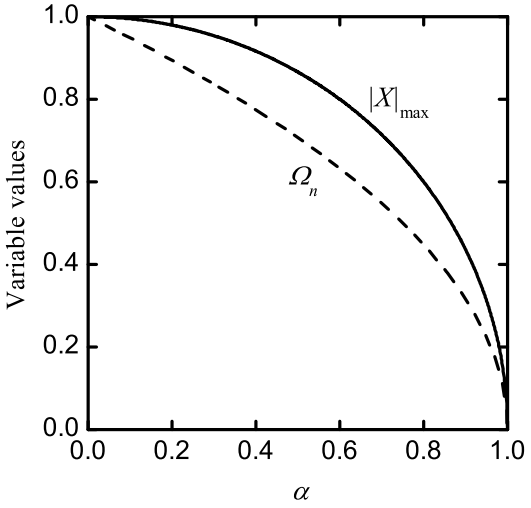

FIGURE 9.20: Variations of $|X|_{max}$ and Ω_n with respect to parameter α. Solid line $|X|_{max}$ and dashed line Ω_n.

For practical applications, it is necessary to consider the maximum allowable deflection $|X|_{max}$ of the mass from the stable equilibrium to avoid reaching $X = \pm 1$. The restriction on $|X|_{max}$ can be determined by ensuring that the restoring force always points to the static equilibrium $X = 0$, which leads to

$$|X| < \sqrt{1-\alpha^2}. \tag{9.36}$$

Thus $|X|_{max}$ should be $\sqrt{1-\alpha^2}$, which indicates the mass should not deflect beyond the two unstable equilibriums $(\pm\sqrt{1-\alpha^2})$ of the unforced system. In Figure 9.20, $|X|_{max}$ and Ω_n are plotted with respect to parameter α. It is observed that an increase

in α reduces both $|X|_{max}$ and Ω_n. As stated earlier, a low fundamental frequency Ω_n is expected for a larger frequency band of effective vibration isolation, but it will also restrict the allowable maximum deflection. Thus the value of parameter α should be properly chosen with consideration of both lowering the natural frequency of the linearised system and ensuring sufficient tolerable deflection.

9.4.2 Suppressing sub-harmonic resonances

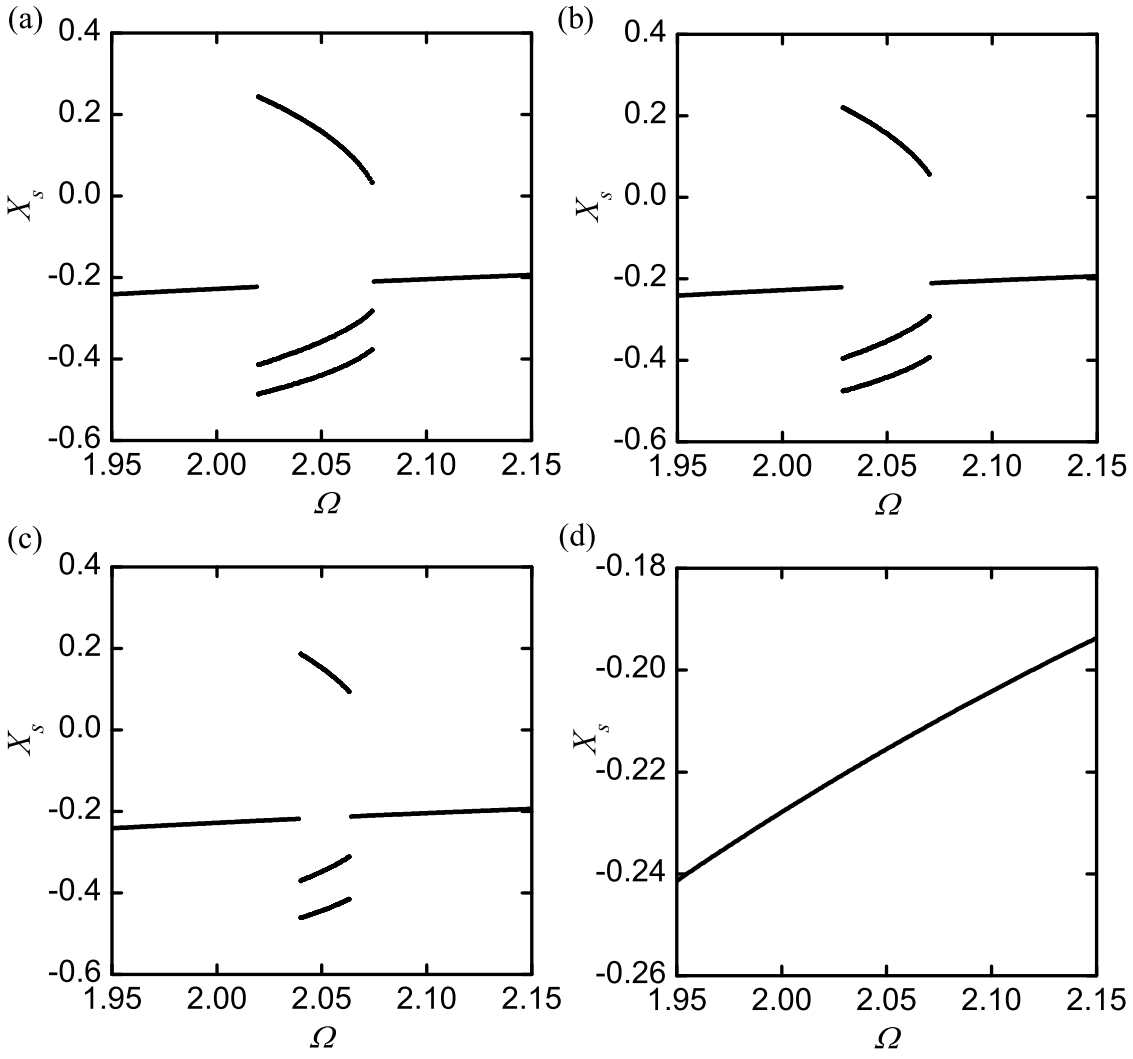

FIGURE 9.21: Diagrams to demonstrate the suppression of sub-harmonic resonances ($\alpha = 0.5, f_0 = 1.0$). For (a), (b), (c) and (d) ξ was set as 0.0050, 0.0054, 0.0058 and 0.0060, respectively.

For a more robust isolation of vibration, the sub-harmonic resonances should be avoided. Note that for small deflections of $X^4 \ll 1$, the higher order terms in Eq. (9.5) may be neglected, so that we have

$$X'' + 2\xi X' + X(1-\alpha) - \frac{\alpha}{2}X^3 = f_0 \cos \Omega\tau. \tag{9.37}$$

This equation corresponds to a Duffing system with a softening stiffness. Its sub-harmonic resonances were studied by using a multi-scaled method (see Nayfeh and Mook (1979)). It was shown that sub-harmonic resonances of a softening Duffing system only happen when the excitation frequency is less than three times the natural frequency of the linearized system. Hence, for the current nonlinear system, α may be chosen such that $3\Omega_n$ is still smaller than Ω. When the excitation frequency Ω is around $3\Omega_n$, the following condition has to be satisfied for a nontrivial solution of the sub-harmonic response (see Nayfeh and Mook (1979)).

$$(\frac{-63\alpha\Lambda^2}{8\sqrt{1-\alpha}}+\sigma)^2 < \sigma^2 - 63\xi^2, \tag{9.38}$$

where $\Lambda = 0.5f_0/(\Omega^2 - \Omega_n^2)$ and $\sigma = \Omega - 3\Omega_n$. With an increase in damping coefficient ξ, the value of f_0 will be confined to a smaller range for the occurrence of sub-harmonic resonances. Moreover, when f_0 is fixed, the frequency band for sub-harmonic resonances will become narrower and eventually disappear. This is shown by Figure 9.21, which is obtained by using the similar sampling method as used for the data in Figure 9.13(a). It clearly suggests that an increase in damping can reduce the frequency band for sub-harmonic resonances, which disappear when $\xi = 0.0060$.

9.5 Conclusions

A nonlinear vibration isolation system with a negative stiffness mechanism has been investigated with emphasis on its intrinsic nonlinear dynamic behaviour and power flow characteristics. The responses of the forced system were obtained analytically and numerically. Nonlinear transmissibility for this system was defined based on the averaging method. Power flow behaviour of the system was examined to for a better evaluation of the vibration isolation performance. It was shown that a negative stiffness mechanism provides benefits for low vibration isolation by enlarging the frequency range where there is low power input. It was also shown that time-averaged input power provides a good index of isolation performance by incorporating the effects of many frequency components in the response.

Adding NSM to the original linear isolator is beneficial for low-frequency vibration isolation. This is successfully demonstrated by the following findings: (1) a much lower natural frequency is achieved than the corresponding linear isolation system; (2) the effective isolation frequency range is enlarged, as shown by transmissibility curves; (3) power input into the system is reduced when the natural frequency is close to the resonance frequency range of the corresponding linear isolator. However, adding NSM also introduces a restriction on maximum deflection, which should be taken into consideration in the design stage.

The investigation reveals the dynamical and power flow characteristics of this nonlinear system as follows. (1) Multiple static equilibria with a pitchfork bifurcation exist for the unforced system. (2) The primary resonance curves bend to the low-frequency range which is beneficial to isolation. (3) Non-uniqueness of time-averaged input power might be encountered in the steady state and the power flow is sensitive to initial conditions. (4) The system exhibits sub-harmonic resonances which can considerably increase the averaged input power as well as maximum kinetic energy. Increasing damping can assist the suppression of sub-harmonic responses. (5) The peak values of averaged input power increase as damping decreases and/or as excitation amplitude increases. (6) The peak values of maximum kinetic energy and averaged input power are not sensitive to the nonlinear parameter α.

Chapter 10

Conclusions and future work

Power flow behaviour of linear dynamical systems has been widely investigated using established theoretical and numerical approaches. However, in spite of the potential scientific and engineering benefits, the fundamental principles governing the flow of vibration energy in nonlinear dynamical systems remain unclear. This thesis focuses on developing the power flow analysis approach for nonlinear dynamical systems, investigating their power flow behaviour arising from different kinds of damping/stiffness nonlinearities, and demonstrating applications for energy harvesting and passive vibration control.

Following a review of basic concepts and approaches in power flow analysis as well as fundamentals in nonlinear dynamics in Chapter 2, methods for power flow analysis of nonlinear dynamical systems were discussed in Chapter 3. Then two typical nonlinear systems, the Duffing and the Van der Pol oscillators, were investigated in Chapters 4 and 5 using the developed approach to reveal and understand their power flow behaviour due to nonlinear stiffness and nonlinear damping, respectively. Based on analytical approximations as well as numerical simulations, the thesis re-examined the nonlinear phenomena, such as multiple responses, limit cycle oscillations, bifurcation and chaos, from the viewpoint of vibrational power flows. Chapter 6 and 7 continued to study the power flows in two degrees-of-freedom nonlinear vibration systems with nonlinear isolators and nonlinear dynamic absorbers, respectively. Their effectiveness in vibration control was assessed using time-averaged power flows as well as system kinetic energies as performance indicators. These investigations provide insights for better designs of engineering dynamical systems, the performance of which can be analysed and assessed by the developed PFA approach. Inspired by the behaviour of the unforced Van der Pol oscillator, a nonlinear flapping foil system was proposed for vibration energy harvesting in Chapter 8. A nonlinear system with a negative stiffness mechanism for vibration isolation was presented in Chapter 9, with its effectiveness measured by the amount of time-averaged input power.

10.1 Conclusions

The investigations of the power flow behaviour of these nonlinear systems yield the following findings and observations, which contribute to a better understanding of power flow mechanisms in nonlinear dynamical systems and provide useful guidance for dynamical designs of engineering systems.

(1) The power flow characteristics of a nonlinear system in steady-state motion are dependent on the type of response it exhibits. Based on the categories of responses, we have:

- For equilibrium solutions, there may be transient power flows before reaching the steady-state motion, but no power input or exchange in the steady state;
- For periodic solutions, the instantaneous power flow variables will also be periodic. It was shown in Chapter 4 that only the in-phase velocity component with the same frequency as the harmonic excitation will contribute to the time-averaged input power;
- For quasi-periodic motions of the Van der Pol oscillator, the instantaneous input power in the steady state contains frequency components which are not commensurate with each other. However, it was shown in Chapter 5 that only the velocity component in-phase and with the same frequency as the harmonic excitation contributes to the time-averaged input power if the averaging time is large enough;
- For a chaotic response of the Duffing oscillator, it was shown in Chapter 4 that the associated time-averaged input power is insensitive to the initial conditions but tends to an asymptotic value as the averaging time increases.

(2) The associated power flow behaviour of nonlinear systems when they exhibit nonlinear phenomena was investigated in different Chapters. It was shown that

- When there are multiple solutions, instantaneous and time-averaged power flows may change significantly with initial conditions, as shown in Chapters 4 and 9. Basins of attraction can be examined to identify different regions of initial conditions with varying time-averaged power flow levels;
- When sub- or super- harmonic resonances occur, the instantaneous power flow variables may contain large sub-/super- harmonic components, and the time-averaged power flows can increase significantly, as studied in Chapters 4 and 9;
- For limit cycle oscillations of the unforced Van der Pol oscillator, the associated instantaneous dissipated power is positive when its displacement is large, but becomes negative for small deflections. The time-averaged dissipated power will be zero over an oscillation cycle;

- When bifurcation occurs, there may be substantial changes in instantaneous power flow characteristics. However, the influence on time-averaged power flows varies with the type of bifurcation, as shown in Chapters 4 and 5. For systems with nonlinear springs characterised by cubic restoring forces, bifurcation can lead to large jumps in time-averaged power flow curves (Chapters 4, 6 and 7). For the Van der Pol oscillator, however, it was analytically shown that there may be continuous variation of time-averaged power flows at a critical frequency where the system bifurcates from periodic to quasi-periodic motions;
- The associated power flow behaviour of a system with chaotic responses is discussed in Chapter 4, with the findings listed in point (1).

(3) The effects of nonlinear stiffness on power flows were examined in Chapters 4, 6, 7 and 9, while the influences of nonlinear damping were shown in Chapter 5 and 6. It was observed that

- Hardening or softening stiffness has a strong influence on time-averaged power flows when the excitation frequency is close to resonance frequencies by bending the peaks to higher or lower frequency ranges. The stiffness nonlinearity may also lead to non-unique values of time-averaged power flows. Away from the resonant regions, time-averaged input powers are not sensitive to the stiffness nonlinearity;
- Because of the stiffness nonlinearity, the double-well potential Duffing oscillator can display chaotic motions over a large range of excitation frequencies. The corresponding time-averaged power flow behaviour was examined and was summarised previously in point (1);
- The damping term in the VDP oscillator can lead to negative instantaneous/time-averaged input power, as shown in Chapter 5. Cubic damping may be beneficial for vibration isolations by reducing the local peaks in time-averaged power flow curves, as shown in Chapter 6. At excitation frequencies far away from resonant frequencies, the effects of cubic damping on time-averaged power flows are small.

(4) Investigations of the power flow behaviour of two-DOF nonlinear systems showed that introductions of softening stiffness or nonlinear cubic damping in an isolator can provide benefits for nonlinear vibration isolation. For a softening (or hardening) stiffness primary structure, hardening (or softening) nonlinear stiffness absorbers, instead of their linear counterparts, may be attached for better vibration absorption performance.

(5) Adding hardening stiffness in the supporting springs of a flapping foil can assist in stable energy harvesting using the device. In comparison, introducing a negative-stiffness-mechanism with a softening stiffness characteristic benefits low-frequency vibration isolation by reducing time-averaged input powr as well as the maximum kinetic energy over a large range of excitation frequencies.

To summarise, this thesis developed methods for power flow analysis of nonlinear systems and revealed their power flow characteristics. The findings enhanced the understanding of power flow behaviour in nonlinear dynamical systems. The knowledge created in the research can be employed for better designs and applications of nonlinear devices, as demonstrated by the studies on a nonlinear flapping foil energy harvesting system as well as on a nonlinear vibration isolation system with a negative stiffness mechanism.

10.2 Future research

Because of the complex nature of power flow problems associated with nonlinearities, much work is still required to analyse the vibration power flows in more complicated systems. A number of recommendations for further research are provided below.

- Power flow analysis of other single degree-of-freedom nonlinear dynamical systems, such as the parametrically excited systems is needed. Typical nonlinear systems subject to multiple-term excitations or random excitations should be examined to explore their power flow characteristics.
- More detailed investigations on power flow characteristics of two degrees-of-freedom nonlinear dynamical systems are also desirable. The power flow behaviour due to occurrences of complicated nonlinear phenomena, such as saturation and internal resonances, should be clarified.
- Power flow problems of complex multiple degrees-of-freedom systems or continuous sub-systems connected by nonlinear springs/dampers are challenging and need exploration.
- Work on the engineering applications of nonlinear PFA should also be emphasised. For example, parameter optimisation of the flapping foil nonlinear energy harvesting device could be conducted to enhance its efficiency. Experimental work is needed to validate the results obtained using numerical simulations. New configurations of nonlinear devices could be introduced for efficient energy harvesting from the environment. Novel configurations of nonlinear vibration isolators or absorbers may be proposed for vibration control.

Appendix

List of publications

- J. Yang, Nonlinear energy harvesting using a flapping foil, *UK Marine Technology Postgraduate Conference*, Southampton, UK, 2011.
- J. Yang, Y.P. Xiong, J.T. Xing, Investigations on a nonlinear energy harvesting device consisting of a flapping foil and an electro-magnetic generator using power flow analysis, *Proceedings of ASME 2011 International Design Engineering Technical Conferences and Computers and Information in Engineering Conference (IDETC/CIE2011)*, Washington, DC,USA, 2011, pp.1-8.
- J. Yang, Y.P. Xiong, J.T. Xing, Examinations of nonlinear isolators using power flow approach, *Proceedings of the 23rd International Congress of Theoretical and Applied Mechanics (ICTAM)*, Beijing, China, 2012, pp.1-2.
- J. Yang, Y.P. Xiong, J.T. Xing, Power flow behaviour of the Duffing oscillator, *Proceedings of the International Conference on Noise and Vibration Engineering (ISMA 2012)*, Leuven, Belgium, 2012, pp.2601-2610.
- J. Yang, Y.P. Xiong, J.T. Xing, Dynamics and power flow behaviour of a nonlinear vibration isolation system with a negative stiffness mechanism, *Journal of Sound and Vibration* 332 (2013) 167-183.
- J. Yang, Y.P. Xiong, J.T. Xing, Nonlinear power flow analysis of the Duffing oscillator, *Mechanical Systems and Signal Processing* (submitted).

Bibliography

Abramowitz, M. and Stegun, I. A. (1965). *Handbook of mathematical functions: with formulas, graphs, and mathematical tables*, volume 55. Dover Publications.

Ahmed, T. M., Hudson, D. A., and Temarel, P. (2010). An investigation into parametric roll resonance in regular waves using a partly non-linear numerical model. *Ocean Engineering*, 37(14-15):1307 – 1320.

Arnold, F. R. (1955). Steady-state behavior of systems provided with nonlinear dynamic vibration absorbers. *Journal of Applied Mechanics*, 22:487–492.

Beale, L. S. and Accorsi, M. L. (1995). Power flow in two- and three-dimensional frame structures. *Journal of Sound and Vibration*, 185(4):685 – 702.

Bercin, A. N. and Langley, R. S. (1996). Application of the dynamic stiffness technique to the in-plane vibrations of plate structures. *Computers & Structures*, 59(5):869 – 875.

Bernitsas, M. M., Raghavan, K., Ben-Simon, Y., and Garcia, E. M. H. (2008). VIVACE (vortex induced vibration aquatic clean energy): A new concept in generation of clean and renewable energy from fluid flow. *Journal of Offshore Mechanics and Arctic Engineering*, 130(4):041101–041115.

Beshara, M. and Keane, A. J. (1998). Vibrational energy flows between plates with compliant and dissipative couplings. *Journal of Sound and Vibration*, 213(3):511 – 535.

Bisplinghoff, R. L., Ashley, H., and Halfman, R. L. (1955). *Aeroelasticity*. Addision-Wesley Publication.

Cao, Q., Wiercigroch, M., Pavlovskaia, E., Thompson, J., and Grebogi, C. (2008). Piecewise linear approach to an archetypal oscillator for smooth and discontinuous dynamics. *Philosophical Transactions of the Royal Society A: Mathematical, Physical and Engineering Sciences*, 366(1865):635–652.

Cartwright, J. H. E., Víctor, M. E., Hernández-García, E., and Piro, O. (1999). Dynamics of elastic excitable media. *International Journal of Bifurcation and Chaos*, 9(11):2197–2202.

Cho, S., Ha, S.-H., and Park, C.-Y. (2006). Topological shape optimization of power flow problems at high frequencies using level set approach. *International Journal of Solids and Structures*, 43(1):172 – 192.

Choi, W., Xiong, Y., and Shenoi, R. (2009). Power flow analysis for a floating sandwich raft isolation system using a higher-order theory. *Journal of Sound and Vibration*, 319(1-2):228 – 246.

Clarkson, B. L. (1991). Estimation of the coupling loss factor of structural joints. *Proceedings of the Institution of Mechanical Engineers, Part C: Journal of Mechanical Engineering Science*, 205(1):17–22.

Cuschieri, J. M. (1990a). Structural power-flow analysis using a mobility approach of an L-shaped plate. *The Journal of the Acoustical Society of America*, 87(3):1159–1165.

Cuschieri, J. M. (1990b). Vibration transmission through periodic structures using a mobility power flow approach. *Journal of Sound and Vibration*, 143(1):65–74.

Den Hartog, J. . (1934). *Mechanical vibrations*. Dover Publications.

Dimitriadis, E. K. and Pierce, A. D. (1988). Analytical solution for the power exchange between strongly coupled plates under random excitation: a test of statistical energy analysis concepts. *Journal of Sound and Vibration*, 123(3):397–412.

Dong, J. H., Dong, R. G., Rakheja, S., Welcome, D. E., McDowell, T. W., and Wu, J. Z. (2008). A method for analyzing absorbed power distribution in the hand and arm substructures when operating vibrating tools. *Journal of Sound and Vibration*, 311(3):1286–1304.

Dowell, E. H. (1981). Non-linear oscillator models in bluff body aero-elasticity. *Journal of Sound and Vibration*, 75(2):251 – 264.

Fahy, F. J. (1994). Statistical energy analysis: a critical overview. *Philosophical Transactions of the Royal Society of London. Series A: Physical and Engineering Sciences*, 346(1681):431–447.

Fahy, F. J. and Price, W. G. (1998). *IUTAM symposium on statistical energy analysis*, volume 67. Kluwer Academic Publishers.

Farag, N. H. and Pan, J. (1996). Dynamic response and power flow in two-dimensional coupled beam structures under in-plane loading. *The Journal of the Acoustical Society of America*, 99:2930.

Frahm, H. (1911). Devices for damping vibrations of bodies. *US patent-989958*.

Fredö, C. R. (1997). A SEA-like approach for the derivation of energy flow coefficients with a finite element model. *Journal of Sound and Vibration*, 199(4):645–666.

Fung, Y. C. (1969). *An introduction to the theory of aeroelasticity*. Dover Publications.

Gardonio, P. and Elliott, S. J. (1999). Active control of structure-borne and airborne sound transmission through double panel. *Journal of Aircraft*, 36(6):1023–1032.

Gardonio, P., Elliott, S. J., and Pinnington, R. J. (1997a). Active isolation of structural vibration on a multiple-degree-of-freedom system, part I: the dynamics of the system. *Journal of Sound and Vibration*, 207(1):61–93.

Gardonio, P., Elliott, S. J., and Pinnington, R. J. (1997b). Active isolation of structural vibration on a multiple-degree-of-freedom system, part II: Effectiveness of active control strategies. *Journal of Sound and Vibration*, 207(1):95–121.

Gerald, C. F. and Green, C. J. (2003). *Numerical analysis*. Addison.

Goyder, H. G. D. and White, R. G. (1980a). Vibrational power flow from machines into built-up structures, part I: Introduction and approximate analyses of beam and plate-like foundations. *Journal of Sound and Vibration*, 68(1):59–75.

Goyder, H. G. D. and White, R. G. (1980b). Vibrational power flow from machines into built-up structures, part II: Wave propagation and power flow in beam-stiffened plates. *Journal of Sound and Vibration*, 68(1):77–96.

Goyder, H. G. D. and White, R. G. (1980c). Vibrational power flow from machines into built-up structures, part III: Power flow through isolation systems. *Journal of Sound and Vibration*, 68(1):97–117.

Guckenheimer, J. and Holmes, P. (1983). *Nonlinear oscillator, dynamical dystems, and bifurcations of vector fields*. Springer-Verlag.

Guyomar, D., Lallart, M., Petit, L., and Wang, X. J. (2011). Impact localization and energy quantification based on the power flow: A low-power requirement approach. *Journal of Sound and Vibration*, 330(13):3270–3283.

Horner, J. L. and White, R. G. (1991). Prediction of vibrational power transmission through bends and joints in beam-like structures. *Journal of Sound and Vibration*, 147(1):87–103.

Hunt, J. and Nissen, J.-C. (1982). The broadband dynamic vibration absorber. *Journal of Sound and Vibration*, 83(4):573 – 578.

Ibrahim, R. A. (2008). Recent advances in nonlinear passive vibration isolators. *Journal of Sound and Vibration*, 314(3):371–452.

Ibrahim, R. A. and Pettit, C. L. (2005). Uncertainties and dynamic problems of bolted joints and other fasteners. *Journal of Sound and Vibration*, 279(3):857–936.

Jenkins, M., Nelson, P., Pinnington, R., and Elliott, S. (1993). Active isolation of periodic machinery vibrations. *Journal of Sound and Vibration*, 166(1):117 – 140.

Ji, J. C. and Zhang, N. (2010). Suppression of the primary resonance vibrations of a forced nonlinear system using a dynamic vibration absorber. *Journal of Sound and Vibration*, 329(11):2044–2056.

Ji, L., Mace, B. R., and Pinnington, R. J. (2003). A power mode approach to estimating vibrational power transmitted by multiple sources. *Journal of Sound and Vibration*, 265(2):387 – 399.

Jones, K. D., Davids, S., and Platzer, M. F. (1999). Oscillating-wing power generation. In *Proceedings of the 3rd ASME/JSME Joint Fluids Engineering Conference*, pages 18–23, San Francisco, CA.

Jones, K. D. and Platzer, M. F. (1997). Numerical computation of flapping-wing propulsion and power extraction. *AIAA paper*, 97:0826.

Jones, R. T. (1940). The unsteady lift of a wing of finite aspect ratio. *NACA report*.

Keane, A. J. and Price, W. G. (1997). *Statistical energy analysis: an overview, with applications in structural dynamics*. Cambridge University Press.

Khun, M. S., Lee, H. P., and Lim, S. P. (2003). Computation of structural intensity for plates with multiple cutouts. *Structural Engineering and Mechanics*, 16(5):627 – 641.

Kim, G. and Singh, R. (1995). A study of passive and adaptive hydraulic engine mount systems with emphasis on non-linear characteristics. *Journal of Sound and Vibration*, 179(3):427 – 453.

Kittel, C. (1967). *Berkeley Physics Courses*. McGraw-Hill.

Kompella, M. S. and Bernhard, R. J. (1993). Measurement of the statistical variation of structural-acoustic characteristics of automotive vehicles. In *SAE Noise and Vibration Conference*, volume 931272.

Kwon, H.-W., Hong, S.-Y., Lee, H.-W., and Song, J.-H. (2011). Power flow boundary element analysis for multi-domain problems in vibrational built-up structures. *Journal of Sound and Vibration*, 330(26):6482 – 6494.

Langley, R. S. (1989). Application of the dynamic stiffness method to the free and forced vibrations of aircraft panels. *Journal of Sound and Vibration*, 135(2):319–331.

Langley, R. S. (1992). A wave intensity technique for the analysis of high frequency vibrations. *Journal of Sound and Vibration*, 159(3):483–502.

Lee, B. H. K., Jiang, L. Y., and Wong, Y. S. (1999). Flutter of an airfoil with a cubic restoring force. *Journal of Fluids and Structures*, 13(1):75–101.

Lee, C. M., Goverdovskiy, V. N., and Temnikov, A. I. (2007a). Design of springs with "negative"stiffness to improve vehicle driver vibration isolation. *Journal of Sound and Vibration*, 302(4):865–874.

Lee, H. P., Lim, S. P., and Khun, M. S. (2006). Diversion of energy flow near crack tips of a vibrating plate using the structural intensity technique. *Journal of Sound and Vibration*, 296(3):602–622.

Lee, Y. S., Vakakis, A. F., Bergman, L. A., McFarland, D. M., and Kerschen, G. (2007b). Suppressing aeroelastic instability using broadband passive targeted energy transfers, Part 1: Theory. *AIAA Journal*, 45(3):693–711.

Li, T. Y., Liu, J. X., and Zhang, T. (2004a). Vibrational power flow characteristics of circular plate structures with peripheral surface crack. *Journal of Sound and Vibration*, 276(3):1081–1091.

Li, T. Y., Zhang, T., Liu, J. X., and Zhang, W. H. (2004b). Vibrational wave analysis of infinite damaged beams using structure-borne power flow. *Applied Acoustics*, 65(1):91–100.

Li, T. Y., Zhang, W. H., and Liu, T. G. (2001). Vibrational power flow analysis of damaged beam structures. *Journal of Sound and Vibration*, 242(1):59–68.

Li, W. L. and Lavrich, P. (1999). Prediction of power flows through machine vibration isolators. *Journal of Sound and Vibration*, 224(4):757–774.

Liu, C. C., Li, F. M., Fang, B., Zhao, Y., and Huang, W. H. (2010). Active control of power flow transmission in finite connected plate. *Journal of Sound and Vibration*, 329(20):4124–4135.

Liu, L., Dowell, E. H., and Hall, K. C. (2007). A novel harmonic balance analysis for the Van der Pol oscillator. *International Journal of Non-Linear Mechanics*, 42(1):2–12.

Luzzato, E. and Ortola, E. (1988). The characterization of energy flow paths in the study of dynamic systems using S.E.A. theory. *Journal of Sound and Vibration*, 123(1):189 – 197.

Lyon, R. H. (1975). *Statistical energy analysis of dynamical systems: Theory and applications*. MIT Press.

Lyon, R. H. and Maidanik, G. (1962). Power flow between linearly coupled oscillators. *The Journal of the Acoustical Society of America*, 34(5):623–639.

Mace, B. (2003). Statistical energy analysis, energy distribution models and system modes. *Journal of Sound and Vibration*, 264(2):391–409.

Mace, B. R. (2005). Statistical energy analysis: coupling loss factors, indirect coupling and system modes. *Journal of Sound and Vibration*, 279(1):141–170.

Mace, B. R. and Shorter, P. J. (2000). Energy flow models from finite element analysis. *Journal of Sound and Vibration*, 233(3):369–389.

Mahajan, S. and Redfield, R. (1998). Power flow in linear, active vibration isolation systems. *Journal of Vibration and Acoustics*, 120(2):571–578.

Manning, J. E. (1994). Formulation of SEA parameters using mobility functions. *Philosophical Transactions of the Royal Society of London. Series A: Physical and Engineering Sciences*, 346(1681):477–488.

Manohar, C. S. and Keane, A. J. (1994). Statistics of energy flows in spring-coupled one-dimensional subsystems. *Philosophical Transactions of the Royal Society of London. Series A: Physical and Engineering Sciences*, 346(1681):525–542.

McKinney, W. and DeLaurier, J. (1981). The wingmill: An oscillating-wing windmill. *Journal of Energy*, 5(2):109–115.

Miller, D. W. and Von Flotow, A. (1989). A travelling wave approach to power flow in structural networks. *Journal of Sound and Vibration*, 128(1):145–162.

Ming, R. S., Pan, J., and Norton, M. P. (1999). The mobility functions and their application in calculating power flow in coupled cylindrical shells. *The Journal of the Acoustical Society of America*, 105:1702.

Moon, F. C. and Holmes, P. J. (1979). A magnetoelastic strange attractor. *Journal of Sound and Vibration*, 65(2):275–296.

Nayfeh, A. and Balachandran, B. (1995). *Applied nonlinear dynamics : Analytical, computational, and experimental methods*. Wiley.

Nayfeh, A. H. (1973). *Perturbation methods*. John Wiley & Sons.

Nayfeh, A. H. and Mook, D. T. (1979). *Nonlinear oscillations*. Wiley.

Nefske, D. and Sung, S. H. (1989). Power flow finite element analysis of dynamic systems-basic theory and application to beams. *ASME, Transactions, Journal of Vibration, Acoustics, Stress, and Reliability in Design*, 111:94–100.

Niu, J. C., Leung, A. Y. T., Lim, C. W., and Ge, P. Q. (2008). An active vibration control model for coupled flexible systems. *Proceedings of the Institution of Mechanical Engineers, Part C: Journal of Mechanical Engineering Science*, 222(11):2087–2098.

Nucera, F., Vakakis, A. F., McFarland, D. M., Bergman, L. A., and Kerschen, G. (2007). Targeted energy transfers in vibro-impact oscillators for seismic mitigation. *Nonlinear Dynamics*, 50(3):651–677.

Oueini, S. S., Nayfeh, A. H., and Pratt, J. R. (1998). A nonlinear vibration absorber for flexible structures. *Nonlinear Dynamics*, 15(3):259–282.

Pan, J., Pan, J., and Hansen, C. H. (1992). Total power flow from a vibrating rigid body to a thin panel through multiple elastic mounts. *The Journal of the Acoustical Society of America*, 92:895.

Peng, Z. and Zhu, Q. (2009). Energy harvesting through flow-induced oscillations of a foil. *Physics of Fluids*, 21:1 – 9.

Petyt, M. (2010). *Introduction to finite element vibration analysis*. Cambridge University Press.

Pinnington, R. J. and White, R. G. (1981). Power flow through machine isolators to resonant and non-resonant beams. *Journal of Sound and Vibration*, 75(2):179–197.

Pipes, L. A. (1953). Analysis of a non-linear vibration absorber. *Journal of Applied Mechanics*, 20:515–518.

Platus, D. L. (1991). Negative-stiffness-mechanism vibration isolation systems. In *Proceedings of SPIE-The International Society for Optical Engineering, Vibration Control in Microelectronics, Optics, and Metrology*, volume 1619, pages 44–54.

Popov, G. and Sankar, S. (1995). Modelling and analysis of non-linear orifice type damping in vibration isolators. *Journal of Sound and Vibration*, 183(5):751–764.

Press, W. H., Flannery, B. P., Teukolsky, S. A., and Vetterling, W. T. (1992). *Numerical Recipes: The Art of Scientific Computing*, volume 1. Cambridge University Press.

Ramlan, R., Brennan, M. J., Mace, B. R., and Kovacic, I. (2010). Potential benefits of a non-linear stiffness in an energy harvesting device. *Nonlinear Dynamics*, 59(4):545–558.

Rivin, E. I. (2003). *Passive vibration isolation*. ASME Press.

Roberson, R. E. (1952). Synthesis of a nonlinear dynamic vibration absorber. *Journal of the Franklin Institute*, 254(3):205–220.

Rowat, P. F. and Selverston, A. (1993). Modeling the gastric mill central pattern generator of the lobster with a relaxation-oscillator network. *Journal of Neurophysiology*, 70(3):1030–1053.

Royston, T. J. and Singh, R. (1996). Optimization of passive and active non-linear vibration mounting systems based on vibratory power transmission. *Journal of Sound and Vibration*, 194(3):295–316.

Royston, T. J. and Singh, R. (1997). Vibratory power flow through a nonlinear path into a resonant receiver. *The Journal of the Acoustical Society of America*, 101:2059–2069.

Sciulli, D. and Inman, D. J. (1999). Isolation design for fully flexible systems. *Journal of Intelligent Material Systems and Structures*, 10(10):813–824.

Shankar, K. and Keane, A. J. (1995a). Energy flow predictions in a structure of rigidly joined beams using receptance theory. *Journal of Sound and Vibration*, 185(5):867–890.

Shankar, K. and Keane, A. J. (1995b). A study of the vibrational energies of two coupled beams by finite element and green function (receptance) methods. *Journal of Sound and Vibration*, 181(5):801–838.

Shankar, K. and Keane, A. J. (1997). Vibrational energy flow analysis using a substructure approach: The application of receptance theory to FEA and SEA. *Journal of Sound and Vibration*, 201(4):491–513.

Shimizu, E., Isogai, K., and Obayashi, S. (2008). Multiobjective design study of a flapping wing power generator. *Journal of Fluids Engineering*, 130(2).

Simmons, C. (1991). Structure-borne sound transmission through plate junctions and estimates of SEA coupling loss factors using the finite element method. *Journal of Sound and Vibration*, 144(2):215–227.

Steel, J. A. and Craik, R. J. M. (1994). Statistical energy analysis of structure-borne sound transmission by finite element methods. *Journal of Sound and Vibration*, 178(4):553–561.

Thomsen, J. J. (2003). *Vibrations and stability: Advanced theory, analysis, and tools*. Springer.

Ueda, Y. (1980). Explosion of strange attractors exhibited by Duffing's equation. *Annals of the New York Academy of Sciences*, 357(1):422–434.

Unruh, J. F. (1987). Structure-borne noise control for propeller aircraft. In *American Institute of Aeronautics and Astronautics Conference*, volume 1.

Vakakis, A. F., Gendelman, O. V., Bergman, L. A., McFarland, D. M., Kerschen, G., and Lee, Y. (2008). *Nonlinear targeted energy transfer in mechanical and structural systems*, volume 156. Springer.

Van der Pol, B. (1920). A theory of the amplitude of free and forced triode vibrations. *Radio Review*, 1:701–710,754–762.

Viguié, R. and Kerschen, G. (2009). Nonlinear vibration absorber coupled to a nonlinear primary system: A tuning methodology. *Journal of Sound and Vibration*, 326(3):780–793.

Viguié, R. and Kerschen, G. (2010). On the functional form of a nonlinear vibration absorber. *Journal of Sound and Vibration*, 329(25):5225–5232.

Viguié, R., Kerschen, G., Golinval, J. C., McFarland, D. M., Bergman, L. A., Vakakis, A. F., and van de Wouw, N. (2009). Using passive nonlinear targeted energy transfer to stabilize drill-string systems. *Mechanical Systems and Signal Processing*, 23(1):148–169.

Virgin, L. N., Santillan, S. T., and Plaut, R. H. (2008). Vibration isolation using extreme geometric nonlinearity. *Journal of Sound and Vibration*, 315(3):721–731.

von Groll, G. and Ewins, D. J. (2001). The harmonic balance method with arc-length continuation in rotor/stator contact problems. *Journal of Sound and Vibration*, 241(2):223 – 233.

Wang, X. Q., Wong, W. O., and Cheng, L. (2009). Modal power flow with application to damage detection. *International Journal of Engineering Science*, 47(4):512–523.

Wang, Z. H., Xing, J. T., and Price, W. G. (2002a). An investigation of power flow characteristics of L-shaped plates adopting a substructure approach. *Journal of Sound and Vibration*, 250(4):627–648.

Wang, Z. H., Xing, J. T., and Price, W. G. (2002b). Power flow analysis of indeterminate rod/beam systems using a substructure method. *Journal of Sound and Vibration*, 249(1):3–22.

Wang, Z. H., Xing, J. T., and Price, W. G. (2004). A study of power flow in a coupled plate–cylindrical shell system. *Journal of Sound and Vibration*, 271(3):863–882.

Whittaker, E. T. and Watson, G. N. (1996). *A course of modern analysis*. Cambridge University Press.

Winterflood, J. (2001). *High performance vibration isolation for gravitational wave detection*. PhD thesis, University of Western Australia.

Wohlever, J. C. and Bernhard, R. J. (1992). Mechanical energy flow models of rods and beams. *Journal of Sound and Vibration*, 153(1):1–19.

Wolf, A., Swift, J. B., Swinney, H. L., and Vastano, J. A. (1985). Determining Lyapunov exponents from a time series. *Physica D: Nonlinear Phenomena*, 16(3):285–317.

Wong, W. O., Wang, X. Q., and Cheng, L. (2009). Modal power flow analysis of a damaged plate. *Journal of Sound and Vibration*, 320(1):84–100.

Wu, T. Y., Q., W. X., and Cheng, L. (1972). Extraction of flow energy by a wing oscillating in waves. *Journal of Ship Research*, 16(66):66–78.

Xing, J. T. and Price, W. G. (1999a). Correction for Xing and Price, A power-flow analysis based on continuum dynamics. *Proceedings of the Royal Society of London. Series A: Mathematical, Physical and Engineering Sciences*, 455:4385–4385.

Xing, J. T. and Price, W. G. (1999b). A power–flow analysis based on continuum dynamics. *Proceedings of the Royal Society of London. Series A: Mathematical, Physical and Engineering Sciences*, 455(1982):401–436.

Xing, J. T. and Price, W. G. (2004). A substructure method for power flow analysis of non-linear systems consisting of linear substructures and non-linear controllers. In *Proceedings of the Eleventh International Congress on Sound and Vibration*, pages 2657–2664.

Xing, J. T., Xiong, Y. P., Wiecigroch, M., and Cao, Q. (2011). A mathematical modelling for an integrated electric converter-nonlinear oscillator-water interaction system to harness wave energy. In *Proceedings of the Seventh European Nonlinear Dynamics Conference (ENOC)*, pages 1–6.

Xiong, Y. P. and Cao, Q. (2011). Power flow characteristics of coupled linear and nonlinear oscillators with irrational nonlinear stiffness. In *Proceedings of the Seventh European Nonlinear Dynamics Conference (ENOC)*, pages 1–6.

Xiong, Y. P., Wang, X. P., Xing, J. T., and Price, W. G. (2000). Hybrid active and passive control of vibratory power flow in flexible isolation system. *Shock and Vibration*, 7(3):139–148.

Xiong, Y. P., Xing, J. T., and Price, W. G. (2001). Power flow analysis of complex coupled systems by progressive approaches. *Journal of Sound and Vibration*, 239(2):275–295.

Xiong, Y. P., Xing, J. T., and Price, W. G. (2003). A general linear mathematical model of power flow analysis and control for integrated structure–control systems. *Journal of Sound and Vibration*, 267(2):301–334.

Xiong, Y. P., Xing, J. T., and Price, W. G. (2005a). Interactive power flow characteristics of an integrated equipment-nonlinear isolator-travelling flexible ship excited by sea waves. *Journal of Sound and Vibration*, 287(1):245–276.

Xiong, Y. P., Xing, J. T., and Price, W. G. (2005b). A power flow mode theory based on a system's damping distribution and power flow design approaches. *Proceedings of the Royal Society A: Mathematical, Physical and Engineering Science*, 461(2063):3381–3411.

Yang, J., Xiong, Y. P., and Xing, J. T. (2011). Investigations on a nonlinear energy harvesting device consisting of a flapping foil and an electro-magnetic generator using power flow analysis. In *Proceedings of ASME 2011 International Design Engineering Technical Conferences and Computers and Information in Engineering Conference (IDETC/CIE2011)*, pages 1–8.

Yang, J., Xiong, Y. P., and Xing, J. T. (2012a). Examinations of nonlinear isolators using power flow approach. In *Proceedings of the 23rd International Congress of Theoretical and Applied Mechanics (ICTAM)*, pages 1–2.

Yang, J., Xiong, Y. P., and Xing, J. T. (2012b). Power flow behaviour of the duffing oscillator. In *Proceedings of the International Conference on Noise and Vibration Engineering (ISMA 2012)*, pages 2601–2610.

Yang, J., Xiong, Y. P., and Xing, J. T. (2013). Dynamics and power flow behaviour of a nonlinear vibration isolation system with a negative stiffness mechanism. *Journal of Sound and Vibration*, 332:167–183.

Zhu, Q., Haase, M., and Wu, C. H. (2009). Modeling the capacity of a novel flow-energy harvester. *Applied Mathematical Modelling*, 33(5):2207–2217.

Zhu, Q. and Peng, Z. (2009). Mode coupling and flow energy harvesting by a flapping foil. *Physics of Fluids*, 21(3):033601–033601.

Zhu, X., Li, T. Y., Zhao, Y., and Liu, J. X. (2006). Structural power flow analysis of Timoshenko beam with an open crack. *Journal of Sound and Vibration*, 297(1):215–226.

Zhu, X., Li, T. Y., Zhao, Y., and Yan, J. (2007). Vibrational power flow analysis of thin cylindrical shell with a circumferential surface crack. *Journal of Sound and Vibration*, 302(1):332–349.

Zong, Z., Lee, H. P., and Lu, C. (2006). A three-dimensional human head finite element model and power flow in a human head subject to impact loading. *Journal of Biomechanics*, 39(2):284–292.